Studies of Solution-Processed Organic Light-Emitting Diodes and All-Polymer Solar Cells

Taeshik Earmme

A dissertation

Submitted in partial fulfillment of the

Requirements for the degree of

Doctor of Philosophy

University of Washington

2014

Reading Committee:

Samson A. Jenekhe, Chair

Lilo D. Pozzo

Hong Shen

Program Authorized to Offer Degree:

Department of Chemical Engineering

University of Washington

Abstract

Studies of Solution-Processed Organic Light-Emitting Diodes

and All-Polymer Solar Cells

Taeshik Earmme

Chair of the Supervisory Committee:

Professor Samson A. Jenekhe

Department of Chemical Engineering

Organic electronics, commonly referred as plastic electronics, is an emerging technology for addressing many challenges that our society is facing. Over the past two decades, organic electronics has gained enormous attention due to its many advantages, including low power consumption, low-cost, scalable, and flexible design. Development of high-performance devices by designing new materials and related device engineering is crucial to the future advances in organic electronics. This dissertation focuses on studies of two classes of optoelectronic devices, organic light-emitting diodes (OLEDs) and all-polymer solar cells, fabricated by solution-processing of organic semiconductors, and aims to better understand structure-property-performance relationships resulting from solution-based fabrication.

Study of bisindenoanthrazolines and dendritic oligoquinolines were found to be promising new electron-transport materials (ETMs) for high-performance phosphorescent OLEDs (PhOLEDs). Solution-processed multilayered blue PhOLEDs with orthogonal solution-processed ETMs were found to have the highest efficiency (luminous efficiency = 28.3 cd/A and external quantum efficiency = 15.5 %) observed to date among polymer-based devices. The surface morphology and charge-transport properties of the ETMs were successfully tuned by solution-deposition, which made it possible to eliminate the need for interfacial materials and low work function metals commonly used as cathode materials in OLEDs. High-performance solution-processed PhOLEDs using commercial ETMs were also demonstrated using orthogonal solution-processing. The bulk conductivity and charge transport properties of ETMs were enhanced by a novel solution n-doping with alkali metal salts.

Sulfone- and dibenzosuberane-based materials were demonstrated as promising new classes of ETMs that possess high triplet energies (> 2.8 - 3.0 eV). Multilayered PhOLEDs with a solution-processed blue triplet emission layer using high triplet energy ETMs as an electron-transport layer were found to have significantly improved performance, including high current efficiency and external quantum efficiency (~ 20 %).

Finally, solution-processed polymer/polymer blend solar cells using new naphthalene diimide-based acceptor copolymers were investigated and found to be the most efficient all-polymer solar cells reported to date. Controlling polymer blend morphology by solution-processing from a co-solvent system also led to further enhancement of device performance.

Table of Contents

List of Figures and Charts

List of Tables

Acknowledgements

I wish to express my sincere appreciation to my PhD dissertation advisor, Professor Samson A. Jenekhe, for his guidance and support. His insightful advices and invaluable suggestions have been strong stimulus to the successful completion of my work. I also appreciate Professors Lilo D. Pozzo, Hong Shen, and Christine K. Luscombe for their time serving on my supervisory committee and providing valuable comments.

During my graduate study, I have experienced precious opportunity of interacting with fellow students and researchers. I thank the past and present memebers of the Jenekhe group – Dr. Felix Sunjoo Kim, who had been sitting next to my desk for almost 6 years as a senior and also a junior to me with useful discussions and squabbling, Ye-Jin Hwang, Dr. Soon Ok Jeon, Dr. Eilaf Ahmed, Dr. Pei-Tzu Wu, Dr. Jessica M. Hancock, Dr. Abhishek P. Kulkarni, Dr. Haiyan Li, Dr. Nishit M. Murari, Dr. Selvam Subramaniyan, Dr. Hao Xin, Dr. Guoqiang Ren, Karl Kerr, Matthew J. Crane, Brett Courtright, Frank Eberle, and Sam Davydov. I thank to all visiting scholars throughout my years - Dr. Takahiro Kojima, Dr. Masashi Mamada, Dr. Kazuhiro Nakabayashi, Prof. Taewoo Kwon, Prof. Unyong Jeong, and Yujeong Lee. I also thank to Material Science guys, Nam Chul Cho and Dr. Jungho Jin for hanging out with me, and all the GLC members in South Korea for their kind support.

I would like to acknowledge the Department of Chemical Engineering at the UW, the National Science Foundation, the U. S. Department of Energy, and Solvay S. A. for the financial support.

Finally, I would like to express my sincere thankfulness to my parents and twin brother - Prof. Youn Young Earmme for his enthusiastic support and advice, Ms. Young Choo Cho for her prayer, and Dr. Taemin Earmme. Especially I would also like to take this opportunity to express

my heartfelt gratitude and love to my wife Yuna and my young Padawan, Albert. Without their dedication and strong support, this work would not have been possible at all.

Chapter 1. Introduction

1.1. Overview

Since Tang and VanSlyke in 1987 developed novel electroluminescent (EL) device using organic materials with a double-layered structure[1] and Tsutsui and Saito in 1988 with separate hole and electron-transport layers,[2] tremendous research effort has been made in the field of organic light-emitting diodes (OLEDs). The Nobel Prize for Chemistry awarded in 2000 to Heeger, MacDiarmid and Shirakawa for their discovery of "conductive plastics (polymers)" boosted the research in the field of organic electronics. Among these organic based electronics, OLEDs would be the nearest future technology which has been already launched into market as commercial products. It demonstrates the final outcome from a fascinating small discovery to our daily life that we may enjoy from our palm as small hand-held electronic devices to large domestic appliances, automobiles, or even inner/outer lighting sources. The relevant materials, device engineering, and manufacturing skills will not only be limited to OLEDs but will definitely give a way to open the real era of organic electronics, such as organic solar cells (OSCs), organic field-effect transistors (OFETs), and organic sensors, etc. It is therefore appropriate to review the progress and current status of research in organic light-emitting diodes at this stage.

Advanced organic semiconducting material is crucial factor to achieve high device performance, durability, feasible processability and low-cost. A carefully designed molecular architecture made possible to tune the electronic structure, charge carrier mobility, morphology, physical and chemical characteristics of the organic semiconductors. Most materials of interest in organic electronics have either hole-transport (*p-type*) or electron-transport (*n-type*) characteristics. However, it is rather challenging to achieve efficient electron-transport

characteristics compared to hole-transport due to the difficulty in the formation of very stable anion in the organic semiconductor by preventing trapping of the electron by intrinsic chemical impurities and extrinsic factors such as molecular oxygen.[3] High electron affinity (EA) with good electron-accepting ability is known to achieve high electron-transport in the presence of oxygen-containing atmosphere.

1.2. Organic Light-Emitting Diodes (OLEDs)

1.2.1. Basic Principles of OLEDs

Organic Light-Emitting Diodes. OLEDs are basically double charge injection diodes, requiring simultaneous injection of holes and electrons to the organic material sandwiched between both electrodes. The schematic diagram of the basic operation of OLEDs and energy level diagram of OLEDs are presented in Figure 1.1a and 1.1b, respectively. The key processes involved are: (i) *Double charge injection*: Upon applying a bias on both electrodes, holes are injected from the anode into the highest occupied molecular orbital (HOMO) energy level of adjunct layer and electrons are injected from the cathode into the lowest unoccupied molecular orbital (LUMO) energy level. (ii) *Charge transport*: The injected charge carriers move towards each other under the applied electric field. The charge carriers are then directly or via hole / electron transport layers transport into emission layer. (iii) *Charge recombination (exciton generation)*: Inside the emission layer, the opposite charge carrier make contact and annihilate each other leading to the excited state formation of hole-electron pairs, called excitons. The excitons could be either singlet or triplet excitons. (iv) *Light emission*: The radiative decay of the excitons releases light from the device. The decay of singlet excitons is called *electroluminescence* (fluorescent

emission) and that of the triplet excitons is called *electrophophorescence* (phosphorescent emission).

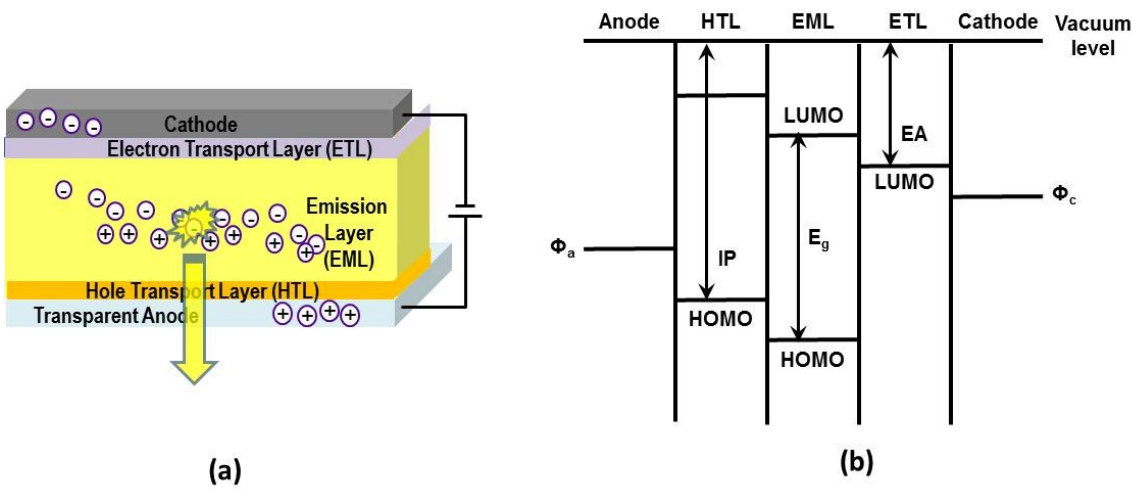

Figure 1.1. (a) Schematic of basic operation of OLEDs; and (b) Energy-level diagrams of OLEDs.

Device Structure and Efficiency. The simplest structure of OLEDs is single emitting layer (EML) device. However, device with single layered architecture is not preferred in order to achieve high-performance OLEDs. In a single layer OLED, the electron affinity (EA) or LUMO level and the ionization potential (IP) or HOMO level relative to the cathode work function and the anode work function, respectively, determine the feasibility of the charge injection into the emission layer. Large mismatches, thus large energy barriers for hole injection at the anode and electron injection at the cathode, lead to poor OLED performance. To overcome the mismatch of energy barrier between the adjunct layers, multilayered device architectures are used. Hole injection and/or transport layers (HTL) are used at the anode and electron injection and /or transport layers (ETL) are used at the cathode to overcome the barrier between the organic layers and electrodes (Figure 1.1b). The use of more additional layers to enhance charge injection and

transport properties has resulted significant improvement in device performance, although more complicated OLED architecture is needed.

There are many factors that may determine the overall performance of the OLEDs. To discuss the device efficiency in OLEDs, precise definition of internal quantum efficiency (η_{int}) and external quantum efficiency (η_{ext}) is essential. The internal quantum efficiency is defined as the ratio of the total number of photons generated within the device structure to the number of electrons (charge carriers) injected. While the generally known definition of the external quantum efficiency is that the ratio of the number of photons emitted by the device into the viewing angle to the number of electrons injected.[5,6] From the above, the internal quantum efficiency and external quantum efficiency were differed by the fraction of photons coupled out from the device (η_c), a.k.a. outcoupling efficiency (η_c). The relationship can be expressed as: $\eta_{ext} = \eta_c \cdot \eta_{int}$ (eq. 1) The internal quantum efficiency can be divided into three different factors. Those are: (i) Fraction of total excitons formed which result in radiative transitions (η_{ex}). By the spin statistics the ratio of singlet to triplet excitons are known to be 1 to 3, which means η_{ex} = 25% for fluorescent molecules and polymers and it can approach η_{ex} = 100% for highly phosphorescent materials. (ii) Intrinsic photoluminescence quantum efficiency (Φ_p) for radiative decay (quantum yield of the emitting material), including both fluorescence and phosphorescence. (iii) Ratio of electrons to holes injected from opposite contacts (γ), which we commonly call charge carrier balance. As a result, we can rewrite the equation (eq. 1.1): $\eta_{ext} = \eta_c \cdot \gamma \cdot \eta_{ex} \cdot \Phi_p$ (eq.1.2).

OLEDs has been mainly fabricated with the multilayered device structure with emission layer (EML) sandwiched between hole-injection / -transport layers (HIL/HTL) and electron-injection / -transport layers (EIL/ETL) with the electrode located on either side. General OLED structure consisted of: Anode/HIL/HTL/EML/ETL/EIL/Cathode. Additional layers can be

inserted or doped layers can be used to further enhance device performance. For the electrodes, transparent conductive metal oxides (TCOs) such as ITO (In_2O_3:Sn), FTO (SnO_2:F), IZO (In_2O_3:Zn), or AZO (ZnO:Al)[7] and metal electrodes such as Al, Ag, Au, Pt Cu, or Ni are commonly used. Most of the conventional OLEDs use ITO glass substrate as transparent anode to inject holes while it can also be used as cathode to inject electrons depending on the sequence of the multilayered structure (*i.e.* inverted OLEDs). On the opposite side, metals are usually deposited as either cathode or anode to inject counter charges into the adjunct layer. Figure 1.2 shows schematic of typical OLED structures where ITO electrode is used as transparent anode **(**Figure 1.2a**)** or used as transparent cathode (Figure 1.2b). Furthermore, if transparent electrodes are used in both sides of the electrodes, transparent OLEDs can be fabricated to emit light from both sides. Various types of transparent electrodes based on nanoscale materials other than TCOs have emerged recently. Percolative networks with randomly distributed carbon nanotubes (CNTs)[8-10] or graphene[11-13], metal thin films,[14] nanogrids, nanowires, and nanofibers[15-17] are applied as promising transparent electrodes. An easiness of adopting various types of electrodes or rigid/flexible substrates provides an opportunity of innovative product design.

Fabrication method of OLEDs can be largely divided into two categories: vacuum thermal evaporation (dry-process) and solution-based deposition (wet-process). Optoelectronic devices with small molecular organic semiconductors are conventionally deposited using vacuum thermal evaporation. This traditional method has ability to deposit films with monolayer precision and preserves the purity of source material. Especially, vacuum thermal evaporation has been widely used in fabrication of high-performance OLEDs, since the multilayered structure can be achieved by the carefully controlled sequential evaporation of organic semiconductors.

Although current small-molecules have enabled the development of highly efficient OLEDs with multilayered structures, vacuum thermal deposition of small molecules is an expensive process.[18,19] Solution-processing can be an economically attractive alternative to vacuum thermal evaporation method. Solution-based device fabrication methods, such as spray-on or spin-on deposition, ink-jet printing, screen printing, and roll-to-roll printing processes, are considered critical to next generation, low cost, large area, high performance OLEDs. However, fabrication of multilayered devices by solution-based processing is challenging because of the requirement of orthogonal solvents that would not dissolve or disrupt the underlying emissive layer.[20-22]

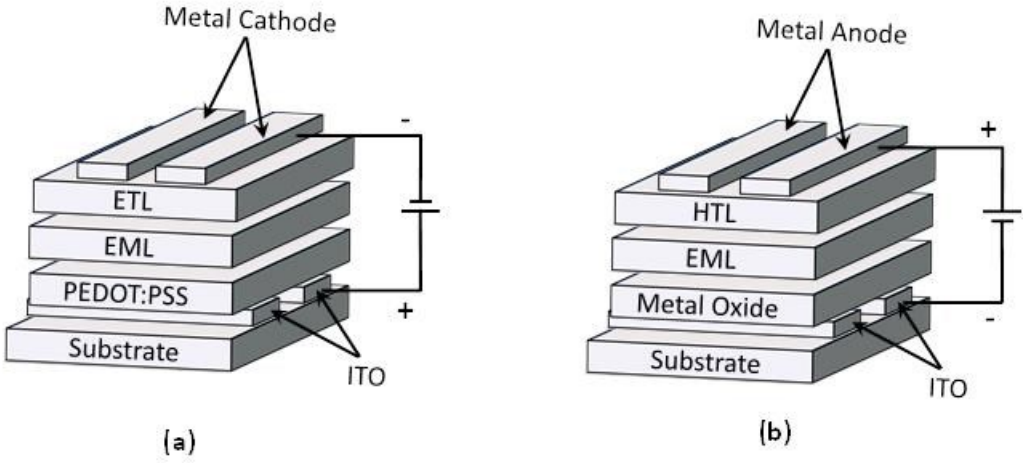

Figure 1.2. Schematic of OLED structure: (a) Conventional OLED with ITO as transparent anode and PEDOT:PSS as hole-injection/-transport layer; (b) Inverted OLED with ITO as transparent cathode and metal oxide as electron-injection layer.

1.2.2. Advantages of OLEDs

The primary reason for the high interest in the organic light-emitting diodes (OLEDs) technology is that it offers many advantages over traditional displays such as liquid-crystal displays (LCD). These advantages can be categorized as following: (i) Potential low manufacturing cost. In the near future, the manufacturing cost of the OLEDs can be reduced from the feasible low-temperature processing organics by dry or wet processing techniques. (ii)

Thin, lightweight, and flexibility. OLEDs have only several hundred nanometers of thin film structure which can be easily deposited onto various types of substrates. OLEDs can be embedded to flexible plastic substrates, clothing, and fabrics that can be easily carried and rolled up. There can be unlimited potential applications as variety of substrates and device architectures are being developed. (iii) Low power consumption and bright contrast. Inactive OLED pixels do not consume power or emit light which make more efficient than the LCDs that require a consistently turned-on white backlight. The ability of completely turned off states offers better contrast with darker blacks. (iv) Wide viewing angle with fast response time. As the OLED pixels directly emit light, it enables wider viewing angle almost 180 degrees. OLEDs also have a quick response time of less than 0.01 milliseconds which is 100 to 1000 times faster than LCDs. (v) Wide operating temperature range. OLEDs have a larger range of operating temperatures, particularly at low temperature (~ -40 °C), compared to the LCDs (~ -10 °C). It enables the use of displays or lighting in extreme environmental conditions.

1.3. Organic Solar Cells (OSCs)

1.3.1. Basic Principles of OSCs

Organic Solar Cells. A solar cell (or photovoltaic cell) is a semiconductor device that converts absorbed sunlight (photons) into electricity. Incident photons in a semiconductor create excitons (bound electron-hole pairs) whose subsequent dynamics, relaxation, and dissociation are crucial to the photoconversion process. Equally important to the overall efficiency of the photon-to-electricity conversion is the nature of the charge carrier transport to collecting electrodes after exciton dissociation into free charge carriers. Unlike Si and other inorganic semiconductors, in which photoexcitation produces free charge carriers directly or delocalized excitons with small

binding energies (~10 meV) light absorption in current organic/polymer semiconductors creates Frenkel excitons with large binding energies (~ 0.4 - 1.0 eV) and small diffusion lengths (5-20 nm). Consequently, photogeneration of free charge carriers in organic semiconductors requires dissociation of excitons at a heterojunction with another material having energy band offsets suitable for exciton dissociation. Furthermore, carrier mobilities in inorganic semiconductors are orders of magnitude larger than their organic counterparts. These fundamental differences in the photoconversion and charge transport mechanisms translate to a huge difference in photovoltaic power conversion efficiency: ~ 15-35 % for inorganic semiconductors (Si, GaAs, etc.) compared to ~ 3-10 % for organic semiconductors.

The bulk heterojunction (BHJ) organic photovoltaic (OPV) cell, consisting of a binary blend or composite of a donor polymer and an acceptor material, was introduced in 1995 by Heeger to address the problem of small exciton diffusion lengths (L_d = 5-20 nm) in current organic/polymer semiconductors. Extensive studies of such BHJ-OPV cells have focused largely on blends or nanocomposites of donor polymer with acceptor materials based on fullerenes although CdSe and PbS nanocrystals, TiO_2 nanoparticles, carbon nanotubes, acceptor polymers and acceptor small molecules have also been explored to a much lesser extent. BHJ-OPV cells based on fullerene (PCBM) acceptors and donor polymers currently give the highest power conversion efficiencies (~10 % PCE). Optimization of factors such as blend composition, processing conditions, various annealing protocols, and use of processing additives has recently led to enhanced photovoltaic performance.

Operation of OSCs. OSC (or organic photovoltaics, OPVs) s are basically consisted of double charge collection diodes, requiring simultaneous collection of holes and electrons generated by dissociation of excitons from the conjugated organic material sandwiched between both

electrodes. The schematic diagram and the basic operation of OSCs are presented in Figure 1.3a and 1.3b, respectively. The key processes involved are: (i) *Absorption of photons (exciton generation) and exciton diffusion*: Under illumination of a sun light on transparent electrodes, excitons, *i.e.* hole-electron pairs are formed by excitation of ground state electrons inside the active layer which consisted of p-n binary junction or heterojuction, and then they are diffused into the active layer. (ii) *Charge dissociation*: Diffused excitons make contact with the interfacial junction between *p*- and *n*- type semiconductors result in charge separation to create separate charge carriers. (iii) *Charge transport*: The separated charge carriers move towards each side of the electrodes via the highest occupied molecular orbital (HOMO) energy level of donor materials and the lowest unoccupied molecular orbital (LUMO) energy level of the acceptor materials. (iv) *Charge collection*: Both charge carriers are collected by each electrode and thus generate photovoltage and photocurrent throughout the circuit between anode and cathode electrodes.

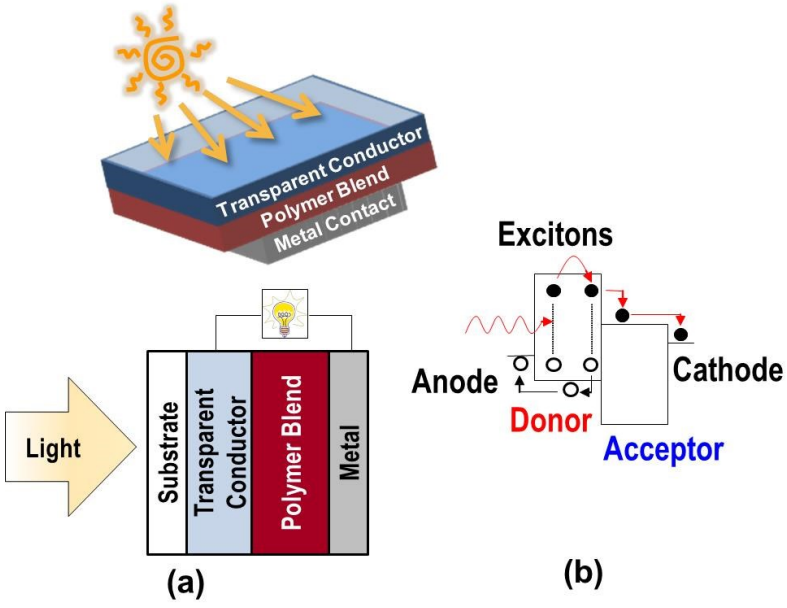

Figure 1.3. (a) Schematic diagram of OSCs; and (b) Operation schematic of OSCs.

1.3.2. Advantages of OSCs

The main reason for the high interest in the organic solar cell technology is that it offers many advantages over traditional silicon-based photovoltaic devices. These advantages can be categorized as following: (i) Potential low manufacturing and processing cost. In the near future, the manufacturing cost of the OSCs can be reduced from the feasible low-temperature processing organics by dry or wet processing techniques. (ii) Thin, lightweight, transparent and flexibility. OSCs have only several hundred nanometers of thin film structure which can be easily deposited onto various types of substrates. OSCs can be embedded to flexible plastic substrates, clothing, and fabrics that can be easily carried and rolled up. Furthermore, there can be unlimited potential applications in windows or buildings as a clean energy source as well as satisfying the design needs resulted from their flexibility and transparency. (iii) Tailoring molecular structure. Since conjugated polymers and small molecules can be designed and modified to obtain specific electronic structures and absorption properties, it is feasible to obtain desired properties which can be used for various photovoltaic applications.

1.4. Major Challenges and Research Objectives

1.4.1. Major Challenges

In the past few decades, extensive studies of organic electronics have been performed by academia and industry to understand the underlying principles/mechanisms, develop new materials and fabrication methods, to improve device performance by engineering for real commercialization of products. However, there are still many challenges in the research field such as designing suitable organic materials, control solid-state morphology to desired form,

achieving durability for the improved cycle life, and manufacturing technology in a large scale with assured productivity.

Organic light-emitting diodes (OLEDs) have been already launched into market for applications in full-color display panels, flexible displays, and solid-state lighting. Recently, much progress has been made in developing phosphorescent OLEDs (PhOLEDs) compared to traditional fluorescent OLEDs since nearly 100% internal quantum efficiency can be achieved. However, blue emitting PhOLEDs remain challenging since high energy triplet excitons tend to flow out without radiative decay in the emissive layer (EML). Insertion of a wide-energy-gap / high triplet energy electron-transport material between the cathode and the blue-phosphorescent EML represents a successful strategy for confining excitons to the EML and for blocking holes, facilitating a good charge balance in the EML. However, most of the high-performance PhOLEDs achieved to date have been mainly based on vacuum-deposited small-molecules involving thermal evaporation processes to obtain multilayered device structures. Solution-based PhOLEDs provide an economically attractive alternative to those processed by vacuum deposition, and are considered essential to low-cost, large area lighting devices. Although sequential solution-processing of highly efficient multilayered device structures has great potential, it is very challenging because the solvent used to deposit the subsequent layer tends to dissolve or swell the underlying layer.

Among the field of organic electronics, organic solar cells (OSCs) or polymer solar cells (PSCs) are of great interest as promising economic technology to convert solar energy to electricity. So far, significant progress has been made in developing polymer/fullerene bulk heterojunction (BHJ) solar cells with around 10.0% of power conversion efficiency (PCE) to date. However, polymer/polymer BHJ solar cells have been investigated in order to overcome

disadvantages of fullerene acceptors and also to take advantages of polymer/polymer systems despite of much lower PCE compared to polymer/fullerene solar cells. All-polymer BHJ solar cells consisted of binary blends of *p-type* (donor) and *n-type* (acceptor) polymers have potential benefits compared to polymer/fullerene system, including enhanced absorption coefficient and increased open-circuit voltage (V_{oc}) of the devices, easy control of viscous solution for industrial coating, and superior life durability and thermal / mechanical robustness of the devices due to the morphological stability. Despite of these advantages, the main drawback of all-polymer solar cells is their relatively low short-circuit current density and external quantum efficiency (EQE), rarely exceeding 5.0 mA/cm^2 and 30%, respectively, and thus low PCE value generally not more than 3.0%.

Further advances in improving the efficiencies of polymer/polymer solar cell systems to commercially useful levels require major innovations in acceptor and donor materials and optimization of device architectures at the molecular- and nano-scales. Although fullerene molecules have proven to be excellent acceptor materials in bulk heterojunction (BHJ) polymer/fullerene solar cells, they are inherently chemically, thermally, and photochemically unstable in ambient air, which limits their potential in practical OSCs. In addition, a better fundamental understanding of the photoconversion processes, charge transport, charge collection, and blend morphology in polymer/polymer BHJ solar cells is critical towards achieving the theoretical device conversion efficiency. The intrinsic, photochemical, and environmental stability/durability of all-polymer solar cells is also a major scientific challenge that requires investigation.

1.4.2. Research Objectives

The primary objective of this research is to investigate and demonstrate high-performance organic optoelectronic devices enabled by new electron-transport materials and novel solution-processing that could be exploited in low-cost, large scale device fabrications. The objectives of this research focus on addressing several current issues in the field.

(i) Development of novel electron-transport materials and understand the factors affecting electronic/optoelectronic properties to demonstrate high-performance optoelectronic devices. To be effective in enhancing the performance of optoelectronic devices, electron transport material must combine (i) a high electron affinity to enable efficient electron-injection and (ii) a high electron mobility to enhance electron flux, with (iii) a high ionization potential and (iv) a high triplet energy to confine excitons within the emissive layer. Thus far, few electron transport materials (ETMs) satisfy these criteria. The development of new electron transport materials with optimum properties achieved by molecular design, device engineering, and processing optimization are essential for next generation optoelectronic devices, especially for PhOLEDs. For this purpose, intensive development of novel electron-transport materials has been performed (Chapter 2, 3, and 5), regarding detailed case studies of the relationships between molecular structures, morphology, electronic and charge transport properties of various series of electron-transport materials. Especially Chapter 5 describes new classes of electron-transport materials based with high triplet energies.

(ii) Engineering and studying novel orthogonal solution-processing for multilayered device structures. The longstanding challenge in solution-based fabrication of high performance optoelectronic and other devices is achieving orthogonal sequential solution deposition of multilayered structures. This requirement that the solvent used to deposit the overlayer thin film

not dissolve or swell the underlying layer can conflict with the factors essential to good surface wetting properties of the second solution on top of the underlying layer. Chapter 3 discusses new orthogonoal solution-processing of new oligoquinole-based electron-transport materials in PhOLEDs. The structure-morphology-property relationship has been studied to demonstrate high-performance all-solution-processed optoelectronic devices. Furthermore, the orthogonal solution-processing strategy of electron-transport materials has been extended to commercially available materials, demonstrating the advantage of the developed processing method in general.

(iii) Studying solution n-doping enabled by orthogonal solution-processing. Solution n-doping of the electron-transport materials by orthogonal solution-processing was investigated in Chapter 4. The small-molecule electron-transport material doped with alkali metal salts by solution-processing of the electron transport layer to achieve high-performance all-solution-processed PhOLEDs was investigated. It was found that incorporation of the dopant into the electron-transport layer by orthogonal solution-processing significantly changes the surface morphology leading to better charge-transport and facile electron-injection from the electrode.

(iv) Studying highly efficient all-polymer solar cells. Recently, polymer/polymer solar cells have gained much attention due to their various advantages compared to polymer/fullerene solar cells. Chapter 6 describes highly efficient all-polymer solar cells based on new acceptor copolymers. Record power conversion efficiency with high photovoltaic parameters in all-polymer solar cells was demonstrated and investigated. Further device optimization of polymer/polymer blend by the control of blend morphology to achieve state-of-the-art performance of all-polymer solar cells was also discussed.

1.5. References

1. Tang, C. W.; VanSlyke, S. A., *Appl. Phys. Lett.* **1987**, *51*, 913.
2. Adachi, C.; Tokito, S.; Tsutsui, T.; Saito, S., *Jpn. J. Appl. Phys.* **1988**, *27*, L269.
3. Briseno, A. L.; Kim, F. S.; Babel, A.; Xia, Y. N.; Jenekhe, S. A., *J. Mater. Chem.* **2011**, *21*, 16461.
4. Kulkarni, A. P.; Tonzola, C. J.; Babel, A.; Jenekhe, S. A., *Chem. Mater.* **2004**, *16*, 4556.
5. Forrest, S. R.; Bradley, D. D. C.; Thompson, M. E., *Adv. Mater.* **2003**, *15*, 1043.
6. Sze, S. M.; Ng, K. K., *Physics of Semiconductor Devices* 3rd ed.; Wiley-Interscience: 2006.
7. Sessolo, M.; Bolink, H. J., *Adv. Mater.* **2011**, *23*, 1829.
8. Hu, L.; Hecht, D. S.; Grüner, G., *Chem. Rev.* **2010**, *110*, 5790.
9. Hu, L.; Hecht, D. S.; Grüner, G., *Nano Lett* **2004**, *4*, 2513.
10. Wu, Z.; Chen, Z.; Du, X.; Logan, J. M.; Sippel, J.; Nikolou, M.; Kamaras, K.; Reynolds, J. R.; Tanner, D. B.; Hebard, A. F.; Rinzler, A. G., *Science* **2004**, *305*, 1273.
11. Bae, S.; Kim, H.; Lee, Y.; Xu, X.; Park, J.-S.; Zheng, Y.; Balakrishnan, J.; Lei, T.; Ri Kim, H.; Song, Y. I.; Kim, Y.-J.; Kim, K. S.; Ozyilmaz, B.; Ahn, J.-H.; Hong, B. H.; Iijima, S., *Nat. Nanotechnol.* **2010**, *5*, 574.
12. Wassei, J. K.; Kaner, R. B., *Mater Today* **2010**, *13*, 52.
13. Wu, J.; Agrawal, M.; Becerril, H. A.; Bao, Z.; Liu, Z.; Chen, Y.; Peumans, P., *Acs Nano* **2009**, *4*, 43.
14. O'Connor, B.; Haughn, C.; An, K.-H.; Pipe, K. P.; Shtein, M., *Appl. Phys. Lett.* **2008**, *93*, 223304.
15. Hu, L.; Wu, H.; Cui, Y., *MRS Bull.* **2011**, *36*, 760.
16. Li, D.; Xia, Y., *Adv. Mater.* **2004**, *16*, 1151.
17. Kang, M.-G.; Xu, T.; Park, H. J.; Luo, X.; Guo, L. J., *Adv. Mater.* **2010**, *22*, 4378.
18. Forrest, S. R., *Nature* **2004**, *428*, 911.
19. Arias, A. C.; MacKenzie, J. D.; McCulloch, I.; Rivnay, J.; Salleo, A., *Chem. Rev.* **2010**, *110*, 3.
20. Earmme, T.; Ahmed, E.; Jenekhe, S. A., *J. Phys. Chem. C* **2009**, *113*, 18448.
21. Ahmed, E.; Earmme, T.; Jenekhe, S. A., *Adv. Funct. Mater.* **2011**, *21*, 3889.
22. Earmme, T.; Ahmed, E.; Jenekhe, S. A., *Adv. Mater.* **2010**, *22*, 4744.

Chapter 2. Highly Efficient Phosphorescent Organic Light-Emitting Diodes Enabled by Bisindenoanthrazolines as a New Class of n-Type Organic Semiconductors

This chapter presents a study of bisindenoanthrazolines as a new class of n-type organic semiconductors. Novel electron-transport materials with π-conjugated heptacyclic framework have been studied as efficient electron-transport layers for high-performance phosphorescent OLEDs. The results in this chapter are reprinted in part with permission from Earmme, *et al*. (Copyright 2009, American Chemical Society), and from Ahmed and Earmme, *et al*. (Copyright 2010 American Chemical Society).

2.1. Introduction

Organic semiconductors are of broad interest for applications in electronic and optoelectronic devices[1-20] such as photovoltaic cells,[1-2] light-emitting diodes[3,20] and field-effect transistors.[4] Among the classes of organic semiconductors, large polycyclic heteroaromatics are of special interest due to their extended quasi-two dimensional (2D) π-conjugation that results in planar backbone framework, improved intermolecular interactions and improved thermal properties.[5-22] The vast majority of the literature to date has focused on the design, synthesis and structure-property relationships of *p*-type organic semiconductors,[5-10] including: oligoacenes,[8] fused oligothiophenes,[9] anthradithiophenes,[8] bisindolocarbazoles,[10] oligophenylenes and oligofluorenes,[6,11] some of which have resulted in field-effect transistors with performance superior to amorphous silicon.[8] In contrast, the development of *n*-type oligomer and polymer semiconductors has lagged behind *p*-type materials.[12-24] A common strategy in the design of n-type organic semiconductors is the substitution of hydrocarbons with electron-deficient moieties

such as fluorine,[12,13,25] cyano groups,[14-17] carbonyls,[15] and/or imine nitrogens.[19-24] Among n-type ladder oligomers studied to date are perfluorinated oligoacenes[25] and thiophenes,[26] oligoindenofluorenes,[11,15] naphthalene diimides,[13,17,18] perylene diimides,[16,27] and imine nitrogen-rich oligomers.[19-24] The design and synthesis of new n-type organic semiconductors is necessary for understanding structure-property relationships in the materials and for improving their performance in organic electronics and optoelectronics.

Ladder polycyclic aromatic molecules that contain imine nitrogens are of increasing interest in the development of *n*-type semiconductors.[14-24] Incorporation of imine nitrogens into ladder-type conjugated oligomers can result in: (i) an increase in electron affinity;[19-24] (ii) enhancement of the propensity of π-stacking;[21-24] (iii) ability to tune the electronic and optoelectronic properties by protonation or metal ion complexation[21a-b,22a] and (iv) result in a substantial improvement in photo-oxidative stability of the molecules. Experimental[14-23] and theoretical[24] studies have shown that heteroaromatic rings containing imine nitrogens have higher reduction potential compared to similar hydrocarbons. Theoretical studies have also showed that linear expansion of size in such imine nitrogen-containing polycyclic molecules is very beneficial toward increasing the reduction potential[24] and reducing intrinsic energy barriers and trapping centers that cause low carrier mobility.[28a-b] Examples of such an extension

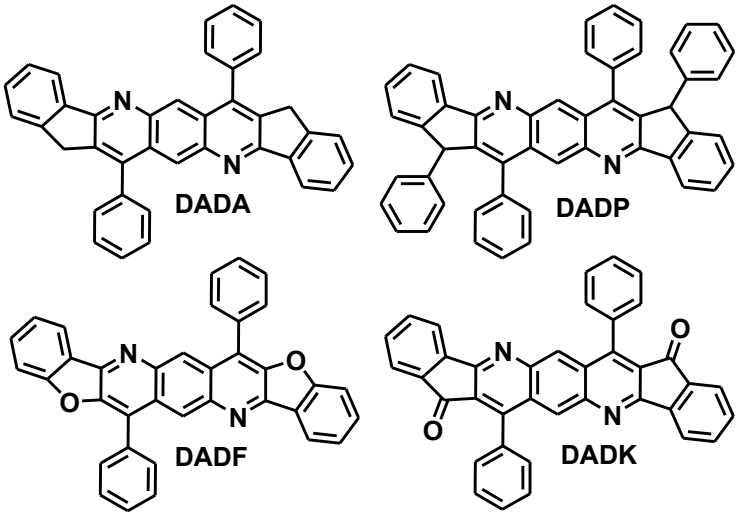

Chart 2.1. Molecular Structures of Bisindenoanthrazolines

of the size of π-conjugated polycyclic molecules and incorporation of imine nitrogens and/or heteroatoms to increase the reduction potentials include core-expanded perylene bisimides,[29] quinoxaline and pyrazinoquionoxaline derivatives,[21,22] bisphenazine derivatives[23] and indenofluorenes/bisindenofluorenes derivatives.[11,15]

In this chapter, we report the synthesis, electrochemical properties, photophysics, electron-transport, and light-emitting properties of novel ladder-type bisindenoanthrazolines (BIDAs). The molecular structures of the four bisindenoanthrazolines (DADA, DADP, DADF, and DADK) investigated are shown in Chart 2.1. The series of BIDAs has a common framework of a highly planar heptacyclic ring that contains a core of anthrazoline ring with two imine nitrogens in the backbone. Various substitutions were examined towards tuning the electronic properties and solid-state structures. The simplicity and flexibility of the synthesis allows for the retention of n-type characteristics while tuning the electronic structures and intermolecular interactions by simple substitutents (X = methylene, benzyl, carbonyl, and ether). We discovered that small changes in the molecular structures result in drastic effects on both the solid-state packing and the electronic and optoelectronic properties. Structure-property relationships of the bisindenoanthrazolines were investigated by cyclic voltammetry, photophysical measurements, space charge limited current (SCLC) measurements of electron mobility, and electroluminescent devices. The new n-type materials had reversible electrochemical reductions from which an electron affinity of 3.6-3.7 eV was estimated.

We also found that highly efficient and bright green polymeric phosphorescent OLEDs (PhOLEDs) can be achieved by means of a new electron transport material (ETM), 4,9-diphenylbisindenoanthrazoline (DADA). By virtue of its high electron affinity (3.67 eV) and efficient π-stacking, DADA as an electron-transport layer (ETL) offers new features that can

potentially enhance the performance of OLEDs. DADA was placed between the Al cathode and the polymeric emissive layer (EML) as an ETL to facilitate electron injection and transport from the high work-function metal.

2.2. Experimental Section

Materials. All commercially available reagents were purchased from Sigma-Aldrich and used without further purification.

Synthetic Procedures. 2,5-Dibenzoyl-1,4-diphenylenediamine was synthesized according to the known literature method.[7a]

General Procedure for Synthesis of BIDAs. A mixture of 2,5-dibenzoyl-1,4-diphenylenediamine (1.0 equiv), indanone-functionalized compound (2.1 equiv) and diphenyl phosphate (8 equiv) in 5 mL of toluene were refluxed in inert atmosphere for 12 hours. The reaction mixture was precipitated from 10% methanol/triethylamine and the solid was collected by vacuum filteration. The resulting product was recrystallized from THF/ MeOH.

DADA. A mixture of indanone (0.53 g, 4.0 mmol), 2,5-dibenzoyl-1,4-diphenylenediamine (0.6 g, 1.89 mmol) and diphenyl phosphate were refluxed in toluene. DADA was extracted and purified according to the above general procedure in 96 % yield as a yellow solid. ^{1}H-NMR (300 MHz, $CDCl_3$): δ ppm = 8.677 (s, 2H), 8.303 (d, 2H), 7.674-7.606 (m, 10H), 7.530 (m, 6H), 3.943 (s, 4H). ^{13}C-NMR (TFA-d_6): δ ppm 160.00, 153.70, 150.38, 137.50, 134.07, 131.67, 131.27, 130.59, 129.53, 128.59, 128.21, 126.39, 124.55, 34.04. HRMS (FAB) calcd for $C_{38}H_{24}N_2$ 508.19395 Found M+. 508.19418.

DADP. A mixture of 3-phenyl-1-indanone (0.69 g, 3.3 mmol), 2,5-dibenzoyl-1,4-diphenylenediamine (0.5 g, 1.58 mmol) and diphenyl phosphate were refluxed in toluene overnight. DADP was extracted and purified according to the above general procedure to give a

yellow solid in 91 % yield. ^{1}H-NMR (300 MHz, $CDCl_3$): δ ppm = 8.5271 (s, 2H), 8.2989 (d, 2H), 7.575-7.402 (m, 12H), 7.159 (t, 2 H), 6.694 (d, 2H), 6.579 (d, 2H), 5.217 (s, 2H). ^{13}C-NMR (TFA-d_6): δ ppm = 160.41, 155.51, 154.57, 142.19, 138.14, 135.19, 134.06, 131.16, 130.45, 129.96, 129.70, 129.56, 129.28, 128.65, 128.49, 128.04, 127.81, 127.57, 126.77, 124.15, 119.46. HRMS (FAB) calcd for $C_{50}H_{32}N_3$ 660.25387 Found M+. 660.25469.

DADF. A mixture of 2H-benzofuran-3-one (0.466 g, 3.48 mmol), 2,5-dibenzoyl-1,4-diphenylenediamine (0.5 g, 1.58 mmol) and diphenyl phosphate were refluxed in toluene overnight. DADF was extracted and purified according to the above general procedure to give an orange solid in 85 % yield. ^{1}H-NMR (300 MHz, TFA-d_6): δ ppm = 9.519 (s, 2H), 8.586 (d, 2H), 8.220 (t, 2H), 8.022-7.907 (m, 12H), 7.803 (t, 2H). ^{13}C-NMR (TFA-d_6): δ ppm = 163.39, 139.79, 139.39, 132.53, 132.16, 130.08, 129.44, 127.61, 126.42, 124.62, 120.09, 115.83, 114.53, 113.54. HRMS (FAB) calcd for $C_{36}H_{20}N_2O_2$ 513.1603 Found M+. 513.16092.

DADK. A mixture of 1,3-indanedione (0.509 g, 3.48 mmol), 2,5-dibenzoyl-1,4-diphenylenediamine (0.5 g, 1.58 mmol) and diphenyl phosphate were refluxed in toluene. DADA was extracted and purified according to the above general procedure in 90 % yield as an orange solid. ^{1}H-NMR (300 MHz, TFA-d_6): δ ppm = 8.999 (s, 2H), 8.454-8.427 (m, 2H), 8.184-8.079 (m, 6H), 7.957-7.841 (m, 6H), 7.704-7.677 (m, 4H). ^{13}C-NMR (TFA-d_6): δ ppm = 186.07, 157.50, 138.81, 138.53, 137.90, 135.89, 133.49, 132.37, 131.94, 129.14, 128.79, 128.17, 126.18, 125.81, 125.55, 124.45. HRMS (FAB) calcd for $C_{38}H_{20}N_2O_2$ 537.1603 Found M+. 537.16054.

Characterization. ^{1}H-NMR spectra were recorded on a Bruker AV300 at 300 MHz using deuterochloroform ($CDCl_3$) or deuterotrifluoroacetic acid (CF_3COOD) as the solvent. Mass spectra were obtained from JEOL/HX-110 using 2-nitrophenyloctylether as a matrix. Thermogravimetric analysis of the molecules was conducted on a TA Instruments model Q50

TGA. A heating rate of 10 °C/min under a flow of N_2 was used with runs conducted from room temperature to 500 °C. Cyclic voltammetry was done on an EG&G Princeton Applied Research Potentiostat/Galvanostat (Model 273A). Data were analyzed by using a Model 270 Electrochemical Analysis System Software on a PC computer. A three-electrode cell was used, using platinum wire electrodes as both counter and working electrode. Silver/silver ion (Ag in 0.1 M $AgNO_3$ solution, Bioanalytical System, Inc.) was used as a reference electrode. Ferrocene/ferrocenium (Fc/Fc^+) was used as an internal standard. The potential values obtained in reference to Ag/Ag^+ were converted to the saturated calomel electrode (SCE) scale. Solution cyclic voltammetry was performed in 1 mM solution of the compound in a mixed 1,3-dichlorobenzene/acetonitrile (1.6:1 v/v) solvent containing 0.1 M $TBAPF_6$ as electrolyte at 100 °C. All solutions were purged with N_2 for 20 minutes before each experiment. UV-vis absorption spectra were collected on a Perkin-Elmer model Lambda 900 UV/vis/near-IR spectrophotometer. The photoluminescence (PL) emission spectra were obtained with a Photon Technology International (PTI) Inc. model QM2001-4 spectrofluorimeter.

Fabrication and Characterization of OLEDs. We fabricated multilayer OLEDs using the indenoanthrazolines as an emitter. ITO-coated glass substrates (10 Ω/sq, Shanghai B. Tree Tech. Consult Co., Ltd., Shanghai, China) were cleaned sequentially in ultrasonic baths of acetone, deionized water, isopropanol, and then dried at 60 °C in a vacuum oven overnight. The commercially available 1 wt % dispersion of PEDOT:PSS (Clevios PVP4083, H.C. Starck) in water was used after it was filtered through 0.45μm GHP syringe filters. A 50 nm thick PEDOT:PSS layer was spin coated on top of ITO glass and dried at 150 °C under a vacuum to get rid of residual water molecules. A 15-20 nm thick TAPC (1,1-bis-(di-4-tolylaminophenyl)cyclohexane) hole-transport/electron-blocking layer was spin-coated from its

0.3 – 0.5 wt% toluene solution onto the PEDOT:PSS layer and dried at 60 °C overnight under a vacuum. A 20 nm thick film of each bisindenoanthrazoline was obtained on top of TAPC layer by evaporation from resistively heated quartz crucibles at a rate of ca. 0.1-0.3 nm/s in a vacuum evaporator (Edwards Auto 306) at base pressure of < 7 x 10^{-7} Torr. When TPBI (1,3,5-tris(N-phenylbenzimidizol-2-yl)benzene) was used, it was evaporated right after evaporation of bisindenoanthrazoline. Then LiF and Al were sequentially deposited onto the organic layer without breaking vacuum.

To investigate PhOLEDs using bisindenoanthrazolines as an ETL, we fabricated green PhOLEDs using blends of poly(*N*-vinylcarbazole) (PVK) and 1,3-bis(2-(4-*tert*-butylphenyl)-1,3,4-oxadiazo-5-yl)benzene (OXD-7) (PVK:OXD-7=60:40 wt/wt) as the host doped with 1.0 wt% *fac*-tris(2-phenylpyridine)iridium ($Ir(ppy)_3$) as the green triplet emitter in the EML. For the hole injection layer, a solution PEDOT:PSS was spin-coated to make a 30-nm thick layer onto a pre-cleaned ITO glass and annealed at 150 ºC under vacuum. A 70-nm thick EML was obtained by spin-coating of the PVK:OXD-7:$Ir(ppy)_3$ blend in chlorobenzene onto the PEDOT:PSS layer and vacuum-dried t at 100 ºC. Then 20-nm thick bisindenoanthorazolines followed by LiF and Al cathode are thermally vacuum evaporated to obtain the device structures: ITO/PEDOT/EML/BIDA/LiF/Al.

Film thickness was measured by an Alpha-Step 500 profilometer (KLA-Tencor, San Jose, CA). EL (Electroluminescence) spectra were obtained using the same spectrofluorimeter in photophysical properties. Current-voltage characteristics of the OLEDs were measured by using a HP4155A semiconductor parameter analyzer (Yokogawa Hewlett-Packard, Tokyo). The luminance was simultaneously measured by using a model 370 optometer (UDT Instruments, Baltimore, MD) equipped with a calibrated luminance sensor head (Model 211) and a 5x

objective lens. The device external quantum efficiencies were calculated by using procedures reported previously.[20d,e] All the device fabrication and device characterization steps were carried out under ambient laboratory condition.

Devices for space-charge limited current (SCLC) measurement were fabricated with Al/bisindenoanthrazolines/Al structure. The Al electrode and organic layer were obtained by the same evaporation method as the fabrication of OLED devices. Current-voltage characteristics of SCLC devices were measured using the same semiconductor parameter analyzer as for OLED devices. The measurements were performed under dark and ambient conditions.

2.3. Results and Discussion

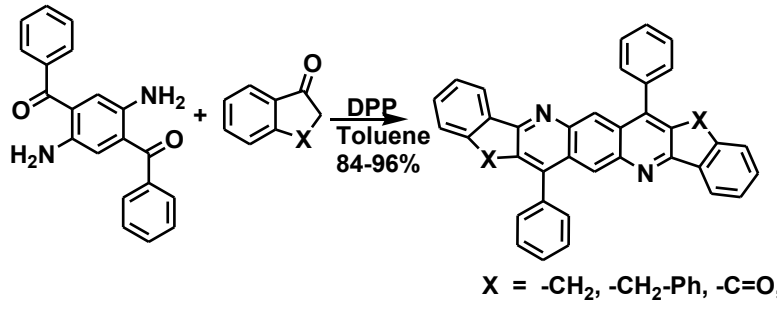

Scheme 2.1. Synthesis of Bisindenoanthrazolines.

Synthesis and Characterization. The bisindenanthrazoline framework contains seven-fused rings, including 5 hexagons and 2 pentagons. The synthesis of the heptacyclic bisindenoanthrazolines involved a cyclization reaction of 2,5-dibenzoyl-1,4-phenylenediamine (**1**) as outlined in Scheme 2.1. The four BIDAs were synthesized in high yield via Friedlander condensation using diphenyl phosphate (DPP) as an acid catalyst. The diphenyl phosphate (DPP) catalyst was readily removed by precipitation into a 10 % triethylamine/methanol solution.[34] DADA, DADP, DADF and DADK were recrystallized from 1:1 THF:MeOH solvent mixture. ^{1}H-NMR spectra, ^{13}C-NMR spectra, and high resolution mass spectrometry of the molecules and X-ray single crystal determination on two of them confirmed the structures. The four BIDAs are soluble in common organic solvents (chloroform,

toluene, dichlorobenzene, etc.) to varying degrees. Thin-films of the molecules were easily obtained by vacuum deposition. The decomposition temperatures are in the range of 418-498 °C as determined by thermogravimetric analysis (TGA). Glass transition temperature and melting points were not observed by differential scanning calorimetry (DSC) up to 300 °C.

Photophysics. Figure 2.1A shows the normalized absorption spectra of the four bisindenoanthrazolines in dilute tetrahydrofuran (THF) solutions. The spectra show two bands, a lower intensity band in the range of 340-410 nm and a higher intensity band in the 280-310 nm range. These absorption bands in DADA, DADP, and DADF spectra are associated with π-π* transitions. However, the lowest energy absorption band in DADK is due to n- π* transition whereas the higher energy band is from π-π* transition. All the solution absorption spectra show clear vibronic structures, indicative of well-defined rigid chromophores. All the BIDA molecules except DADF show an absorption maximum that corresponds to the 0-1 optical transition (the highest oscillator strength). The

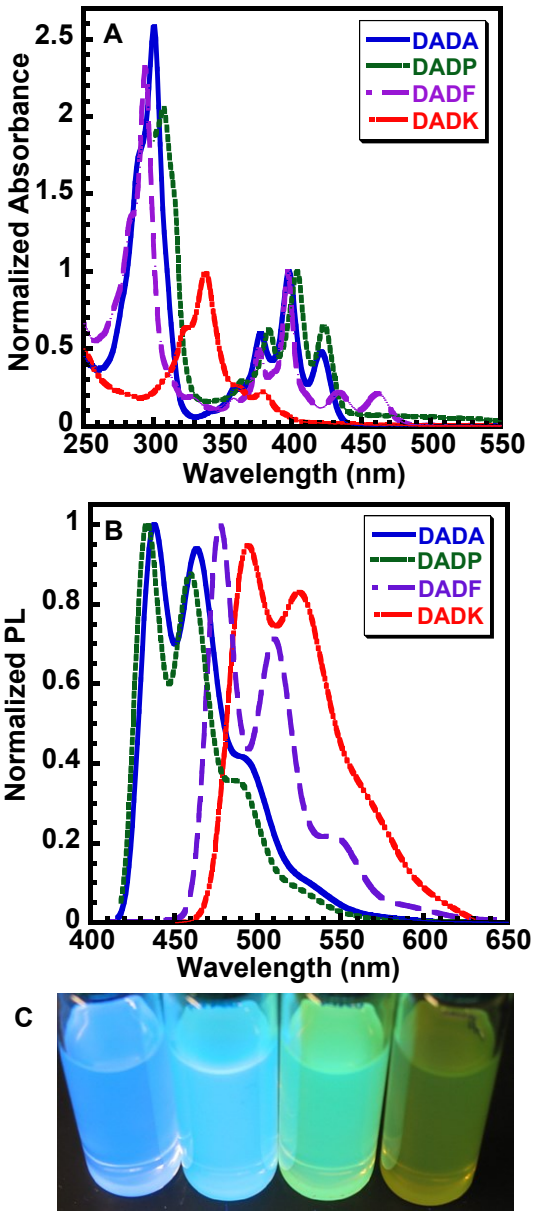

Figure 2.1. Optical absorption (A) and PL (B) spectra of bisindenoanthrazolines in THF solutions. (C) Photograph of bisindenoanthrazolines in toluene solution under UV irradiation.

absorption maximum of DADF corresponds to the 0-2 transition. The absorption maxima (λ_{max}) of DADA, DADP and DADF are 398, 404, 397 nm, respectively; whereas that of DADK (340 nm) is blue shifted by 58 nm compared to DADA (Table 2.1).

Figure 2.1B shows the normalized PL emission spectra of the four BIDAs in dilute THF solution (10^{-6} M). The four PL emission spectra have structured bands. DADA and DADP have almost identical blue emission spectra with PL maximum of 438 and 434 nm, respectively, implying that the benzyl groups in DADP have no influence on the transition energies. However, a bathochromic shift of 40 and 56 nm are observed in the PL spectra of DADF and DADK compared to DADA and DAP. The PL emission of DADF and DADK are green and orange with PL maxima of 478, and 494 nm, respectively. When the 0-0 transition in the emission is compared with the 0-0 transition of the corresponding absorption bands, the Stokes shift is small

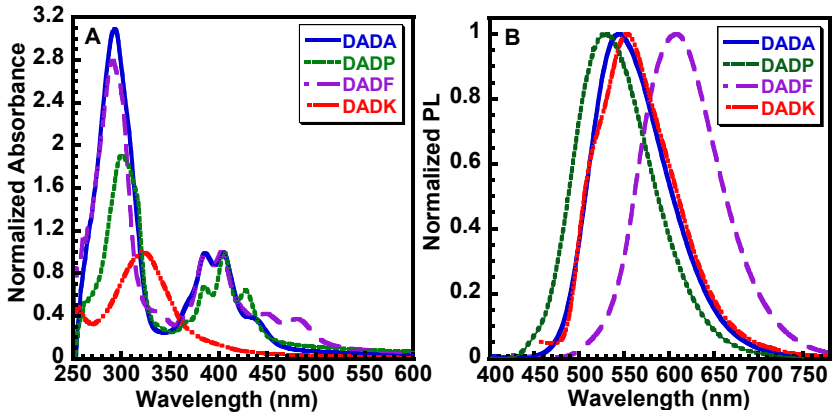

Figure 2.2. Optical absorption (a) and PL (b) spectra of bisindenoanthrazolines thin films.

for all the molecules except for DADK. In the case of DADK, there is a large Stokes shift of 114 nm, indicating an intramolecular energy transfer due to carbonyl moieties.[11a,15a] The PL quantum yields of the BIDAs in dilute toluene solution are summarized in Table 2.1. The PL quantum yields of DADA, DADP, and DADF are 52%, 47%, and 33%, respectively. However, a

Table 2.1. Photophysical and Electrochemical Properties of Bisindenoanthrazolines.

Compd	T_D (˚C)	λ_{max}^{abs} (soln) (nm)	λ_{max}^{abs} (film) (nm)	E_g^{opt} (eV)	λ_{max}^{em} (soln) (nm)	λ_{max}^{em} (film) (nm)	ϕ_f (soln)	E_{red}^{onsest} (V)	EA (eV)	IP (eV)
DADA	420	398	405	2.67	438	545	0.52	-0.73	3.67	6.34
DADP	418	404	406	2.76	434	531	0.47	-0.75	3.65	6.41
DADF	498	397	403	2.43	478	608	0.33	-0.68	3.72	6.15
DADK	490	340	321	2.99	494	553	0.03	-0.70	3.70	6.69

significantly lower quantum yield for DADK (3%) was observed, evidence of fluorescence quenching due to the carbonyl moieties.[11a,15a] Figure 2.1C shows a photograph of the bisindenanthrazolines in toluene solutions under UV irradiation. Emission spanning blue to yellow is seen in the solutions corresponding to various substituents in bisindenanthrazoline backbone.

Figure 2.2a shows the thin film optical absorption spectra of the four BIDAs. The structured absorption bands and the two absorption peaks observed in dilute solution are also seen in evaporated thin films, except for DADK thin film which has only one broad absorption peak. The thin film absorption bands of DADA, DADP, DADF are almost identical to those in dilute solution whereas that of DADK has a red shift of 20 nm. The optical band gaps were determined from the onset thin film absorption and are shown in Table 2.1. The optical band gaps are 2.43 eV for DADF, 2.67 eV for DADA, 2.76 eV for DADP, and 2.99 eV in the case of DADK.

The PL emission spectra of the thin films of BIDAs are shown in Figure 2.2B. The emission spectra are significantly red shifted compared to the solution emission spectra by 60-130 nm. In addition, the thin film emission spectra have broad, featureless characteristics. This suggests that the thin film luminescence is from "static" excimer states formed as a result of the π-stacking of the molecules in the solid-state.[35] The PL maxima of DADA, DADP, and DADF are summarized in Table 2.1. DADA and DADP have similar green-yellow emission spectra with PL maxima of 545 and 531 nm, respectively. Orange emission spectra with PL maximum of 608 nm and green

emission spectra with PL maximum of 553 nm were observed for DADF and DADK, respectively.

Electrochemical Properties. Cyclic voltammetry was performed in millimolar solutions of the BIDAs in 1,2-dichlorobenzene/acetonitrile (10:3 v/v) at 100˚C. The electrochemical data are collected in Table 2.1. The reduction cyclic voltammograms (CVs) of the four molecules in solution are shown in Figure 2.3. DADA and DADP show two reduction waves which are quasi-reversible. One reversible reduction wave was observed in the CVs of DADF and DADK. The onset reduction potential of the BIDAs are -0.73, -0.75, -0.68, and -0.70 V (vs SCE) for DADA, DADP, DADF, and DADK, respectively. We note that the reduction potentials of all the four molecules are comparable with a difference of only 0.1 V. It is evident that the heptacyclic bisindenoanthrazolines can be more easily reduced than the tricyclic anthrazolines which show reversible reduction with onset reduction potential of -1.30 V (vs. SCE).[20a] Irreversible oxidation potentials were observed for DADA and DADP with onset oxidation potential of 1.33 and 1.48 V (vs. SCE), respectively. However, oxidation potentials were not observed for DADF and DADK. The electron affinity (EA) or LUMO level and ionization potential (IP) or HOMO level were estimated from the onset of either the reduction waves or the oxidation waves in CVs, respectively by using an SCE energy level of -4.4 eV vs vacuum (EA = E_{red}^{onset} + 4.4 eV; IP = E_{ox}^{onset} + 4.4 eV).[20b] The electron affinity was in the range of 3.65-3.72 eV for the series of BIDAs. The ionization potentials (IP) or the HOMO levels for DADA and DADP are 5.73 and 5.88 eV, respectively. We estimated an IP of 6.15 eV and 6.69 eV for DADF and DADK, respectively, from optical band gap, IP = EA + E_g^{opt}.

The observed electron affinity of ~3.7 eV in the series of BIDA molecules is important and it clearly suggests a good potential for electron transport in these n-type materials. Although the

EA and IP values derived from cyclic voltammetry can be significantly different from absolute values measured by photoemission techniques,[20b] we believe that our estimates based on an SCE energy level of -4.4 eV relative to vacuum are conservative. We also conclude from the estimated IP values of 5.73-6.69 eV that the bisindenoanthrazolines could not transport holes and indeed would be excellent for blocking holes in OLEDs.

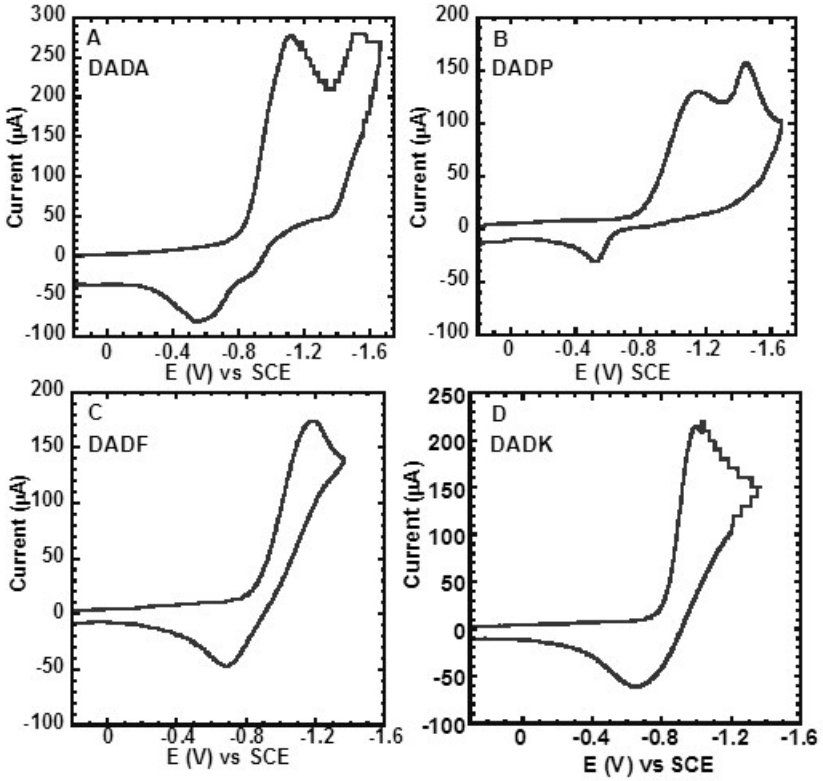

Figure 2.3. Cyclic voltammograms of (A) DADA; (B) DADP; (C) DADF; and (D) DADK (1.5-3 mM) in 1,2-dichlorobenzene/acetonitrile (10:3 v/v), 0.1 M TBPF6 at 100 °C. Scan rate = 300 mV/s.

Electron Transport. The mobility of electrons in films of the bisindenoanthrazolines was evaluated by the space-charge limited current (SCLC) method in ambient conditions. Figure 2.4 shows the current-density/ voltage (*J-V*) characteristics of SCLC devices which have the structure Al/BIDA (< 190 nm)/Al. The electron mobility was extracted by fitting the *J-V* curves in the near quadratic region according to the modified Mott-Gurney equation[36],

$$J = \frac{9}{8}\varepsilon\varepsilon_0\mu\frac{V^2}{L^3}exp\left(0.89\beta\frac{\sqrt{V}}{\sqrt{L}}\right)$$

where J is the current density, V is the applied voltage, L is the thickness of active layer, μ is the mobility, ε is the permittivity of free space, ε_0 is the permittivity of free space, and β is the field-activation factor (Table 2.2).[36] The solid lines in Figure 2.4 represent the best fitting curves in the quadratic SCLC region.

The mobility of electrons was calculated to be 3.84 x 10^{-4}, 3.07 x 10^{-5}, 2.29 x 10^{-6}, 4.33 x 10^{-7} cm^2/Vs for DADK, DADA, DADF, and DADP, respectively. The SCLC electron mobility of

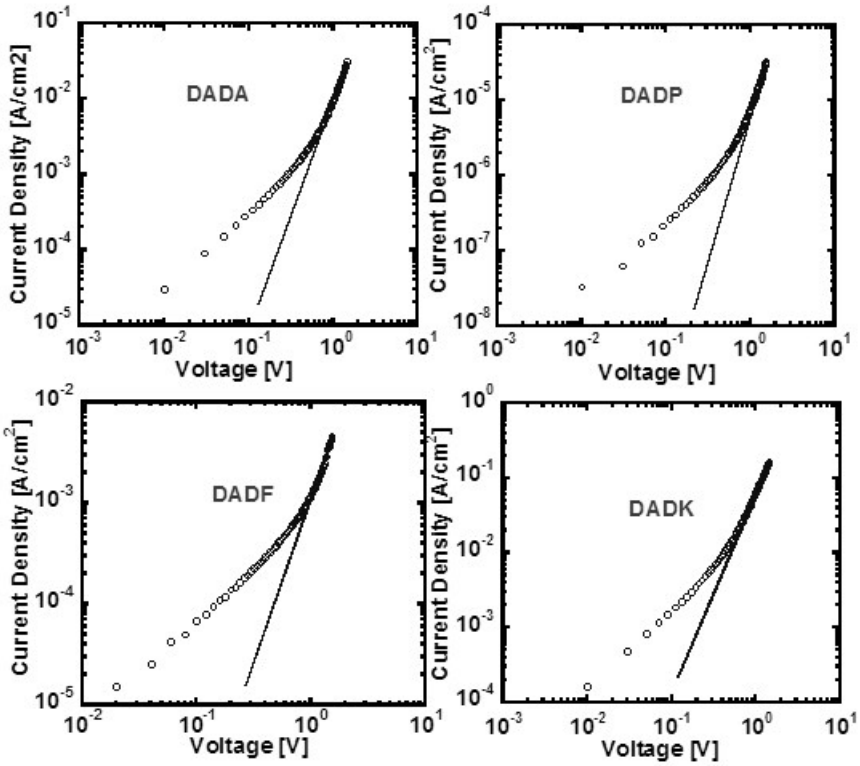

Figure 2.4. Current density , *J vs. V* of Al/Bisindenoanthrazoline/Al devices in ambient conditions. The solid lines represent SCLC model with field-dependent mobility.

DADK was the highest observed among the series of molecules. The electron mobility is an order of magnitude higher than that of DADA and two orders of magnitude higher than that of

DADF. The high mobility of DADK could be explained by the close intermolecular π–π distance that results in a better intermolecular orbital overlap than DADF. The SCLC electron mobility of DADP was two orders of magnitude lower than that of DADA. The charge carrier mobility of DADA and DADK is about one to two orders of magnitude higher than those of conventional electron transport materials such as Alq_3,[37a] oxadiazole derivatives,[37b] and diphenylphenanthroline (BPhen).[37c] The low carrier mobility in DADP could be due to the poor intermolecular interactions as a result of the benzyl groups. Based on the previously discussed EA and IP values for the 4 BIDA molecules the small energy barrier for electron injection from Al (Φ = 4.3 eV) [20b] is small and comparable in all 4 molecules. Thus, the observed 3 orders of magnitude variation in the SCLC electron mobility of the series of BIDAs must be due to variation in the solid state morphology of the materials. Nevertheless, the fact that a simple substitution in the structure of the bisindenoanthrazolines can translate into a huge variation in charge transport properties is instructive in the design of organic semiconductors.[28c] The observed low carrier mobility measured by SCLC could be due to the fact that the mobility is not measured along the π-stacking direction which is the optimum direction for charge transport. This is because the direction of charge transport measured by SCLC method is perpendicular to the substrate whereas the π-stacking direction is generally parallel to the substrate.

Table 2.2. SCLC Characteristics of Bisindenoanthrazolines.

Compound	*L* *(nm)*	β $(cm/V)^{1/2}$	E_{max} *(V/cm)*	μ_e *(E=0)* $(cm^2/V\ s)$
DADA	182	8.9×10^{-3}	8.0×10^{4}	3.1×10^{-5}
DADP	179	1.1×10^{-2}	8.6×10^{4}	4.3×10^{-7}
DADF	144	7.9×10^{-3}	1.1×10^{5}	2.3×10^{-6}
DADK	161	4.9×10^{-3}	8.4×10^{4}	3.8×10^{-4}

Initial attempts to measure the electron mobility of single-crystalline self-assembled nanowires of DADK using the field effect transistor geometry[32a,e] were unsuccessful. This lack of n-channel field effect charge transport may be due to the high injection barrier between the gold source/drain electrodes (Φ = -5.1 eV) and the LUMO level of DADK (-3.7 eV). In addition, n-channel transport is highly unstable in ambient conditions, especially in bottom contact and bottom gate devices used in our study.

Organic Light-Emitting Diodes (OLEDs). The BIDAs were explored in electroluminescent (EL) devices both as emissive materials in OLEDs and as electron transport materials in phosphorescent OLEDs (PhOLEDs). The following three different device structures incorporating a BIDA as the emitter were fabricated and tested: ITO/PEDOT:PSS/BIDA/LiF/Al (diode I); ITO/PEDOT:PSS/TAPC/BIDA/LiF/Al (diode II); and ITO/PEDOT:PSS/TAPC/ BIDA/TPBI/LiF/Al (diode III). The EL properties of diodes I-III are summarized in Tables 2.3 and 2.4. The EL spectra of diode III incorporating DADA, DADP, or DADF as the emissive layer and diode II using DADK as the emitter are shown in Figure 2.5. The EL spectra of DADA, DADP, and DADF are very similar to their respective PL spectra with EL maximum of 547, 540 and 608 nm, respectively. The EL spectra of these three BIDA molecules (DADA, DADP, DADF) are very similar with the PL spectra, which as discussed above, originated from excimer emission.[35] In contrast, the EL spectrum of DADK has a peak at 685 nm, which is significantly

different from the PL emission maximum at 553 nm. We propose that EL emission from DADK-based diode II results from the recombination of charges at the interface of the hole transport layer (TAPC) and DADK layer and thus exciplex formation.[38] We attempted to directly confirm this hypothesis by obtaining the PL emission spectrum of a TAPC/DADK bilayer. However, the PL emission spectrum from the bilayer was different from the EL spectrum. The CIE coordinates of the EL emission of the four compounds are shown in Figure 2.5B. Greenish-yellow EL with CIE coordinates of [(0.33, 0.57), (0.32, 0.56)] was observed for DADA and DADP whereas orange with CIE coordinates (0.53, 0.46) and red EL with CIE coordinates of (0.65, 0.35) were observed in DADF and DADK, respectively.

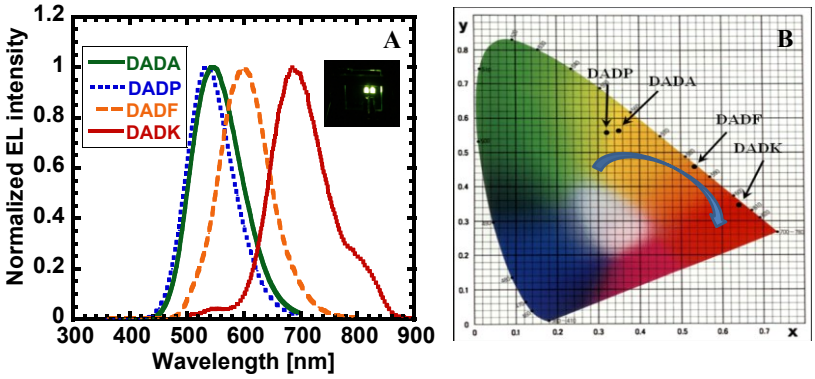

Figure 2.5. (A) Normalized EL spectra of bisindenoanthrazolines (inset is a photo of a DADA-based device III). (B) CIE coordinates of the EL spectra of device III.

Figure 2.6 A-D shows the current density-voltage and luminance-voltage characteristics of diode III based on DADA, DADP, DADF, or DADK as the emissive layer. The turn-on voltage of the three diodes was in the range of 3.8-4.0 V, indicating low charge injection barriers. Device III gave the best performance for DADA, DADP and DADF as expected from the incorporation of both a TAPC hole transport layer (HTL) and a TPBI hole blocking layer (HBL). Among the bisindenoanthrazolines, DADA gave the best performance as an emissive material in EL diodes, giving a maximum brightness of 7610 cd/m^2, an EQE of 0.66 %, and a luminous efficiency of 2.1 cd/A (Table 2.4). The maximum luminous efficiency of diode III containing DADA was 6.6 cd/A with an EQE of 2.0 % at a brightness of 936 cd/m^2 (Table 2.3). In the case

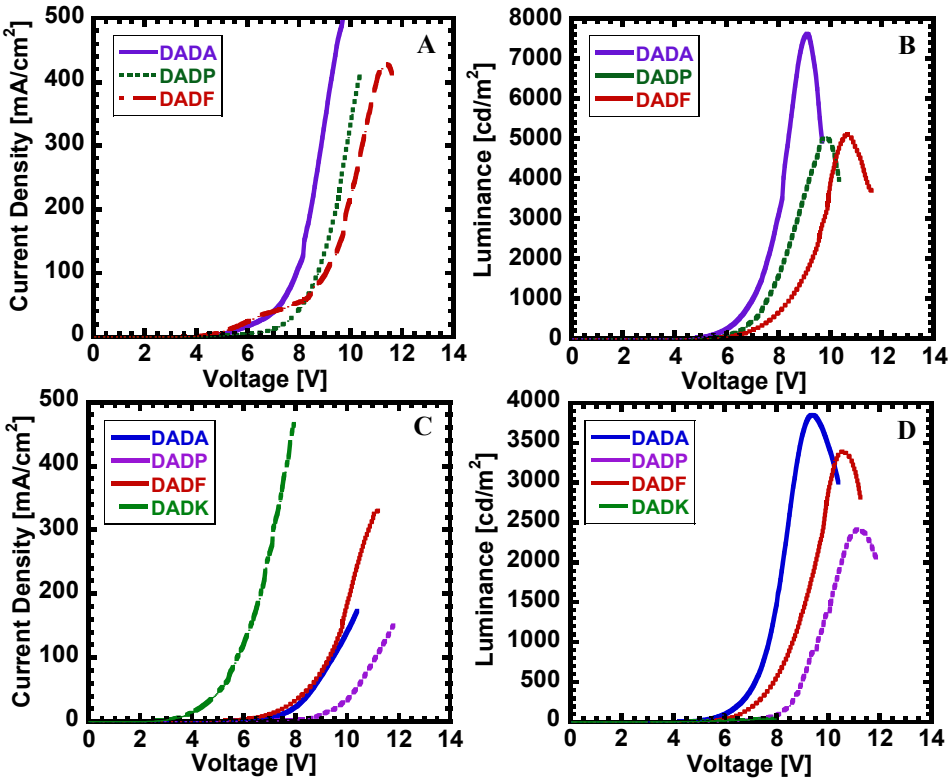

Figure 2.6. Current density-voltage (A) and luminance-voltage (B) characteristics of diode III with device geometry of: ITO/PEDOT(50 nm)/TAPC (20 nm)/BIDA (20 nm)/TPBI (20 nm)/LiF (2 nm)/Al. Current density-voltage (C) and luminance-voltage (D) characteristics of diode III with device geometry of: ITO/PEDOT(50 nm)/TAPC (10 nm)/BIDA (20 nm)/TPBI (20 nm)/LiF (2 nm)/Al.

of DADP, the maximum brightness was 5040 cd/m^2 with an EQE of 0.55% and a luminous efficiency of 1.7 cd/A (Table 2.4). The maximum efficiency of diode III containing DADP was 4.8 cd/A at a brightness of 604 cd/m^2 with an EQE of 1.55 % (Table 2.3). The maximum brightness of diode III containing DADF was 5110 cd/m^2 with an EQE of 0.42% and a current efficiency of 1.5 cd/A. EL performance of diodes I-II containing DADK was very poor. EL from diode III containing DADK did not originate from DADK but rather from an exciplex emission.[35,38] An alternative possibility is that the red EL of DADK originates from electrophosphorescence. However, additional photophysical studies at low temperatures will be required to confirm such an unprecedent phenomenon in a molecule without a heavy atom. The higher brightness and efficiency of DADA compared to DADP could be explained by its relatively higher fluorescence quantum yield and higher electron mobility. Single-layer diode I further confirms that DADA is a superior electron transport material than DADP; a brightness of 584 cd/m^2 was obtained from DADA compared to a brightness of 2 cd/m^2 from DADP. The low

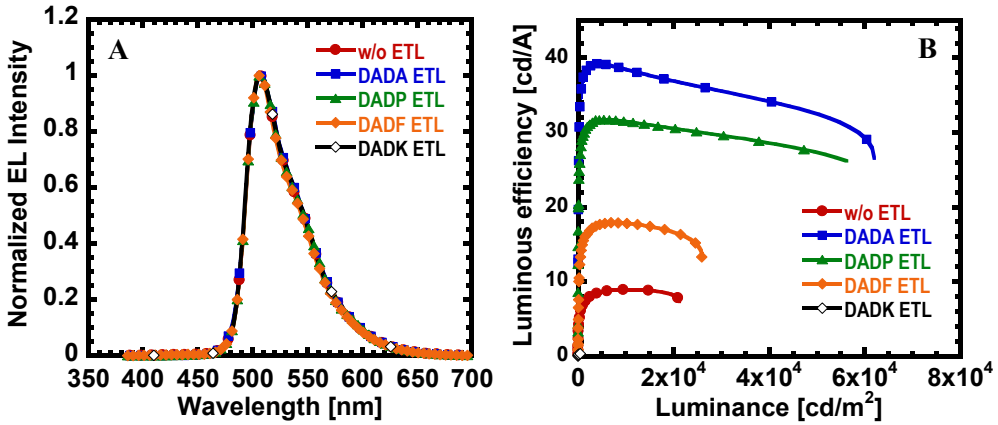

Figure 2.7. (A) Normalized EL spectra of the PhOLEDs at a drive voltage of 17.6-20.4 V. (B) Luminous efficiency - luminance (LE-L) curves of PhOLEDs with the structures: ITO/PEDOT:PSS/EML/LiF/Al and ITO/PEDOT:PSS/EML/BIDA (ETL)/LiF/Al.

luminous efficiency and brightness in diodes I-III containing DADF and DADK can be explained by the low fluorescence quantum yield in the materials.

Electron Transport Properties of BIDAs in PhOLEDs. We also evaluated the new bisindenoanthrazolines as electron transport materials (ETMs) in phosphorescent OLEDs (PhOLEDs). A blend of poly(*N*-vinylcarbazole) (PVK) and 1,3-bis(2-(4-*tert*-butylphenyl)-1,3,4-oxadiazo-5-yl)benzene (OXD-7) (PVK:OXD-7=60:40 wt/wt) served as the host to which a 1.0 wt% *fac*-tris(2-phenylpyridine)iridium ($Ir(ppy)_3$) green triplet emitter was doped, resulting in an emissive polymer layer (EML). Five sets of devices were investigated, including: ITO/PEDOT:PSS/EML/LiF/Al without an electron-transport layer (ETL) which served as a reference. Four diodes, each containing a BIDA molecule as an ETL, were fabricated with the structure: ITO/PEDOT:PSS/EML/ETL/LiF/Al. The normalized EL emission spectra of the PhOLEDs are shown in Figure 2.7A. At all drive voltages, EL emission was observed only from the green triplet emitter, which has a maximum emission peak at 512 nm due to the $Ir(ppy)_3$. EL emission from the BIDA ETMs was not observed. This clearly means that the BIDA molecules function exclusively as electron-transport materials, efficiently confining charge carriers and excitons within the EML.[39]

The luminous efficiency-luminance (*LE*-*V*) curves of the PhOLEDs are shown in Figure 2.7B and the associated device performance are collected in Table 2.5. PhOLEDs using a DADA ETL showed the highest brightness of 62 000 cd/m^2 and the highest luminous efficiency (*LE*) value of 39.2 cd/A (EQE of 12.6%) at a brightness of 4270 cd/m^2, which is almost 4-fold higher than PhOLEDs without an ETL. DADP ETL also enhanced the PhOLED performance, showing a LE value of 31.7 cd/A (EQE of 10.2%) at a brightness of 4470 cd/m^2. PhOLEDs with a DADF as ETL also showed improved performance (Table 2.5). Unexpectedly, PhOLEDs using DADK as an ETL showed a severely quenched EL with a brightness of only 630 cd/m^2, which is two orders of magnitude less than the device without an ETL. This means that whereas DADA,

DADP, and DADF are good ETMs for use in PhOLEDs, DADK is not an effective ETL material. We note that it is better for an electron-transport layer to have an amorphous morphology.[20b] Aggregation of the molecules of an ETM and crystallization of the ETL can result in poor charge-injection at the interface. The strong intermolecular interactions in DADF and DADK were already evident in their self-assembled nanostructures discussed above. This could explain the poor performance of PhOLEDs based on DADK and DADF ETLs. Overall, these results demonstrate that DADA and DADP are very promising electron-transport materials for applications in PhOLEDs, whereas DADF and DADK are not as promising apparently because of their tendency to crystallize readily.

Table 2.3. EL Properties of Bisindenoanthrazolines.[a]

Compound	Diode	V_{on} [b]	Drive voltage (V)	Current density (mA/cm^2)	Luminance (cd/m^2)	Luminous efficiency (cd/A) [EQE[c] %]	λ_{max}^{EL} (nm)
DADP	I	5.0	6.0	452	2	0.05 [0.0002]	539
	II	2.8	7.0	217	1850	0.85 [0.32]	540
			5.2	*15*	*335*	*2.2* [*0.71*]	
	III	4.5	11.1	100	2410	2.4 [0.79]	540
			9.1	*13*	*604*	*4.8* [*1.55*]	
DADA	I	4.0	8.7	410	584	0.14 [0.045]	545
	II	3.0	10.8	215	2140	1.00 [0.30]	547
			8.5	*31*	*604*	*2.0* [*0.60*]	
	III	3.8	9.3	91	3840	4.2 [1.29]	547
			7.7	*14*	*936*	*6.6* [*2.03*]	
DADF	I	3.8	7.5	388	189	0.05 [0.022]	599
	II	2.8	8.5	361	912	0.25 [0.11]	601
			5.6	*36*	*102*	*0.29* [*0.13*]	
	III	4.0	10.6	266	3400	1.3 [0.58]	601
			9.0	*75*	*1330*	*1.8* [*0.81*]	
DADK	I	4.0	5.6	266	1	0.0005 [-]	683
	II	3.0	7.9	449	37	0.008 [-]	685
			5.4	*66*	*9*	*0.01* [-]	
	III[d]	-	-	-	-	-	

[a] Values in italic correspond to those for maximum device efficiencies at a practical brightness of at least 100 cd/m^2 except values in DADK case. [b] Turn-on voltage (at which EL is visible to the eye). [c] EQE = External quantum efficiency.[20d,e] [d] EL from diode III did not originate from DADK. The structure of device III is ITO/PEDOT(50 nm)/TAPC (20 nm)/BIDA (20 nm)/TPBI (20 nm)/LiF (2 nm)/Al.

Table 2.4. Device Characteristics with Maximum Brightness[a].

Compound	V_{on} (V)	Drive voltage (V)	Current density (mA/cm^2)	Luminance (cd/m^2)	Luminous efficiency (cd/A) [EQE %]	λ_{max}^{EL} (nm)
DADP	4.0	9.8	290	5040	1.7 [0.55]	540
DADA	3.8	9.1	367	7610	2.1 [0.66]	547
DADF	4.0	10.4	349	5110	1.5 [0.42]	601

[a] Device structure is ITO/PEDOT(50 nm)/TAPC (10 nm)/BIDA(20 nm)/TPBI (20 nm)/LiF (2 nm)/Al.

Table 2.5. PhOLEDs Performances Using Bisindenoanthrazolines as ETMs.

ETL	V_{on} (V)	Drive voltage (V)	Current Density (mA/cm^2)	Luminance (cd/m^2)	Luminous Efficiency (cd/A) [EQE %]
-	10.8	18.9 *17.9*	290 *116*	21 300 *10 326*	7.3 [2.3] *8.9* [*2.9*]
DADA	8.1	16.9 *13.5*	233 *11.8*	62 000 *4270*	26.6 [8.7] *39.2* [*12.6*]
DADP	8.2	16.8 *13.6*	215 *14.1*	56 300 *4470*	26.2 [8.5] *31.7* [*10.2*]
DADF	9.5	17.6 *15.6*	194 *38.5*	25 900 *6900*	13.3 [4.3] *17.9* [*5.8*]
DADK	12.0	20.4 *19.5*	233 *136*	630 *460*	0.27 [0.13] *0.34* [*0.16*]

[a] Values in italic correspond to those for maximum device efficiencies.

2.4. Conclusions

A novel π-conjugated heptacylic framework has been synthesized and found to be a new class of n-type organic semiconductors. The high electron affinity (3.7 eV) and high electron mobility (10^{-7} to 10^{-4} cm^2/V.s) of the bisindenoanthrazolines makes them attractive candidates for electron transport in organic electronics. The bisindenoanthrazoline emitted electroluminescence with a high brightness (7610 cd/m^2), and high efficiency (6.6 cd/A with EQE of 2.0 % at a brightness of 936 cd/m^2). Some of the BIDAs (DADA and DADP) were excellent electron-transport materials in realizing high performance phosphorescent OLEDs, a brightness of 62 000 cd/m^2 and luminous efficiency of 39.2 cd/A at a brightness of 4270 cd/m^2 was achieved in green PhOLEDs. These results demonstrate that the bisindenoanthrazolines is a promising new class of n-type semiconductors for organic electronics and optoelectronics.

2.5. References

(1) *For recent reviews see*: (a) Günes, S.; Neugebauer, H.; Sariciftci, N. S. *Chem. Rev*. **2007**, *107*, 1324. (b) Thompson, B. C.; Fréchet, J. M. J. *Angew. Chem. Int. Ed*. **2008**, *47*, 58. (c) Dennler, G.; Scharber, M. C.; Brabec, C. J. *Adv. Mater*. **2009**, *21*, 1323.

(2) (a) Halls, J. J. M.; Walsh, C. A.; Greenham, N. C.; Marseglia, E. A.; Friend, R. H.; Moratti, S. C.; Holmes, A. B. *Nature*, **1995**, *376*, 498. (b) Alam, M. M.; Jenekhe, S. A. *Chem. Mater*. **2004**, *16*, 4647. (c) Liang, Y.; Xu, Z.; Xia, J.; Tsai, S.-T.; Wu, Y.; Li, G.; Ray, C.; Yu, L. *Adv. Mater.* **2010**, *22*, E135. (d) Wu, P.-T.; Bull, T.; Kim, F. S.; Luscombe, C. K.; Jenekhe, S. A.; *Macromolecules* **2009**, *42*, 671. (e) Ren, G.; Wu, P.-T.; Jenekhe, S. A. *Chem. Mater*. **2010**, *22*, 2020.

(3) (a) Grimsdale, A. C.; Chan, K. L.; Martin, R. E.; Jokisz, P. G.; Holmes, A. B. *Chem. Rev.* **2009**, *109*, 897. (b) Shirota, Y.; Kageyama, H. *Chem. Rev*. **2007**, *107*, 953. (c) Jenekhe, S. A.; Lu, L.; Alam, M. M. *Macromolecules* **2001**, *34*, 7315. (d) Friend, R. H.; Gymer, R. W.; Holmes, A. B.; Burroughs, J. H.; Marks, R. N.; Taliani, C.; Bradly, D. D. C.; Dos Santos, D. A.; Brédas, J. L.; Lögdlund, M.; Salaneck, W. R. *Nature (London)* **1999**, *397*, 121. (e) Kulkarni, A. P.; Gifford, A. P.; Tonzola, C. J.; Jenekhe, S. A. *Appl. Phys. Lett*. **2005**, *86*, 061106.

(4) (a) Coropceanu, V.; Cornil, J.; da Silva, D. A.; Olivier, Y.; Silbey, R.; Brédas, J.-L. *Chem. Rev.* **2007**, *107*, 926. (b) Murphy, A. R.; Fréchet, J. M. J. *Chem. Rev*. **2007**, *107*, 1066. (c) Zaumseil, J.; Sirringhaus, H. *Chem. Rev.* **2007**, *107*, 1296.

(5) (a) *Electronic Materials: The Oligomer Approach*, Müllen, K.; Wegner, G.; Eds. Wiley-VCH: Weinheim, Germany, **1998**. (c) Pope, M.; Swenberg, C. E. *Electronic Processes in Organic Crystals*; Oxford University Press: New York, **1999**.

(6) (a) Scherf, U. *J. Mater. Chem*. **1999**, *9*, 1853. (b) Yang, C.; Scheiber, H.; List, E. J. W.; Jacob, J.; Müllen, K. *Macromolecules* **2006**, 39, 5213. (c) Setayesh, S.; Marsitzky, D.; Müllen, K.; *Macromolecules* **2000,** 39, 2016.

(7) (a) Ahmed, E.; Briseno, A. L.; Xia, Y.; Jenekhe, S. A. *J. Am. Chem. Soc*. **2008**, 130, 1118. (b) Mass-Torrent, M.; Hadley, P.; Bromley, S. T.; Ribas, X.; Tarrés, J.; Mas, M.; Molins, E.; Veciana, J.; Rovira, C. *J. Am. Chem. Soc*. **2004**, *126*, 8546.

(8) (a) Anthony, J. E. *Angew. Chem. Int. Ed*. **2008**, *47*, 452. (b) Anthony, J. E. *Chem. Rev*. **2006**, *106*, 5028. (c) Subramanian, S.; Park, S. K.; Parkin, S. R.; Podzorov, V.; Jackson, T. N. Anthony, J. E. *J. Am. Chem. Soc*. **2008**, *130*, 2706. (d) Kim, D. H.; Lee, D. Y.; Lee, H. S.; Lee, W. H.; Kim, Y. H.; Han, J. I.; Cho, K. *Adv. Mater*. **2007**, *19*, 678. (e) Tang, M. L.; Reichardt, A. D.; Miyaki, N.; Stoltenberg, R. M.; Bao, Z. *J. Am. Chem. Soc*. **2008**, *130*, 6064.

(9) (a) Gao, P.; Beckmann, D.; Tsao, H. N.; Feng, X.; Enkelmann, V.; Baumgarten, M.; Pisula, W.; Müllen, K. *Adv. Mater*. **2009**, *21*, 213. (b) Gao, P.; Feng, X.; Yang, Enkelmann, V.; Baumgarten, M.; Müllen, K. *J. Org. Chem*. **2008**, 73, 9207. (c) Takimiya, K.; Ebata, H.; Sakamoto, K.; Izawa, T.; Otsubo, T.; Kunugi, Y. *J. Am. Chem. Soc*. **2006**, *128*, 12604. (d) Ebata,

H.; Izawa, T.; Miyazaki, E.; Takimiya, K.; Ikeda, M.; Kuwabara, H.; Yui, T. *J. Am. Chem. Soc.* **2007**, *129*, 15732. (e) Zhang, X.; Coté, A. P.; Matzger, A. J. *J. Am. Chem. Soc*. **2005**, *127*, 10502.

(10) (a) Boudreault, P.-L. T.; Wakim, S.; Blouin, N.; Simard, M.; Tessier, C.; Tao, Y.; Leclerc, M. *J. Am. Chem. Soc*. **2007**, *129*, 9125. (b) Boudreault, P.-L. T.; Wakim, S.; Tang, M. L.; Tao, Y.; Bao, Z.; Leclerc, M. *J. Mater. Chem*. **2009**, *19*, 2921. (c) Wakim, S.; Bouchard, J.; Blouin, N.; Michaud, A.; Leclerc, M. *Org. Lett*. **2004**, *6*, 3413. (d) Guo, Y.; Zhao, H.; Yu, G.; Di, C.-A.; Liu, W.; Jiang, S.; Yan, S.; Wang, C.; Zhang, H.; Sun, X.; Tao, X.; Liu, Y. *Adv. Mater*. **2008**, *20*, 4835.

(11) (a) Jacob, J.; Sax, S.; Piok, T.; List, E. J. W.; Grimsdale, A. C.; Müllen, K. *J. Am. Chem. Soc.* **2004**, *126,* 6987. (b) Zhou, Y.; Liu, W.-J.; Ma, Y.; Wang, H.; Qi, L.; Cao, Y.; Wang, J.; Pei, J. *J. Am. Chem. Soc*. **2007**, *129*, 12386.

(12) Bao, Z.; Lovinger, A. J.; Brown, J. *J. Am. Chem. Soc.* **1998**, *120*, 207.

(13) (a) Katz, H. E.; Lovinger, A. J.; Johnson, J.; Kloc, C.; Seigrist, T.; Li, W.; Lin, Y.-Y.; Dodablapur, A. *Nature* **2000**, *404*, 478. (b) Katz, H. E.; Johnson, J.; Lovinger, A. J.; Li, W. *J. Am. Chem. Soc.* **2000**, *122*, 7787.

(14) (a) Handa, S.; Miyazaki, E.; Takimiya, K.; Kunugi, Y. *J. Am. Chem. Soc*. **2007**, *129*, 11684. (b) Pappenfus, T. M.; Chesterfield, R. J.; Frisbie, C. D.; Mann, K. R.; Casado, J.; Raff, J. D.; Miller, L. L. *J. Am. Chem. Soc*. **2002**, *124*, 4184.

(15) (a) Usta, H.; Facchetti, A.; Marks, T. J. *Org. Lett*. **2008**, *10*, 1385. (b) Usta, H.; Risko, C.; Wang, Z.; Huang, H.; Deliomeroglu, M. K.; Zhukhovitskiy, A.; Facchetti, A.; Marks, T. J. *J. Am. Chem. Soc*. **2009**, *131*, 5586.

(16) Jones, B. A.; Ahrens, M. J.; Yoon, M. H.; Facchetti, A.; Marks, T. J.; Wasielewski, M. R. *Angew. Chem. Int. Ed*. **2004**, *43*, 6363.

(17) Jones, B. A.; Facchetti, A.; Wasielewski, M. R.; Marks, T. J. *Chem. Mater*. **2007**, *19*, 2703.

(18) (a) Kim, F. S.; Guo, X.; Watson, M. D.; Jenekhe, S. A. *Adv. Mater*. **2010**, *22*, 478. (b) Yan, H.; Chen, Z.; Zhen, Y.; Newman, C.; Quinn, J. R.; Dötz, F.; Kastler, M.; Facchetti, A. *Nature* **2009**, *457*, 679.

(19) (a) Babel, A.; Jenekhe, S. A. *J. Am. Chem. Soc*. **2003**, *125*, 13656. (b) Babel, A.; Jenekhe, S. A. *Adv. Mater*. **2002**, *14*, 371.

(20) (a) Tonzola, C. J.; Alam, M. M.; Kaminsky, W.; Jenekhe, S. A. *J. Am. Chem. Soc.* **2003**, *125*, 13548. (b) Kulkarni, A. P. ; Tonzola, C. J. ; Babel, A. ; Jenekhe, S. A. *Chem. Mater*. **2004**, *16*, 4556. (c) Tonzola, C. J.; Kulkarni, A. P.; Gifford, A. P.; Kaminsky, W.; Jenekhe, S. A. *Adv. Funct. Mater*. **2007**, *17*, 863. (d) Kulkarni, A. P.; Jenekhe, S. A. *Macromolecules* **2003**, *36*, 5285. (e) Zhang, X.; Shetty, A. S.; Jenekhe, S. A. *Macromolecules* **1999**, *32*, 7422.

(21) (a) Jenekhe, S. A. *Macromolecules* **1991**, *24*, 1. (b) Miao, S.; Bromobosz, S. M.; Schleyer, P. v. R.; Wu, J. I.; Barlow, S.; Marder, S. R.; Hardcastle, K. I.; Bunz, U. H. F. *J. Am. Chem. Soc*.

2008, *130*, 7339. (c) Nishida, J.-I.; Naraso; Murai, S.; Fujiwara, E.; Tada, H.; Tomura, M.; Yamashita, Y. *Org. Lett*. **2004**, *6*, 2007. (d) Kaafarani, B. R.; Kondo, T.; Yu, J.; Zhang, Q.; Dattilo, D.; Risko, C.; Jones, S. C.; Barlow, S.; Domercq, B.; Amy, F.; Kahn, A.; Brédas, J.-L.; Kippelen, B.; Marder, S. R. *J. Am. Chem. Soc.* **2005**, *127*, 16358.

(22) (a) Fogel, Y.; Kastler, M.; Wang, Z.; Andrienko, D.; Bodwell, G. J.; Müllen, K. *J. Am. Chem. Soc*. **2007**, *129*, 11743. (b) Lee, D.-C.; Jang, K.; McGrath, K. K.; Uy, R.; Robins, K. A.; Hatchett, D. W. *Chem. Mater*. 2008, *20,* 3688. (c) Gao, B.; Wang, M.; Jing, X.; Wang, F. *J. Am. Chem. Soc*. **2008**, *130*, 8297. (d) Zhu, Y.; Yen, C.-T.; Jenekhe, S. A.; Chen, W.-C. *Macromol. Rapid Commun.* **2004**, *25*, 1829.

(23) Nakagawa, T.; Kumaki, D.; Nishida, J.-I.; Tokito, S.; Yamashita, Y. *Chem. Mater*. **2008**, *20*, 2615.

(24) Winkler, M.; Houk, K. N. *J. Am. Chem. Soc*. **2007**, *129*, 1805.

(25) (a) Sakamoto, Y. Suzuki, T.; Kobayashi, M.; Gao, Y.; Fukai, Y.; Inoue, Y.; Sato, F.; Tokito, S. *J. Am. Chem. Soc.* **2004**, *126*, 8138. (b) Tang, M. L.; Reichardt, A. D.; Wei, P.; Bao, Z. *J. Am. Chem. Soc*. **2009**, *131*, 5264.

(26) (a) Facchetti, A.; Yoon, M.-H.; Stern, C. L.; Hutchison, G. R.; Ratner, M. A.; Marks, T. J. *J. Am. Chem. Soc*. **2004**, *126*, 13480. (b) Wang, Y.; Parkin, S. R.; Gierschner, J.; Watson, M. D. *Org. Lett*. **2008**, *10*, 3307.

(27) (a) Schenning, A. P. H. J.; Meijer, E. W. *Chem. Commun*. **2005**, 3245. (b) Würthner, F. *Chem. Comm*. **2004**, *14*, 1564. (c) Chesterfield, R. J.; McKeen, J. C.; Newman, C. R.; Ewbank, P. C.; daSilva, Filho, D. A.; Brédas, J.-L.; Miller, L. L.; Mann, K. R.; Frisbie, C. D. *J. Phys. Chem. B* **2004**, *108*, 19281. (d) Schemidt, R.; Oh, J. H.; Sun, Y.-S.; Deppisch, M.; Krause, A.-M.; Radacki, K.; Braunschweig, H.; Könemann, M.; Erk, P.; Bao, Z.; Würthner, F. *J. Am. Chem. Soc*. **2009**, *131*, 6215.

(28) (a) Norton, J. E.; Brédas, J.-L. *J. Am. Chem. Soc*. **2008**, *130,* 12377. (b) Verlaak, S.; Heremans, P. *Phys. Rev. B: Condens. Matter. Mater. Phys*. **2007**, *75*, 115127/1. (c) Ruiz Delgade, M. C.; Kim, E.-G.; da Silva Filho, D. A.; Brédas, J.-L. *J. Am. Chem. Soc.* **2010**, *132*, 3375.

(29) (a) Tsao, H. N.; Wojciech, P.; Liu, Z.; Osikowicz, W.; Salaneck, W. R.; Müllen, K. *Adv. Mater*. **2008**, *20*, 2715. (b) Avlasevich, Y.; Müller, S.; Erk, P.; Müllen, K. *Chem. Eur. J*. **2007**, *13,* 6555. (c) Qian, H.; Negri, F.; Wang, C.; Wang, Z. *J. Am. Chem. Soc.* **2008**, *130*, 17970.

(30) *For recent reviews see*: (a) Schenning, A. P. H. J.; Meijer, E. W. *Chem. Commun*. **2005**, 3245. (b) Würthner, F. *Chem. Comm*. **2004**, *14*, 1564. (c) Zang, L.; Che, Y.; Moore, J. S. *Acc. Chem. Res*. **2008**, *41*, 1596. (d) Briseno, A. L.; Mannsfeld, S. C. B.; Jenekhe, S. A.; Bao, Z.; Xia, Y. *Materials Today* **2008**, *11*, 38.

(31) (a) Xin, H.; Kim, F. S.; Jenekhe, S. A. *J. Am. Chem. Soc*. **2008**, *130*, 5424. (b) Xin, H.; Ren, G.; Kim, F. S.; Jenekhe, S. A. *Chem. Mater*. **2008**, *20*, 6199. (c) Xin, H.; Reid, O. G.; Ren, G.; Kim, F. S.; Ginger, D. S.; Jenekhe, S. A. *ACS Nano* **2010**, *4*, 1861.

(32) (a) Briseno, A. L.; Mannsfeld, S. C. B.; Reese, C.; Hancock, J. M.; Xiong, Y.; Jenekhe, S. A.; Bao, Z.; Xia, Y. *Nano Letters* **2007**, *7*, 2847. (b) Che, Y.; Datar, A.; Balakrishnan, K.; Zang, L. *J. Am. Chem. Soc*. **2007**, *129*, 7234. (c) Balakrishnan, K.; Datar, A.; Oitker, R.; Chen, H.; Zuo, J.; Zang, L. *J. Am. Chem. Soc.* **2005**, *127*, 10496. (d) Lee, D.-C.; McGrath, K. K.; Jang, K. *Chem. Commun*. **2008**, 3636. (e) Briseno, A. L.; Mannsfeld, S. C. B.; Shamberger, P. J.; Ohuchi, F.; Bao, Z.; Jenekhe, S. A.; Xia, Y. *Chem. Mater*. **2008**, *20*, 4712.

(33) (a) Briseno, A. L.; Mannsfeld, S. C. B.; Ling, M.; Liu, S.; Tseng, R. J.; Reese, C.; Roberts, M.; Yang, Y.; Wudl, F.; Bao, Z. *Nature* **2006**, *444*, 913. (b) de Boer, R. W. I.; Gershenson, M. E.; Morpurgo, A. F.; Podzorov, V. *Phys. Stat. Solidi(a)* **2004**, *201*, 1302. (c) Gershenson, M. E.; Podzorov, V.; Morpurgo, A. F. *Rev. Mod. Phys.* **2006**, *8*, 973.

(34) (a) Agrawal, A. K.; Jenekhe, S. A. *Macromolecules* **1991**, *24*, 6806. (b) Agrawal, A. K.; Jenekhe, S. A. *Macromolecules* **1993**, *26*, 633.

(35) (a) Jenekhe, S. A., Osaheni, J. A. *Science* **1994**, 265, 765. (b) Osaheni, J. A., Jenekhe, S. A. *Macromoleclues* **1994**, 27, 739.

(36) (a) Murgatroyd, P. N. *J. Phys*. *D* **1970**, *3*, 1488. (b) Mott, N. F.; Gurney, D. *Electronic Processes in Ionic Crystals*; Academic Press: New York, 1970. (c) Campbell, A. J.; Bradley, D. D. C.; Lidzey, D. G. *J. Appl. Phys*. **1997**, *82*, 6326.

(37) (a) Choudhury, K. R.; Yoon, J.-H.; So, F. *Adv. Mater*. **2008**, *20*, 1456. (b) Chu, T.-Y.; Song, O.-K.; *Appl. Phys. Lett*. **2007**, *90*, 203512. (c) Khan, M. A.; Xu, W.; Haq, K.-U.; Bai, Y.; Jiang, X. Y.; Zhang, Z. L.; Zhu, W. Q.; Zhang, Z. L.; Zhu, W. Q. *J. Appl. Phys*. **2008**, *103*, 014509.

(38) (a) Jenekhe, S. A. *Adv. Mater*. **1995**, *7*, 309. (b) Kulkarni, A. P.; Jenekhe, S. A. *J. Phys. Chem. C* **2008**, *112*, 5174.

(39) Earmme, T.; Ahmed, E.; Jenekhe, S. A. *J. Phys. Chem. C* **2009**, *113*, 18448.

Chapter 3. High-Performance Phosphorescent OLEDs (PhOLEDs) Enabled by Orthogonal Solution-Processing

This chapter investigates orthogonal solution-processing of organic semiconductors to achieve highly efficient multilayered phosphorescent OLEDs. The results in this chapter are reprinted in part with permission from Earmme, *et al*. (Copyright 2010 Wiley-VCH), Ahmed and Earmme, *et al*. (Copyright 2011 Wiley-VCH), and from Earmme, *et al*. (Copyright 2012 Royal Society).

3.1. Solution-Prcessed Phosphorescent OLEDs Using New Dendritic Oligoquinoline-based Electron-Transport Materials

3.1.1. Introduction

Organic light emitting diodes (OLEDs) are finding applications in various next generation flat-panel displays and solid state lighting.[1-4] To date, highly efficient OLEDs are based on phosphorescent emitters which can convert both singlet and triplet excitons into photons and have resulted in 100 % internal quantum efficiency.[5-11] Despite advances in red[12] and green[13] phosphorescent OLEDs (PhOLEDs), the development of blue PhOLEDs remains challenging due to the high photon energy of blue phosphorescent emitters. An effective approach toward improving the efficiency of PhOLEDs is the incorporation of an electron-transport material between the emissive layer and the cathode.[7-21] To be effective in enhancing the performance of blue PhOLEDs, such an electron transport material must combine (i) a high electron affinity to enable efficient electron-injection and (ii) a high electron mobility to enhance electron flux, with (iii) a high ionization potential and (iv) a high triplet energy to confine excitons within the emissive layer.[5,9] Thus far, few electron transport materials (ETMs) satisfy these criteria for

blue PhOLEDs.[9,19-21] The development of new electron transport materials with optimum properties are needed for next generation PhOLEDs.

Imine-nitrogen rich heterocyclic capable of high electron mobility are of increasing interest in the development of ETMs and hole-blocking layers (HBLs).[7-9,14-21] Incorporation of imine nitrogens into aromatic organic semiconductors provide many advantages, including increase in electron affinity, improved photo-oxidative stability, and processbility from both aprotic and protic organic solvents. To date, only a few classes of n-type materials have been used as ETMs/HBLs for blue PhOLEDs,[14-20] including phenanthroline,[15,16] benzoimidazole,[17] and triazole[18] derivatives. However, these materials generally have low carrier mobility and their triplet energy is significantly lower than that of the blue phosphorescent emitters. Recently, high performance blue PhOLEDs were achieved by the use of wide-energy-gap ETMs/HBLs based on phenylpyridine[9,19] and phenylpyrimidine[20] derivatives fabricated by vacuum deposition.

Although small-molecule ETMs have enabled the development of highly efficient PhOLEDs with multilayered structures, vacuum thermal deposition of small molecules is an expensive process.[22,23] Solution-processed PhOLEDs provide an economically attractive alternative to vacuum-deposition. However, fabrication of multilayered devices by solution-based processing is challenging because of the requirement of orthogonal solvents that would not dissolve or disrupt the underlying emissive layer. Only several solution-processed PhOLED devices have been reported.[24-32] Although the emissive layer is solution-processed, the polymer-based PhOLEDs generally include a thermally deposited ETM, HBL, cathode interfacial layers (e.g. LiF, CsF) or low work-function metal cathode. [24-31] Our group has previously reported multilayered solution-based processing of heterocyclic polymer electron-transport layers (ETLs) onto various emissive layers in multilayered OLEDs using organic acid solvents.[33-42] More

recently, polyfluorene-based polyelectrolytes were also used as ETLs in multilayered OLEDs.[43-45] However, ionic side groups in the conjugated polyelectrolytes can result in electrochemical doping at the polymer/electrode interface.[46] Recently, we reported a wide-energy-gap electron-transport material based on 1,3,5-tris(4-phenylquinolin-2-yl)benzene (TQB) that enabled highly efficient polymer-based blue PhOLEDs to be fabricated by sequential solution-processing.[7]

In this section, we discuss the synthesis, electrochemical properties, and photophysics of a series of new dendritic oligoquinolines and their use as electron-transport layers in solution-processed highly efficient polymer-based blue PhOLEDs. The molecular structures of the oligoquinolines (TMQB, TQB, TFQB, and TPyQB) are shown in Chart 3.1. The molecular design of these oligoquinolines focused on connecting tris(quinolin-2-yl)benzene with *meta*-linkage to confine the π-conjugation length and thus to enable wide-energy-gap. Various substitutions (R_1 = methyl, phenyl, 4-fluorophenyl, and 4-pyridyl) on the quinoline rings were examined towards tuning the electronic and solid state properties. We found that simple variation of R_1 group in the quinoline rings leads to a 100-fold variation in charge carrier mobility among the four oligoquinolines.

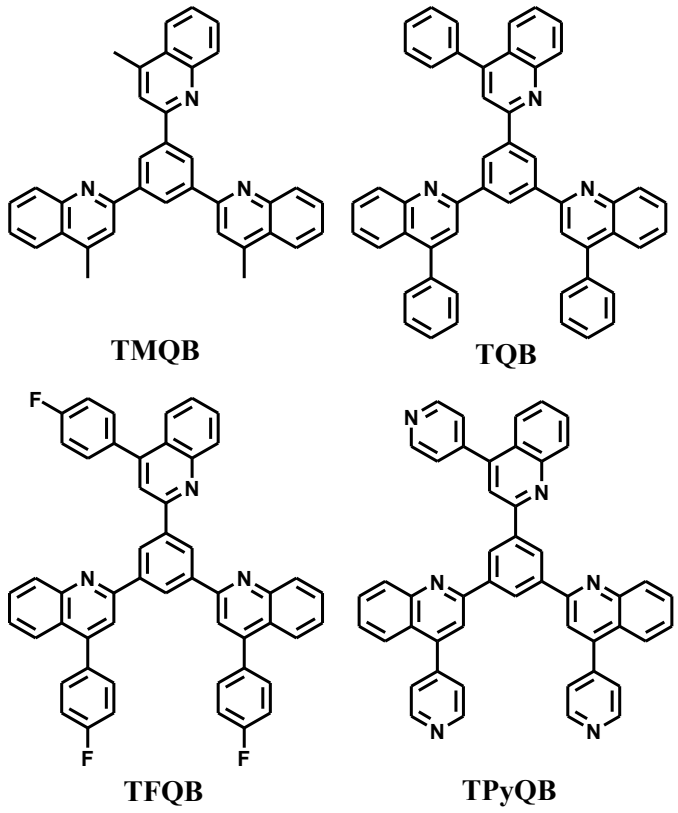

Chart 3.1 Chemical Structure of Oligoquinolines.

Blue PhOLEDs based on FIrpic triplet emitter-doped poly(*N*-vinylcarbazole) (PVK) emission layer and a solution-processed oligoquinoline electron-transport layer (ETL) gave a high luminous efficiency of 30.5 cd A^{-1} at a brightness of 4130 cd m^{-2} with an external quantum efficiency (EQE) of 16.0 %. These solution-processed PhOLEDs exhibit the highest performance observed to date in polymer-based blue PhOLEDs. The approach of using solution-processed oligoquinoline ETLs has resulted in high performance blue PhOLEDs while eliminating the need for a cathode interfacial layer (e.g. LiF, CsF) in OLEDs. The results also clearly demonstrate that small-molecule electron-transport layer/hole-blocking layer (ETL/HBL) can be solution-processed to fabricate high-performance PhOLEDs instead of using vacuum-deposition. We also found that the solution-processed ETL films exhibit a unique morphology which facilitates improved carrier mobility, higher device performance, and better ETL/electrode interface compared with vacuum deposited films. Structure-property relationships of the series of oligoquinolines were investigated by cyclic voltammetry, photophysical measurements, space-

charge-limited current (SCLC) measurements of electron mobility, electrophosphorescent devices, and atomic force microscopy (AFM).

3.1.2. Experimental Section

Synthetic Procedures. All commercially available reagents were used without further purification.

Synthesis of 1,3,5-Tris(4-methylquinolin-2-yl)benzene ***(TMQB).*** A mixture of 2-aminoacetophenone (3.0 g, 14.7 mmol), 1,3,5-triacetylbenzene (6.2 g, 45.5 mmol) and diphenyl phophate (8 equiv) in 12 mL of toluene were refluxed under argon for 18 h. The reaction mixture was precipitated from 10% methanol/triethylamine and the solid was collected by vacuum filteration. The product was purified by flash column chromatography using dichloromethane and acetonitrile mixture (9.5:0.5). The product was then recrystallized twice from dichloromethane and once from THF/ MeOH mixture (2:1 v:v) to give a white solid (3.69 g, 50% yield). ^{1}H NMR (300 MHz, $CDCl_3$): δ ppm = 9.102 (s, 3H), 8.325 (d, *J* = 8.0 Hz, 3H), 8.101-8.068 (m, 6H), 7.788 (t, *J* = 8.1 Hz, 3H), 7.614 (m, 3H), 2.882 (s, 9 H). ^{13}C NMR (500 MHz, $CDCl_3$): δ ppm = 156.76, 148.20, 144.99, 140.90, 130.40, 129.38, 127.53, 126.16, 123.73, 120.14, 19.08. HRMS(FAB) *m/z* calcd for $[(M+H)^+]$ $C_{36}H_{28}N_3$ (502.22879), found 502.22908.

Synthesis of 1,3,5-tris(4-phenylquinolin-2-yl)benzene ***(TQB)****:* A mixture of 2-aminobenzophenone (6 g, 30.5 mmol), 1,3,5-triacetylbenzene (2.0 g, 9.79 mmol) and diphenyl phophate (DPP, 8 equiv.) in 12 mL of toluene was refluxed in argon for 18 h. The reaction mixture was precipitated into 10% methanol/triethylamine and the solid was collected by vacuum filtration. The product was purified by flash column chromatography using dichloromethane and acetonitrile mixture (9.5:0.5), followed by recrystallization from

tetrahydrofuran/methanol solvent mixture (2:1, v/v) to give a white solid (5 g, 74% yield). ^{1}H NMR (300 MHz, $CDCl_3$): δ ppm = 9.175 (s, 3H), 8.3714 (d, 3H), 8.139 (s, 3H), 7.979 (d, 3H), 7.784 (t, 3H), 7.679-7.5067 (m, 18H). ^{13}C NMR (300 MHz, $CDCl_3$): δ ppm = 156.4905, 149.3806, 148.8507, 140.9459, 130.2619, 129.7142, 129.5713, 128.8807, 128.6283, 128.4425, 127.7615, 126.4845, 125.7167, 125.3298, 119.5872. HRMS (FAB) *m/z* calcd for [$(M+H)^+$] $C_{51}H_{34}N_3$ (688.27551), found 688.27619.

Synthesis of 1,3,5-tris(4-(4-fluorophenyl)quinolin-2-yl)benzene ***(TFQB).*** A mixture of 2-amino-4′-fluorobenzophenone (3.2 g, 14.9 mmol), 1,3,5-triacetylbenzene (1.0 g, 4.9 mmol) and diphenyl phophate (8 equiv) in 12 mL of toluene were refluxed under argon for 18 h. The reaction mixture was precipitated from 10% methanol/triethylamine and the solid was collected by vacuum filteration. The product was purified by flash column chromatography using chloroform and acetonitrile mixture (9.5:0.5). The product was then recrystallized from from chlorofrom/ MeOH mixture (1:1 v:v) to give a white solid (3.1 g, 85% yield). ^{1}H NMR (300 MHz, $CDCl_3$): δ ppm = 9.158 (s, 3H), 8.352 (d, *J* = 8.4 Hz, 3H), 8.106 (s, 3H), 7.927 (d, *J* = 8.1 Hz, 2H), 7.787 (t, 3H), 7.620 (m, 9H), 7.328 (m, 6H), 2.882 (s, 9 H). ^{13}C NMR (500 MHz, $CDCl_3$): δ ppm = 163.972, 161.997, 156.400, 148.824, 148.351, 140.845, 134.304, 131.452, 130.275, 129.744, 127.761, 126.717, 125.991, 125.479, 119.640, 115.816, 115.644. HRMS (FAB) *m/z* calcd for [$(M+H)^+$] $C_{51}H_{31}F_3N_3$ (742.24625), found 742.24393.

Synthesis of 1,3,5-tris(4-pyridinquinolin-2-yl)benzene **(TPyQB).** A mixture of 4-(2-aminobenzoyl)pyridine (1.0 g, 5.04 mmol), 1,3,5-triacetylbenzene (338 mg, 1.66 mmol) and diphenyl phophate (8 equiv) in 12 mL of toluene were refluxed under argon for 18 h. The reaction mixture was precipitated from 10% methanol/triethylamine and the solid was collected by vacuum filteration. The product was then recrystallized from chloroform/ MeOH mixture

(1:1 v:v) to give a white solid (840 mg, 89% yield). ^{1}H NMR (300 MHz, $CDCl_3$): δ ppm = 9.184 (s, 3H), 8.887 (d, *J* = 6.0 Hz, 6H), 8.391 (d, *J* = 8.4 Hz, 3H), 8.120 (s, 3H), 7.886-7.813 (m, 6H), 7.602-7.582 (m, 9H). ^{13}C NMR (500 MHz, $CDCl_3$): δ ppm =156.24, 150.25, 148.77, 146.60, 146.22, 140.70, 130.47, 130.18, 127.83, 127.28, 125.04, 124.96, 124.45, 119.12. HRMS (FAB) *m/z* calcd for $[(M+H)^+]$ $C_{48}H_{31}N_6$ (691.26046), found 691.25988.

Characterization. ^{1}H NMR spectra were recorded on a Bruker AV300 at 300 MHz, whereas ^{13}C NMR spectra were recorder on a Brucker AV 500 at 500 MHz using $CDCl_3$ as the solvent. Mass spectra were obtained from Bruker Esquire LC/ Ion Trap Mass spectrometer and JEOL/ HX-110. Cyclic voltammetry was measured on an EG&G Princeton Applied Research Potentiostat/Galvanostat (Model 273A). Data were analyzed by Model 270 Electrochemical Analysis System Software on a PC computer. A three-electrode cell was used, consisting of platinum wire electrodes as both counter and working electrode. Silver/silver ion (Ag in 0.1 M $AgNO_3$ solution, Bioanalytical System, Inc.) was used as a reference electrode. Ferrocene/ferrocenium (Fc/Fc^+) was used as an internal standard. The potential values obtained in reference to Ag/Ag^+ were converted to the saturated calomel electrode (SCE) scale. Thin film cyclic voltammetry was performed in acetonitrile containing 0.1M $TBAPF_6$. Thin films of each oligoquinoline were coated onto a platinum electrode from a concentrated solution (10 mg mL^{-1}) in formic acid and dried in vacuum for 2 hours. All solutions were purged with N_2 for 10-15 minutes before each experiment. UV-vis absorption spectra were collected on a Perkin-Elmer model Lambda 900 UV/vis/near-IR spectrophotometer. The photoluminescence (PL) spectra were obtained with a Photon Technology International (PTI) Inc. Model QM 2001-4 spectrofluorimeter.

Fabrication and Characterization of PhOLEDs. The blue EML consisted of a blend of poly(N-vinyl carbazole) (PVK, M_w = 135,600, M_n = 56,400, Polysciences) and 1,3-bis(2-(4-*tert*-butylphenyl)-1,3,4-oxadiazo-5-yl)benzene (OXD-7, LumTec., Taiwan) (PVK:OXD-7 = 60:40, wt/wt) as a host and 10 wt% bis(3,5-difluoro-2-(2-pyridyl)phenyl-(2-carboxypyridyl)iridium (FIrpic, LumTec., Taiwan) as the dopant. A solution of PEDOT:PSS (poly-(ethylenedioxythiophene)-polystyrenesulfonate, H.C.Starck, Clevios PVP Al 4083) in water was spin-coated to make a 30-nm hole-injection layer onto a pre-cleaned ITO glass and annealed at 150 ºC under vacuum. The 70-nm blue EML was obtained by spin coating of the PVK:OXD-7:FIrpic blends in chlorobenzene onto the PEDOT:PSS layer and vacuum dried at 100 ºC. A 20-nm film of each oligoquinoline was evaporated in a vacuum (< 6.0 x 10^{-7} torr) or spun cast from a 16 mg mL^{-1} solution oligoquinoline in formic acid:water (3:1) mixture at a spin speed of 7000 rpm onto the EML, followed by vacuum drying at 50 ºC overnight. After drying, 100-nm Al was deposited onto the ETL. The structure of devices I and II were identical: ITO/PEDOT:PSS (30 nm)/EML (70 nm)/oligoquinoline (20 nm)/Al (100 nm). Film thickness was measured by an Alpha-Step 500 profilometer (KLA-Tencor, San Jose, CA). Electroluminescence (EL) spectra were obtained using the same spectrofluorimeter described above. Current-voltage characteristics of the PhOLEDs were measured by using a HP4155A semiconductor parameter analyzer (Yokogawa Hewlett-Packard, Tokyo). The luminance was simultaneously measured by using a model 370 optometer (UDT Instruments, Baltimore, MD) equipped with a calibrated luminance sensor head (Model 211) and a 5x objective lens. The device external quantum efficiencies (EQEs) were calculated from the luminance, current density and EL spectrum assuming a Lambertian distribution using procedures reported previously.[7,33] All the device fabrication and device characterization steps were carried out under ambient laboratory condition.

Devices for space-charge-limited current (SCLC) measurement were fabricated with ITO/oligoquinoline/Al structure. The Al electrode and organic layer were obtained by the spin-coating of oligoquinolines onto the substrate followed by deposition of Al electrode. Current-voltage characteristics of SCLC devices were measured using the same semiconductor parameter analyzer as for PhOLED devices. The SCLC measurements were performed under dark and ambient conditions.

AFM characterization of surface morphology was done on a Veeco Dimension 3100 Scanning Probe Microscope (SPM) system. The AFM topographical images were directly measured on the same PhOLEDs used for device characterization.

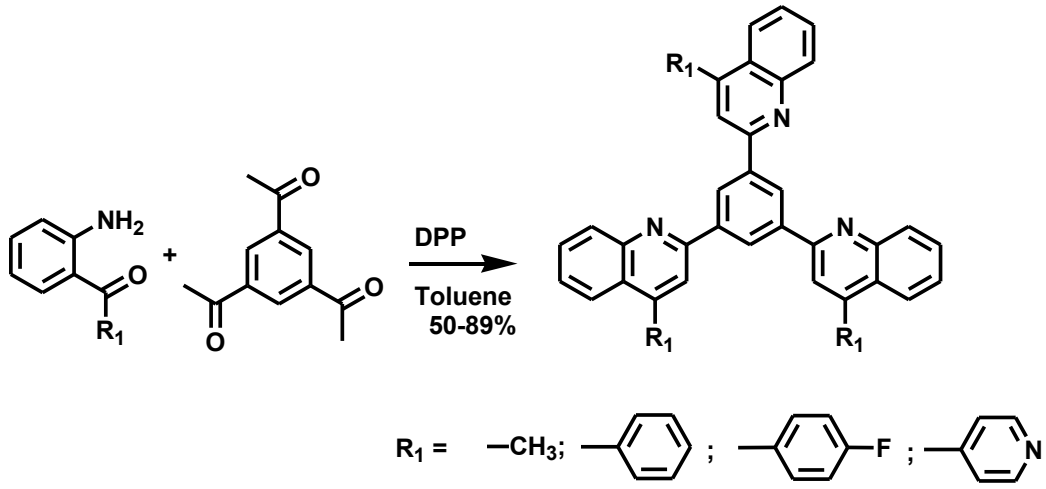

Scheme 3.1. Synthesis of Oligoquinolines.

3.1.3. Results and Discussion

Synthesis and Characterizations. The synthesis of the four dendritic oligoquinolines, 1,3,5-tris(4-methylquinolin-2-yl)benzene (TMQB), 1,3,5-tris(4-phenylquinolin-2-yl)benzene (TQB), 1,3,5-tris(4-(4-fluorophenyl)quinolin-2-yl)benzene (TFQB), and 1,3,5-tris(4-pyridinquinolin-2-

yl)benzene (TPyQB), is outlined in Scheme 3.1. They were synthesized by acid-catalyzed Friedlander condensation using diphenyl phosphate (DPP).[47,48] The products were precipitated from 10% methanol/triethylamine mixture. TMQB, TQB, and TFQB were purified by flash

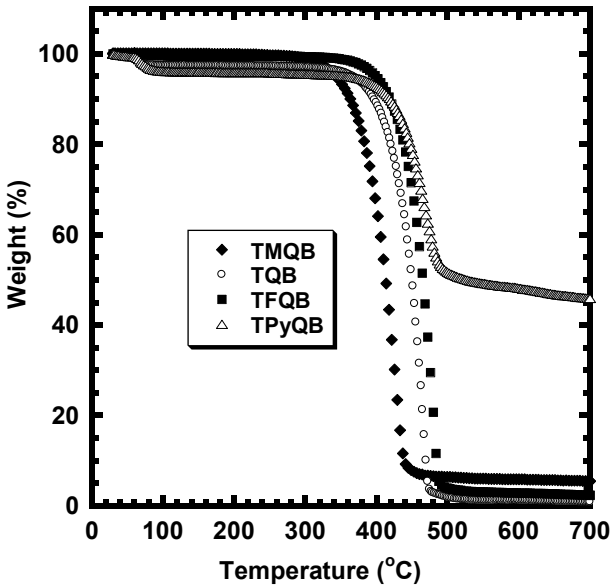

Figure 3.1. Thermogravimetric analysis (TGA) curves of oligoquinolines.

column chromatography followed by recrystallization to give the final products in 50-85% yield. TPyQB was purified by recrystallization from chloroform and methanol mixture to give the final product in 89% yield. The oligomers were soluble in chloroform, toluene, and tetrahydrofuran to varying degrees and they were readily soluble in formic acid. ^{1}H NMR, ^{13}C NMR and high resolution mass spectrometry confirmed the proposed structure.

The thermal stability and thermal transition properties of the oligoquinolines were investigated by thermogravimetric analysis (TGA) and differential scanning calorimetry (DSC). The TGA scans (**Figure 3.1**) showed that the four oligoquinolines are thermally robust materials with onset decomposition temperatures (T_D) in the range of 378-437 °C. The observed T_D values are slightly lower than those of *para*-substituted oligoquinolines (T_D ~ 417-492 °C).[47] The

second-heating DSC scans of the oligoquinolines are examplified by those of TQB and TFQB in Figure 3.2. and TMQB and TPyQB are shown in Figure 3.3. A clear glass transition temperature (T_g) of 172 °C was only observed in TPyQB. The thermal properties including the melting transition (T_m), crystallization transition (T_c) and onset decomposition temperature (T_D) are summarized in Table 3.1. The T_m slightly decrease from 300 °C in TMQB to 276 °C in TQB and 281 °C in TFQB and then significantly increase to 390 °C in TPyQB. The higher T_m value observed in TMQB compared to TQB and TFQB suggest that TMQB has better intermolecular packing in the solid-state. On the other hand, the T_m of TPyQB is higher by 114 °C than that of TQB, where the main difference between the two derivatives is the substitution of carbon atom with nitrogen. This suggest that in addition to the π-π intermolecular interactions, additional strong intermolecular interactions such as CH···N hydrogen-bonding is also present in TPyQB and likely responsible for the observed high T_m value. All four oligomers showed clear thermal transitions during the cooling from the melt.

Photophysical Properties. The normalized optical absorption spectra of vacuum-deposited and solution-deposited thin films of the four oligoquinolines on quartz substrates are shown in Figure 3.4 (a). The thin film absorption spectra of the oligoquinolines show two bands, a lower intensity band in the range of 310-340 nm and a higher intensity band in the 250-280 nm range. These absorption bands in TMQB, TQB, TFQB and TPyQB spectra are associated with π-π* transitions. Absorption maxima (λ_{max}) of the oligoquinolines in solution and as thin films and the optical band gaps (E_g^{opt}) are listed in Table 3.1. The λ_{max} values of the vacuum-deposited thin films of the materials are very similar ranging from 256 nm in TMQB to 276 nm in TFQB and TPyQB (Table 3.2). Solution-deposited thin films of TMQB, TQB, TFQB, and TPyQB have similar λ_{max} (256, 276, 274, and 273 nm; respectively) to that of the vacuum-deposited films. Solution-

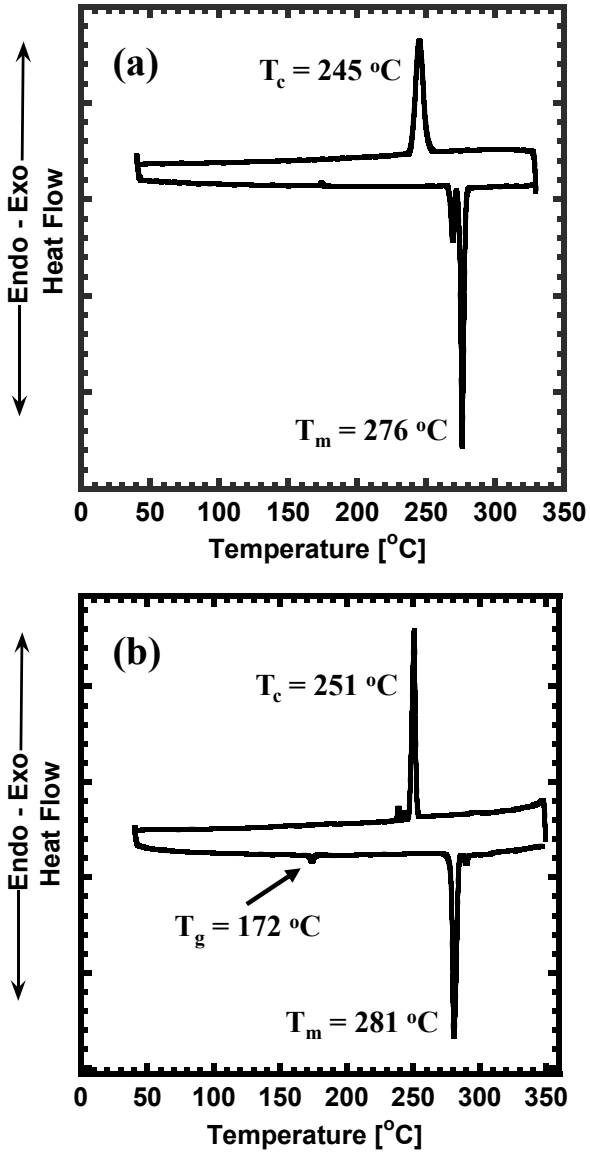

Figure 3.2. DSC scans of (a) TQB and (b) TFQB at a heating/cooling rate of 10 °C min^{-1} in nitrogen.

deposited films of TMQB, TQB, and TFQB showed enhanced absorption at 330 nm compared to their vacuum-deposited films. In contrast, solution-deposited film of TPyQB showed enhanced absorption at 230 nm compared to the vacuum-deposited films. The enhanced absorption in solution-deposited films (e.g. at 330 nm) suggests the formation of aggregates due to improved intermolecular interactions. The solution- and vacuum-deposited films showed identical band gaps. The optical band gap from the absorption edge of the thin films was in the range of 3.40 eV in TQB to 3.33 eV in TPyQB. The E_g^{opt} of these *meta*-substituted oligoquinolines is higher by 0.3-0.5 eV compared to previously reported *para*-substituted oligoquinolines[47].

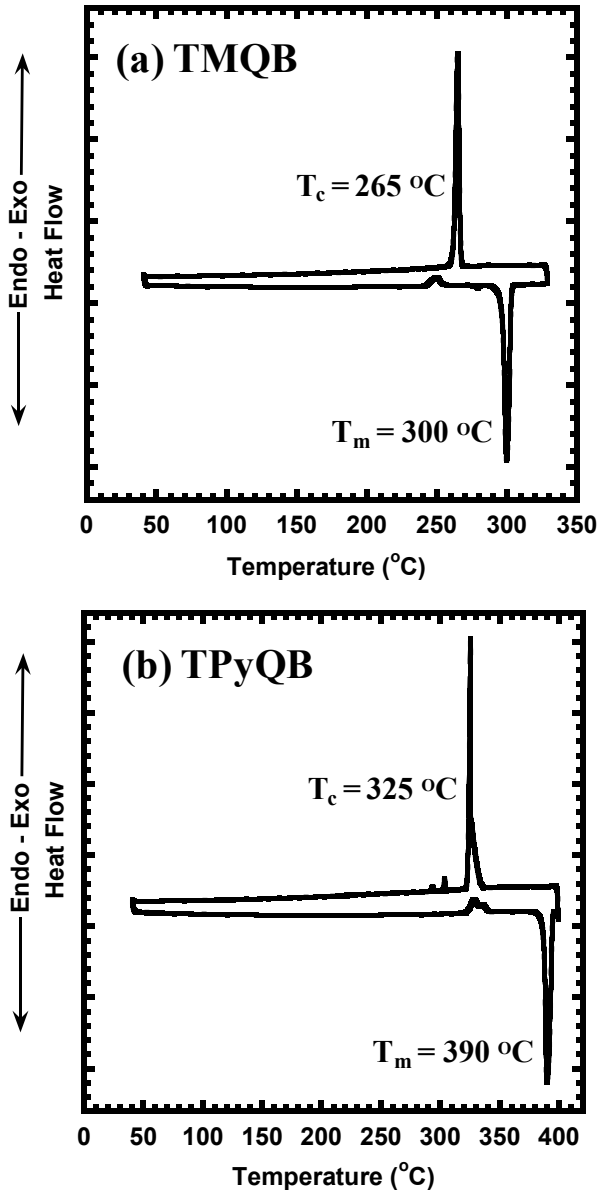

Figure 3.3. DSC scans of (a) TMQB and (b) TPyQB at a heating/cooling rate of 10 °C min^{-1} in nitrogen.

The photoluminescence (PL) emission spectra of the solution-deposited and vacuum-deposited thin films of oligoqouinolines are shown in Figure 3.4 (b). Vacuum-deposited films of

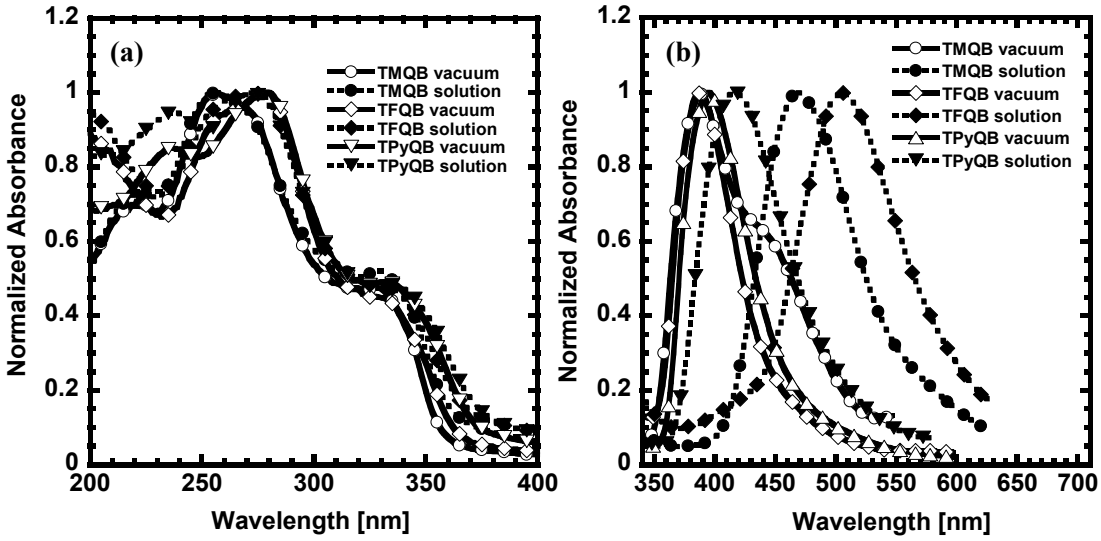

Figure 3.4. (a) Optical absorption spectra and (b) PL emission spectra of vacuum-deposited and solution-deposited thin films of the oligoquinolines.

all four oligoquinolines showed violet PL emission spectra. TQB, TFQB, TPyQB have almost identical violet emission spectra with PL maximum in the range of 391-395 nm and a narrow full-width-half-maxim (*fwhm*) ranging from 57 nm in TQB to 63 nm in TPyQB. In contrast, TMQB has a broad PL spectrum with shoulder peak at 441 nm and a *fwhm* of 100 nm. The broad PL emission spectrum of TMQB suggests that it favors strong aggregation compared to the other three oligoquinolines. The PL emission spectra of the solution-deposited films were significantly different compared to the vacuum-deposited films. The PL spectra in solution-deposited films were red shifted and broader. TQB and TPyQB showed similar PL spectra with PL maximum of 413-416 nm with *fwhm* of 84-88 nm. In contrast, TMQB and TFQB PL spectra show significant bathochromic shift with PL maximum of 468 and 505 nm and *fwhm* of 92 and 102 nm, respectively. The significant bathochromic shift and broader PL spectra of the solution-deposited TMQB and TFQB films suggest that the photoluminescence originates from excimer or aggregate states formed as a result of aggregation from solution.[49,50]

Electrochemical properties. We estimated the lowest unoccupied molecular orbital (LUMO) energy levels or electron affinity (EA) and the highest occupied molecular orbital (HOMO) energy levels or the ionization potential (IP) of the oligoquinolines from cyclic voltammograms of thin films. The reduction CVs of the oligoquinolines exemplified by those of TMQB and TFQB are shown in Figure 3.5 while the reduction CVs of TQB and TPyQB are shown in Figure 3.6. The onset reduction potentials of the oligomers are summarized in Table 3.2. The reduction CVs scans of TQB and TFQB show one reversible reduction wave, whereas a quasi-reversible reduction wave was observed in TMQB, and irreversible reduction wave was observed in TPyQB. The onset reduction potentials of the oligoquinolines are in the range of -1.85 V to -1.60 V (vs SCE). The various substitutions in the quinoline rings lead to a slighty more positive reduction potentials by 0.1-0.2 V. The EA values or LUMO energy levels, estimated from the onset reduction potential [EA = E_{red}^{onset} + 4.4 eV][21], are in the range of -2.55 eV in TMQB to -2.8 eV in TPyQB. These values are similar to previously reported EA values of *para*-linked oligoquinolines[47]

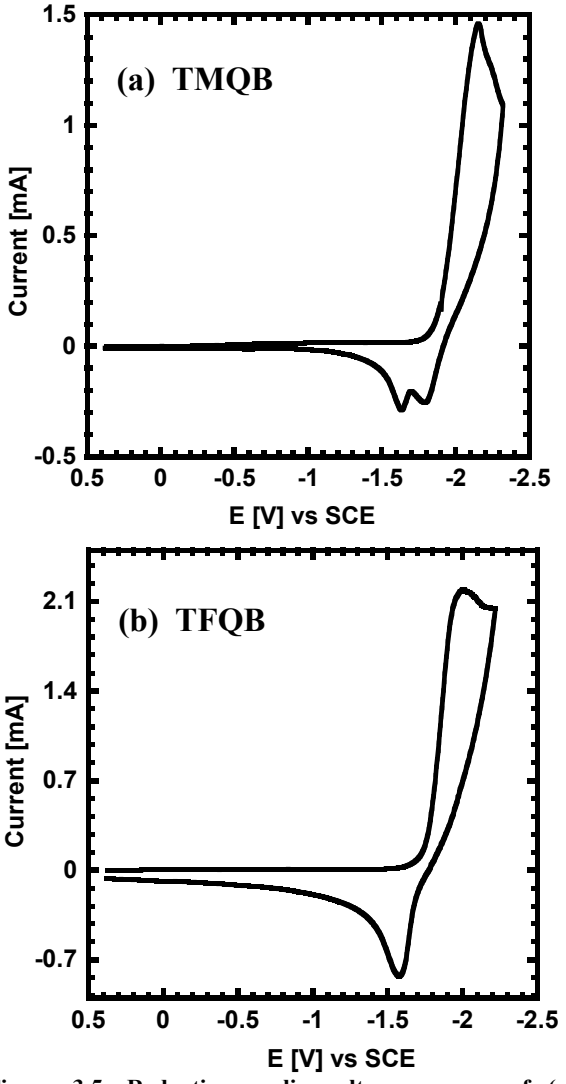

Figure 3.5. Reduction cyclic voltammograms of (a) TMQB and (b) TFQB thin films in 0.1 M TBAPF6/MeCN. Scan rate = 50 mV s^{-1}.

and polyquinolines.[35-37]

The oxidation CVs of the oligoquinoline thin films were similarly used to estimate the HOMO energy levels (IP values). Irreversible oxidation waves were observed for all four materials with onset oxidation potential of 1.68-1.85 V (vs SCE) **(**Table 3.2**).** The estimated IP [IP = E_{ox}^{onset} + 4.4 eV][21] values of 6.08-6.25 eV show rather deep HOMO energy levels for this class of electron transport materials. These IP values are significantly higher than that of well-known ETMs, including tris(8-hydroxyquinoline)aluminum (Alq_3) (IP = 5.7-5.9 eV),[51] and previously reported oligoquinolines (IP = 5.53-5.81 eV).[47] The IP values of the present *meta*-substituted oligoquinolines are higher by up to 0.7 eV compared to those of *para*-substituted oligoquinolines[47]. This suggests that *meta*-substitution of the oligoquinolines mainly leads to a lowering of the HOMO energy levels while the LUMO energy levels essentially remain unchanged, which in turn leads to the desired wide-energy gap ETMs that could also function as an excellent hole-

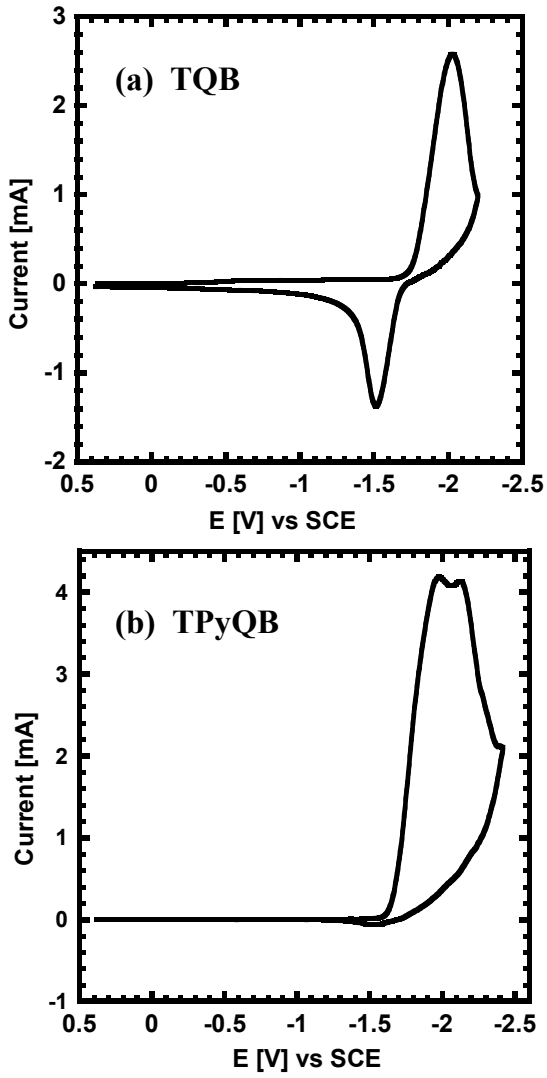

Figure 3.6. Reduction cyclic voltammograms of (a) TQB and (b) TPyQB thin films in 0.1 M TBAPF6/MeCN. Scan rate = 50 mV s^{-1}.

blocking layer in PhOLEDs. These results clearly demonstrate that the HOMO energy levels or IP values of oligoquinolines can be varied significantly (0.7 eV) by simply changing the substitution of the conjugated core from *para*-substitution to *meta*-substitution.

Charge transport. We investigated the electron mobilities of the oligoquinoline films by the space-charge-limited current (SCLC) method in ambient conditions. The current density-voltage (*J-V*) characteristics of the SCLC devices, which have the structure ITO/oligoquinoline/Al, are shown in Figure 3.7. The electron mobility was extracted by fitting the *J-V* curves in the near quadratic region according to the modified Mott-Gurney equation[52] (eq.2.1), where J is the current density, ε is the relative permittivity, ε_0 is the permittivity of free space, μ is the zero-field mobility, V is the applied voltage, L is the thickness of active layer, and β is the field-activation factor (Table 3.3). The solid lines in Figure 3.7 represent the SCLC fitting curves in the quadratic SCLC region.

The zero-field electron mobility of the solution-deposited oligoquinoline films varied from 5.0×10^{-5} cm^2 $V^{-1}s^{-1}$ in TMQB to 3.3×10^{-3} cm^2 $V^{-1}s^{-1}$ in TPyQB (Table 3.3). The electron mobility in TPyQB is an order of magnitude higher than that of TQB and two orders of magnitude higher than that of TMQB. However, the charge carrier mobility of TMQB and TPyQB is still about one to three orders of magnitude higher than those of conventional electron transport materials such as Alq_3,[53] oxadiazole derivatives,[54] and phenylphenanthroline.[55] The general trend among the four molecules is an increase in carrier mobility as EA increased. However, it is unlikely that the high carrier mobility in TPyQB compared to TMQB is to due the slightly higher electron affinity. Based on the EA of the four molecules, the large energy barrier for electron injection from Al (Φ = 4.3 eV)[21] is comparable in all four molecules. Thus, the observed two orders of magnitude variation in the SCLC electron mobility of the oligoquinoline

series must be due to variation in the solid state morphology of the materials and/or the relative ease of electron injection at oligoquinoline/Al interface. Attempt to measure the electron mobility of vacuum-deposited oligoquinoline films were unsuccessful due to a lack of clear SCL current. This could be due to poor interfacial contact between the vacuum-deposited oligoquinolines/Al interface.

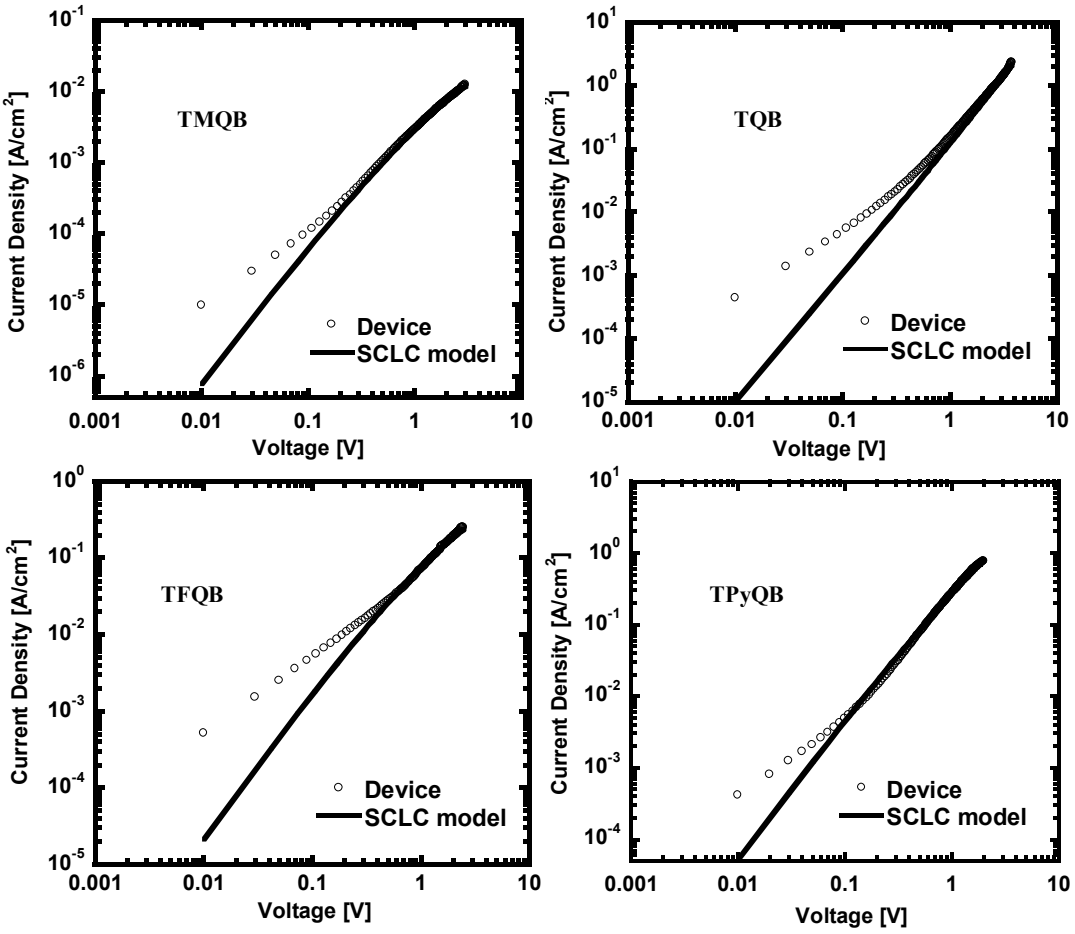

Figure 3.7. Current density-voltage (J-V) curves of ITO/oligoquinoline/Al devices in ambient conditions. The solid lines represent the SCLC model with field-dependent mobility.

Table 3.1. Thermal and Photophysical Properties of Oligoquinolines.

	TMQB	TQB	TFQB	TPyQB
T_D [°C]	378	429	437	427
T_m/T_c [°C]	300/265	276/245	281/251	390/325
λ_{max}^{abs} [soln] [nm] [a]	249, 323	274, 325	276, 325	273, 326
λ_{max}^{abs} [film] [nm] [b]	256, 329	261, 332	276, 332	276, 333
λ_{max}^{abs} [film] [nm] [c]	256, 331	276, 332	274, 333	273, 337
E_g^{opt} [eV]	3.38	3.40	3.39	3.33
λ_{max}^{PL}[film] [b], [*fwhm*] [nm]	387 [*100*]	391 [*57*]	389 [*57*]	395 [*63*]
λ_{max}^{PL} [film] [c], [*fwhm*] [nm]	468 [*92*]	413 [*88*]	505 [*102*]	416 [*84*]

[a] Absorption in dilute (1.3-1.8 × 10^{-6} M) THF solution. [b] Vacuum-deposited films. [c] Solution-deposited films.

Table 3.2. Electrochemical Properties of Oligoquinolines.

Compound	E_{red}^{onset} [V]	E_{ox}^{onset} [V]	EA [eV]	IP [eV]	E_g^{el} [eV]
TMQB	-1.85	1.85	2.55	6.25	3.70
TQB	-1.75	1.73	2.65	6.13	3.48
TFQB	-1.73	1.68	2.67	6.08	3.41
TPyQB	-1.60	1.74	2.80	6.14	3.34

Table 3.3. SCLC Electron Mobilities of Oligoquinolines.

Compound	L [nm]	β [$cm^{1/2} V^{-1/2}$]	E_{max} [$V\ cm^{-1}$]	μ_e ($E=0$) [$cm^2 V^{-1} s^{-1}$]
TMQB	102	4.2×10^{-4}	3.3×10^{5}	5.0×10^{-5}
TQB	100	6.9×10^{-4}	3.8×10^{5}	3.6×10^{-4}
TFQB	107	5.5×10^{-4}	3.1×10^{5}	8.0×10^{-4}
TPyQB	120	2.9×10^{-3}	3.8×10^{5}	3.3×10^{-3}

PhOLED Characterization. We fabricated blue PhOLED

s using the new oligoquinolines as electron-transport layers (ETLs) deposited by both vacuum-deposition and solution-processing methods. The emission layer (EML) consisted of blends of poly(*N*-vinylcarbazole) (PVK) and 1,3-bis(2-(4-tert-butylphenyl)-1,3,4-oxadiazo-5-yl)benzene (OXD-7) as the polymeric host doped with the blue triplet emitter FIrpic as described in the Experimental Section. Initially, a series of four devices using different ETLs deposited by vacuum thermal evaporation were fabricated to verify and compare the effectiveness of oligoquinolines as electron-transport materials in blue PhOLEDs: device IA, ITO/PEDOT:PSS/EML/vacuum-deposited TMQB/Al; device IB, ITO/PEDOT:PSS/EML/vacuum-deposited TQB/Al; device IC, ITO/PEDOT:PSS/EML/vacuum-deposited TFQB/Al; and device ID, ITO/PEDOT:PSS/EML/vacuum-deposited TPyQB/Al. The current density-voltage-luminance (brightness) (*J*-*V*-*L*) and luminous efficiency-luminance (*LE*-*L*) characteristics of these series of diodes are shown in Figure 3.8. Device IA with vacuum-deposited TMQB ETL showed the lowest device performance overall. This may be due to the relatively low electron mobility (~10^{-5} cm^2 $V^{-1}s^{-1}$) and small EA value (2.55 eV) of TMQB, which creates a large energy barrier for electrons to be

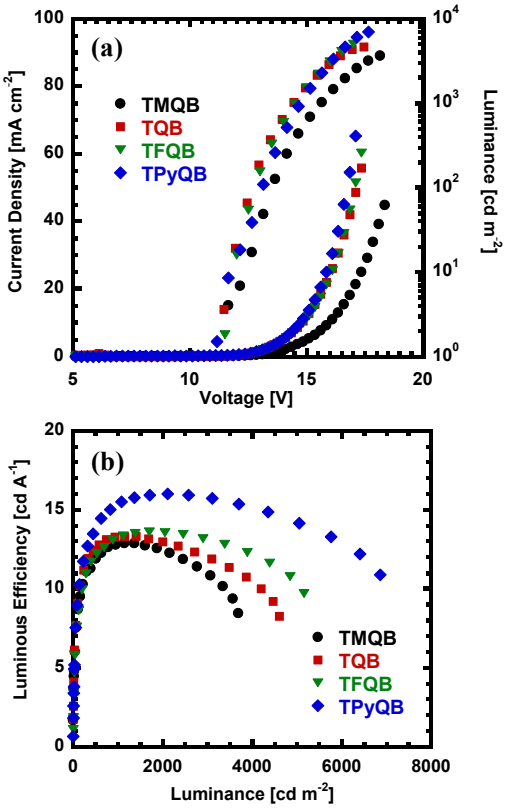

Figure 3.8. (a) Current density (*J*) – voltage (*V*), and luminance (*L*) - voltage (*V*); and (b) luminous efficiency (*LE*) - luminance (*L*) curves of PhOLEDs with vacuum-deposited ETLs.

injected from high work-function Al cathode (4.3 eV). Device IC with vacuum-deposited TFQB ETL showed a slightly better performance, giving a maximum brightness of 5240 cd m^{-2} and an LE value of 13.6 cd A^{-1} (at 1700 cd m^{-2}) whereas device IB with a TQB ETL had a maximum brightness of 4020 cd m^{-2} (at 16.6 V) and an LE value of 12.2 cd A^{-1}(at 1060 cd m^{-2}). Device ID with vacuum-deposited TPyQB ETL showed the highest performance, giving an LE value of 16.0 cd A^{-1} (at 2200 cd m^{-2}) and a maximum brightness of 6970 cd m^{-2} (at 17.8 V). These blue PhOLEDs with vacuum-deposited oligoquinoline ETLs have decent device performances with high LE values (> 12 cd A^{-1}) and high brightness values (> 3000 cd m^{-2}), demonstrating that the new of oligoquinolines can function as good electron-injection and electron-transport materials in blue PhOLEDs.

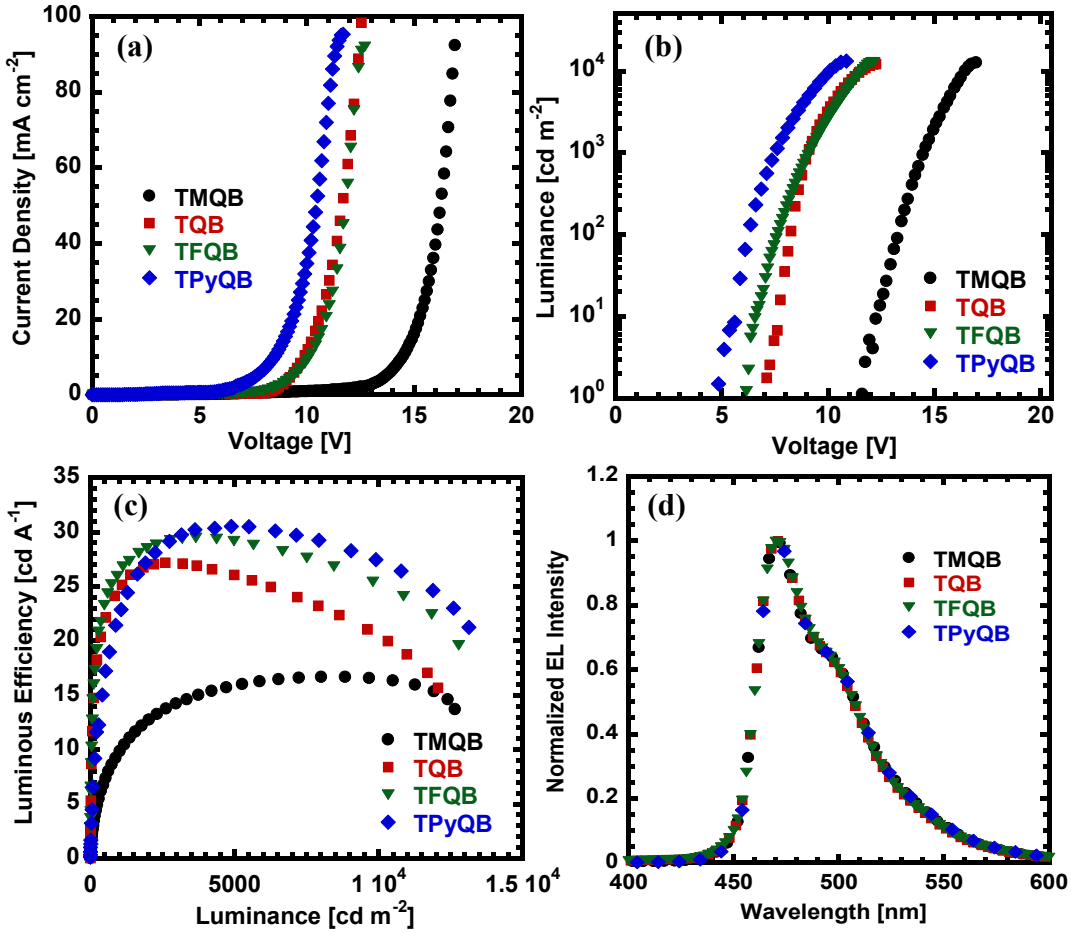

Figure 3.9. (a) Current density (*J*) – voltage (*V*), (b) luminance (*L*) - voltage (*V*) and (c) luminous efficiency (*LE*) - luminance (*L*) curves of blue PhOLEDs with solution-deposited ETLs using a formic acid/water (3:1 v/v) mixture. (d) Electroluminescence (EL) spectra.

Towards our main goal of achieving highly efficient multilayered blue PhOLEDs by sequential solution-processing, we also fabricated a series of four devices with solution-processed oligoquinoline ETLs (device IIA to IID). The oligoquinoline ETMs were dissolved and spin-coated onto the EML from a formic acid/water mixture solvent (FA:H_2O = 3:1) as introduced in our preliminary report.[7] For device II, the device structure and layer thicknesses were exactly the same as device I except that the ETLs were solution-processed onto the EML: ITO/PEDOT:PSS/EML/oligoquinoline ETL/Al. All the blue PhOLEDs with solution-processed ETLs (device IIA to IID) indeed show far superior performance compared to those with vacuum-deposited ETLs (device IA to ID).

The *J-V*, *L-V* and the *LE-L* characteristics of the blue PhOLEDs with solution-processed ETLs are shown in Figure 3.9. Although device IIA with a solution-processed TMQB ETL showed a similar turn-on voltage to device IA, it had increased efficiency and brightness with an LE value of 16.7 cd A^{-1} (at 8420 cd m^{-2}) and a maximum brightness of 12700 cd m^{-2} (at 17.0 V). Devices IIB and IIC with solution-processed TQB and TFQB ETLs also showed significant improvement in performance compared to devices IB and IC with vacuum-deposited ETLs. The LE value of device IIB was 27.2 cd A^{-1} (at 2750 cd m^{-2}) with a maximum brightness of 12200 cd m^{-2} (at 12.3 V) whereas the LE value of device IIC was 29.5 cd A^{-1} (at 3660 cd m^{-2}) with a maximum brightness of 12900 cd m^{-2} (at 12.4 V), which is more than two-fold superior relative to the vacuum-deposited TQB (device IB) and TFQB (device IC). As we can see in Figure 3.9a-c and Table 3.4, the best performance was obtained in device IID with a solution-processed TPyQB ETL. The blue PhOLEDs of device IID had the lowest turn-on voltage (4.7 V) and highest brightness of 13300 cd m^{-2} at lowest drive voltage (10.9 V). The LE value was 30.5 cd A^{-1} (EQE of 16.0 % and a power efficiency (PE) value of 10.9 lm W^{-1}) at a brightness of 4130 cd m^{-2}. Even at extremely high brightness (~10^4 cd m^{-2}), device IID remained very efficient showing an LE value higher than 20 cd A^{-1}. The relatively large EA value (2.8 eV) and high electron mobility of TPyQB (~ 10^{-3} cm^2 V^{-1} s^{-1}) should facilitate enhanced electron-injection and transport in the diode and thus can explain the high PhOLED performance. All fabricated device characteristics of the blue PhOLEDs are summarized in Table 3.4.

Electroluminescence (EL) spectra of the PhOLEDs with the solution-processed oligoquinoline ETL and without an ETL are shown in Figure 3.9d. The EL emission of all the devices are identical with an EL maximum of 472 nm, corresponding to the EL of the blue triplet emitter FIrpic. The Commision Internationale de L'Eclairage (CIE) 1931 coordinates of all the

devices were identical at the maximum brightness of ~ 12000 cd m^{-2} (0.14, 0.28). This clearly demonstrate that the solution-processed oligoquinoline function solely as the electron-transport layer, efficiently confining charge carriers and exciton within the EML. These results demonstrate that high-performance multilayered blue PhOLEDs can be readily fabricated by sequential solution-processing while also eliminating the need for interface modification layers such as NaF, LiF, and CsF.

Table 3.4. Device Characteristics of Blue PhOLEDs. [a]

Device [b]	ETL	ETL deposition method	V_{on}[c] [V]	Drive voltage [V]	Current density [mA cm^{-2}]	Luminance [cd m^{-2}]	Device efficiency [cd A^{-1}, (%EQE)]
Device IA	TMQB	Vacuum	11.5	18.5 *15.8*	47.2 *8.6*	3710 *1110*	7.9, (4.0) *12.9, (6.8)*
Device IB	TQB	Vacuum	9.6	16.6 *14.0*	54.9 *8.7*	4020 *1060*	7.3, (4.0) *12.2, (6.9)*
Device IC	TFQB	Vacuum	11.2	17.4 *15.2*	60.2 *12.5*	5240 *1700*	8.7, (4.3) *13.6, (7.2)*
Device ID	TPyQB	Vacuum	11.0	17.8 *15.6*	72.0 *20.6*	6970 *2200*	9.7, (4.8) *16.0, (8.5)*
Device IIA	TMQB	Solution	11.6	17.0 *16.3*	96.2 *50.4*	12700 *8420*	13.2, (6.9) *16.7, (8.9)*
Device IIB	TQB	Solution	7.0	12.3 *9.8*	82.9 *10.1*	12200 *2750*	14.7, (7.6) *27.2, (14.9)*
Device IIC	TFQB	Solution	6.2	12.2 *10.4*	71.9 *12.4*	12900 *3660*	17.9, (8.7) *29.5, (15.7)*
Device IID	TPyQB	Solution	4.7	10.9 *8.9*	69.5 *16.0*	13300 *4130*	19.2, (9.9) *30.5, (16.0)*

[a] Values in italic correspond to those at maximum device efficiencies. [b] Device I with vacuum-deposited ETL and device II with solution-deposited ETL (TMQB, TQB, TFQB, or TPyQB). [c] Turn-on voltage (at brightness of 1 cd m^{-2}).

Surface Morphology of ETLs. We used atomic force microscopy (AFM) to investigate the surface morphology of both vacuum-deposited and solution-deposited oligoquinoline ETLs to understand the likely ETL/Al cathode interface morphology that underlies the observed trends in charge transport and the efficiency of the blue PhOLEDs. Figure 3.10 shows the 2D and the corresponding 3D topological surface morphologies of the vacuum-deposited oligoquinoline thin

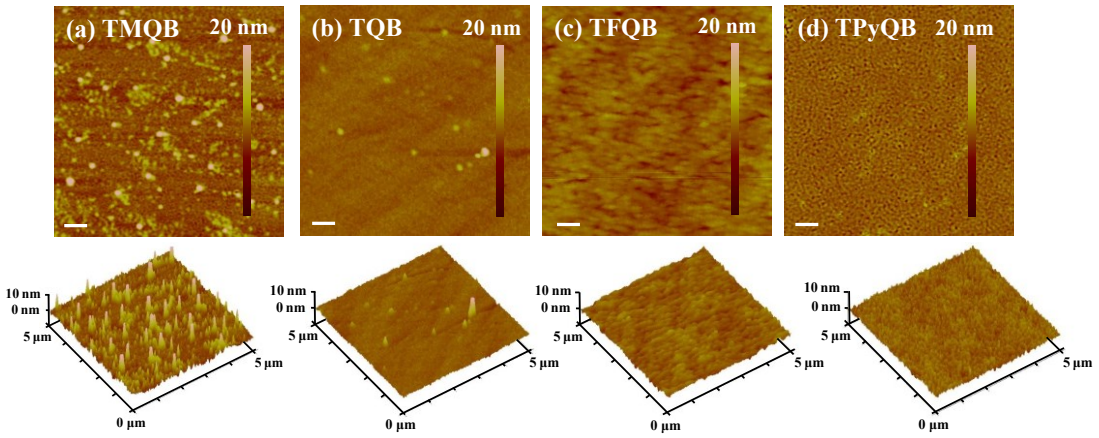

Figure 3.10. AFM topographical images (5 × 5 µm) and the corresponding 3D height images of vacuum-deposited oligoquinoline films. Scale bar is 500 nm.

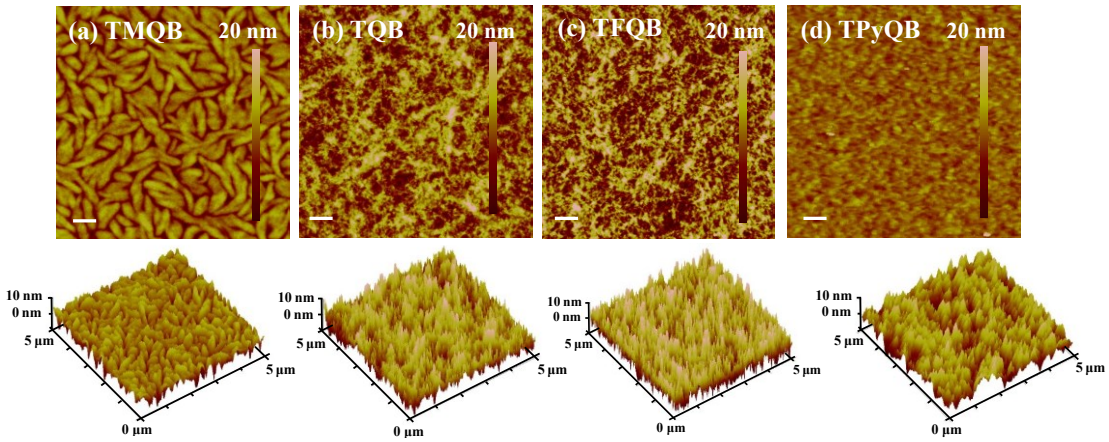

Figure 3.11. AFM topographical images (5 × 5 µm) and the corresponding 3D height images of solution-deposited oligoquinoline films. Scale bar is 500 nm.

films. The thin films have smooth surfaces with RMS values of surface roughness of 1.75, 0.553, 0.754, and 0.867 nm for TMQB, TQB, TFQB and TPyQB, respectively. Vacuum-evaporated

TMQB film shows some vertical aggregates dispersed on the surface, which likely resulted in the higher RMS value compared to the other vacuum-deposited thin films. In contrast, the surface morphologies of the solution-deposited oligoquinoline ETLs (Figure 3.11) are significantly different from those of the vacuum-deposited ETLs. The RMS values of the solution-deposited ETLs increased to 2.35, 3.35, 4.01 and 3.75 nm for TMQB, TQB, TFQB and TPyQB films, respectively. We can clearly see from the 3D surface morphology shown in Figure 3.11, that the solution-deposited thin films form a high density of vertically aligned nanopillars with the exception of TMQB. The morphology of solution-processed TMQB thin films is characterized by horizontally oriented large crystallites or aggregates (~ 500 nm width). The observed morphology of TMQB thin films is consistent with its poor carrier mobility and poor PhOLED performance. On the other hand, the observed vertically oriented nanopillars in solution-deposited TQB, TFQB, and TPyQB thin films, and thus high surface roughness, suggest that the area of the ETL/cathode contact is maximized, facilitating efficient electron injection. The observed nanopillar morphology of the solution-deposited ETLs implies that maximum charge transport can be expected in the vertical direction, which is consistent with measured high electron mobility by the SCLC method. Furthermore, the oligoquinoline/Al interface is expected to involve a chemical bonding between Al metal and the nitrogen heteroatom in the organic electron-transport materials.[35,56] The additional nitrogen and fluorine[57] heteroatoms in TFQB and TPyQB are likely to result in improved interactions between the ETL and Al at the ETL/cathode interface, thus leading to improved electron injection and charge transport compared to TQB and TMQB.

3.1.4. Conclusions

In summary, novel wide-energy-gap n-type organic semiconductors based on dendritic oligoquinolines were synthesized and were demonstrated to be effective solution-processable electron-transport layers in blue PhOLEDs. The new oligoquinolines have robust thermal stability with high decomposition temperatures and high melting temperatures. The new electron transport materials have enabled orthogonal sequential solution-processing of multilayered blue polymer-based PhOLEDs with the highest efficiency to date. The molecular design of the new n-type oligomers with *meta*-linkages enabled achievement of large band gaps (~ 3.4 eV) and low-lying HOMO energy levels (~ -6.1 eV) that also facilitate excellent hole-blocking properties. The high electron affinity and high electron mobility (3.3×10^{-3} cm^2 V^{-1} s^{-1}) of the solution-deposited thin films facilitated good electron-injection/transport properties. Blue PhOLEDs based on FIrpic triplet emitter-doped PVK host emission layer and a solution-processed oligoquinoline electron-transport layer gave a high luminous efficiency of 30.5 cd A^{-1} at a brightness of 4130 cd m^{-2} with an external quantum efficiency (EQE) of 16.0 %. AFM imaging of the solution-deposited oligoquinoline ETLs revealed a high density of vertically oriented nanopillars which lead to a rough surface that enhance electron injection and transport compared to the smooth vacuum-deposited ETLs. These results demonstrate that small-molecule electron-transport layers can be readily processed from solution to fabricate high performance multilayered PhOLEDs. These results are also instructive in the design of ETMs with high electron mobilities, low-lying HOMO energy levels, and high performance solution-processable PhOLEDs for next-generation flat-panel displays and solid state lighting.

3.1.5. References

[1] R. H. Friend, R. W. Gymer, A. B. Holmes, J. H. Burroughes, R. N. Marks, C. Taliani, D. D. C. Bradley, D. A. D. Santos, J. L. Brédas, M. Logdlund, W. R. Salaneck, *Nature* **1999**, *397*, 121.

[2] F. So, J. Kido, P. Burrows, *MRS Bulletin* **2008**, *33*, 663.

[3] J. Kido, M. Kimura, K. Nagai, *Science* **1995**, *267*, 1332.

[4] S. Reineke, F. Lindner, G. Schwartz, N. Seidler, K. Walzer, B. Lussem, K. Leo, *Nature* **2009**, *459*, 234.

[5] L. Xiao, Z. Chen, B. Qu, J. Luo, S. Kong, Q. Gong, J. Kido, *Adv. Mater* **2011**, *23*, 926.

[6] M. A. Baldo, D. F. O'Brien, Y. You, A. Shoustikov, S. Sibley, M. E. Thompson, S. R. Forrest, *Nature* **1998**, *395*, 151.

[7] T. Earmme, E. Ahmed, S. A. Jenekhe, *Adv. Mater*. **2010**, *22*, 4744.

[8] T. Earmme, E. Ahmed, S. A. Jenekhe, *J. Phys. Chem. C* **2009**, *113*, 18448.

[9] H. Sasabe, E. Gonmori, T. Chiba, Y. J. Li, D. Tanaka, S. J. Su, T. Takeda, Y. J. Pu, K. I. Nakayama, J. Kido, *Chem. Mater.* **2008**, *20*, 5951.

[10] N. Chopra, J. Lee, Y. Zheng, S.-H. Eom, J. Xue, F. So, *Appl. Phys. Lett.* **2008**, *93*, 143307.

[11] F. M. Hsu, C. H. Chien, P. I. Shih, C. F. Shu, *Chem. Mater.* **2009**, *21*, 1017.

[12] D. F. O'Brien, M. A. Baldo, M. E. Thompson, S. R. Forrest, *Appl. Phys. Lett*. **1999**, *74*, 442.

[13] Y. –J. Li, H. Sasabe, S. –J Su, D. Tanaka, Y. –J. Pu, J. Kido, *Chem. Lett.* **2010**, *39*, 140.

[14] N. Chopra, J. Lee, Xue, J.; F. So, *IEEE Trans. Electron Devices* **2010**, *57*, 101.

[15] R. J. Holmers, B. W. D'Andrade, S. R. Forrest, X. Ren, M. E. Thompson *Appl. Phys. Lett*. **2003**, *83*, 3818.

[16] Y. Zhen, S.-H. Eom, N. Chopra, J. Lee, F. So, J. Xue, *Appl. Phys. Lett*. **2008**, *92*, 223301.

[17] S.-J. Yeh, M.-F. Wu, C.-T. Song, Y. Chi, M.-H., S.-F. Hus, C. H. Chen, *Adv. Mater*. **2005**, *17*, 285.

[18] M.-H. Tsai, H.-W. Lin, H.-C. Su, T.-H Ke, C.-C. Wu, F.-C. Fang, Y.-L. Liao, K.-T. Wong, C.-L. Wu, *Adv. Mater*. **2006**, *18*, 1216.

[19] S.-J. Su, Y. Takahashi, T. Chiba, T. Takeda, J. Kido, *Adv. Funct. Mater*. **2009**, *19*, 1260.

[20] H. Sasabe, D. Tanaka, D. Yokoyama, T. Chiba, Y.-J. Pu, K.-I. Nakayama, M. Yokoyama, J. Kido, *Adv. Funct. Mater*. **2011**, *21*, 336.

[21] (a) A. P. Kulkarni, C. J. Tonzola, A. Babel, S. A. Jenekhe, *Chem. Mater.* **2004**, *16*, 4556. (b) G. Hughes, M. R. Bryce, *J. Mater. Chem*. **2005**, 15, 94.

[22] S. R. Forrest, *Nature* **2004**, *428*, 911.

[23] A. C. Arias, J. D. MacKenzie, I. McCulloch, J. Rivnay, A. Salleo, *Chem. Rev.* **2010**, *110*, 3.

[24] S. C. Lo, R. N. Bera, R. E. Harding, P. L. Burn, I. D. W. Samuel, *Adv. Funct. Mater.* **2008**, *18*, 3080.

[25] S. J. Lee, J. S. Park, M. Song, I. A. Shin, Y. I. Kim, J. W. Lee, J. W. Kang, Y. S. Gal, S. Kang, J. Y. Lee, S. H. Jung, H. S. Kim, M. Y. Chae, S. H. Jin, *Adv. Funct. Mater.* **2009**, *19*, 2205.

[26] S. C. Lo, R. E. Harding, C. P. Shipley, S. G. Stevenson, P. L. Burn, I. D. W. Samuel, *J. Am. Chem. Soc.* **2009**, *131*, 16681.

[27] J. Ding, B. Zhang, J. Lu, Z. Xie, L. Wang, X. Jing, F. Wang, *Adv. Mater.* **2009**, *21*, 4983.

[28] X. Gong, M. R. Robinson, J. C. Ostrowski, D. Moses, G. C. Bazan, A. J. Heeger, *Adv. Mater.* **2002**, *14*, 581.

[29] L. Wang, Y. Jiang, J. Luo, Y. Zhou, J. H. Zhou, J. Wang, J. Pei, Y. Cao, *Adv. Mater.* **2009**, *21*, 4854.

[30] X. H. Yang, F. Jaiser, S. Klinger, D. Neher, *Appl. Phys. Lett.* **2006**, *88*, 021107.

[31] F. So, B. Krummacher, M. K. Mathai, D. Poplavskyy, S. A. Choulis, V. E. Choong, *J. Appl. Phys.* **2007**, *102*, 091101.

[32] S. Sax, N. Rugen-Penkalla, A. Neuhold, S. Schuh, E. Zojer, E. J. W. List, K. Mullen, *Adv. Mater.* **2010**, 22, 2087.

[33] X. J. Zhang, A. S. Shetty, S. A. Jenekhe, *Macromolecules* **1999**, *32*, 7422.

[34] C. J. Tonzola, M. M. Alam, S. A. Jenekhe, *Adv. Mater.* **2002**, *14*, 1086.

[35] C. J. Tonzola, M. M. Alam, B. A. Bean, S. A. Jenekhe, *Macromolecules* **2004**, *37*, 3554.

[36] C. J. Tonzola, M. M. Alam, S. A. Jenekhe, *Macromolecules* **2005**, *38*, 9539.

[37] X. J. Zhang, D. M. Kale, S. A. Jenekhe, *Macromolecules* **2002**, *35*, 382.

[38] T. W. Kwon, M. M. Alam, S. A. Jenekhe, *Chem. Mater.* **2004**, *16*, 4657.

[39] Y. T. Cui, X. J. Zhang, S. A. Jenekhe, *Macromolecules* **1999**, *32*, 3824.

[40] M. M. Alam, S. A. Jenekhe, *Chem. Mater.* **2002**, *14*, 4775.

[41] A. K. Agrawal, S. A. Jenekhe, *Macromolecules* **1991**, *24*, 6806.

[42] A. K. Agrawal, S. A. Jenekhe, *Chem. Mater.* **1996**, *8*, 579.

[43] B. Liu, W.-L. Yu, Y.-H. Lai, W. Huang, *Macromolecules* **2002**, *35*, 4975.

[44] F. Huang, L. T. Hou, H. B. Wu, X. H. Wang, H. L. Shen, W. Cao, W. Yang, Y. Cao, *J. Am. Chem. Soc.* **2004**, *126*, 9845.

[45] Y. Xu, R. Yang, J. Peng, A. A. Mikhailovsky, Y. Cao, T.-Q. Nguyen, G. C. Bazan, *Adv. Mater.* **2009**, *21*, 584.

[46] S. Sax, G. Mauthner, T. Piok, S. Pradhan, U. Scherf, E. J. W. List, *Org. Electron.* **2007**, *8*, 791.

[47] C. J. Tonzola, A. P. Kulkarni, A. P. Gifford, W. Kaminsky, S. A. Jenekhe, *Adv. Funct. Mater.* **2007**, *17*, 863.

[48] E. Ahmed, T. Earmme, S. A. Jenekhe, *Chem. Mater*. **2010**, *22*, 5786.

[49] S. A. Jenekhe, J. A. Osaheni, *Science* **1994**, 265, 765.

[50] J. A. Osaheni, S. A. Jenekhe, *Macromoleclues* **1994**, 27, 739.

[51] (a) A. Rajagopal, A. Kahn, *Adv. Mater.* **1998**, *10*, 140. (b) T. Mori, H. Kim, T. Mizutani, D. Lee, *Jpn. J. Appl. Phys.* **2001**, *40*, 5346.

[52] (a) P. N. Murgatroyd, *J. Phys*. *D* **1970**, *3*, 1488. (b) A. J. Campbell, D. D. C. Bradley, D. G. Lidzey, *J. Appl. Phys*. **1997**, *82*, 6326.

[53] R. K. Choudhury, J.-H. Yoon, F. So, *Adv. Mater*. **2008**, *20*, 1456.

[54] T.-Y. Chu, O.-K. Song, *Appl. Phys. Lett*. **2007**, *90*, 203512.

[55] M. A. Khan, W. Xu, K.-U. Haq, Y. Bai, X. Y. Jiang, Z. L. Zhang, W. Q. Zhu, *J. Appl. Phys*. **2008**, *103*, 014509.

[56] T. Oyamada, H. Yoshizaki, H. Sasabe, C. Adachi, *Chem. Lett.* **2004**, *33*, 1034.

[57] L. M. Tang, Z. Bao, C*hem. Mater.* **2011**, *23*, 44.

3.2. High-Performance Multilayered Phosphorescent Organic Light-Emitting Diodes by Solution-Processed Commercial Electron-Transport Materials

3.2.1. Introduction

Organic light-emitting diodes (OLEDs) are of current scientific and commercial interest for applications in full-color display panels, flexible displays, and solid-state lighting.[1-7] Compared to conventional fluorescent OLEDs, considerable recent efforts have gone into developing phosphorescent OLEDs (PhOLEDs), which utilize triplet excitons to achieve superior performance.[2] However, most of the high-performance PhOLEDs achieved to date have been mainly based on vacuum-deposited small-molecules involving thermal evaporation processes to obtain multilayered device structures. Solution-based PhOLEDs provide an economically attractive alternative to those processed by vacuum deposition, and are considered essential to low-cost, large area lighting devices.[3] In contrast to the considerable progress made in developing highly efficient vacuum-processed PhOLEDs, reports on solution-processed PhOLEDs are relatively few.[4] Surprisingly, most of the prior reports on solution-processed PhOLEDs have mainly focused on solution-processable hole-transporting materials,[5] or emissive materials,[6] or host materials for triplet emitter guest[7] while still using vacuum-deposited small molecule electron-transport layer (ETL) / hole-blocking layer (HBL) and/or vacuum-evaporated thin layer of low work-function metals (e.g. Ba, Ca) or cathode interfacial materials (e.g. LiF, CsF) between the organic layer and metal cathode in multilayered device structures.

Although sequential solution-processing of highly efficient multilayered device structures has great potential, it is very challenging because the solvent used to deposit the subsequent layer tends to dissolve or swell the underlying layer. One general strategy towards overcoming this problem is to utilize orthogonal sequential solvent processing.[8] We have showed that many

heterocyclic conjugated polymers or dendrimers can be solution-processed from an organic acid solvent as ETLs onto various emissive polymer layers to fabricate multilayered OLED structures[9] and multilayered polymer solar cells.[10] Others also have reported alcohol/water-soluble polyelectrolytes as ETLs in multilayered OLEDs.[11] Although sequential solution-processed multilayer can be obtained using alcohol/water soluble polyelectrolyte ETLs, the choice of the materials is rather limited and the ionic groups in such polyelectrolytes can induce undesired electrochemical doping effect, reducing the air-stability of high work function metal cathodes such as Al.[8]

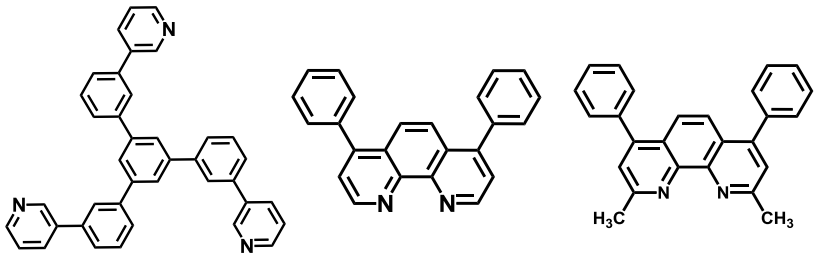

Chart 3.2. Molecular structures of commerical electron-transport materials.

In contrast to several prior reports of sequential solution-processing of multilayered devices based on conjugated polymers,[8-11] solution-based processing of small molecules as an overlayer in multilayered devices has been rarely reported.[12-13] The utilization of small-molecule electron-transport materials through orthogonal sequential solution-processing, while highly attractive, is quite challenging due to their poor film-forming and surface wetting properties. A few studies have reported the use of alcohol-based solutions to deposit small molecules as ETLs in multilayered OLEDs.[12] However, the poor solubility of small-molecule ETMs in alcoholic solvents limits the thickness of the layer and indeed severely affects the film quality.[7d,12a,13] Recently, we successfully demonstrated highly efficient blue PhOLEDs fabricated by orthogonal

sequential solution-processing, involving new solution-processable dendritic oligoquinoline electron-transport materials (ETMs).[14] We showed that an organic acid/water mixture solvent for the new oligoquinoline ETMs can enable orthogonal solution-processing without harming the underlying poly(N-vinylcarbazole)-based emissive layer.

3.2.2. Experimental Section

Materials. All commercially available materials were purchased and used as received without further purification.

Device fabrication. The phosphorescent emission layer (EML) consisted of a blend of Poly(*N*-vinyl carbazole) (PVK, M_w = 1,100,000; Sigma-Aldrich) and 1,3-bis(2-(4-tert-butylphenyl)-1,3,4-oxadiazo-5-yl)benzene (OXD-7, LumTec., Taiwan) (PVK:OXD-7 = 60:40, wt/wt) as a host and 1.0 wt% *fac*-tris(2-phenylpyridine)iridium ($Ir(ppy)_3$, LumTec., Taiwan) as the dopant. A solution of PEDOT:PSS (poly-(ethylenedioxythiophene) : polystyrenesulfonate, H. C. Starck, Clevios P VP Al 4083) in water was spin-coated to make a 30-nm hole-injection layer onto a pre-cleaned ITO glass and annealed at 150 ºC under vacuum. The 70-nm polymer EML was obtained by spin coating of the PVK:OXD-7:$Ir(ppy)_3$ blend in cholorobenzene onto the PEDOT:PSS layer and vacuum dried at 100 ºC. Commercial small-molecule electron-transport materials (ETMs), 1,3,5-tri(3-pyrid-3-yl-phenyl)benzene (TmPyPB, LumTec., Taiwan), 4,7-diphenyl-1,10-phenanthroline (BPhen, sublimed grade, Sigma-Aldrich) and 2,9-dimethyl-4,7-diphenyl-1,10-phenanthroline (BCP, sublimed grade, Sigma-Aldrich) were evaporated in a vacuum (< 8.0 x 10^{-7} torr) or spun cast from different concentration of ETMs in formic acid:water (FA:H_2O = 3:1) mixture at a spin speed of 7000 rpm onto the EML followed by vacuum drying at 50 ºC. After drying, 100-nm Al was deposited onto the ETL. The structure of

devices IA, IIA, and IIIA was ITO/PEDOT:PSS(30 nm)/EML(70 nm)/vacuum-deposited ETM/Al (100 nm). The structure of devices IB-D, IIB-D, and IIIB-D was identical except electron-transport layer was solution-processed, ITO/PEDOT:PSS(30 nm)/EML(70 nm)/solution-deposited ETM/Al (100 nm). Film thickness was measured by an Alpha-Step 500 profilometer (KLA-Tencor, San Jose, CA).

Device Characterization. Electroluminescence (EL) spectra were obtained using a Photon Technology International (PTI) Inc. Model QM 2001-4 spectrofluorimeter. Current-voltage (*J-V*) characteristics of the PhOLEDs were measured by using a HP4155A semiconductor parameter analyzer (Yokogawa Hewlett-Packard, Tokyo). The luminance was simultaneously measured by using a model 370 optometer (UDT Instruments, Baltimore, MD) equipped with a calibrated luminance sensor head (Model 211) and a 5x objective lens. The device external quantum efficiency (EQE) was calculated from the luminance, current density and EL spectrum assuming a Lambertian distribution using procedures previously reported.[21b] All the device fabrication and device characterization steps were carried out under ambient laboratory conditions.

Devices for space-charge-limited current (SCLC) measurement were fabricated with electron-dominant device structure: ITO/Al(100 nm)/PVK:OXD-7 (60:40, wt/wt, 100 nm)/ETL/Al. The 100-nm thick Al electrode was deposited onto ITO substrate followed by spin-coating of subsequent polymer host layer. ETL was vacuum-deposited or solution-deposited using the exact same condition as for PhOLED fabrication followed by deposition of Al electrode. Current-voltage characteristics of SCLC devices were measured using the same semiconductor parameter analyzer as for the characterization of PhOLED devices. The SCLC measurements were performed under dark and ambient conditions.

Atomic force microscopy (AFM) characterization of ETL surface morphology was done on a Veeco Dimension 3100 Scanning Probe Microscope (SPM) system. The AFM topographical images were measured with the same PhOLEDs used for device characterization.

3.2.3. Results and Discussion

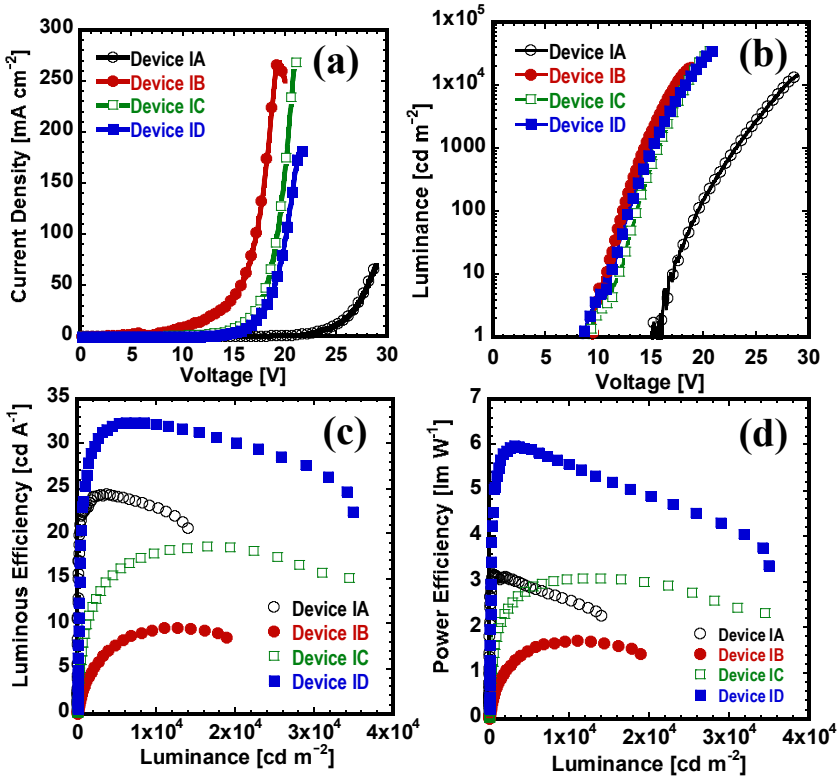

Figure 3.12. PhOLEDs with TmPyPB ETLs: (a) Current density (*J*) – voltage (*V*); (b) luminance (*L*) - voltage (*V*); (c) luminous efficiency (*LE*) - luminance (*L*); and (d) power efficiency (*PE*) - luminance (*L*) curves. Device structures, device IA: ITO/PEDOT:PSS/EML/*vacuum-deposited TmPyPB*/Al and devices IB, IC, and ID: ITO/PEDOT:PSS/EML/*solution-deposited TmPyPB*/Al with TmPyPB deposited from 8, 16, and 24 mg mL^{-1} solution, respectively.

PhOLEDs with vacuum- and solution-deposited ETMs. We fabricated multilayered PhOLEDs using the commercial electron-transport materials (ETMs), TmPyPB, BPhen and BCP as the electron-transport layers(ETLs). The emissive polymer layer (EML) consisted of a blend of PVK and OXD-7, doped with triplet emitter tris(2-phenylpyridine)iridium(III) (Ir(ppy)3) as

described in Experimental section. To facilitate comparison in PhOLED performance, the commercial ETMs were deposited by vacuum or solution methods to create an ETL thin film onto the EML. For the solution-processing method, the ETMs were deposited from formic acid (FA) and water (H2O) solvent mixture (FA:H2O = 3:1) as previously reported,14 while varying the concentration of the ETM in solution. Three sets of PhOLEDs were fabricated using the different commercial ETMs: Device IA, ITO/PEDOT:PSS/EML/*vacuum-deposited TmPyPB*/Al; devices IB, IC, and ID, ITO/PEDOT:PSS/EML/*solution-deposited TmPyPB*/Al with different casting concentrations of TmPyPB; Device IIA, ITO/PEDOT:PSS/EML/*vacuum-deposited BPhen*/Al; devices IIB, IIC, and IID, ITO/PEDOT:PSS/EML/*solution-deposited BPhen*/Al with different casting concentrations of BPhen; Device IIIA, ITO/PEDOT:PSS/EML/*vacuum-deposited BCP*/Al; devices IIIB, IIIC, and IIID, ITO/PEDOT:PSS/EML/*solution-deposited BCP*/Al with different casting concentrations of BCP.

Figure 3.12a-d shows the performance of PhOLEDs using TmPyPB as an ETL. Devices IB, IC, and ID with solution-deposited TmPyPB were obtained by spin-coating onto the EML from 8, 16, and 24 mg mL^{-1} solutions to deposit 15, 30, and 40 nm of TmPyPB ETL, respectively. Device IA included a vacuum-deposited 40-nm thick TmPyPB ETL. As shown in Figure 1a, device IB with the ETL deposited from 8 mg mL^{-1} solution showed a higher current density than

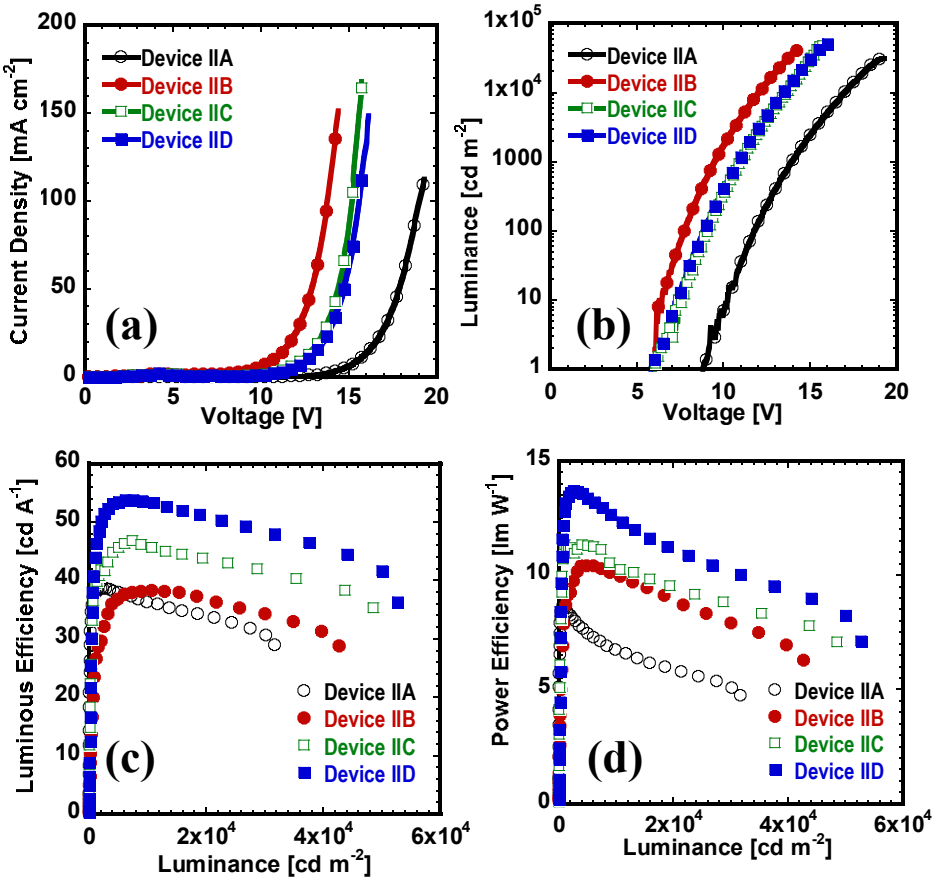

Figure 3.13. PhOLEDs with BPhen ETLs: (a) Current density (*J*) – voltage (*V*); (b) luminance (*L*) - voltage (*V*); (c) luminous efficiency (*LE*) - luminance (*L*); and (d) power efficiency (*PE*) - luminance (*L*) curves. Device structures, device IIA: ITO/PEDOT:PSS/EML/*vacuum-deposited BPhen*/Al and devices IIB, IIC, and IID: ITO/PEDOT:PSS/EML/*solution-deposited BPhen*/Al with BPhen deposited from 16, 20, and 24 mg mL^{-1} solution, respectively.

devices IC and ID due to its smaller thickness (15 nm). On the other hand, device IA with vacuum-deposited TmPyPB showed very low current density even though it has the same ETL thickness (40 nm) as device ID with TmPyPB ETL deposited from 24 mg mL^{-1} solution. Despite

their different current densities, devices IC and ID showed similar turn-on voltages (9.1 and 8.5 V), and luminance (brightness)-voltage (*L*-*V*) characteristics with similar maximum brightness of 34900 - 35100 cd m^{-2} (Figure 1b). Device ID showed the highest luminous efficiency (LE) value of 32.4 cd A^{-1} and power efficiency (PE) of 5.7 lm W^{-1} (Figure 4.1c,d) with an external quantum efficiency (EQE) of 9.7% (Table 4.1). Surprisingly, device IA containing vacuum-deposited

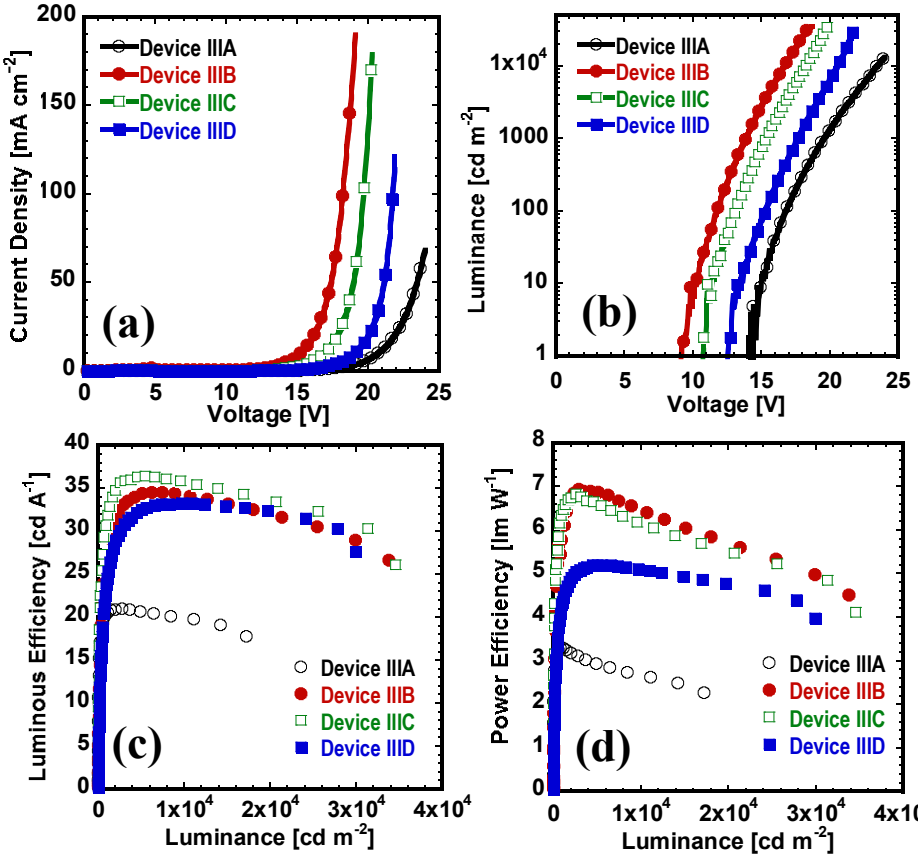

Figure 3.14. PhOLEDs with BCP ETLs: (a) Current density (*J*) – voltage (*V*); (b) luminance (*L*) - voltage (*V*); (c) luminous efficiency (*LE*) - luminance (*L*); and (d) power efficiency (*PE*) - luminance (*L*) curves. Device structures, device IIIA: ITO/PEDOT:PSS/EML/*vacuum-deposited BCP*/Al and devices IIIB, IIIC, and IIID: ITO/PEDOT:PSS/EML/*solution-deposited BCP*/Al with BCP deposited from 16, 20, and 24 mg mL^{-1} solution, respectively.

TmPyPB ETL had a very high turn-on voltage of 15.0 V and a very low maximum brightness of 14100 cd m^{-2} at high drive voltage of 29.0 V. Device IA showed an LE value of 24.4 cd A^{-1} and a power efficiency (PE) value of 3.0 lm W^{-1} (EQE of 7.3%), higher than devices IB and IC but

lower than device ID. However, device IA showed severe efficiency roll-off as the luminance increases (Figure 3.12c,d). Although devices IB and IC showed lower efficiencies than device IA, their turn-on voltages (9.4 and 9.1 V) and drive voltages (18.8 and 20.6 V) were much lower than device IA. These results clearly demonstrate that the PhOLEDs with solution-deposited TmPyPB ETLs show significantly decreased operating voltage, higher brightness and efficiency, depending on the solution-processing condition, compared to the device with vacuum-deposited TmPyPB ETL.

The *J-V*, *L-V*, *LE-L*, and the *PE-L* characteristics of PhOLEDs with BPhen ETLs are shown in Figure 3.13. In devices IIB, IIC, and IID, the solution-deposited BPhen ETL was spin-coated onto the EML from 16, 20, and 24 mg mL^{-1} solutions to deposit 20, 30, and 40 nm of BPhen ETLs, respectively. Device IIA contained a 40-nm thick vacuum-deposited BPhen ETL. Similar to devices IB-ID, device IIB from a lower concentration of BPhen solution showed a higher current density than devices IIC and IID (Figure 3.13a), whereas device IIA with vacuum-deposited BPhen showed a very low current density. As shown in Figure 4.2b-d, devices IIC and IID with solution-processed BPhen ETL showed significant improvement in performance compared to device IIA containing vacuum-deposited BPhen. The operating voltages for devices IIC and IID were much lower with turn-on voltages of 5.8-6.0 V and drive voltages of 15.8-16.1 V, compared to device IIA with vacuum-deposited BPhen with a turn-on voltage of 8.8 V and a drive voltage of 19.3 V. The luminous efficiency of device IIC was 46.9 cd A^{-1} (EQE of 14.1% at 8200 cd m^{-2}), showing a PE value of 11.1 lm W^{-1} with a maximum brightness of 42800 cd m^{-2} (at 15.8 V). Device IID gave the best performance with a luminous efficiency of 53.8 cd A^{-1} (EQE of 16.1% at 5900 cd m^{-2}) while showing a PE value of 13.3 lm W^{-1} with a maximum brightness of 52800 cd m^{-2} (at 16.1 V). It is noteworthy that device IID has a 40% higher

efficiency and brightness than device IIA with vacuum-deposited BPhen (LE = 38.7 cd A^{-1} , EQE = 11.6% and PE = 8.7 lm W^{-1}). We also note that device IIB with solution-deposited BPhen ETL from 16 mg mL^{-1} solution also enhanced power efficiency and brightness.

PhOLEDs with BCP ETL were also fabricated using vacuum- and solution-deposition methods. Devices IIIB, IIIC, and IIID had solution-deposited BCP ETLs, spin-coated onto the EML from 16, 20, and 24 mg mL^{-1} of solutions to deposit 20, 30, and 40 nm ETLs, respectively. In the case of device IIIA, BCP was thermally deposited to form a 30-nm thick ETL onto the EML. Although the *J-V* and *L-V* characteristics of devices IIIB-D with BCP ETLs (Figure 3.13a,b) showed similar characteristics as devices IIB-D with solution-deposited BPhen ETLs, the luminous and power efficiencies did not significantly increase with increasing BCP solution concentration (Figure 4.3c,d). The LE value of device IIIB was 34.6 cd A^{-1} (EQE of 10.4% at 5970 cd m^{-2}) with a maximum brightness of 34600 cd m^{-2} whereas the LE value of device IIIC was only slightly higher at 36.5 cd A^{-1} (EQE of 10.9% at 4880 cd m^{-2}) with a maximum brightness of 34600 cd m^{-2}. Device IIID with 30-nm thick solution-deposited BCP ETL showed a slightly lower LE value of 33.3 cd A^{-1} (EQE of 10.0% at 8910 cd m^{-2}) with a maximum brightness of 30400 cd m^{-2}. Thus, the performance of all devices IIIB-D with solution-deposited BCP ETL is essentially comparable in LE values (33.3 - 36.5 cd A^{-1}), EQEs (10.0 - 10.9 %) and maximum brightnesses (30400 - 34600 cd m^{-2}) in contrast to devices IIB-D with solution-deposited BPhen ETL which showed a significant increase of performance with increasing BPhen solution concentration. Compared to devices IIIB-D with solution-deposited BCP ETLs, device IIIA containing vacuum-deposited BCP ETL had a significantly lower performance in all measures with an LE value of 21.0 cd A^{-1} (EQE of 6.3% at 2450 cd m^{-2}), a maximum brightness of 18100 cd m^{-2} with very high turn-on (14.4 V) and drive voltage (25.0 V). These results

demonstrate that the PhOLEDs with solution-deposited ETLs have superior performance compared to the corresponding devices with vacuum-deposited ETLs. Device characteristics of all PhOLEDs are summarized in Table 3.6.

Table 3.6. Device chracteristics of PhOLEDs with commercial ETMs. [a]

Device [b]	ETL	ETL deposition method	V_{on}[c] [V]	Drive voltage [V]	Current density [mA cm^{-2}]	Luminance [cd m^{-2}]	Device efficiency [cd A^{-1}, lm W^{-1}, (%EQE)]
Device IA	TmPyPB	Vacuum	15.0	29.0 *25.5*	70.0 *14.1*	14100 *3460*	20.1, 2.2, (6.0) *24.4, 3.0, (7.3)*
Device IB	TmPyPB	Solution 8 mg mL^{-1}	9.4	18.8 *9.6*	234.9 *132.2*	19100 *12600*	8.1, 1.4, (2.4) *9.6, 1.7, (2.9)*
Device IC	TmPyPB	Solution 16 mg mL^{-1}	9.1	20.6 *19.1*	234.0 *88.9*	35100 *16500*	15.0, 2.3, (4.5) *18.5, 3.0, (5.5)*
Device ID	TmPyPB	Solution 24 mg mL^{-1}	8.5	20.9 *19.6*	155.6 *24.5*	34900 *7950*	22.4, 3.4, (6.7) *32.4, 5.7, (9.7)*
Device IIA	BPhen	Vacuum	8.8	19.3 *14.6*	112.8 *4.6*	31900 *1800*	28.2, 4.6, (8.4) *38.7, 8.3, (11.6)*
Device IIB	BPhen	Solution 16 mg mL^{-1}	6.5	14.4 *12.1*	151.8 *26.8*	42800 *10300*	28.2, 6.2, (8.4) *38.5, 10.0, (11.5)*
Device IIC	BPhen	Solution 20 mg mL^{-1}	6.0	15.8 *13.4*	168.6 *21.0*	48700 *8200*	34.7, 6.7, (10.4) *46.9, 11.0, (14.1)*
Device IID	BPhen	Solution 24 mg mL^{-1}	5.8	16.1 *12.8*	148.8 *10.9*	52800 *5860*	35.5, 7.0, (10.7) *53.8, 13.3, (16.1)*
Device IIIA	BCP	Vacuum	14.4	25.0 *20.9*	111.0 *11.7*	18100 *2450*	16.3, 2.0, (4.9) *21.0, 3.1, (6.3)*
Device IIIB	BCP	Solution 16 mg mL^{-1}	9.1	18.7 *16.0*	145.8 *17.2*	34600 *5970*	23.7, 4.0, (7.1) *34.6, 6.8, (10.4)*
Device IIIC	BCP	Solution 20 mg mL^{-1}	10.7	20.0 *17.3*	132.3 *13.8*	34600 *5060*	26.2, 4.1, (7.8) *36.5, 6.1, (10.9)*
Device IIID	BCP	Solution 24 mg mL^{-1}	12.5	21.9 *20.4*	121.0 *26.7*	30400 *8910*	25.2, 3.6, (7.6) *33.3, 5.1, (10.0)*

[a] Values in italic correspond to those at maximum device efficiencies. [b] Devices I with TmPyPB, devices II with BPhen, and devices III with BCP ETLs with the structure: ITO/PEDOT:PSS/EML/ETL/Al. [c] Turn-on voltage (at brightness of 1 cd m^{-2}).

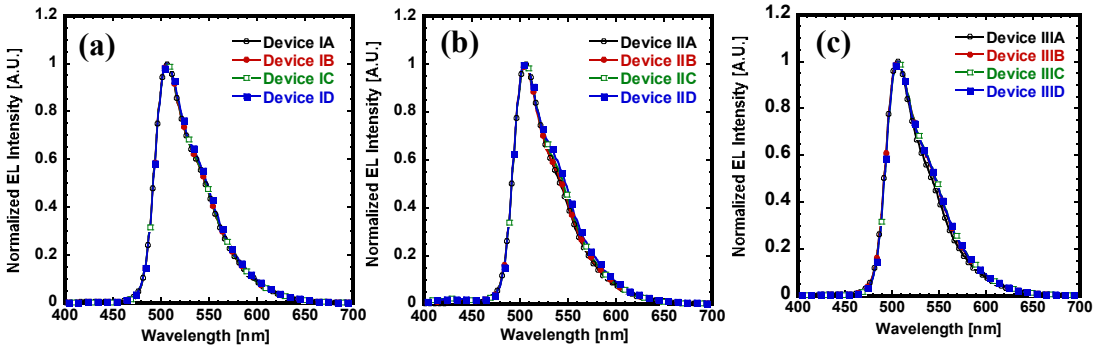

Figure 3.15. Normalized EL spectra of PhOLEDs with: (a) TmPyPB; (b) BPhen; and (c) BCP ETLs at drive voltages.

The electroluminescence (EL) spectra of the PhOLEDs are all shown in Figure 3.15. The EL spectra of all the devices are identical in lineshape with a maximum peak at 507 nm, which is originated from the $Ir(ppy)_3$ green triplet emitter.[2k] The Commission Internationale de L'Eclairage (CIE) 1931 coordinates of the devices were identical at (0.24, 0.63). However, we observed slight increase of the shoulder around 550 nm with the PhOLEDs with solution-processed ETLs, presumably due to the microcavity effect.[4d]

Surface morphology of vacuum- and solution-deposited ETLs. In order to understand the improved performance of the PhOLEDs with solution-deposited commercial ETMs, the surface morphology of both vacuum-deposited and solution-deposited ETLs was investigated by atomic force microscopy (AFM). Figure 3.16 shows the 2D and the corresponding 3D topological surface morphologies of vacuum-deposited (Figure 3.16a) and solution-deposited TmPyPB ETLs casted from different concentrations (Figure 3.16b-d). The vacuum-deposited TmPyPB ETL has a smooth surface with root-mean-square (RMS) roughness value of 0.792 nm whereas the solution-deposited thin films show a significant change in morphology as the casting solution concentration increases. TmPyPB ETL deposited from 8 mg mL^{-1} solution shows a low density of vertically aligned nanopillars (Figure 3.16b) throughout the surface while a progressively

higher density of vertically aligned nanopillars was observed in TmPyPB ETLs that were solution-deposited from 16 and 24 mg mL^{-1} (Figure 3.16c,d). The RMS roughness values were 1.41, 1.40, and 2.39 nm for solution-deposited TmPyPB ETLs from 8, 16, and 24 mg mL^{-1}, respectively. The relatively poor performance of device IB while device ID with solution-deposited TmPyPB from 24 mg mL^{-1} has the highest performance among the PhOLEDs with TmPyPB ETLs suggest a good correlation of performance with the roughness and density of the vertical nanopillars on ETL surface.

A similar trend in surface morphology was observed in the vacuum- and solution-deposited BPhen ETLs. A smooth surface was observed in the AFM images of the vacuum-deposited BPhen ETL (RMS value = 0.459 nm, Figure 3.17a) and the solution-deposited BPhen ETL from 16 mg mL^{-1} (RMS value = 0.545 nm, Figure 3.17b). In contrast, a much rougher surface was observed in the solution-deposited BPhen ETL from higher concentrations of 20 (RMS value = 1.84 nm, Figure 4.6c) and 24 mg mL^{-1} (RMS = 2.63 nm, Figure 4.6d). We can also clearly see that the density of the vertical nanopillars on the ETL surface increases dramatically with increasing solution concentration. Similar to TmPyPB ETLs, the observed variation of the surface morphology of BPhen ETLs with solution concentration is consistent with the enhanced performance of the PhOLEDs with BPhen ETLs. The observed high surface roughness and high density vertical nanopillars in the solution-deposited ETLs imply maximized area of ETL/Al cathode interface which facilitates efficient electron-injection. Furthermore, we expect that the vertically oriented nanopillars would result in improved charge-transport in the vertical direction.[14b]

On the other hand, the surface morphology of BCP ETL did not show noticeable change by solution-processing (Figure 3.18). However, in contrast to the very smooth surface of

vacuum-deposited BCP ETL (Figure 3.18a), we can still see a relatively rougher surface of the solution-deposited BCP ETLs (Figure 3.18b-d). The RMS roughness value of vacuum-deposited BCP was 0.311 nm whereas the RMS values of solution-deposited BCP ETLs was 0.467-0.504 nm. Although the change in surface morphology of the solution-processed BCP ETLs is small, the PhOLEDs with solution-deposited BCP ETLs showed superior performance compared with devices with vacuum-deposited BCP ETL. Thus, overall these results are consistent with the performance PhOLEDs with TmPyPB and BPhen ETLs, demonstrating that higher performance PhOLEDs can be achieved by solution-processing of ETLs compared to vacuum-processing.

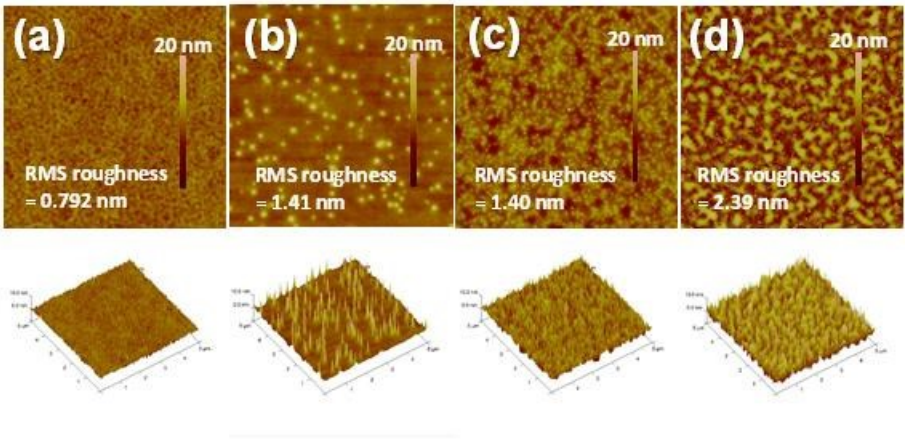

Figure 3.16. AFM topographical images (5 × 5 µm) and the corresponding 3D height images of TmPyPB ETL films. (a) vacuum-deposited TmPyPB; solution-deposited TmPyPB from (b) 8 mg mL^{-1}; (c) 16 mg mL^{-1}; and (d) 24 mg mL^{-1}.

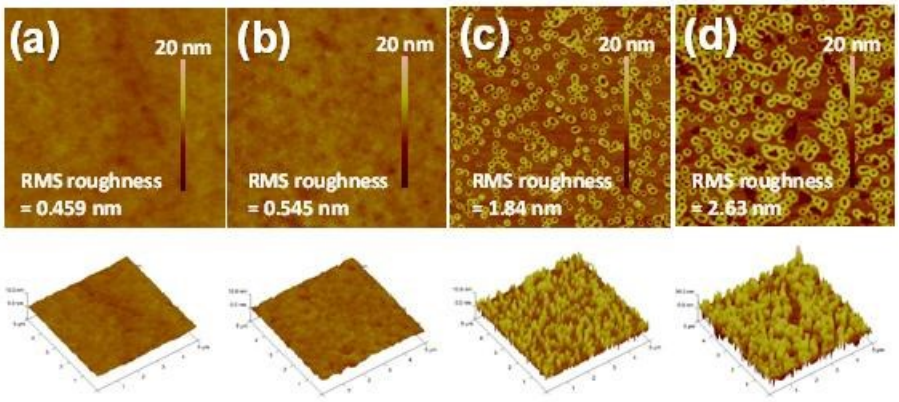

Figure 3.17. AFM topographical images (5 × 5 µm) and the corresponding 3D height images of BPhen ETL films. (a) vacuum-deposited BPhen; solution-deposited BPhen from (b) 16 mg mL^{-1}; (c) 20 mg mL^{-1}; and (d) 24 mg mL^{-1}.

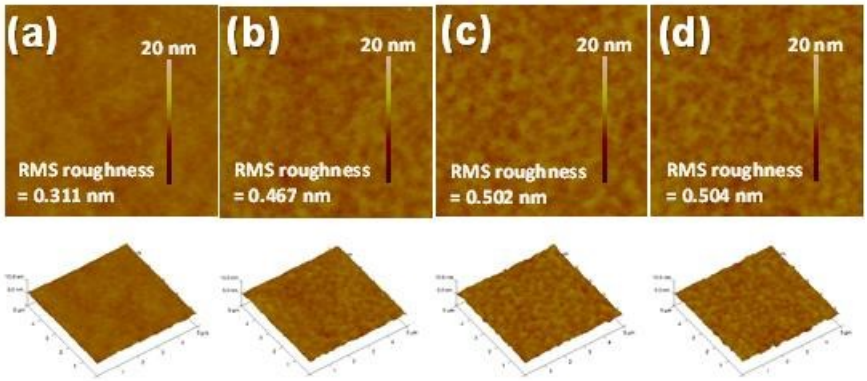

Figure 3.18. AFM topographical images (5 × 5 µm) and the corresponding 3D height images of BCP ETL films. (a) vacuum-deposited BCP; solution-deposited BCP from (b) 16 mg mL^{-1}; (c) 20 mg mL^{-1}; and (d) 24 mg mL^{-1}.

Electron-injection and transport properties. We investigated electron-injection and transport in the vacuum- and solution-deposited commercial electron-transport materials by using electron-dominant devices: ITO/Al(100 nm)/PVK:OXD-7(60:40 wt/wt, 100 nm)/ETL(15-40 nm)/Al, which were fabricated and their current density - voltage (*J-V*) characteristics were measured and analyzed. The ETL thickness and deposition method were exactly the same as used in the PhOLEDs I-III with TmPyPB, BPhen, and BCP ETLs, as already discussed. The electron mobility of the devices was measured by the space-charge-limited current (SCLC) method under ambient conditions. In Figure 3.19, the current density-electric field (*J-E*)

characteristics of the devices with TmPyPB (Figure 3.19a), BPhen (Figure 4.8b), and BCP (Figure 4.8c) ETLs are shown. Applied voltage (V) was converted to electric field (V m^{-1}) by using the active layer thickness, allowing a relative comparison of electron-injection ability at the same electrical bias. The electron mobility was extracted by fitting the *J-V* curves in the near quadratic region according to the following modified Mott-Gurney equation,[14,18] where J is the current density, ε_0 is the permittivity of free space, ε is the relative permittivity, μ is the zero-field mobility, V is the applied voltage, L is the thickness of active layer, and β is the field-activation factor (Table 3.7). The solid lines in Figure 4.8 represent the SCLC fitting curves in the quadratic SCLC region.

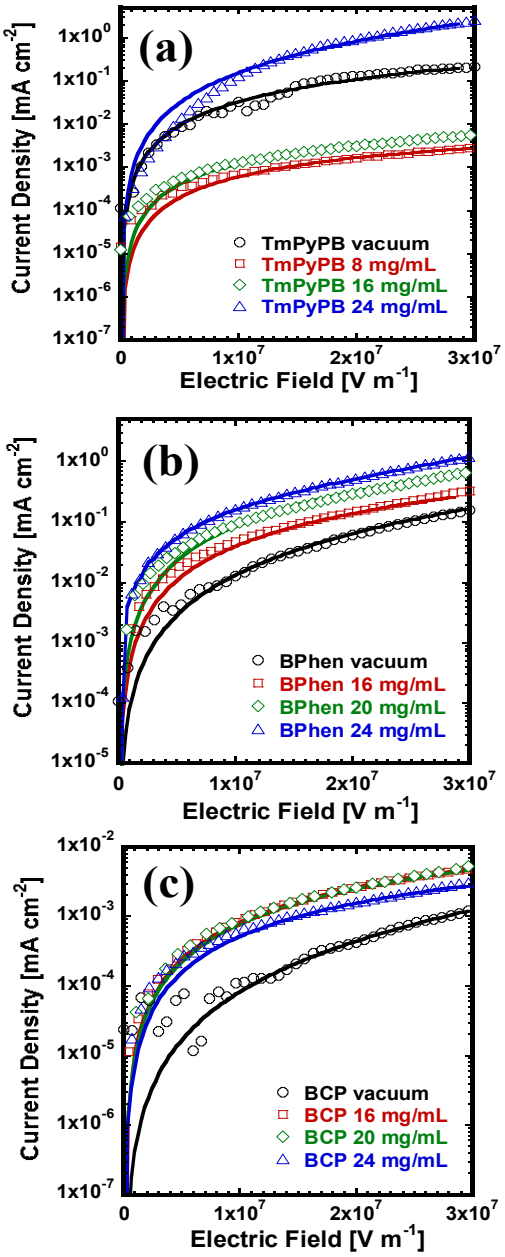

Figure 3.19. Current density vs electric field (J vs E) of ITO/Al/PVK:OXD-7/commercial ETM/Al devices in ambient conditions. ETM: (a) TmPyPB; (b) BPhen; and (c) BCP. The solid lines represent SCLC model with field-dependent mobility.

As shown by the highest current density in Figure 3.19a, electron-injection was the most efficient in the device with TmPyPB ETL from 24 mg mL^{-1} solution compared to other devices with a TmPyPB ETL. This

trend matches well with the observed highest PhOLED performance compared to other devices with a TmPyPB ETL. The electron mobility estimated from these devices showed a three orders of magnitude increase, from ~10^{-9} to ~10^{-6} cm^2 V^{-1} s^{-1}, with increasing TmPyPB solution concentration (Table 3.7). Devices with a BPhen ETL showed similar results, *i.e.* efficient electron-injection and increased electron mobility (from ~10^{-7} to ~10^{-5} cm^2 V^{-1} s^{-1}) with increasing BPhen solution concentration (Figure 3.19b, Table 3.7). The highest electron mobility of 1.3×10^{-5} cm^2 V^{-1} s^{-1} was measured from the device with a BPhen ETL deposited from 24 mg mL^{-1} solution which also corresponds very well to the observed highest PhOLED performance. The previously discussed surface morphology, *i.e.* high surface roughness and high density of nanopillars of the surface of BPhen ETL deposited from a 24 mg mL^{-1} solution, implies that maximum charge-transport can be expected, which is consistent with the measured high electron mobility of the electron-dominant device by the SCLC method. We note that it has been reported in the case of organic photovoltaic cells, that rough surface features of small-molecule thin films deposited from solution can increase the crystallinity and the roughness of the layer and thus increase device efficiency through improved charge-transport.[19]

The *J-E* characteristics of electron-dominant devices with solution-deposited BCP ETL showed ETL are shown in Figure 3.19c. The current density characteristics indicate similar electron-injection properties as of the devices with BCP ETL. The extracted electron mobilities of the devices were $(4.3 - 5.8) \times 10^{-9}$ cm^2 V^{-1} s^{-1}. However, the device with vacuum-deposited BCP ETL showed a relatively lower current density compared to the devices with solution-deposited BCP ETL as well as a significantly lower device electron mobility of 1.8×10^{-10} cm^2 V^{-1} s^{-1}, which explains the relatively poor performance of the corresponding PhOLED (device IIIA). The *J-E* characteristics of the electron-dominant devices with solution processed ETLs

well-matched with the performance of the PhOLEDs and are also in accord with the observed AFM surface morphology of the ETLs. In general, the results suggest that the rough surface morphology with a high density of vertically aligned nanopillars formed by strong intermolecular interactions[20] of solution-processed ETL maximize the contact area between the ETL and Al cathode, facilitating efficient electron-injection and transport which lead to much higher device performance compared to PhOLEDs with vacuum-deposited ETL.

Table 3.7. SCLC Electron Mobilities of Electron-Dominant Devices.

ETL	Deposition method	μ ($E=0$) [$cm^2\ V^{-1}\ s^{-1}$]	β [$cm^{1/2}\ V^{-1/2}$]	E_{max} [$V\ m^{-1}$]	Device layer thickness [nm]
TmPyPB	8mg mL^{-1}	6.1×10^{-9}	1.1×10^{-5}	3.5×10^{7}	115
TmPyPB	16 mg mL^{-1}	1.2×10^{-8}	1.2×10^{-5}	3.1×10^{7}	130
TmPyPB	24 mg mL^{-1}	3.7×10^{-6}	9.6×10^{-6}	2.9×10^{7}	140
TmPyPB	Vacuum	2.5×10^{-7}	5.9×10^{-6}	2.9×10^{7}	140
BPhen	16 mg mL^{-1}	1.6×10^{-7}	3.7×10^{-6}	3.3×10^{7}	120
BPhen	20 mg mL^{-1}	3.6×10^{-6}	2.8×10^{-6}	3.1×10^{7}	130
BPhen	24 mg mL^{-1}	1.3×10^{-5}	2.8×10^{-5}	3.1×10^{7}	140
BPhen	Vacuum	3.8×10^{-8}	6.0×10^{-6}	3.1×10^{7}	140
BCP	16 mg mL^{-1}	5.7×10^{-9}	7.7×10^{-7}	3.3×10^{7}	120
BCP	20 mg mL^{-1}	5.8×10^{-9}	8.9×10^{-6}	3.1×10^{7}	130
BCP	24 mg mL^{-1}	4.3×10^{-9}	7.0×10^{-6}	3.1×10^{7}	140
BCP	Vacuum	1.8×10^{-10}	8.0×10^{-6}	3.1×10^{7}	130

3.2.4. Conclusions

In summary, high-performance multilayered phosphorescent OLEDs have been successfully fabricated, for the first time, by sequential solution-processing of commercial small-molecule electron-transport materials (ETMs). The PhOLEDs with solution-processed electron-transport layers (ETLs) showed superior device performance compared to the devices with vacuum-deposited ETLs. Solution processing enabled the tuning and control of the ETL surface morphology by varying the solution concentration. The measured SCLC characteristics of the electron-dominant devices demonstrated that an ETL surface with a high density of vertically oriented nanopillars facilitated efficient electron-injection and transport, leading to enhanced PhOLED performance. The present approach of using a binary organic acid/water mixture as a solvent for the solution processing of ETMs is also applicable to the solution-deposition of many other commercial small-molecule ETMs, such as 2,2'2"-(1,3,5-benzinetriyl)-*tris*(1-phenyl-1-*H*-benzimidazole) (TPBI),[21] and 3-(4-biphenyl)-4-phenyl-5-*tert*-butylphenyl-1,2,4-triazole (TAZ)[22], since they also contain imine nitrogens which facilitate solubility in organic acids.[9,23]

The results also suggest that control of the surface morphology of organic semiconductors by solution-processing is a very important and promising strategy to achieve efficient charge-injection and charge-transport properties. The density of vertically oriented nanopillars on the ETL surface and the device electron mobility strongly depend on the solution-processing condition and can be controlled to improve device performance. Furthermore, we expect that the orthogonal solution-processing approach demonstrated here has potential applications not limited to PhOLEDs but various other multilayered organic electronic devices.

3.2.5. References

1. a) F. So, J. Kido, P. Burrows, *MRS Bull.* 2008, **33**, 663; b) A. C. Grimsdale, K. Leok Chan, R. E. Martin, P. G. Jokisz, A. B. Holmes, *Chem. Rev.* 2009, **109**, 897; c) S. Reineke, F. Lindner, G. Schwartz, N. Seidler, K. Walzer, B. Lussem, K. Leo, *Nature* 2009, **459**, 234; d) H. Sasabe, J. Kido, *Chem. Mater.* 2010, **23**, 621; e) M. C. Gather, A. Köhnen, K. Meerholz, *Adv. Mater.* 2011, **23**, 233; f) K. T. Kamtekar, A. P. Monkman, M. R. Bryce, *Adv. Mater.* 2010, **22**, 572;

2. a) C. Adachi, M. A. Baldo, S. R. Forrest, M. E. Thompson, *Appl. Phys. Lett.* 2000, **77**, 904; b) Y. Kawamura, S. Yanagida, S. R. Forrest, *J. Appl. Phys.* 2002, **92**, 87; c) Y. Sun, N. C. Giebink, H. Kanno, B. Ma, M. E. Thompson, S. R. Forrest, *Nature* 2006, **440**, 908; d) C.-H. Yang, Y.-M. Cheng, Y. Chi, C.-J. Hsu, F.-C. Fang, K.-T. Wong, P.-T. Chou, C.-H. Chang, M.-H. Tsai, C.-C. Wu, *Angew. Chem. Int. Ed.* 2007, **46**, 2418; e) A. Haldi, B. Domercq, B. Kippelen, R. D. Hreha, J. Y. Cho, S. R. Marder, *Appl. Phys. Lett.* 2008, **92**, 253502; f) T. Earmme, E. Ahmed, S. A. Jenekhe, *J. Phys. Chem. C* 2009, **113**, 18448; g) N. Chopra, J. Lee, J. G. Xue, F. So, *IEEE Trans. Electron Devices* 2010, **57**, 101; h) A. Endo, K. Sato, K. Yoshimura, T. Kai, A. Kawada, H. Miyazaki, C. Adachi, *Appl. Phys. Lett.* 2011, **98**, 083302; i) S. L. Gong, Y. H. Chen, J. J. Luo, C. L. Yang, C. Zhong, J. G. Qin, D. G. Ma, *Adv. Funct. Mater.* 2011, **21**, 1168; j) L. Xiao, Z. Chen, B. Qu, J. Luo, S. Kong, Q. Gong, J. Kido, *Adv. Mater.* 2011, **23**, 926; k) S. H. Kim, J. Jang, K. S. Yook, J. Y. Lee, *Appl. Phys. Lett.* 2008, **92**, 023513; k) D. Tanaka, H. Sasabe, Y. -J. Li, S. -J. Su, T. Takeda, J. Kido, *Jpn. J. Appl. Phys.* 2007, **46**, L10.

3. a) S. R. Forrest, *Nature* 2004, **428**, 911; b) A. C. Arias, J. D. MacKenzie, I. McCulloch, J. Rivnay, A. Salleo, *Chem. Rev.* 2010, **110**, 3.

4. a) X. Gong, M. R. Robinson, J. C. Ostrowski, D. Moses, G. C. Bazan, A. J. Heeger, *Adv. Mater.* 2002, **14**, 581; b) P.-I. Shih, C.-F. Shu, Y.-L. Tung, Y. Chi, *Appl. Phys. Lett.* 2006, **88**, 251110; c) X. H. Yang, F. Jaiser, S. Klinger, D. Neher, *Appl. Phys. Lett.* 2006, **88**, 021107; d) F. So, B. Krummacher, M. K. Mathai, D. Poplavskyy, S. A. Choulis, V. E. Choong, *J. Appl. Phys.* 2007, **102**. 091101; e) F. I. Wu, X. H. Yang, D. Neher, R. Dodda, Y. H. Tseng, C. F. Shu, *Adv. Funct. Mater.* 2007, **17**, 1085.

5. a) X. Gong, S. Wang, D. Moses, G. C. Bazan, A. J. Heeger, *Adv. Mater.* 2005, **17**, 2053; b) B. Ma, B. J. Kim, D. A. Poulsen, S. J. Pastine, J. M. J. Fréchet, *Adv. Funct. Mater.* 2009, **19**, 1024; c) J. J. Park, T. J. Park, W. S. Jeon, R. Pode, J. Jang, J. H. Kwon, E.-S. Yu, M.-Y. Chae, *Org. Electron.* 2009, **10**, 189; d) Z. Jiang, T. Ye, C. Yang, D. Yang, M. Zhu, C. Zhong, J. Qin, D. Ma, *Chem. Mater.* 2010, **23**, 771.

6. a) S. C. Lo, R. N. Bera, R. E. Harding, P. L. Burn, I. D. W. Samuel, *Adv. Funct. Mater.* 2008, **18**, 3080; b) S. C. Lo, R. E. Harding, C. P. Shipley, S. G. Stevenson, P. L. Burn, I. D. W. Samuel, *J. Am. Chem. Soc.* 2009, **131**, 16681; c) W. Y. Lai, J. W. Levell, A. C. Jackson, S. C. Lo, P. V. Bernhardt, I. D. W. Samuel, P. L. Burn, *Macromolecules* 2010, **43**, 6986.

7. a) N. Rehmann, D. Hertel, K. Meerholz, H. Becker, S. Heun, *Appl. Phys. Lett.* 2007, **91**, 103507; b) H. Fukagawa, K. Watanabe, S. Tokito, *Org. Electron.* 2009, **10**, 798; c) S. J. Lee, J. S. Park, M. Song, I. A. Shin, Y. I. Kim, J. W. Lee, J. W. Kang, Y. S. Gal, S. Kang, J. Y.

Lee, S. H. Jung, H. S. Kim, M. Y. Chae, S. H. Jin, *Adv. Funct. Mater.* 2009, **19**, 2205; d) K. H. Kim, J. Y. Lee, T. J. Park, W. S. Jeon, G. P. Kennedy, J. H. Kwon, *Synth. Met.* 2010, **160**, 631; e) S. Ye, Y. Liu, J. Chen, K. Lu, W. Wu, C. Du, Y. Liu, T. Wu, Z. Shuai, G. Yu, *Adv. Mater.* 2010, **22**, 4167; f) K. S. Yook, S. E. Jang, S. O. Jeon, J. Y. Lee, *Adv. Mater.* 2010, **22**, 4479; g) K. S. Yook, J. Y. Lee, *Org. Electron.* 2011, **12**, 291; h) M. Zhu, T. Ye, X. He, X. Cao, C. Zhong, D. Ma, J. Qin, C. Yang, *J. Mater. Chem.*, 2011, **21**, 9326.

8. a) S. Sax, G. Mauthner, T. Piok, S. Pradhan, U. Scherf, E. J. W. List, *Org. Electron.* 2007, **8**, 791; b) S. Sax, N. Rugen-Penkalla, A. Neuhold, S. Schuh, E. Zojer, E. J. W. List, K. Mullen, *Adv. Mater.* 2010, **22**, 2087.

9. a) A. K. Agrawal, S. A. Jenekhe, *Chem. Mater.* 1996, **8**, 579; b) X. J. Zhang, A. S. Shetty, S. A. Jenekhe, *Macromolecules* 1999, **32**, 7422; c) M. M. Alam, S. A. Jenekhe, *Chem. Mater.* 2002, **14**, 4775; d) C. J. Tonzola, M. M. Alam, S. A. Jenekhe, *Adv. Mater.* 2002, **14**, 1086; e) C. J. Tonzola, M. M. Alam, W. Kaminsky, S. A. Jenekhe, *J. Am. Chem. Soc.* 2003, **125**, 13548; f) A. P. Kulkarni, C. J. Tonzola, A. Babel, S. A. Jenekhe, *Chem. Mater.* 2004, **16**, 4556; g) T. W. Kwon, M. M. Alam, S. A. Jenekhe, *Chem. Mater.* 2004, **16**, 4657; h) C. J. Tonzola, M. M. Alam, B. A. Bean, S. A. Jenekhe, *Macromolecules* 2004, **37**, 3554.

10. a) S. A. Jenekhe, S. J. Yi, *Appl. Phys. Lett.* 2000, **77**, 2635; b) M. M. Alam, S. A. Jenekhe, *Chem. Mater.* 2004, **16**, 4647.

11. a) H. B. Wu, F. Huang, Y. Q. Mo, W. Yang, D. L. Wang, J. B. Peng, Y. Cao, *Adv. Mater.* 2004, **16**, 1826; b) C. V. Hoven, A. Garcia, G. C. Bazan, T.-Q. Nguyen, *Adv. Mater.* 2008, **20**, 3793.

12. a) J.-D. You, S.-R. Tseng, H.-F. Meng, F.-W. Yen, I. F. Lin, S.-F. Horng, *Org. Electron.* 2009, **10**, 1610; b) Z.-Y. Liu, S.-R. Tseng, Y.-C. Chao, C.-Y. Chen, H.-F. Meng, S.-F. Horng, Y.-H. Wu, S.-H. Chen, *Synth. Met.* 2011, **161**, 426; c) T. L. Ye, S. Y. Shao, J. S. Chen, L. X. Wang, D. G. Ma, *ACS Appl. Mater. Interfaces* 2011, **3**, 410.

13. T.-W. Lee, T. Noh, H.-W. Shin, O. Kwon, J.-J. Park, B.-K. Choi, M.-S. Kim, D. W. Shin, Y.-R. Kim, *Adv. Funct. Mater.* 2009, **19**, 1625.

14. a) T. Earmme, E. Ahmed, S. A. Jenekhe, *Adv. Mater.* 2010, **22**, 4744; b) E. Ahmed, T. Earmme, S. A. Jenekhe, *Adv. Funct. Mater.* 2011, DOI: 10.1002/adfm.201100848, *Early View*.

15. a) S.-J. Su, T. Chiba, T. Takeda, J. Kido, *Adv. Mater.* 2008, **20**, 2125; b) S.-J. Su, Y. Takahashi, T. Chiba, T. Takeda, J. Kido, *Adv. Funct. Mater.* 2009, **19**, 1260.

16. a) S. Naka, H. Okada, H. Onnagawa, T. Tsutsui, *Appl. Phys. Lett.* 2000, **76**, 197; b) M. Y. Chan, C. S. Lee, S. L. Lai, M. K. Fung, F. L. Wong, H. Y. Sun, K. M. Lau, S. T. Lee, *J. Appl. Phys.* 2006, **100**, 094506; c) H. Li, J.-L. Bredas, C. Lennartz, *J. Chem. Phys.* 2007, **126**, 164704.

17. H. Nakada, S. Kawami, K. Nagayama, Y. Yonemoto, R. Murayama, J. Funaki, T. Wakimoto, P. P. K. Imai, *Polym. Prepr. Jpn.* 1994, **35**, 2450.

18. a) P. N. Murgatroyd, *J. Phys. D* 1970, **3**, 1488; b) N. F. Mott, D. Gurney, *Electronic Processes in Ionic Crystals*, Academic Press, New York, 1970.

19. a) G. Wei, S. Wang, K. Renshaw, M. E. Thompson, S. R. Forrest, *ACS Nano* 2010, **4**, 1927; b) G. D. Wei, R. R. Lunt, K. Sun, S. Y. Wang, M. E. Thompson, S. R. Forrest, *Nano Lett* 2010, **10**, 3555.

20. a) A. L. Briseno, S. C. B. Mannsfeld, C. Reese, J. M. Hancock, Y. Xiong, S. A. Jenekhe, Z. Bao, Y. Xia, *Nano Lett* 2007, **7**, 2847; b) E. Ahmed, A. L. Briseno, Y. Xia, S. A. Jenekhe, *J. Am. Chem. Soc.* 2008, **130**, 1118; c) E. Ahmed, T. Earmme, G. Ren, S. A. Jenekhe, *Chem. Mater.* 2010, **22**, 5786; d) F. S. Kim, G. Q. Ren, S. A. Jenekhe, *Chem. Mater.* 2011, **23**, 682.

21. a) J. Shi, C. W. Tang, C. H. Chen, US Patent 5 645 948, 1997; b) A. P. Kulkarni, S. A. Jenekhe, *J. Phys. Chem. C* 2008, **112**, 5174.

22. J. Kido, C. Ohtaki, K. Hongawa, K. Okuyama, K. Nagai, *Jpn. J. Appl. Phys.* 1993, **32**, L917.

23. a) C. Wang, M. Kilitziraki, J. A. H. MacBride, M. R. Bryce, L. E. Horsburgh, A. K. Sheridan, A. P. Monkman, I. D. W. Samuel, *Adv. Mater.* 2000, **12**, 217; b) J. M. Hancock, S. A. Jenekhe, *Macromolecules* 2008, **41**, 6864.

Chapter 4. High Performance Phosphorescent OLEDs with Solution-Processed Doped Electron-Transport Layers

This chapter investigates novel orthogonal solution-doped electron-transport layers in phosphorescent OLEDs. The results in this chapter are reprinted in part with permission from Earmme*, et al*. (Copyright 2012 Wiley-VCH and Copyright 2013 American Institute of Physics).

4.1. Solution-Processed Alkali Metal Salt Doped Electron-Transport Layers for High Performance Phosphorescent Organic Light-Emitting Diodes

4.1.1. Introduction

Organic light-emitting diodes (OLEDs) are finding various applications in full-color display panels, flexible displays, and solid-state lighting.[1-5] Recently, intensive efforts have been focused on developing phosphorescent OLEDs (PhOLEDs), which utilize triplet excitons to achieve superior performance compare to conventional fluorescent OLEDs.[6-11] Highly efficient multilayered PhOLEDs are generally fabricated by sequential deposition of multilayered structures that facilitate charge-injection and transport from both electrodes to the emission layer (EML). Most high-performance PhOLEDs have been achieved by vacuum-deposition of small molecules involving sequential thermal evaporation to obtain the multilayered structures. In contrast to the intensive efforts made on developing highly efficient multilayered PhOLEDs by thermal vacuum evaporation, reports on solution-processed PhOLEDs are relatively few.[12-16]

Although solution-processing has advantages of low-cost fabrication and/or large-area devices,[17] challenges remain in sequential solution-processing of a multilayered device structure because the solvent used to deposit the subsequent layer can easily dissolve or disrupt the underlayer. One general approach to overcome this problem is to employ orthogonal solvent

processing.[18-21] We have reported that many conjugated polymers or dendrimers-based electron-transport materials (ETMs) can be solution-processed from an organic acid solvent onto various underlying polymers, enhancing the performance of polymer OLEDs,[22-26] polymer transistors,[18] or polymer solar cells.[27,28] More recently, we have shown that high performance solution-processed multilayered PhOLEDs can be realized by orthogonal solution-processing of new oligoquinoline ETMs[29,30] and other commercially available small molecule ETMs.[31]

Despite the demonstration of multilayered device structures fabricated by orthogonal solution-processing, improving electron-injection and transport from the metal cathode is a major challenge in realization of all-solution-processed PhOLEDs with higher performance. Because widely used metal cathodes (e.g. Al, Ag) have a high work function (~ 4.2 eV) which leads to high electron-injection barriers between the ETM and the cathode, cathode interfacial materials such as alkali metal halides (e.g. LiF, CsF) or low work function metals (e.g. Ca, Ba, or Mg) are generally inserted as a thin interlayer (~ 0.5 to 2 nm) between the ETM and cathode to achieve facile electron injection. Another approach to improve electron-injection/transport is by doping the ETM with organic,[32-34] inorganic,[35] or low-work-function metal[36] n-type dopants to modify the interface electronic structure and/or to enhance bulk conductivity of the ETMs.

Various n-type doping approaches and basic mechanisms have been proposed and studied to achieve an increased charge carrier concentration with high conductivity to realize high-performance OLEDs. N-type doping of the organic ETMs is known to be challenging due to the difficulty of finding suitable n-type dopants. For efficient doping, the HOMO level of n-type dopant must be higher than the LUMO level of the organic semiconductors, which is generally unstable in the air. [37] The use of alkali metal is well-known approach to improve electron-injection from cathode. For example, an evaporation of Li metal or LiF monolayer or co-

evaporation of the dopants into bulk organic ETMs have been known as an efficient n-type doping method. [38-41] The influence of n-doping by Li metal or LiF on tris(8-hydroxyquinoline)aluminum (Alq_3) ETM has been studied in detail by X-ray photoelectron spectroscopy (XPS) or ultraviolet photoemission spectroscopy (UPS) indicating a chemical reaction of LiF and Al which may release Li ions into the bulk organic ETM. [40,41]

There also have been many efforts on utilizing organic materials with a high-lying HOMO as n-type dopants which would act as strong electron donor to organic ETMs. The use of strong reducing molecule such as cobaltocene ($CoCp_2$) was reported and investigated, showing that the Fermi level shifted toward the unoccupied states of the host ETM, which resulted in three orders of magnitude current increase.[42] Other examples of n-type dopants include electrochemically reduced form of the transition metal complex[43] or salts of cationic dyes as strong molecular donors.[44,45]

Recently, alkali metal salts have proven to be effective n-type dopant to enhance electron-injection and transport of organic ETMs. For example, cesium carbonate (Cs_2CO_3),[46-49] lithium carbonate (Li_2CO_3),[50] cesium fluoride (CsF),[51] and lithium fluoride (LiF)[52] have been co-evaporated as n-type dopants with various organic ETMs. The n-type doping effect of alkali metal salt was demonstrated by surface analysis techniques showing that the Fermi level of the organic ETMs shifts toward the LUMO edge.[35] The proposed mechanism of n-type doping effect was that the alkali metal salt such as Cs_2CO_3 would decompose into a mixture of Cs and oxides of Cs during thermal evaporation, which may have sufficient n-doping ability. [48,49]

Nevertheless, such a doping is mainly carried out by thermal evaporation or co-evaporation under high vacuum especially in the case of alkali metal salts. Furthermore, for the co-evaporation process, a precise control of the co-deposition rate via complicated vacuum thermal

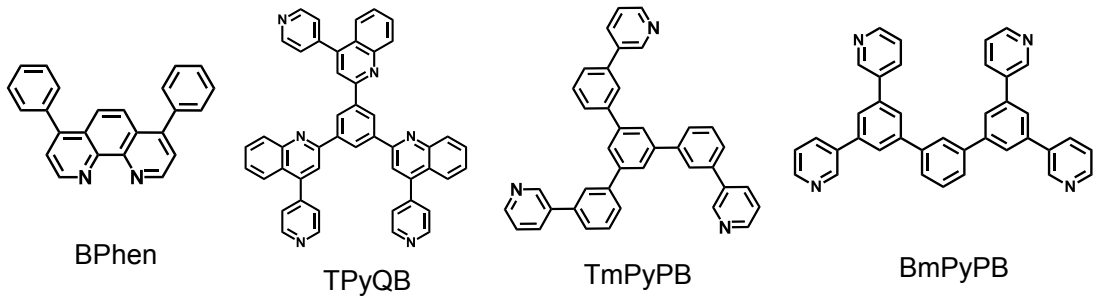

Chart 4.1. Molecular structures of electron-transport materials.

evaporation process is critical to obtain exact dopant to host ratio and this is highly challenging and economically undesirable.

In this chapter, we report for the first time that organic small-molecule electron-transport materials can be doped with alkali metal salts by solution-processing of the electron transport layer (ETL) to achieve high-performance all-solution-processed PhOLEDs. We found that incorporation of the dopant into the ETL by solution-processing significantly changes the surface morphology of ETL forming a good interfacial contact between ETL and metal cathode, leading to facile electron-injection and transport. Our results suggest that solution-processing of metal salt doped small-molecule ETMs is a new strategy that could enable the fabrication of various high-performance multilayered all-solution-processed organic electronic devices. High performance solution-processed blue PhOLEDs were achieved by sequential solution-processing of electron-transport material doped with an alkali metal salt, cesium carbonate (Cs_2CO_3) or lithium carbonate (Li_2CO_3). PhOLEDs based on FIrpic blue triplet emitter-doped poly(*N*-vinylcarbazole) emission layer and a solution-processed 4,7-diphenyl-1,10-phenanthroline

(Bathophenanthroline, BPhen)[53-55] electron-transport layer (ETL) doped with Cs_2CO_3 show a luminous efficiency (LE) of 35.1 cd A^{-1} at a brightness of 1820 cd m^{-2} with a power efficiency of 15.0 lm W^{-1} and an external quantum efficiency of 17.9%. Furthermore, our approach of solution-processing of alkali metal salt doped ETL was readily extended to other small-molecule electron-transport materials, including 1,3,5-tris(4-pyridinquinolin-2-yl)benzene (TPyQB),[30] 1,3,5-tris(*m*-pyrid-3-yl-phenyl)benzene (TmPyPB),[56,57] and 1,3-bis(3,5-di(pyridine-3-yl)phenyl)benzene (BmPyPB) (Chart 4.1).[58] The blue PhOLEDs with solution-processed BmPyPB ETL doped with Cs_2CO_3 show a high LE value of 37.7 cd A^{-1} at a brightness of 1300 cd m^{-2} with a power efficiency of 13.1 lm W^{-1} and an external quantum efficiency of 19.0%, which is the highest performance reported to date for all-solution-processed blue PhOLEDs.

4.1.2. Experimental Section

Materials. Poly(*N*-vinyl carbazole) (PVK, average M_w = 1,100,000 g mol^{-1}), 4,7-diphenyl-1,10-phenanthroline (BPhen, 99%, sublimed grade), cesium carbonate (Cs_2CO_3, 99.9% trace metals basis), and lithium carbonate (Li_2CO_3, 99%) were purchased from Sigma-Aldrich Co. 1,3-Bis(2-(4-tert-butylphenyl)-1,3,4-oxadiazo-5-yl)benzene (OXD-7), bis(3,5-difluoro-2-(2-pyridyl)phenyl-(2-carboxypyridyl)iridium(III) (FIrpic), 1,3,5-Tris(m-pyrid-3-yl-phenyl)benzene (TmPyPB), and 1,3-bis(3,5-di(pyridine-3-yl)phenyl)benzene (BmPyPB) were purchased from Luminescence Technology (LumTec) Co., Taiwan. 1,3,5-tris(4-pyridinquinolin-2-yl)benzene (TPyQB) was synthesized as previously reported. [30] A solution of PEDOT:PSS (poly-(ethylenedioxythiophene):polystyrenesulfonate, Clevios P VP CH 8000) dispersed in water was purchased from Heraeus GmBH, Germany. All purchased chemicals were used as received without further purification.

Device Fabrication. The phosphorescent emission layer (EML) consisted of a blend of PVK and OXD-7 (PVK:OXD-7 = 60:40, wt/wt) as a host and 10.0 wt% FIrpic as the blue dopant. A solution of PEDOT:PSS was diluted with DI water by 1:1 ratio and filtered before spin-coating to make a 30-nm hole-injection layer onto a pre-cleaned ITO glass. Clevios P VP CH 8000 (PEDOT:PSS) was used to prevent current leakage and suppressing of hole-current.[63] The film was then annealed at 150 ºC under vacuum to remove residual water. The 70-nm polymer EML was obtained by spin coating of the PVK:OXD-7:FIrpic blend in chlorobenzene onto the PEDOT:PSS layer and vacuum dried at 100 ºC. A small-molecule electron-transport material (ETM, e.g. BPhen) was co-dissolved with alkali metal salt (Cs_2CO_3 or Li_2CO_3) in formic acid:water (FA:H_2O = 3:1) mixture and spun cast onto the EML at a spin speed of 7000 rpm followed by vacuum drying at 50 ºC to form an electron-transport layer (ETL). After drying, thermally evaporated Al cathode was deposited onto the ETL. The structure of PhOLEDs with solution-processed ETLs was: ITO/PEDOT:PSS(30 nm)/EML(70 nm)/solution-processed ETM:alkali metal salt (20 nm)/Al (100 nm). The device structure of PhOLEDs with a vacuum-deposited bilayer of BPhen ETL and alkali metal salt was: ITO/PEDOT:PSS(30 nm)/EML(70 nm)/vacuum-deposited BPhen ETL (20 nm)/vacuum-deposited Cs_2CO_3 or Li_2CO_3 (1 nm)/Al. BPhen and alkali metal salt were sequentially vacuum-deposited by thermal evaporation onto EML using Edwards Auto Vacuum 306, followed by a deposition of Al without breaking the vacuum ($< 2.0 \times 10^{-6}$ torr).

For the single charge carrier-dominant devices, two types of devices were fabricated. Electron-dominant devices: ITO/polymer host (70 nm)/solution-deposited BPhen:M_2CO_3 ETL (20nm)/Al; and hole-dominant devices: ITO/PEDOT:PSS (30 nm)/polymer host (70

nm)/solution-deposited BPhen: M_2CO_3 ETL (20 nm)/Au. All layers were deposited under exactly the same conditions as the fabrication of PhOLEDs.

Devices for space-charge-limited current (SCLC) measurement were fabricated with ITO/solution-processed BPhen:M_2CO_3 ETL (~ 200 nm)/Al structure. The organic layer was obtained by the spin-coating of ETM solution onto the substrate followed by deposition of Al electrode.

Characterization. Film thickness was measured by an Alpha-Step 500 profilometer (KLA-Tencor, San Jose, CA) and also confirmed by Atomic Force Microscopy (AFM). Electroluminescence (EL) spectra were obtained using the same spectrofluorimeter described above. Current-voltage (*J-V*) characteristics of the PhOLEDs were measured by using a HP4155A semiconductor parameter analyzer (Yokogawa Hewlett-Packard, Tokyo). The luminance (brightness) was simultaneously measured by using a model 370 optometer (UDT Instruments, Baltimore, MD) equipped with a calibrated luminance sensor head (Model 211) and a 5x objective lens. The device external quantum efficiencies (EQEs) were calculated from the forward viewing luminance, current density and EL spectrum assuming a Lambertian distribution using procedures reported previously.[64] All the device fabrication and device characterization steps were carried out under ambient laboratory condition.

Current-voltage characteristics of single charge carrier dominant and SCLC devices were measured using the same semiconductor parameter analyzer as used for PhOLED devices. The measurements were performed under dark and ambient conditions. AFM characterization of surface morphology was done on a Veeco Dimension 3100 Scanning Probe Microscope (SPM) system. The AFM topographical images were directly measured on the same PhOLEDs used for device characterization.

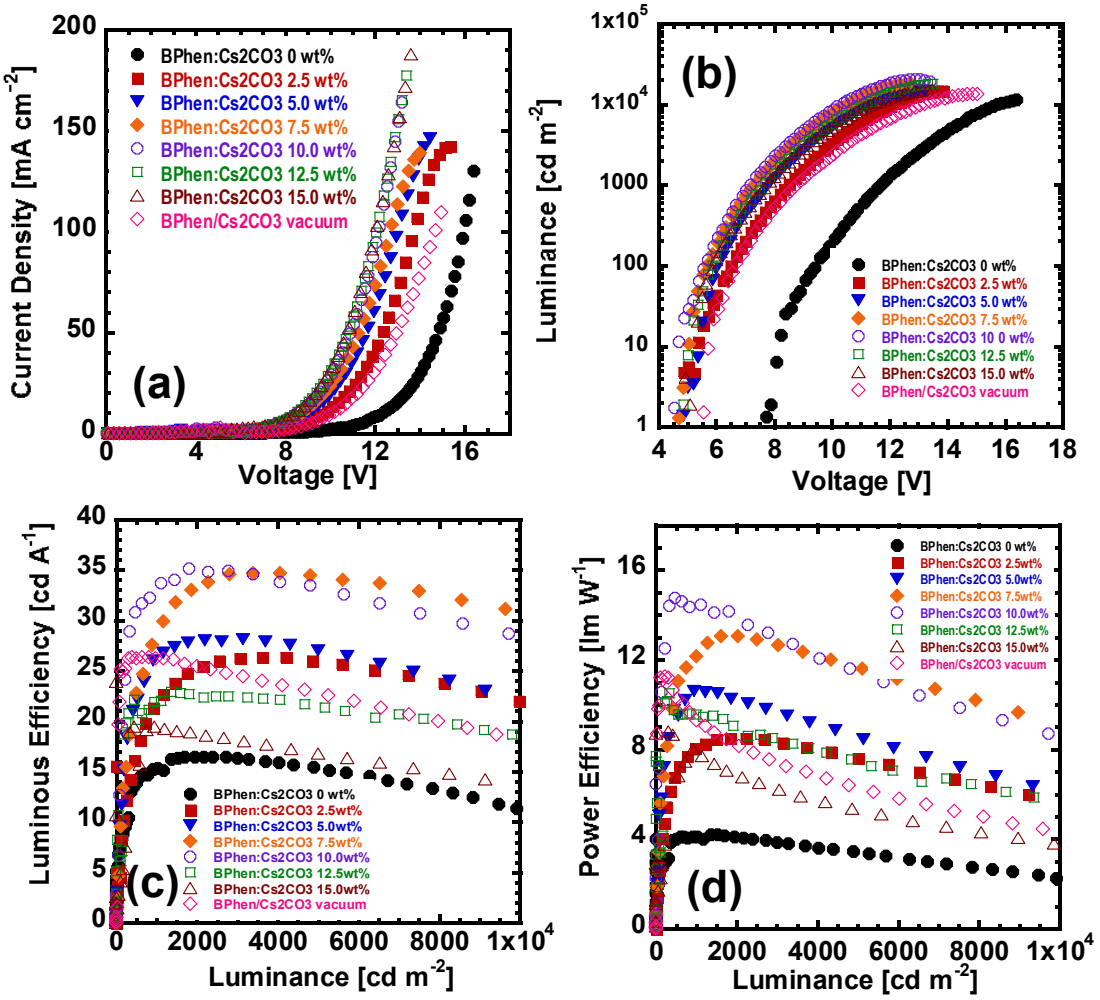

Figure 4.1. Blue PhOLEDs with BPhen ETL doped with Cs_2CO_3: (a) Current density (*J*) – voltage (*V*); (b) luminance (*L*) - voltage (*V*); (c) luminous efficiency (*LE*) - luminance (*L*); and (d) power efficiency (*PE*) - luminance (*L*) curves. Device structures: ITO/PEDOT:PSS(30 nm)/EML(70 nm)/solution-processed BPhen:Cs_2CO_3 ETL(20 nm)/Al (100 nm), ETL doped with different concentration of Cs_2CO_3; and ITO/PEDOT:PSS(30 nm)/EML(70 nm)/vacuum-deposited BPhen ETL(20 nm)/vacuum-deposited Cs_2CO_3(1 nm)/Al (100 nm).

4.1.3. Results and Discussion

Performance of PhOLEDs with alkali metal salt doped BPhen ETLs. We fabricated solution-processed multilayered PhOLEDs with polymer-based blue phosphorescent emission layer (EML) and solution-deposited BPhen electron-transport layer (ETL) doped with an alkali metal salt (M_2CO_3, M= Li, Cs) dopant, Cs_2CO_3 or Li_2CO_3. The concentration of the dopant in the ETL was: 2.5, 5.0, 7.5, 10.0, 12.5 or 15.0 wt% Cs_2CO_3 and 1.0, 2.5, 5.0, 7.5 or 10.0 wt% Li_2CO_3. The

blend of BPhen and alkali metal salt, BPhen:Cs_2CO_3 or BPhen:Li_2CO_3 ETL, was deposited from a formic acid (FA) / water (H_2O) solvent mixture (FA:H_2O = 3:1) onto the EML.[29,30] A series of PhOLEDs with solution-processed BPhen:M_2CO_3 ETL were fabricated:

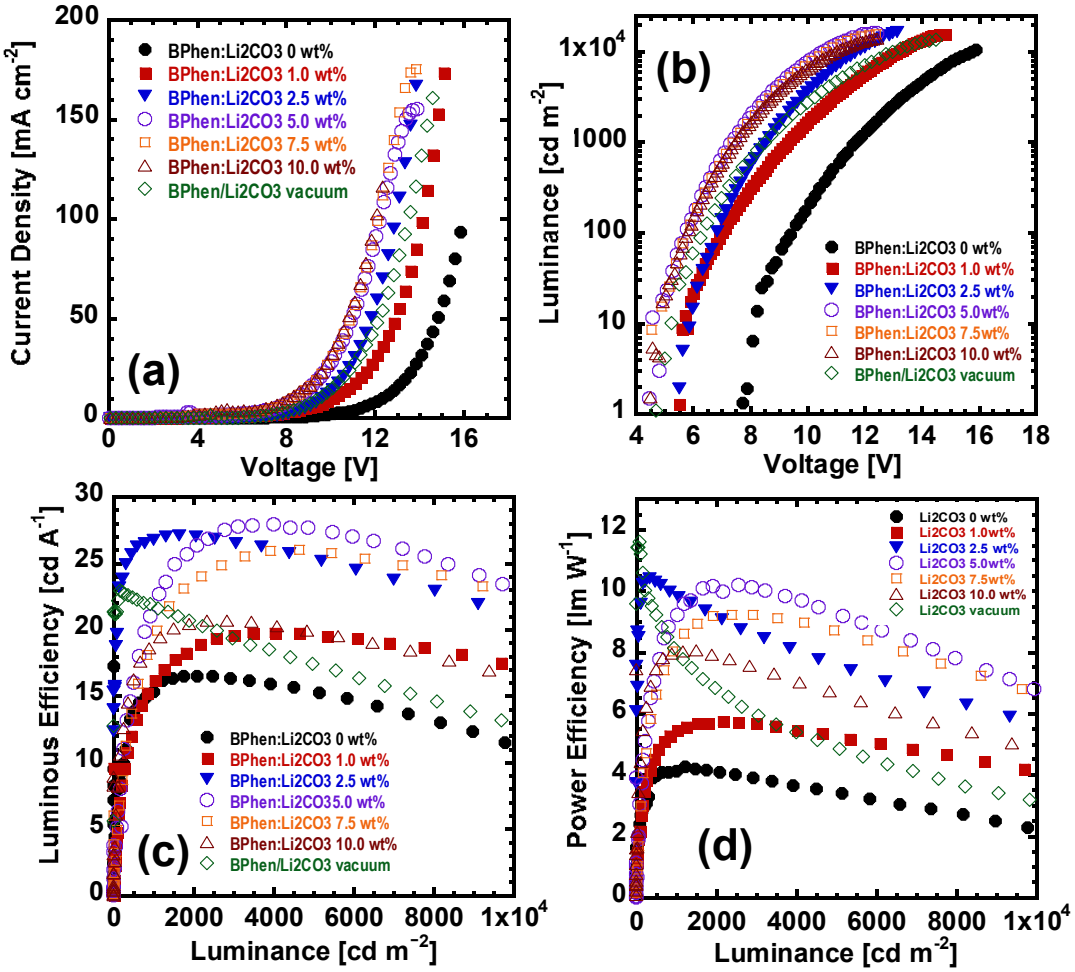

Figure 4.2. Blue PhOLEDs with BPhen ETL doped with Li_2CO_3: (a) Current density (*J*) – voltage (*V*); (b) luminance (*L*) - voltage (*V*); (c) luminous efficiency (*LE*) - luminance (*L*); and (d) power efficiency (*PE*) - luminance (*L*) curves. Device structures: ITO/PEDOT:PSS(30 nm)/EML(70 nm)/solution-processed BPhen:Li_2CO_3 ETL(20 nm)/Al (100 nm), BPhen ETL doped with different concentration of Li_2CO_3; and ITO/PEDOT:PSS(30 nm)/EML(70 nm)/vacuum-deposited BPhen ETL(20 nm)/vacuum-deposited Li_2CO_3(1 nm)/Al (100 nm).

ITO/PEDOT:PSS/EML/BPhen:M_2CO_3/Al; the metal salt (M_2CO_3, M = Cs, Li) concentration was varied in the ETL. To verify the relative effectiveness of the solution-processed BPhen:M_2CO_3-doped ETLs, PhOLEDs with a vacuum-deposited BPhen ETL and an alkali metal

salt electron-injection layer (EIL) were also fabricated: ITO/PEDOT:PSS/EML/vacuum-deposited BPhen/vacuum-deposited Cs_2CO_3 or Li_2CO_3/Al. The detailed PhOLED fabrication procedures are described in the Experimental Section.

Figure 4.1 shows the performance of PhOLEDs with solution-processed BPhen:Cs_2CO_3 ETL. As shown in Figure 4.1a-d, the PhOLEDs with solution-deposited BPhen ETL without Cs_2CO_3 dopant (BPhen: Cs_2CO_3 0 wt%) showed a high turn-on voltage of 7.7 V, a drive voltage of 16.4 V and lower current density compared to other devices with BPhen ETL doped with Cs_2CO_3. The performance of the PhOLEDs dramatically changes when Cs_2CO_3 is incorporated into BPhen ETL **(**Figure 4.1, Table 4.1). PhOLEDs with 2.5 wt% Cs_2CO_3 dopant showed a significantly reduced turn-on voltage (4.8 V), drive voltage (13.9 V), and also a significantly increased luminous efficiency (LE) of 26.4 cd A^{-1} with a power efficiency (PE) of 8.5 lm W^{-1} (external quantum efficiency (EQE) = 13.5 %). This represents a 1.6-fold higher efficiency compared to the device without Cs_2CO_3 dopant. As the concentration of Cs_2CO_3 in BPhen ETL increased from 2.5 to 10.0 wt%, the PhOLEDs showed much enhanced performance; the current density and maximum luminance (brightness) increased while the turn-on voltage and drive voltage decreased (Figure 4.1a,b, Table 4.1). The blue PhOLEDs with solution-processed BPhen:Cs_2CO_3 (10.0 wt% Cs_2CO_3) showed the highest luminous efficiency (LE) of 35.1 cd A^{-1} (at 1820 cd m^{-2}) (Figure 4.1c) and the maximum power efficiency (PE) of 15.0 lm W^{-1} (Figure 4.1d) with an EQE of 17.9 %, which is more than two-fold superior compared to the devices without Cs_2CO_3 doping. Even compared to the devices with vacuum-deposited BPhen ETL and Cs_2CO_3 EIL layers, PhOLEDs with solution-processed BPhen ETL doped with Cs_2CO_3 showed much superior performance. We note that PhOLEDs with solution-processed ETL reached the maximum efficiency at high brightness (1820 - 3600 cd m^{-2}) while the devices with vacuum-

deposited ETL/EIL showed the maximum efficiency at low brightness of 320 cd m^{-2}. Furthermore, PhOLEDs with vacuum-deposited ETL/EIL showed much more severe efficiency roll-off (Figure 4.1c,d) compared to the devices with solution-processed doped ETLs. These results suggest that the solution-processing of metal salt doped small-molecule electron-transport layer is promising for achieving high efficiency devices with high brightness.

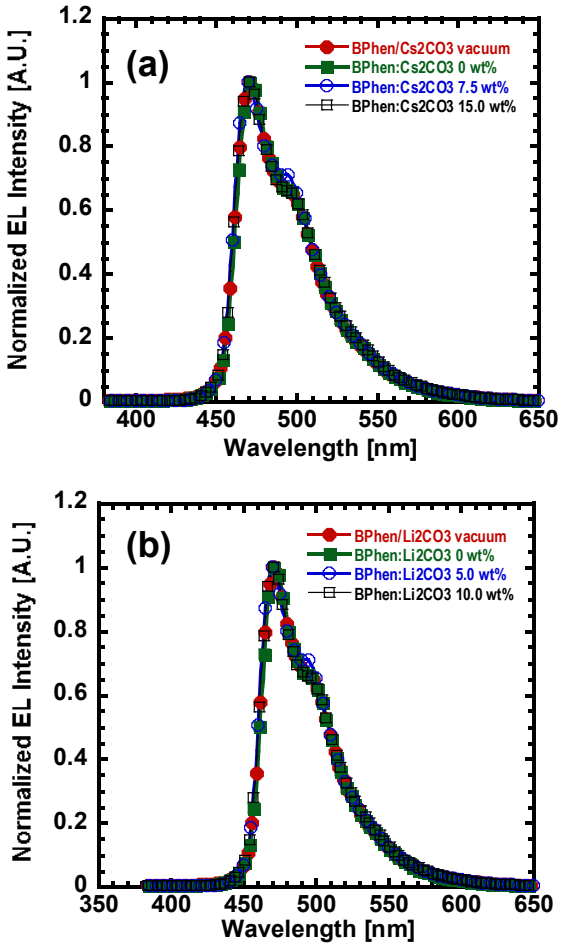

Figure 4.3. Normalized EL spectra of blue PhOLEDs with: (a) BPhen:Cs2CO3; and (b) BPhen:Li2CO3 ETLs at the maximum brightness.

A further increase of the Cs_2CO_3 concentration in BPhen:Cs_2CO_3 ETL to 12.5 and 15.0 wt% resulted in decreased device performance, even though these later PhOLEDs have similar current density (*J-V*) characteristics as the devices with 10.0 wt% Cs_2CO_3 (Figure 4.1a). PhOLEDs with 12.5 and 15.0 wt% Cs_2CO_3 –doped ETLs showed a higher turn-on and drive voltages and lower device efficiencies compared to the devices with 10.0 wt% Cs_2CO_3 (Figure 4.1b-d, Table 4.1). These later PhOLEDs (> 10% Cs_2CO_3 ETLs) also showed severe efficiency roll-off as the brightness increases, similar to the devices with vacuum-

deposited ETL/EIL. The optimum doping concentration in BPhen:Cs_2CO_3 ETLs is thus 10.0 wt% Cs_2CO_3.

The *J-V*, *L-V*, *LE-L*, and the *PE-L* characteristics of PhOLEDs with BPhen ETLs doped with Li_2CO_3 are shown in Figure 4.2. Incorporation of Li_2CO_3 in the solution-processed BPhen ETL show significantly improved device performance. PhOLED with 1.0 wt% of Li_2CO_3 showed an increased LE value of 19.8 cd A^{-1} (at 4030 cd m^{-2}) and a PE value of 5.7 lm W^{-1} (EQE of 10.1 %) compared to the device without Li_2CO_3 doping. As the Li_2CO_3 concentration increased to 2.5 and 5.0 wt%, the PhOLEDs showed much more enhanced performance. PhOLEDs with solution-deposited BPhen ETL doped with 2.5 wt% Li_2CO_3 gave a LE value of 27.1 cd A^{-1} and a PE value of 10.4 lm W^{-1} (EQE of 13.8%), while the PhOLEDs with 5.0 wt% Li_2CO_3 showed the highest device performance with an LE value of 27.9 cd A^{-1} and EQE of 14.2 % (PE = 10.1 lm W^{-1}) with significantly reduced turn-on voltage of 4.4 V and a drive voltage of 12.3 V compared to the devices without Li_2CO_3 dopant (Figure 4.2c,d, Table 4.2). However, a further increase of the Li_2CO_3 concentration to 7.5 and 10.0 wt% resulted in a decreased device performance with LE values of 26.0 and 20.7 cd A^{-1} (PE values of 9.2 and 8.0 lm W^{-1}), respectively, even though the *J-V* characteristics of these later devices were similar compared to the devices with 5.0 wt% Li_2CO_3-doped ETL (Figure 4.2a).

Similar to the PhOLEDs with BPhen:Cs_2CO_3 ETLs, PhOLEDs with solution-processed BPhen ETL doped with 2.5 - 5.0 wt% Li_2CO_3 had superior performances compare to the devices with vacuum-deposited BPhen ETL/Li_2CO_3 EIL. We also note that PhOLEDs with vacuum-deposited ETL/EIL showed the maximum LE value (23.0 cd A^{-1}) and PE value (11.8 lm W^{-1}) at low brightness (~ 120 cd m^{-2}), whereas the devices with solution-processed ETL doped with Li_2CO_3 showed the highest efficiency at high brightness (1720 - 4340 cd m^{-2}). These results

clearly demonstrate that the solution-processing of ETL doped with alkali metal salt is a promising strategy to achieve high-performance blue PhOLEDs with high brightness. The device characteristics of the blue PhOLEDs with solution-processed BPhen ETL are summarized in Table 4.1 and 4.2.

Table 4.1. Device chracteristics of solution-processesd PhOLEDs with BPhen ETL doped with Cs_2CO_3. [a]

ETL[b]	Dopant concentration [wt%]	V_{on}[d] [V]	Drive voltage [V]	Current density [mA cm^{-2}]	Luminance [cd m^{-2}]	Device efficiency [cd A^{-1}, lm W^{-1}, (%EQE)]
BPhen	0.0	7.7	16.4 *12.6*	133.4 *11.5*	11200 *1890*	8.4, 1.6, (4.3) *16.5, 4.1, (8.4)*
BPhen: Cs_2CO_3	2.5	4.8	13.9 *10.2*	108.9 *13.6*	14800 *3600*	13.6, 3.0, (6.9) *26.4, 8.5, (13.5)*
BPhen: Cs_2CO_3	5.0	4.8	13.2 *8.9*	107.5 *9.0*	14600 *2530*	13.6, 3.2, (6.9) *28.1, 10.5, (14.3)*
BPhen: Cs_2CO_3	7.5	4.6	12.8 *8.7*	103.3 *10.2*	18200 *3520*	17.6, 4.3, (8.9) *34.7, 13.1, (17.7)*
BPhen: Cs_2CO_3	10.0	4.5	12.6 *7.8*	144.3 *5.2*	20100 *1820*	13.9, 3.4, (7.0) *35.1, 15.0, (17.9)*
BPhen: Cs_2CO_3	12.5	4.8	12.4 *7.5*	177.5 *6.0*	17700 *1360*	9.6, 2.5, (4.9) *22.9, 9.6, (11.7)*
BPhen: Cs_2CO_3	15.0	4.9	13.6 *7.6*	187.8 *4.2*	15100 *830*	8.0, 1.9, (4.0) *19.6, 8.1, (10.0)*
BPhen / Cs_2CO_3 [c]	-	5.5	15.1 *7.6*	112.6 *1.2*	13400 *320*	11.9, 2.5, (6.1) *26.9, 11.7, (13.7)*

[a] Values in italic correspond to those at maximum device efficiencies. [b] PhOLEDs with solution-deposited BPhen ETL doped with Cs_2CO_3 or with vacuum-deposited BPhen/Cs_2CO_3 ETL/EIL. Device structures: ITO/PEDOT:PSS/EML/ETL/Al with solution-deposited doped BPhen ETL; and [c] ITO/PEDOT:PSS/EML/BPhen/Cs_2CO_3/Al with vacuum-deposited BPhen and Cs_2CO_3. [d] Turn-on voltage (at brightness of 1 cd m^{-2}).

Table 4.2. Device chracteristics of solution-processed PhOLEDs with BPhen ETL doped with Li_2CO_3.[a]

ETL[b]	Dopant concentration [wt%]	V_{on}[d] [V]	Drive voltage [V]	Current density [mA cm^{-2}]	Luminance [cd m^{-2}]	Device efficiency [cd A^{-1}, lm W^{-1}, (%EQE)]
BPhen	0.0	7.7	16.4 *12.6*	133.4 *11.5*	11200 *1890*	8.4, 1.6, (4.3) *16.5, 4.1, (8.4)*
BPhen: Li_2CO_3	1.0	5.5	14.8 *11.4*	148.4 *20.4*	15700 *4030*	10.6, 2.5, (5.4) *19.8, 5.7, (10.1)*
BPhen: Li_2CO_3	2.5	5.4	13.8 *9.1*	162.9 *6.4*	17800 *1720*	11.0, 2.5, (5.6) *27.1, 10.4, (13.8)*
BPhen: Li_2CO_3	5.0	4.4	12.3 *8.9*	100.8 *12.8*	14500 *3600*	14.5, 3.7, (7.4) *27.9, 10.1, (14.2)*
BPhen: Li_2CO_3	7.5	4.5	12.5 *9.2*	120.0 *16.7*	15600 *4340*	13.0, 3.3, (6.6) *26.0, 9.2, (13.2)*
BPhen: Li_2CO_3	10.0	4.6	12.5 *8.4*	162.2 *11.7*	15800 *2430*	9.8, 2.5, (5.0) *20.7, 8.0, (10.6)*
BPhen / Li_2CO_3 [c]	-	4.6	14.7 *6.5*	163.9 *0.52*	13400 *120*	8.1, 1.7, (4.1) *23.0, 11.7, (11.7)*

[a] Values in italic correspond to those at maximum device efficiencies. [b] PhOLEDs with solution-deposited BPhen ETL doped with Li_2CO_3 or with vacuum-deposited BPhen/Li_2CO_3 ETL. Device structures: ITO/PEDOT:PSS/EML/ETL/Al with solution-deposited doped BPhen ETL; and [c] ITO/PEDOT:PSS/EML/BPhen/Li_2CO_3/Al with vacuum-deposited BPhen and Li_2CO_3. [d] Turn-on voltage (at brightness of 1 cd m^{-2}).

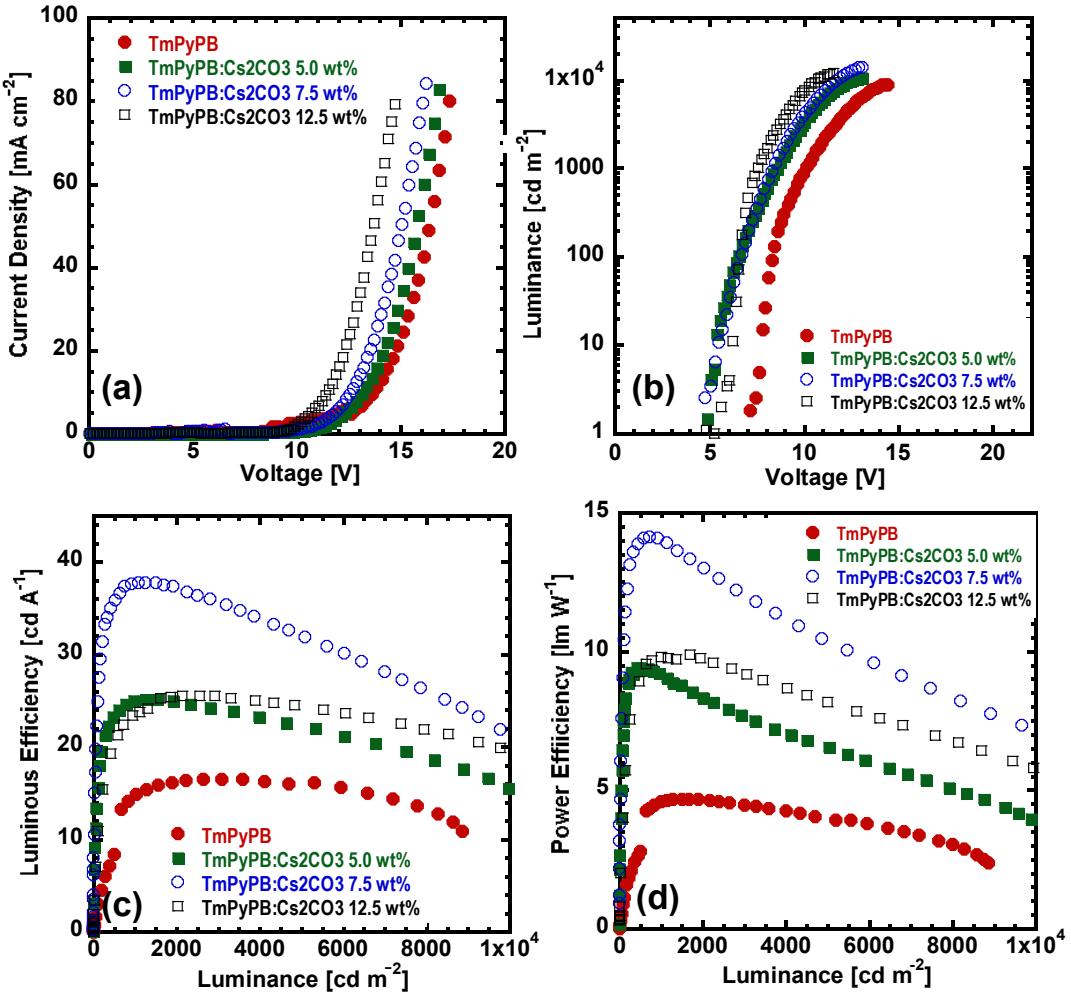

Figure 4.4. Blue PhOLEDs with TmPyPB ETL doped with Cs_2CO_3: (a) Current density (*J*) – voltage (*V*); (b) luminance (*L*) - voltage (*V*); (c) luminous efficiency (*LE*) - luminance (*L*); and (d) power efficiency (*PE*) - luminance (*L*) curves. Device structures: ITO/PEDOT:PSS(30 nm)/EML(70 nm)/solution-processed TmPyPB:Cs_2CO_3 ETL(20 nm)/Al (100 nm), TmPyPB ETL doped with different concentration of Cs_2CO_3.

The electroluminescence (EL) spectra of all the blue PhOLEDs, including those containing BPhen:Cs_2CO_3 or BPhen:Li_2CO_3 ETLs, are identical in lineshape with a maximum peak at 472 nm, which originates from the FIrpic blue triplet emitter (Figure 4.3).[26,27] The Commission Internationale de L'Eclairage (CIE) 1931 coordinates of the devices were identical at (0.14, 0.28).

We observed a slight increase of the vibronic shoulder around 500 nm in the case of PhOLEDs with solution-processed BPhen ETLs doped with 7.5 wt% Cs_2CO_3 and 5.0 wt% Li_2CO_3, which can be due to microcavity effects.[38]

PhOLEDs with various small-molecule ETMs doped with Cs_2CO_3. To test how general our approach of solution-processing of alkali metal salt doped electron transport materials is, we investigated various other known electron transport materials, including 1,3,5-tris(4-pyridinquinolin-2-yl)benzene (TPyQB),[30] 1,3,5-tris(*m*-pyrid-3-yl-phenyl)benzene (TmPyPB),[56,57] and 1,3-bis(3,5-di(pyridine-3-yl)phenyl)benzene (BmPyPB).[58] The solution-processed ETL was doped with 5.0, 7.5, or 12.5 wt% Cs_2CO_3 and incorporated into multilayered blue PhOLEDs similar to BPhen:Cs_2CO_3 ETL devices described above.

Electron-transport materials with pyridyl groups were reported by Kido and co-workers [44,45] as high triplet energy ETMs. For example, TmPyPB was reported to have a high triplet energy of 2.78 eV and a high electron mobility of μ_e = 1.0 x 10^{-3} cm^2 $V^{-1}s^{-1}$. As shown in Figure 4.4, the PhOLEDs with undoped TmPyPB had a much lower performance (LE = 16.5 cd A^{-1}, PE = 4.7 lm W^{-1}, and EQE = 8.4 %), whereas Cs_2CO_3-doped TmPyPB ETL led to a large enhancement of device performance. In Figure 4.4, the performance of PhOLEDs with TmPyPB:Cs_2CO_3 (7.5 wt%) ETL showed a LE value of 37.7 cd A^{-1} (PE = 14.1 lm W^{-1}, EQE = 19.0 %), which is the highest performance reported to date for all-solution-processed blue PhOLEDs. We also fabricated PhOLEDs with solution-processed BmPyPB:Cs_2CO_3 ETLs and, as expected, the PhOLEDs with BmPyPB ETL doped with Cs_2CO_3 similarly had a large enhancement in performance compared to non-doped ETL devices. The devices with BmPyPB ETL doped with 7.5 wt% Cs_2CO_3 showed an LE value of 37.4 cd A^{-1} at a high brightness of 1760 cd m^{-2}, and a PE value of 16.1 lm W^{-1} (with an EQE of 19.0 %). The performance of blue PhOLEDs

incorporating BmPyPB:Cs_2CO_3 ETL at the optimum doping concentration of 7.5 wt% Cs_2CO_3 is essentially identical with that of devices incorporating TmPyPB:Cs_2CO_3 at the same doping concentration. Further increase of the Cs_2CO_3 concentration in the TmPyPB:Cs_2CO_3 and BmPyPB:Cs_2CO_3 ETLs resulted in decreased performance of the PhOLEDs (Figure 4.4) and these trends are very similar to those of PhOLEDs incorporating BPhen:Cs_2CO_3 ETLs.

These results demonstrate that the solution-processing of ETL doped with alkali metal salt is applicable to various small-molecule electron-transport materials[31] of current interest for the

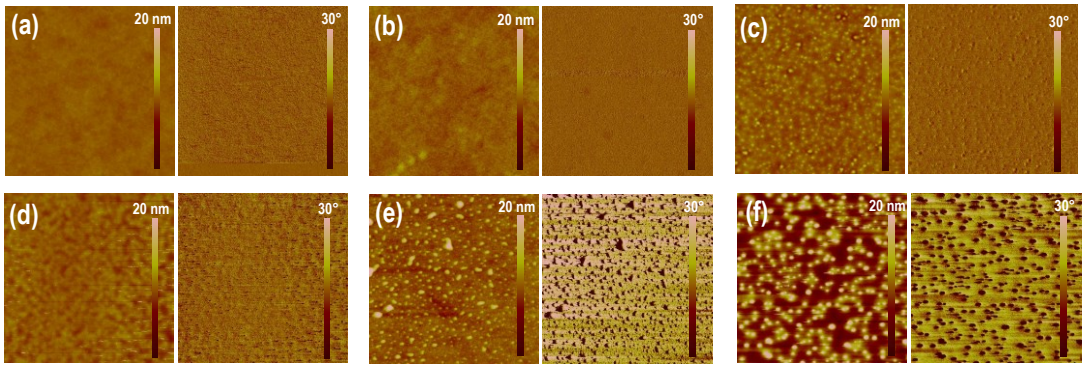

Figure 4.3. AFM topographical height images (left, 5μm × 5μm) and the corresponding phase images (right, 5μm × 5μm) of solution-processed BPhen ETL films doped with different concentration of Cs_2CO_3: (a) 0 wt%; (b) 5.0 wt%; (c) 7.5 wt%; (d) 10.0 wt%; (e) 12.5 wt%; and (f) 15.0 wt%.

fabrication of all-solution-processed multilayered OLEDs and other organic electronic devices. Among the four electron-transport materials investigated, blue PhOLEDs with solution-processed TmPyPB:Cs_2CO_3 ETLs and BmPyPB:Cs_2CO_3 ETLs have the best performance and thus TmPyPB and BmPyPB are superior to BPhen and TPyQB in this respect. We can also conclude that Cs_2CO_3 is superior to Li_2CO_3 as an alkali metal salt dopant of the series of small-molecule electron-transport materials.

Surface morphology of doped BPhen ETLs. The surface morphology of solution-deposited alkali metal salt-doped ETLs was investigated by atomic force microscopy (AFM). Figure 4.5 shows AFM topographical height and the corresponding phase images of solution-deposited BPhen ETLs with different concentrations of Cs_2CO_3. BPhen ETL without Cs_2CO_3 doping has a smooth surface with root-mean-square (RMS) roughness of 0.312 nm (Figure 4.5a) whereas the solution-deposited Cs_2CO_3-doped BPhen ETLs show a significant change in surface morphology as the Cs_2CO_3 concentration increases (Figure 4.5b-f). BPhen ETLs with 5.0 and 7.5 wt%

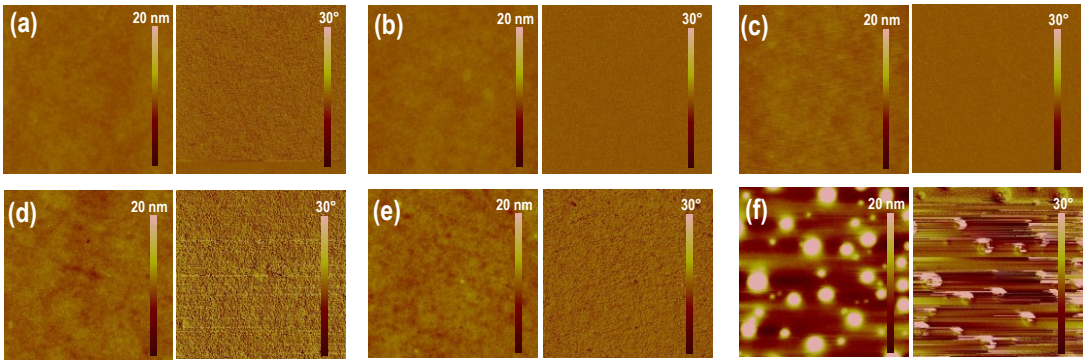

Figure 4.4. AFM topographical height images (left, 5 µm × 5 µm) and the corresponding phase images (right, 5µm × 5µm) of solution-processed BPhen ETL films doped with different concentration of Li_2CO_3: (a) 0 wt%; (b) 1.0 wt%; (c) 2.5 wt%; (d) 5.0 wt%; (e) 7.5 wt%; and (f) 10.0 wt%.

Cs_2CO_3 have rougher surfaces (RMS values = 0.570 and 0.840 nm) compared to the BPhen ETL without Cs_2CO_3 doping (Figure 4.5b,c). As the Cs_2CO_3 concentration increases to 10.0 wt%, the ETL surface morphology becomes even much rougher, having an RMS roughness value of 1.12 nm (Figure 4.5d). In the light of the surface morphology variation with Cs_2CO_3 concentration in the ETL, we suggest that in addition to n-doping effects of the alkali metal salt, the surface roughness of the solution-processed ETL, which enhances the ETL/Al contact area and thus facilitates efficient electron-injection. According to our previous reports, the rough surface morphology and vertical nanopillars formed in the solution-processed ETL leads to enhanced

charge transport in the vertical direction and also provide good contact between ETL and Al cathode for facile electron-injection.[29-31]

On the other hand, BPhen ETLs with a high Cs_2CO_3 concentration of 12.5 and 15.0 wt% have extremely rough surfaces with RMS roughness values of 2.53 and 5.53 nm (Figure 5.5e and 4.5f). At these high concentrations a clear phase separation in the BPhen:Cs_2CO_3 blend appears to occur and explains the observed decrease in device performance at high (> 10.0 wt%) Cs_2CO_3 concentrations. A significantly decreased charge-injection from cathode and charge-transport in the ETL can be expected when a separate insulating Cs_2CO_3 phase emerges in the ETL.

A similar trend was observed in the solution-processed BPhen ETLs doped with Li_2CO_3. A smooth surface was observed in the AFM images of the solution-deposited BPhen ETL without the dopant (RMS value = 0.312 nm, Figure 4.6a) and the BPhen ETL doped with 1.0 wt% Li_2CO_3 (RMS value = 0.331 nm, Figure 4.6b), whereas BPhen ETLs doped with 2.5 (Figure 4.6c) and 5.0 wt% (Figure 5.6d) showed increased surface roughness with RMS values of 0.477 and 0.581 nm, respectively. The increased surface roughness is consistent with the improved performance of PhOLEDs with ETLs at these doping levels. However, solution-processed BPhen ETL at a higher concentration (10.0 wt% Li_2CO_3) showed severe phase-separated surface morphology (Figure 4.6f). We can also understand the decreased performance of devices with BPhen ETLs doped at 10.0 wt% Li_2CO_3 as a consequence of such a phase-separated surface morphology. The observed surface morphology variation with alkali metal salt concentration in the doped ETL correlates very well with a similar observed variation of device performance with concentration of the alkali metal salt.

Electron- and hole-dominant devices. To further investigate the charge-injection and transport properties in PhOLEDs containing solution-processed ETL doped with alkali metal salts

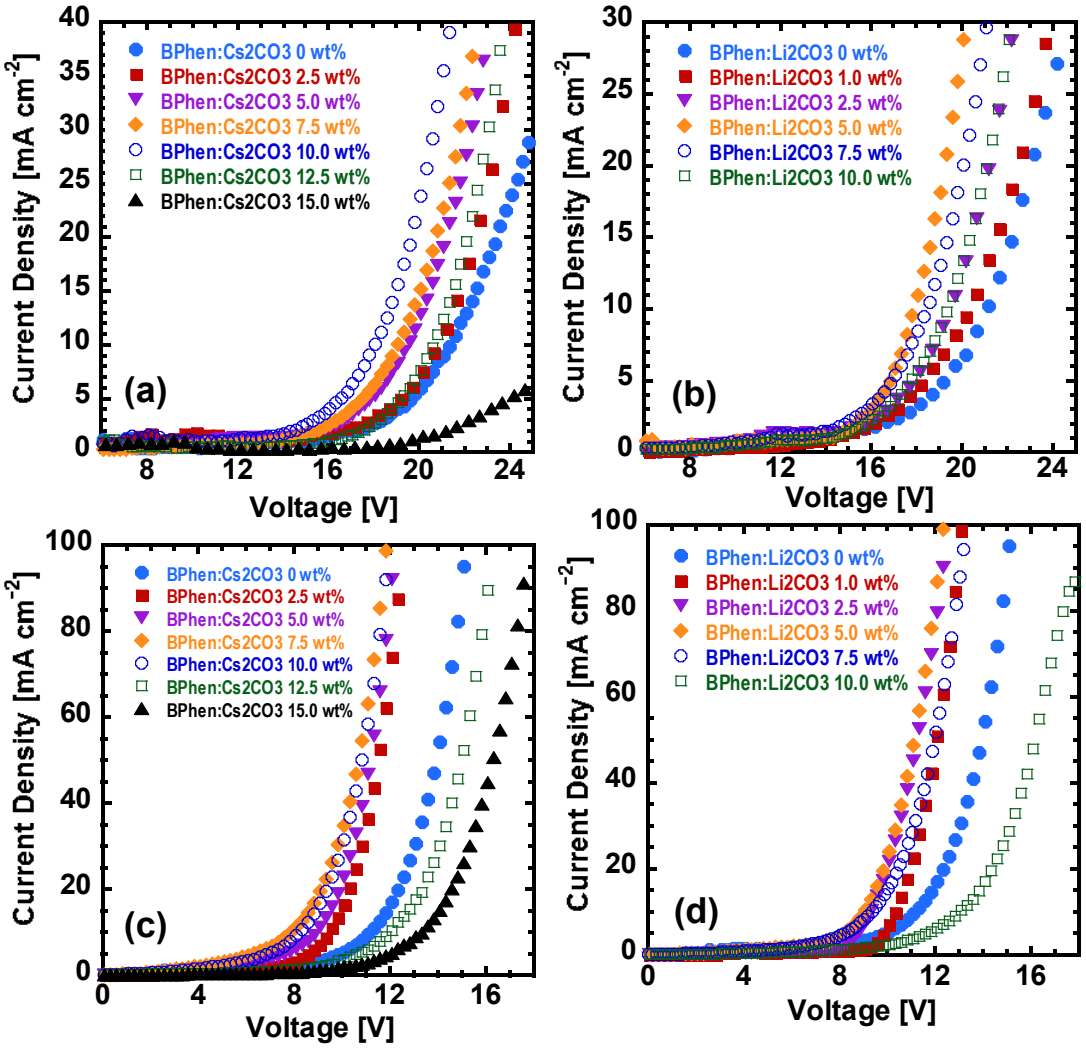

Figure 4.5. Single charge-carrier dominant devices: (a) electron-dominant devices with solution-processed BPhen:Cs_2CO_3 ETLs; (b) electron-dominant devices with solution-processed BPhen:Li_2CO_3 ETLs; (c) hole-dominant devices with solution-processed BPhen:Cs_2CO_3 ETLs; and (d) hole-dominant devices with solution-processed BPhen:Li_2CO_3 ETLs. Device structures of electron-dominant devices: ITO/polymer host(70 nm)/solution-processed BPhen:Cs_2CO_3 ETL (20 nm)/Al; and hole-dominant devices: ITO/PEDOT:PSS(30 nm)/polymer host(70 nm)/ solution-processed BPhen:Li_2CO_3 ETL (20 nm)/Au.

(M_2CO_3, M = Cs, Li), two types of single-carrier dominant devices were fabricated, including electron-dominant devices, ITO/polymer host (70 nm)/solution-deposited BPhen:M_2CO_3 ETL

(20nm)/Al, and hole-dominant devices, ITO/PEDOT:PSS (30 nm)/polymer host (70 nm)/solution-deposited BPhen:M_2CO_3 ETL (20 nm)/Au. The polymer host consisted of PVK and OXD-7 with the same ratio of 6:4 as in the PhOLEDs, except that the blue triplet emitter FIrpic was excluded. It is assumed that hole-injection from the ITO can be suppressed by the large energy barrier between the work function of ITO (Φ_f= ~ 4.5 eV) and the ionization potential (IP) values of the polymer host (5.8 eV for PVK and 6.2 eV for OXD-7) in the electron-dominant devices. Similarly, electron-injection can be prevented by the energy barrier between the work function of Au (Φ_f = 5.0 eV) and the electron affinity (EA) of BPhen (3.0 eV) in the hole-dominant devices.

Figure 4.7 shows the single charge carrier-dominant devices with solution-processed BPhen:M_2CO_3 ETL with varying concentration of the M_2CO_3 dopants (M = Cs, Li). The *J-V* characteristics of the electron-dominant devices with solution-processed BPhen ETL doped with Cs_2CO_3 and Li_2CO_3 are shown in Figure 4.7a and 4.7b, respectively. A significant increase of the current density was observed when the BPhen ETL was doped by the alkali metal salt in electron-dominant devices. As shown by the highest current densities, the electron-injection and transport was the most efficient when the Cs_2CO_3 and Li_2CO_3 doping concentrations were 10.0 wt% and 5.0 wt%, respectively. This trend matches well with the observed highest performance of PhOLEDs with BPhen doped with alkali metal salt. These results imply that electron-injection and transport are enhanced by incorporating alkali metal salt into the ETL, achieving the maximum current density at optimum concentration of the alkali metal salt. However, further increase of the M_2CO_3 dopant concentration (12.5 and 15.0 wt% for Cs_2CO_3, 7.5 and 10.0 wt% for Li_2CO_3) results in decrease of the current density. The trend also matches with the observed decrease PhOLED performance at the higher doping levels, presumably due to the phase

separation in the solution-processed BPhen:M_2CO_3 blend ETLs which interrupts facile electron-injection and transport.

The *J-V* characteristics of the hole-dominant devices containing the solution-processed BPhen ETL doped with Cs_2CO_3 and Li_2CO_3 are shown in Figure 4.7c and 4.7d, respectively. The trends are similar to those for electron-dominant devices in that increased current density is seen with incorporation of alkali metal salt doped ETL. It has been reported that devices with BPhen ETL doped with Li_2CO_3 by vacuum co-deposition showed reduced hole-current as the dopant concentration increased.[50] In contrast, the solution-processed BPhen ETL doped with alkali metal salt show enhanced hole-current and this can be understood to result from a good contact between the ETL and Au electrode enabled by solution-processing. This result implies that the strategy applied to improve charge-injection and transport by tuning the surface morphology of the ETMs to improve the interfacial contact between the ETL and metal cathode is

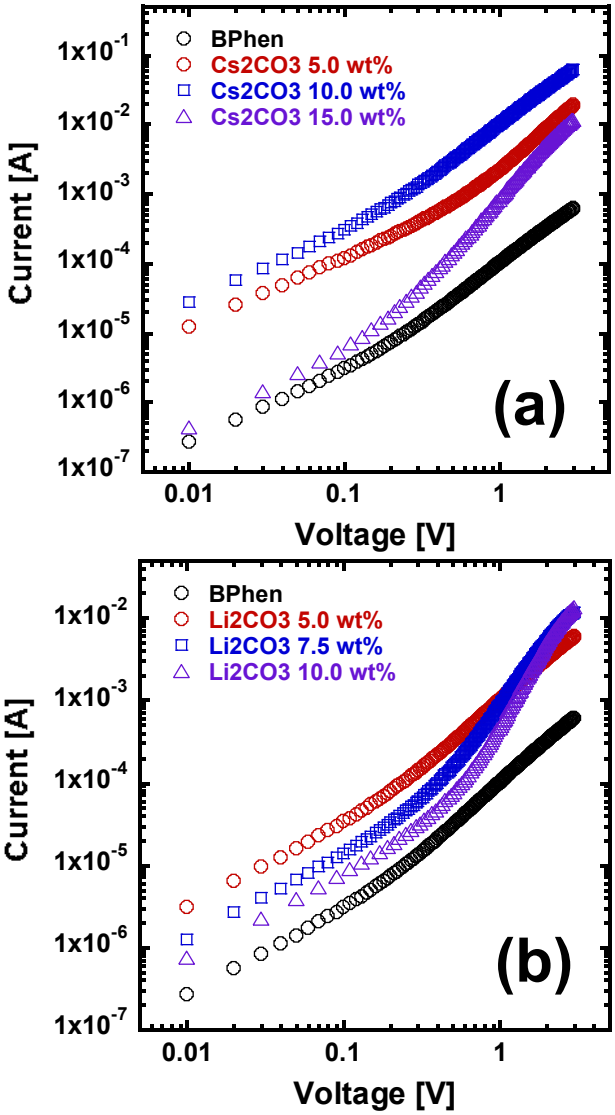

Figure 4.6. Current-voltage (*I-V*) characteristics of ITO/solution-processed BPhen:alkali metal salt dopant film (~200 nm)/Al devices in ambient conditions. (a) BPhen doped with different concentration of Cs_2CO_3; and (b) Li_2CO_3.

not limited to Al, but can also be applied to other metal electrodes. However, the current density of the hole-dominant devices is severely reduced at higher concentrations of the dopant (Cs_2CO_3 = 12.5 - 15.0 wt%, Li_2CO_3 = 10.0 wt%), presumably due to the reduced charge-injection and transport when phase separation occurs in the BPhen:M_2CO_3 blend ETL. This means that for a given electron-transport material there is an optimum alkali metal salt doping level for maximum PhOLED performance.

Space-charge-limited current (SCLC) measurement of solution-processed BPhen ETLs.

We investigated the electron transport properties of the solution-processed alkali metal salt doped BPhen ETL films by space-charge-limited current (SCLC) measurement. The current-voltage (*I-V*) characteristics of the SCLC devices with the structure of ITO/ETL(~200 nm)/Al, are shown in Figure 4.8. The BPhen:M_2CO_3 blend ETLs were spin coated from FA:H_2O (3:1) solutions with different concentrations of the alkali metal salts to form ~ 200-nm thick layers, which were vacuum dried overnight at 50°C followed by Al deposition. The thickness of the BPhen ETLs was measured by a profilometer and also confirmed by AFM measurement. The electron mobility was extracted by fitting the *J-V* curves in the near quadratic region according to the modified Mott-Gurney equation,[59,60]

$$J = \frac{9}{8}\,\varepsilon\varepsilon_0\mu\frac{V^2}{L^3}exp\left(0.89\beta\frac{\sqrt{V}}{\sqrt{L}}\right)$$

where J is the current density, ε_0 is the permittivity of free space, ε is the relative permittivity, μ is the zero-field mobility, V is the applied voltage, L is the thickness of active layer, and β is the field-activation factor (Table 5.3). The zero-field electron mobility of the solution-deposited BPhen:M_2CO_3 blend films varied from 4.2×10^{-5} cm^2 V^{-1} s^{-1} without doping, which is consistent with the reported value by SCLC measurement,[55] to 3.7×10^{-3} cm^2 V^{-1} s^{-1} when the doping concentration is 10.0 wt% Cs_2CO_3 (Figure 5.8a, Table 5.3). The electron mobility of BPhen with

10.0 wt% Cs_2CO_3 was an order of magnitude higher than that with 5.0 wt% Cs_2CO_3 and two orders of magnitude higher than the non-doped BPhen. Similarly, BPhen doped with 2.5 – 5.0 wt% Li_2CO_3 had two orders of magnitude higher mobility (1.3×10^{-3} cm^2 V^{-1} s^{-1}) than that of non-doped BPhen.

However, further increase of the doping concentration to 15.0 wt% for Cs_2CO_3 and 10.0 wt% for Li_2CO_3, resulted in the electron mobilities dropping to 1.8×10^{-5} and 7.5×10^{-5} cm^2 V^{-1} s^{-1}, respectively. Interestingly, *I-V* curves of the SCLC devices with the highest doping concentrations (15.0 wt% Cs_2CO_3, 7.5 - 10.0 wt% Li_2CO_3) showed steep slopes at high electric field, implying that the current increases faster than V^2. These curvatures indicate the presence of charge trapping sites, which likely originate from the phase separated morphology of the solution-processed BPhen:M_2CO_3 blend ETLs.[61,62]

Table 4.3. SCLC electron mobility of BPhen ETL at various doping levels.

Dopant	concentration [wt%]	L [nm]	β [$cm^{1/2}$ $V^{-1/2}$]	E_{max} [V cm^{-1}]	μ_e ($E=0$) [cm^2 V^{-1} s^{-1}]
None	0	200	8.7×10^{-6}	1.8×10^5	4.2×10^{-5}
Cs_2CO_3	5.0	200	6.8×10^{-7}	1.8×10^5	5.6×10^{-4}
Cs_2CO_3	10.0	200	8.3×10^{-6}	1.8×10^5	3.7×10^{-3}
Cs_2CO_3	15.0	200	4.9×10^{-5}	1.8×10^5	1.8×10^{-5}
Li_2CO_3	5.0	200	1.3×10^{-5}	1.5×10^5	1.3×10^{-3}
Li_2CO_3	7.5	200	1.1×10^{-5}	1.5×10^5	1.0×10^{-3}
Li_2CO_3	10.0	190	1.5×10^{-5}	1.6×10^5	7.4×10^{-5}

4.1.4. Conclusions

We have showed for the first time that alkali metal salt doped electron-transport layers (ETLs) can be solution-deposited to fabricate high performance, multi-layered, phosphorescent OLEDs. The solution-processing approach is applicable to diverse electron-transport materials and any desirable metal salt. Blue PhOLEDs with solution-deposited Cs_2CO_3-doped TmPyPB ETLs have a luminous efficiency of 37.7 cd A^{-1} with an EQE of 19.0 % at a high brightness 1300 cd m^{-2}, which is the highest performance reported to date for all-solution-processed blue PhOLEDs. Studies of the surface morphology and electron transport properties of the alkali metal salt doped electron transport layers showed that doping dramatically enhances the electron mobility and modifies the ETL/cathode interface morphology, enabling efficient electron-injection and transport. The results demonstrated that the properties and nanomorphology of the solution-processed ETLs can be fine-tuned by the concentration of the metal salt (M_2CO_3) and type of metal (M = Cs, Li). The orthogonal solution-processing of multilayered high performance PhOLEDs and metal salt-doped ETLs demonstrated here are also useful for the fabrication of other multi-layered organic electronic devices.

4.1.5. References

[1] A. P. Kulkarni, C. J. Tonzola, A. Babel, S. A. Jenekhe, *Chem. Mater.* **2004**, *16*, 4556.

[2] F. So, J. Kido, P. Burrows, *MRS Bull.* **2008**, *33*, 663.

[3] A. C. Grimsdale, K. Leok Chan, R. E. Martin, P. G. Jokisz, A. B. Holmes, *Chem. Rev.* **2009**, *109*, 897.

[4] S. Reineke, F. Lindner, G. Schwartz, N. Seidler, K. Walzer, B. Lussem, K. Leo, *Nature* **2009**, *459*, 234.

[5] K. T. Kamtekar, A. P. Monkman, M. R. Bryce, *Adv. Mater.* **2010**, *22*, 572.

[6] Y. Kawamura, S. Yanagida, S. R. Forrest, *J. Appl. Phys.* **2002**, *92*, 87.

[7] C.-H. Yang, Y.-M. Cheng, Y. Chi, C.-J. Hsu, F.-C. Fang, K.-T. Wong, P.-T. Chou, C.-H. Chang, M.-H. Tsai, C.-C. Wu, *Angew. Chem. Int. Ed.* **2007**, *46*, 2418.

[8] T. Earmme, E. Ahmed, S. A. Jenekhe, *J. Phys. Chem. C* **2009**, *113*, 18448.

[9] E. Ahmed, T. Earmme, G. Ren, S. A. Jenekhe, *Chem. Mater.* **2010**, *22*, 5786.

[10] A. Endo, K. Sato, K. Yoshimura, T. Kai, A. Kawada, H. Miyazaki, C. Adachi, *Appl. Phys. Lett.* **2011**, *98*, 083302.

[11] Y. Zhang, C. Zuniga, S.-J. Kim, D. Cai, S. Barlow, S. Salman, V. Coropceanu, J.-L. Brédas, B. Kippelen, S. Marder, *Chem. Mater.* **2011**, *23*, 4002.

[12] S. C. Lo, R. N. Bera, R. E. Harding, P. L. Burn, I. D. W. Samuel, *Adv. Funct. Mater.* **2008**, *18*, 3080.

[13] B. Ma, B. J. Kim, D. A. Poulsen, S. J. Pastine, J. M. J. Fréchet, *Adv. Funct. Mater.* **2009**, *19*, 1024.

[14] J.-H. Jou, W.-B. Wang, S.-M. Shen, S. Kumar, I. M. Lai, J.-J. Shyue, S. Lengvinaite, R. Zostautiene, J. V. Grazulevicius, S. Grigalevicius, S.-Z. Chen, C.-C. Wu, *J. Mater. Chem.* **2011**, *21*, 9546.

[15] K. S. Yook, J. Y. Lee, *Org. Electron.* **2011**, *12*, 1595.

[16] M. Zhu, T. Ye, X. He, X. Cao, C. Zhong, D. Ma, J. Qin, C. Yang, *J. Mater. Chem.* **2011**, *21*, 9326.

[17] A. C. Arias, J. D. MacKenzie, I. McCulloch, J. Rivnay, A. Salleo, *Chem. Rev.* **2010**, *110*, 3.

[18] F. S. Kim, E. Ahmed, S. Subramaniyan, S. A. Jenekhe, *ACS Appl. Mater. Interfaces* **2010**, *2*, 2974.

[19] S. Sax, N. Rugen-Penkalla, A. Neuhold, S. Schuh, E. Zojer, E. J. W. List, K. Mullen, *Adv. Mater.* **2010**, *22*, 2087.

[20] F. S. Kim, D.-K. Hwang, B. Kippelen, S. A. Jenekhe, *Appl. Phys. Lett.* **2011**, *99*, 173303.

[21] Z.-Y. Liu, S.-R. Tseng, Y.-C. Chao, C.-Y. Chen, H.-F. Meng, S.-F. Horng, Y.-H. Wu, S.-H. Chen, *Synth. Met.* **2011**, *161*, 426.

[22] X. J. Zhang, A. S. Shetty, S. A. Jenekhe, *Macromolecules* **1999**, *32*, 7422.

[23] X. J. Zhang, S. A. Jenekhe, *Macromolecules* **2000**, *33*, 2069.

[24] M. M. Alam, S. A. Jenekhe, *Chem. Mater.* **2002**, *14*, 4775.

[25] C. J. Tonzola, M. M. Alam, W. Kaminsky, S. A. Jenekhe, *J. Am. Chem. Soc.* **2003**, *125*, 13548.

[26] T. W. Kwon, M. M. Alam, S. A. Jenekhe, *Chem. Mater.* **2004**, *16*, 4657.

[27] S. A. Jenekhe, S. J. Yi, *Appl. Phys. Lett.* **2000**, *77*, 2635.

[28] M. M. Alam, S. A. Jenekhe, *Chem. Mater.* **2004**, *16*, 4647.

[29] T. Earmme, E. Ahmed, S. A. Jenekhe, *Adv. Mater.* **2010**, *22*, 4744.

[30] E. Ahmed, T. Earmme, S. A. Jenekhe, *Adv. Funct. Mater.* **2011**, *21*, 3889.

[31] T. Earmme, S. A. Jenekhe, *J. Mater. Chem.* **2012**, *22*, 4660.

[32] A. G. Werner, F. Li, K. Harada, M. Pfeiffer, T. Fritz, K. Leo, *Appl. Phys. Lett.* **2003**, *82*, 4495.

[33] C. K. Chan, W. Zhao, S. Barlow, S. Marder, A. Kahn, *Org. Electron.* **2008**, *9*, 575.

[34] N. Cho, H.-L. Yip, S. K. Hau, K.-S. Chen, T.-W. Kim, J. A. Davies, D. F. Zeigler, A. K. Y. Jen, *J. Mater. Chem.* **2011**, *21*, 6956.

[35] J. Meyer, M. Kröger, S. Hamwi, F. Gnam, T. Riedl, W. Kowalsky, A. Kahn, *Appl. Phys. Lett.* **2010**, *96*, 193302.

[36] K. S. Yook, S. O. Jeon, S.-Y. Min, J. Y. Lee, H.-J. Yang, T. Noh, S.-K. Kang, T.-W. Lee, *Adv. Funct. Mater.* **2010**, *20*, 1797.

[37] K. Walzer, B. Maennig, M. Pfeiffer, K. Leo, *Chem. Rev.* **2007**, *107*, 1233.

[38] D. M. Ivory, G. G. Miller, J. M. Sowa, L. W. Shacklette, R. R. Chance, R. H. Baughman, *The Journal of Chemical Physics* **1979**, *71*, 1506.

[39] J. Kido, K. Nagai, Y. Okamoto, *IEEE Trans. Electron Devices* **1993**, *40*, 1342.

[40] L. S. Hung, C. W. Tang, M. G. Mason, *Appl. Phys. Lett.* **1997**, *70*, 152.

[41] T. Mori, H. Fujikawa, S. Tokito, Y. Taga, *Appl. Phys. Lett.* **1998**, *73*, 2763.

[42] C. K. Chan, F. Amy, Q. Zhang, S. Barlow, S. Marder, A. Kahn, *Chem Phys Lett* **2006**, *431*, 67.

[43] C. J. Bloom, C. M. Elliott, P. G. Schroeder, C. B. France, B. A. Parkinson, *The Journal of Physical Chemistry B* **2003**, *107*, 2933.

[44] A. G. Werner, F. Li, K. Harada, M. Pfeiffer, T. Fritz, K. Leo, *Appl. Phys. Lett.* **2003**, *82*, 4495.

[45] F. Li, A. Werner, M. Pfeiffer, K. Leo, X. Liu, *The Journal of Physical Chemistry B* **2004**, *108*, 17076.

[46] T. Hasegawa, S. Miura, T. Moriyama, T. Kimura, I. Takaya, Y. Osato, H. Mizutani, *SID Symposium Digest of Technical Papers* **2004**, *35*, 154.

[47] C. Wu, C. Lin, Y. Chen, M. Chen, Y. Lu, C. Wu, *Appl. Phys. Lett.* **2006**, *88*, 152104.

[48] Y. Cai, H. X. Wei, J. Li, Q. Y. Bao, X. Zhao, S. T. Lee, Y. Q. Li, J. X. Tang, *Appl. Phys. Lett.* **2011**, *98*, 113304.

[49] Y. Vaynzof, D. Kabra, L. L. Chua, R. H. Friend, *Appl. Phys. Lett.* **2011**, *98*, 113306.

[50] P. Kao, J. Lin, J. Wang, C. Yang, S. Chen, *J. Appl. Phys.* **2011**, *109*, 094505.

[51] M.-H. Chen, Y.-J. Lu, Y.-J. Chang, C.-C. Wu, C.-I. Wu, *Electrochem. Solid-State Lett.* **2010**, *13*, H203.

[52] K. R. Choudhury, J.-H. Yoon, F. So, *Adv. Mater.* **2008**, *20*, 1456.

[53] D. O'Brien, M. A. Baldo, M. E. Thompson, S. R. Forrest, *Appl. Phys. Lett.* **1999**, *74*, 442.

[54] S. Naka, H. Okada, H. Onnagawa, T. Tsutsui, *Appl. Phys. Lett.* **2000**, *76*, 197.

[55] M. A. Khan, W. Xu, H. Khizar ul, Y. Bai, X. Y. Jiang, Z. L. Zhang, W. Q. Zhu, *J. Appl. Phys.* **2008**, *103*, 014509.

[56] S.-J. Su, T. Chiba, T. Takeda, J. Kido, *Adv. Mater.* **2008**, *20*, 2125.

[57] S.-J. Su, Y. Takahashi, T. Chiba, T. Takeda, J. Kido, *Adv. Funct. Mater.* **2009**, *19*, 1260.

[58] S.-J. Su, E. Gonmori, H. Sasabe, J. Kido, *Adv. Mater.* **2008**, *20*, 4189.

[59] N. F. Mott, D. Gurney, *Electronic Processes in Ionic Crystals*. 2nd ed.; University Press: Oxford, 1948.

[60] P. N. Murgatroyd, *J. Phys. D: Appl. Phys.* **1970**, *3*, 1488.

[61] M. A. Lampert, *Phys. Rev.* **1956**, *103*, 1648.

[62] S. Jain, *J. Appl. Phys.* **2001**, *89*, 3804.

[63] J. Zou, H. Wu, C.-S. Lam, C. Wang, J. Zhu, C. Zhong, S. Hu, C.-L. Ho, G.-J. Zhou, H. Wu, W. C. H. Choy, J. Peng, Y. Cao, W.-Y. Wong, *Adv. Mater.* **2011**, *23*, 2976.

[64] A. P. Kulkarni, X. X. Kong, S. A. Jenekhe, *J. Phys. Chem. B* **2004**, *108*, 8689.

4.2. Low-cost, air-stable n-dopant for solution-processed phosphorescent organic light-emitting diodes

4.2.1. Introduction

Organic light-emitting diodes (OLEDs) have been extensively investigated over the last few decades for their various applications in industry such as full-color displays, flexible displays, transparent displays and solid-state lighting.[1-3] Recently, intensive progress has been made on developing highly efficient phosphorescent OLEDs (PhOLEDs) which show internal quantum efficiency of nearly 100%.[4, 5] High-performance PhOLEDs are mainly achieved by sequential thermal vacuum-evaporation of organic semiconductors to fabricate multilayered device structure, whereas solution-processed PhOLEDs have gained much attention recently due to their advantages of economic and/or large area device fabrication.[6] We have demonstrated that highly efficient multilayered solution-processed PhOLEDs can be achieved by new orthogonal solution-processing of oligoquinoline electron-transport materials (ETMs) [7, 8] and also other commercial ETMs.[9] However, challenges yet remain in further developing high-performance solution-processed PhOLEDs. Especially facile electron-injection and transport in electron-transport layer (ETL) are critical and still has a room to improve to enhance the performance of PhOLEDs with balanced charge carriers.[10]

One promising strategy is an n-type doping of ETL by simultaneous co-deposition of ETM and n-dopant to achieve efficient electron-injection and transport in the ETL.[11-13] Since organic semiconductors generally have relatively low bulk conductivity ($< 10^{-11}$ S cm^{-1}), the approach to enhance bulk conductivity of the ETL can reduce the resistance of the layer, realize Ohmic contact and thus facilitates electron-injection and transport.

N-type doping is intrinsically more difficult compared to p-type doping, because it is difficult to find suitable n-dopant due to their instability in air.[14] Typical n-type dopant includes elemental alkali metal[15] and organic n-dopant with a high-lying HOMO [16, 17] which are both highly reactive to oxygen and moisture. As an alternative, alkali metal derivatives such as metal carbonates (e.g. Cs_2CO_3, Li_2CO_3)[18-21], metal fluorides (LiF)[22], metal nitrides (LiN_3, CsN_3)[23, 24], metal phosphates (Cs_3PO_4)[25, 26] have been demonstrated as effective n-dopants to enhance electron-injection and transport of ETMs in organic electronic devices. Although alkali metal derivatives are known to be air-stable, such n-type doping of ETL has been predominantly accomplished by thermal vacuum co-evaporation to obtain n-doped film.

We have recently reported that various organic small-molecule ETMs can be n-doped with alkali metal carbonate (Cs_2CO_3, Li_2CO_3) by orthogonal solution-processing of the ETL to achieve high-performance all-solution-processed PhOLEDs.[27] There are only a few reports on solution-processable n-dopant,[28, 29] the demonstrated orthogonal solution-processing method is very promising and general to utilize various metal salt as n-type dopant in solution-processed ETL.

Sodium bicarbonate ($NaHCO_3$) is well-known material as *baking soda*, widely used in cooking as a leavening agent as well as deodorizer. Sodium chloride (NaCl) is the most common ionic compound that has been not only used for domestic purposes as *table salt*, but much widely consumed in chemical production and de-icing. Both materials are very abundant, very cheap, environmentally friendly and indeed air-stable. The use of NaCl has been scarcely reported only in fluorescent OLEDs, solely employing NaCl as cathode interfacial material between Alq_3 and Al cathode[30] or as a buffer layer between organic layer and electrode [31, 32] to improve overall device performance. However, thin film of NaCl was deposited by thermal vacuum-evaporation

and OLEDs with NaCl as electron-injection layer showed only comparable device performance compared to other cathode interfacial materials (e.g. LiF). Very recently, solution-processed NaCl layer was reported as efficient cathode interfacial layer in P3HT:PCBM-based polymer solar cells, which showed comparable device performance as Ca interlayer.[33] Surprisingly, there

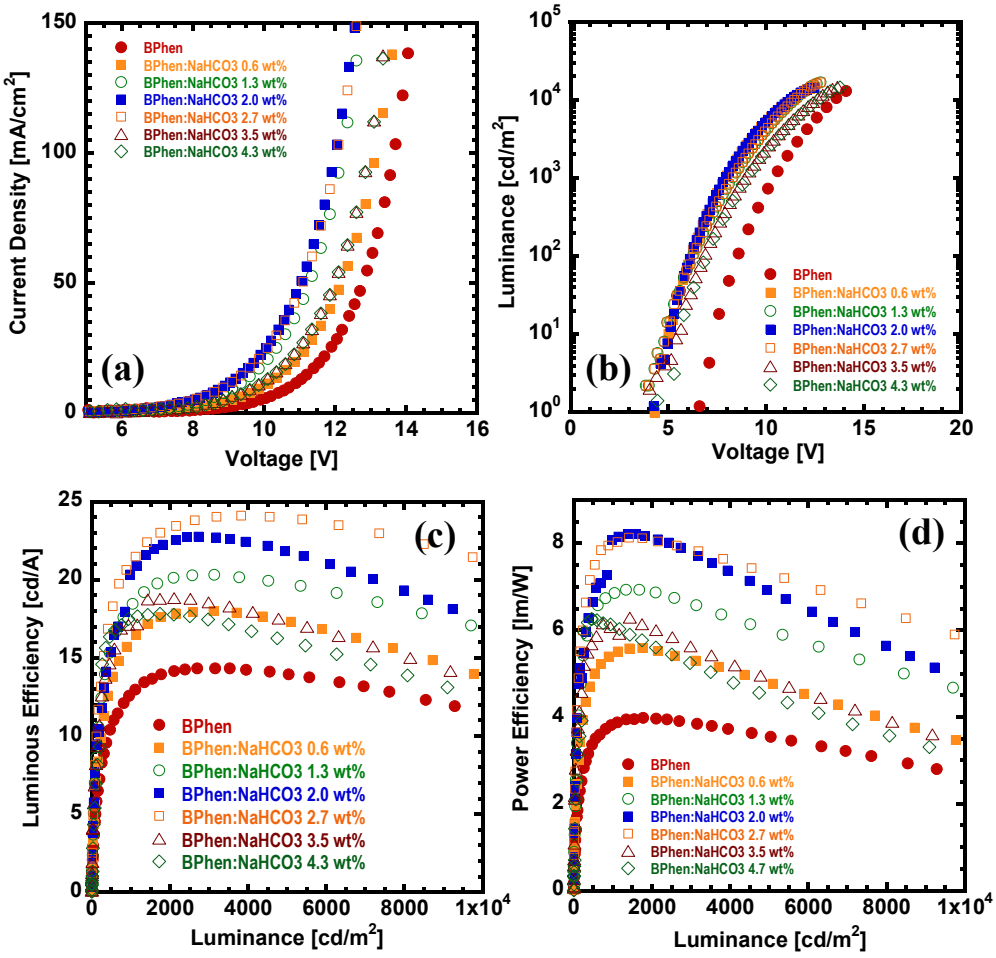

Figure 4.9. Blue PhOLEDs with BPhen ETL doped with $NaHCO_3$: (a) Current density (*J*) – voltage (*V*); (b) luminance (*L*) - voltage (*V*); (c) luminous efficiency (*LE*) - luminance (*L*); and (d) power efficiency (*PE*) - luminance (*L*) curves. Device structures: ITO/PEDOT:PSS(30 nm)/EML(70 nm)/solution-processed BPhen:$NaHCO_3$ ETL(30 nm)/Al (100 nm), BPhen ETL doped with different concentration of $NaHCO_3$.

are no prior reports regarding the use of $NaHCO_3$ in organic electronic devices.

In this chapter, we demonstrate sodium bicarbonate ($NaHCO_3$) and sodium chloride (NaCl) as an effective n-dopant for electron-transport layer (ETL) in solution-processed PhOLEDs. We found

that incorporation of $NaHCO_3$ or NaCl dopant into the ETL by orthogonal solution-processing significantly enhance the performance of PhOLEDs, especially the device doped with $NaHCO_3$ showed much improved performance than NaCl.

4.2.2. Experimental Section

We fabricated solution-processed blue PhOLEDs based on phosphorescent emission layer (EML) doped with triplet emitter. The phosphorescent EML was consisted of a blend of Poly(*N*-vinyl carbazole) (PVK, average M_w = 1,100,000 g mol^{-1}) and 1,3-bis(2-(4-tert-butylphenyl)-1,3,4-oxadiazo-5-yl)benzene (OXD-7, LumTec, Taiwan) (PVK:OXD-7 = 60:40, wt/wt) as a polymer host and 10.0 wt% FIrpic (LumTec, Taiwan) as the blue emitter. A solution of PEDOT:PSS was filtered before spin-coating to make a 30-nm hole-injection layer onto a pre-cleaned, oxagen plasma-treated ITO glass. Then the film was annealed at 150 ºC under vacuum to remove residual water. The polymer EML was obtained by spin coating of the PVK:OXD-7:FIrpic blend in chlorobenzene onto the PEDOT:PSS layer and vacuum dried at 100 ºC. 4,7-diphenyl-1,10-phenanthroline (bathophenanthroline, BPhen, 99%, sublimed grade, Sigma-Aldrich) small-molecule electron-transport material (ETM) was co-dissolved with the dopant ($NaHCO_3$ or NaCl) in formic acid:water (FA:H_2O = 3:1) mixture and spun cast onto the EML followed by vacuum drying to form solution-deposited ETL as previously reported.[7, 8]. The concentration of the dopant in the BPhen ETL was: 0.6, 1.3, 2.0, 2.7, 3.5 or 4.3 wt % (2.5, 5.0, 7.5, 10.0, 12.5 or 15.0 mol%) $NaHCO_3$ and 0.5, 1.0, 1.5, 2.0 or 2.5 wt% (1.0, 2.5, 5.0, 7.5, 10.0 or 12.5 mol%) NaCl. The structure of PhOLEDs: ITO/PEDOT:PSS(30 nm)/EML(70 nm)/solution-processed BPhen:dopant (30 nm)/Al (100 nm). Device characterization, including external quantum efficiency (EQE), was done using the same procedures as previously reported.[5,

[7, 9] All the device fabrication and characterization steps were performed under ambient laboratory conditions.

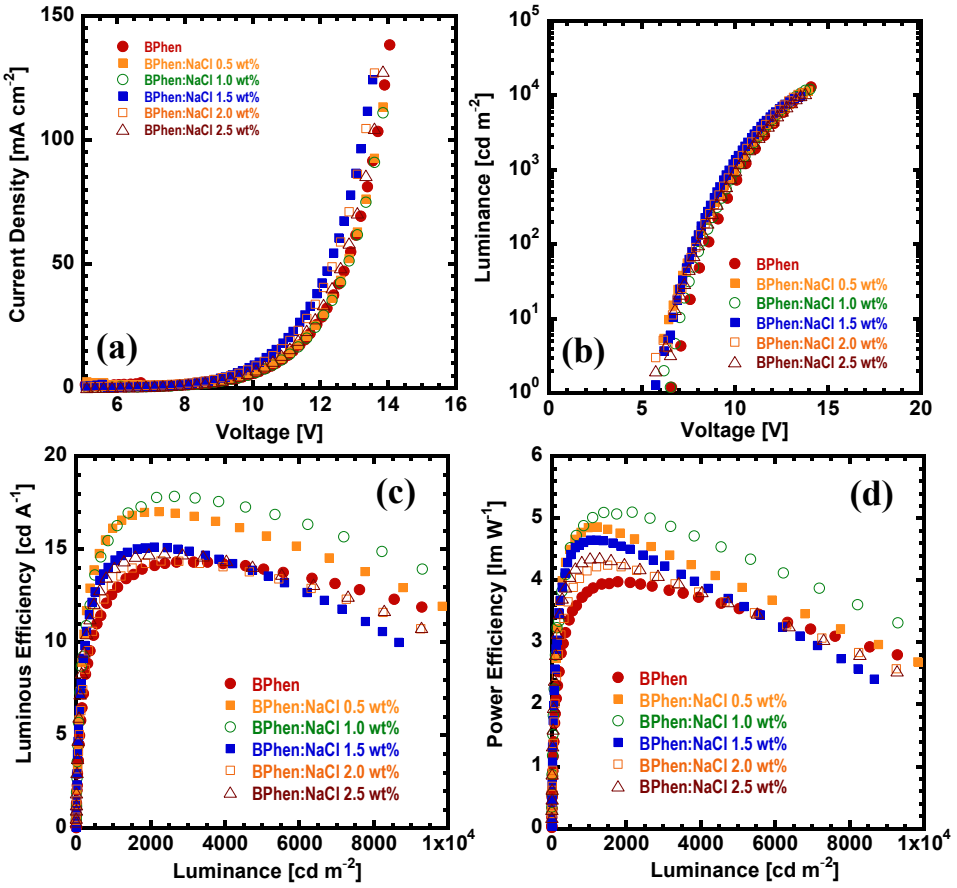

Figure 4.10. Blue PhOLEDs with BPhen ETL doped with NaCl: (a) Current density (*J*) – voltage (*V*); (b) luminance (*L*) - voltage (*V*); (c) luminous efficiency (*LE*) - luminance (*L*); and (d) power efficiency (*PE*) - luminance (*L*) curves. Device structures: ITO/PEDOT:PSS(30 nm)/EML(70 nm)/solution-processed BPhen:NaCl ETL(30 nm)/Al (100 nm), BPhen ETL doped with different concentration of NaCl.

4.2.3. Results and Discussion

The current density-voltage (*J-V*), luminance-voltage (*L-V*), luminous efficiency – luminance (*LE-L*), and power efficiency- luminance (*PE-L*) characteristics of PhOLEDs with BPhen ETLs doped with $NaHCO_3$ are shown in Figure 4.9. Incorporation of $NaHCO_3$ in the solution-processed BPhen ETL show significantly improved device performance. PhOLED with 2.5

mol% of $NaHCO_3$ showed an increased LE value of 18.0 cd A^{-1} (at 3000 cd m^{-2}) and a PE value of 5.6 lm W^{-1} with an EQE of 9.0 % compared to the device without $NaHCO_3$ dopant (LE = 14.3 cd A^{-1}, PE = 4.0 lm W^{-1}, and EQE = 7.2 %). As the concentration of $NaHCO_3$ in BPhen ETL increased from 2.5 to 10.0 mol%, the PhOLEDs showed much enhanced performance with the increased current density (Figure 1a), decreased turn-on voltage and drive voltage (Figure 4.9b). PhOLEDs with BPhen ETL doped with 7.5 mol% $NaHCO_3$ gave a LE value of 22.7 cd A^{-1} and a PE value of 8.2 lm W^{-1} (EQE of 11.4 %), while the PhOLEDs with 10.0 mol% $NaHCO_3$ showed the highest device performance with an LE value of 24.1 cd A^{-1} (at 3680 cd m^{-2}), PE of 8.1 lm W^{-1} with an EQE of 12.1 %, which is 1.6-fold increase compared to the device without dopant (Figure 4.9c,d). PhOLEDs with $NaHCO_3$ dopant also showed significantly reduced turn-on voltage of 3.9 V and a drive voltage of 12.6 V compared to the devices without n-doping (V_{on} = 6.6 V, drive voltage = 14.4 V). However, further increase of the $NaHCO_3$ concentration to 12.5 and 15.0 mol% resulted in a decreased device performance with LE values of 18.8 and 17.8 cd A^{-1} (PE values of 6.3 and 6.2 lm W^{-1}), presumably due to a severe phase separation between BPhen and the dopant in the ETL.[27] Nevertheless, PhOLEDs with high concentration of $NaHCO_3$ (12.5 and 15.0 mol%) still had higher device efficiency than the device with undoped BPhen ETL. These results clearly demonstrate that $NaHCO_3$ performed as effective n-dopant in solution-deposited BPhen ETL with significantly enhanced device performance and decreased operating voltage.

PhOLEDs with BPhen ETL doped with NaCl were also fabricated using solution-deposition of the ETL. The *J-V, L-V, LE-L,* and *PE-L* characteristics were shown in Figure 4.10. PhOLEDs with BPhen ETL doped with NaCl showed similar *J-V* and *L-V* characteristics, which are quite different from the devices with $NaHCO_3$. The *J-V* and *L-V* characteristics only showed slight

increase of the current density and reduced operating voltage when incorporating NaCl dopant into the BPhen ETL (Figure 4.10a,b) However, PhOLED with 2.5 mol% NaCl dopant showed enhanced device performance with LE value of 17.9 cd A^{-1} (at 2540 cd m^{-2}) with an EQE of 9.0% (PE = 5.1 lm W^{-1}) and reduced turn-on voltage (6.0 V) and drive voltage (14.0 V), compared to the device with non-doped ETL (Figure 4.10c,d) A similar trend as PhOLEDs with $NaHCO_3$ was observed when further increasing the NaCl concentration, which resulted in decreased device performance. The result demonstrates that NaCl indeed functions as n-dopant in solution-processed BPhen ETL enhancing the performance of PhOLEDs, although NaCl was less efficient than $NaHCO_3$. We can conclude that $NaHCO_3$ is superior to NaCl as an n-dopant in solution-processed ETL.

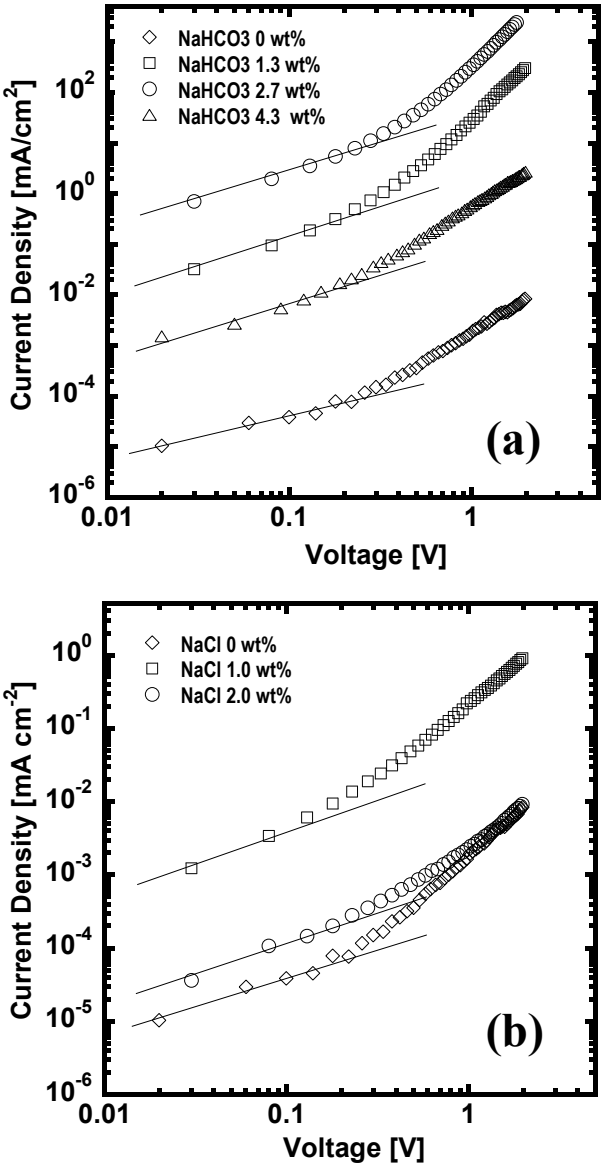

Figure 4.11. Current density (*J*) – voltage (*V*) characteristics of BPhen doped with (a) $NaHCO_3$ and (b) NaCl with different concentration.

In order to investigate the effect of using $NaHCO_3$ and

NaCl on conductivity increase in BPhen ETL, we measured the bulk conductivity of ETL from single carrier device with different dopant concentration. The BPhen:dopant layer was solution-deposited onto a plasma treated ITO glass to form ~150 nm thick ETL, followed by a deposition of Al to fabricate the single carrier device: ITO/BPhen:$NaHCO_3$ or BPhen:NaCl/Al. Figure 4.11 shows the current density-voltage (*J-V*) characteristics of the single carrier devices. The conductivity was calculated from the linear region below 0.1 V, which follows Ohmic law in the *J-V* curves plotted in double logarithmic scale.[22, 25] Pristine BPhen ETL without dopant showed a conductivity of 5.8×10^{-12} S cm^{-1} while incorporating 5.0 mol% of $NaHCO_3$ resulted in conductivity enhancement, showing 1.9×10^{-8} S cm^{-1} which was 4 orders of magnitude increase. BPhen ETL doped with 10.0 mol% of $NaHCO_3$ show increased conductivity of 3.8×10^{-7} S cm^{-1} which is 5 orders of magnitude higher compared to the pristine BPhen ETL. However, further increasing the $NaHCO_3$ concentration to 15.0 mol% had decreased conductivity of 1.1×10^{-9} S cm^{-1}, which is consistent with the device performance shown above.

BPhen ETL doped with NaCl showed a similar trend as $NaHCO_3$. Incorporating 2.5 mol% NaCl into the BPhen ETL showed a slight conductivity increase (6.6×10^{-10} S cm^{-1}) whereas

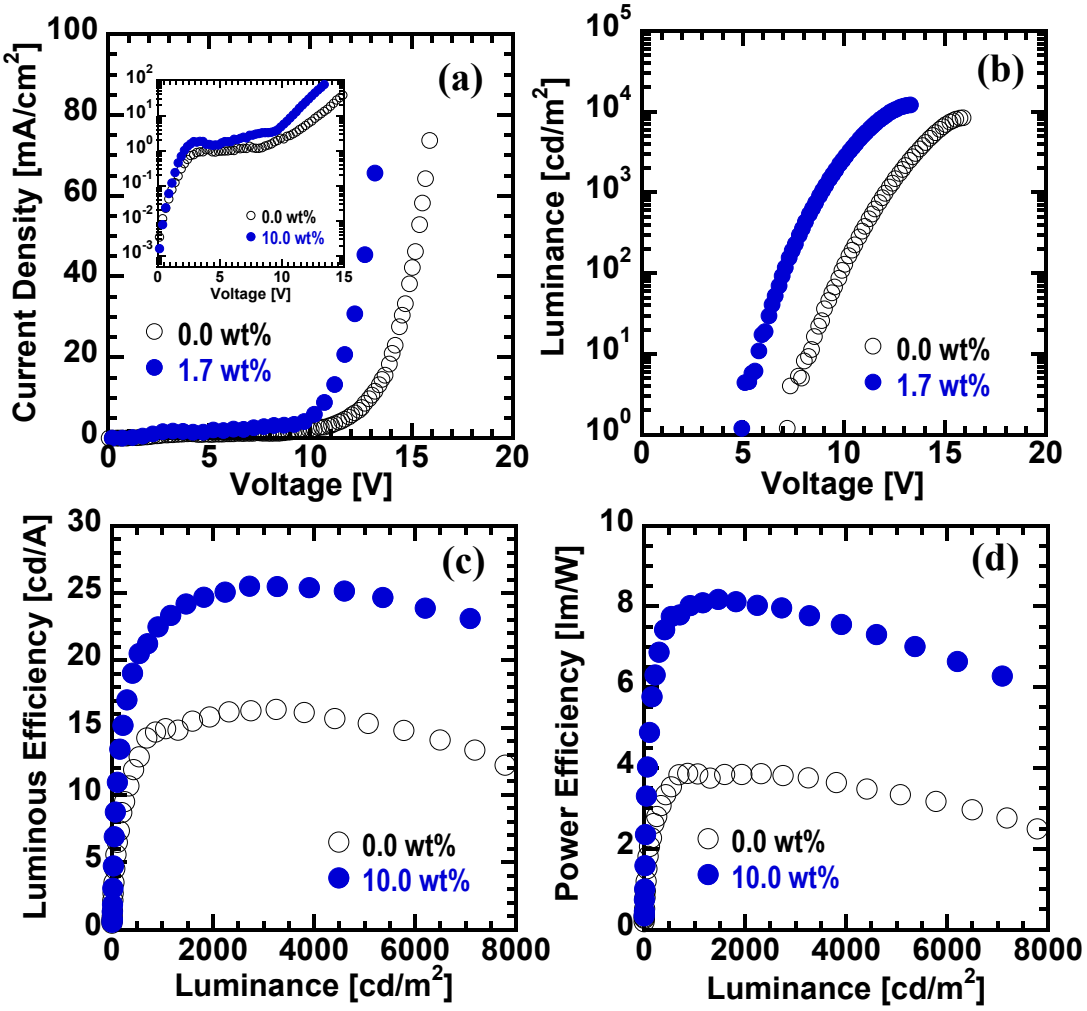

Figure 4.12. Blue PhOLEDs with TmPyPB ETL doped with $NaHCO_3$: (a) Current density (*J*) –voltage (*V*); (b) luminance (*L*) - voltage (*V*); (c) luminous efficiency (*LE*) - luminance (*L*); and (d) power efficiency (*PE*) - luminance (*L*) curves. Device structures: ITO/PEDOT:PSS(30 nm)/EML(70 nm)/solution-processed TmPyPB: $NaHCO_3$ ETL(30 nm)/Al (100 nm), TmPyPB ETL was undoped or doped with 1.7 wt% (10.0% molar) concentration of $NaHCO_3$. The inset in (a) shows semi-log scale of *J-V* characteristics.

with a high concentration of NaCl (10.0 mol%) showed a conductivity of 1.6×10^{-11} S cm^{-1} which is similar to undoped BPhen ETL. A trend of conductivity change by NaCl dopant is consistent with the improved performance of PhOLEDs at these doping levels. Detailed

mechanism of the solution-processed n-type doping by $NaHCO_3$ and NaCl has not been confirmed yet and is currently under investigation. Nevertheless, the observed enhancement of conductivity of BPhen ETL clearly indicates the effectiveness of $NaHCO_3$ and NaCl as n-dopant.

Applicability of $NaHCO_3$ as n-dopant for other electron transport materials in solution-processed blue PhOLEDs was tested by using 1,3,5-tris(m-pyrid-3-yl-phenyl)benzene (TmPyPB).[34] As shown in Fig. 4.12, PhOLEDs with undoped TmPyPB ETL showed a LE of 16.3 cd/A and a PE of 4.0 lm/W with an EQE of 8.2%, whereas those with a 10.0 mol% $NaHCO_3$-doped TmPyPB ETL had a significant enhancement in performance with an LE of 25.5 cd/A and a PE value of 8.2 lm/W (EQE of 12.7 %). The devices with doped ETL also had increased current density and reduced operating voltage (Fig. 4.12a,b). These results demonstrate that $NaHCO_3$ is an effective n-dopant for TmPyPB ETL and solution-processed ETL in general.

4.2.4. Conclusions

In summary, sodium bicarbonate ($NaHCO_3$) and sodium chloride (NaCl) is found to be an effective n-dopant for solution-processed electron-transport layer in optoelectronic devices. Especially blue PhOLEDs with $NaHCO_3$-doped BPhen or TmPyPB ETL were found to have significantly enhanced performance. The bulk conductivity of $NaHCO_3$- or NaCl-doped ETL was increased up to 5 orders magnitude. These results show that widely available, low-cost, and environmentally friendly $NaHCO_3$ and NaCl are a promising n-dopants for high-performance organic electronics.

4.2.5. References

1. So, F.; Kido, J.; Burrows, P., *MRS Bull.* **2008**, *33*, 663.

2. Wang, Z. B.; Helander, M. G.; Qiu, J.; Puzzo, D. P.; Greiner, M. T.; Hudson, Z. M.; Wang, S.; Liu, Z. W.; Lu, Z. H., *Nat. Photon* **2011**, *5*, 753.

3. Reineke, S.; Lindner, F.; Schwartz, G.; Seidler, N.; Walzer, K.; Lussem, B.; Leo, K., *Nature* **2009**, *459*, 234.

4. Adachi, C.; Baldo, M. A.; Forrest, S. R.; Thompson, M. E., *Appl. Phys. Lett.* **2000**, *77*, 904.

5. Earmme, T.; Ahmed, E.; Jenekhe, S. A., *J. Phys. Chem. C* **2009**, *113*, 18448.

6. Arias, A. C.; MacKenzie, J. D.; McCulloch, I.; Rivnay, J.; Salleo, A., *Chem. Rev.* **2010**, *110*, 3.

7. Earmme, T.; Ahmed, E.; Jenekhe, S. A., *Adv. Mater.* **2010**, *22*, 4744.

8. Ahmed, E.; Earmme, T.; Jenekhe, S. A., *Adv. Funct. Mater.* **2011**, *21*, 3889.

9. Earmme, T.; Jenekhe, S. A., *J. Mater. Chem.* 2012, *22*, 4660.

10. Kulkarni, A. P.; Tonzola, C. J.; Babel, A.; Jenekhe, S. A., *Chem. Mater.* **2004**, *16*, 4556.

11. Scholz, S.; Lussem, B.; Leo, K., *Appl. Phys. Lett.* **2009**, *95*, 183309.

12. He, G.; Pfeiffer, M.; Leo, K.; Hofmann, M.; Birnstock, J.; Pudzich, R.; Salbeck, J., *Appl. Phys. Lett.* **2004**, *85*, 3911.

13. Leem, D.-S.; Lee, J.-H.; Kim, J.-J.; Kang, J.-W., *Appl. Phys. Lett.* **2008**, *93*, 103304.

14. Walzer, K.; Maennig, B.; Pfeiffer, M.; Leo, K., *Chem. Rev.* **2007**, *107*, 1233.

15. Kido, J.; Matsumoto, T., *Appl. Phys. Lett.* **1998**, *73*, 2866.

16. Chan, C. K.; Amy, F.; Zhang, Q.; Barlow, S.; Marder, S.; Kahn, A., *Chem. Phys. Lett.* **2006**, *431*, 67.

17. Bloom, C. J.; Elliott, C. M.; Schroeder, P. G.; France, C. B.; Parkinson, B. A., *J. Phys. Chem. B* **2003**, *107*, 2933.

18. Wu, C.-I.; Lin, C.-T.; Chen, Y.-H.; Chen, M.-H.; Lu, Y.-J.; Wu, C.-C., *Appl. Phys. Lett.* **2006**, *88*, 152104.

19. Cai, Y.; Wei, H. X.; Li, J.; Bao, Q. Y.; Zhao, X.; Lee, S. T.; Li, Y. Q.; Tang, J. X., *Appl. Phys. Lett.* **2011**, *98*, 113304.

20. Vaynzof, Y.; Kabra, D.; Chua, L. L.; Friend, R. H., *Appl. Phys. Lett.* **2011**, *98*, 113306.

21. Kao, P.-C.; Lin, J.-H.; Wang, J.-Y.; Yang, C.-H.; Chen, S.-H., *J. Appl. Phys.* **2011**, *109*, 094505.

22. Choudhury, K. R.; Yoon, J.-h.; So, F., *Adv. Mater.* **2008**, *20*, 1456.

23. Yook, K. S.; Jeon, S. O.; Min, S.-Y.; Lee, J. Y.; Yang, H.-J.; Noh, T.; Kang, S.-K.; Lee, T.-W., *Adv. Funct. Mater.* **2010**, *20*, 1797.

24. Yook, K. S.; Jeon, S. O.; Joo, C. W.; Lee, J. Y.; Lee, T.-W.; Noh, T.; Yang, H.-J.; Kang, S.-K., *Synth. Met.* **2009**, *159*, 1664.

25. Wemken, J. H.; Krause, R.; Mikolajick, T.; Schmid, G., *J. Appl. Phys.* **2012**, *111*, 074502.

26. Diez, C.; Reusch, T. C. G.; Lang, E.; Dobbertin, T.; Brutting, W., *J. Appl. Phys.* **2012**, *111*, 103107.

27. Earmme, T.; Jenekhe, S. A., *Adv. Funct. Mater.* **2012**, DOI: 10.1002/adfm.201201366.

28. Wei, P.; Oh, J. H.; Dong, G.; Bao, Z., *J. Am. Chem. Soc.* **2010**, *132*, 8852.

29. Werner, A. G.; Li, F.; Harada, K.; Pfeiffer, M.; Fritz, T.; Leo, K., *Appl. Phys. Lett.* **2003**, *82*, 4495.

30. Kang, S. J.; Park, D. S.; Kim, S. Y.; Whang, C. N.; Jeong, K.; Im, S., *Appl. Phys. Lett.* **2002**, *81*, 2581.

31. Shi, S. W.; Ma, D. G.; Peng, J. B., *Eur. Phys. J-Appl. Phys.* **2007**, *40*, 141.

32. Matsushima, T.; Takamori, M.; Miyashita, Y.; Honma, Y.; Tanaka, T.; Aihara, H.; Murata, H., *Org. Electron.* **2010**, *11*, 16.

33. Nickel, F.; Reinhard, M.; Zhang, Z.; Putz, A.; Kettlitz, S.; Lemmer, U.; Colsmann, A., *Appl. Phys. Lett.* **2012**, *101*, 053309.

34. Su, S.-J.; Chiba, T.; Takeda, T.; Kido, J., *Adv. Mater.* **2008**, *20*, 2125.

Chapter 5. High-Performance Phosphorescent OLEDs Using High Triplet Energy Electron-Transport Materials

This chapter presents the synthesis, characterization and device application of novel high triplet energy electron-transport materials for high-performance phosphorescent OLEDs (PhOLEDs), especially for blue PhOLEDs.

5.1. Blue Phosphorescent OLEDs with New Sulfone-based High Triplet Energy Electron-Transport Materials

5.1.1. Introduction

Organic light-emitting diodes (OLEDs) are finding applications in full-color flat panel displays, flexible displays, and solid-state lighting.[1] Recent research on OLEDs has largely focused on developing new materials and device strategies for achieving highly efficient phosphorescent organic light-emitting diodes (PhOLEDs) because nearly 100% internal quantum efficiency can be realized.[2] One promising strategy towards highly efficient PhOLEDs is through the utilization of high triplet energy materials to confine triplet exitons inside the emission layer (EML) in multilayered device structures.[3-6]

High-performance PhOLEDs[5-19] and OLEDs[20-21] have been achieved by using various classes of electron-transport materials (ETMs) such as pyridine,[5,9,10] phenylpyrimidine,[11] triazine,[12,13] quinoline[14,15] and phosphine oxide (PO) derivatives.[7,16-19] Phosphine-oxide-based ETMs have gained much attention due to their good exciton blocking ability enabled by their high triplet energy.[19] The PO group is known to lower the LUMO level predominantly by inductive electron-withdrawing effect, which facilitates electron-injection while retaining high triplet energy. The sulfonyl group (SO_2) is another attractive group with good electron withdrawing properties

comparable to the phosphine oxide (PO) group. Sulfone-based materials can be expected to have efficient electron-injection and transport due to the strong electron withdrawing character of the disulfoxide group and the high triplet energy and wide band gap of the materials. They are also known to have good electrochemical and thermal stability.[20-23]

High triplet energy materials containing the sulfone group were recently reported for applications in PhOLEDs. Hsu et al. reported bis(phenylsulfonyl)fluorine-based molecule as the host material for red PhOLEDs.[24] More recently, Marder and Kippelen et al. synthesized and evaluated a bis(phenylsulfonyl)biphenyl molecule, and Kido et al. reported a sulfone derivative as a high triplet energy (Calcd. E_T = 3.11 eV) host material for bis(3,5-difluoro-2-(2-pyridyl)phenyl-(2-carboxypyridyl)iridium (FIrpic) triplet emitter in blue PhOLEDs.[25.26] However, all previous reports on sulfone-based materials to date have focused on their use as host materials for PhOLEDs,[24-26] which involves vacuum co-deposition of the host material with a triplet emitter.

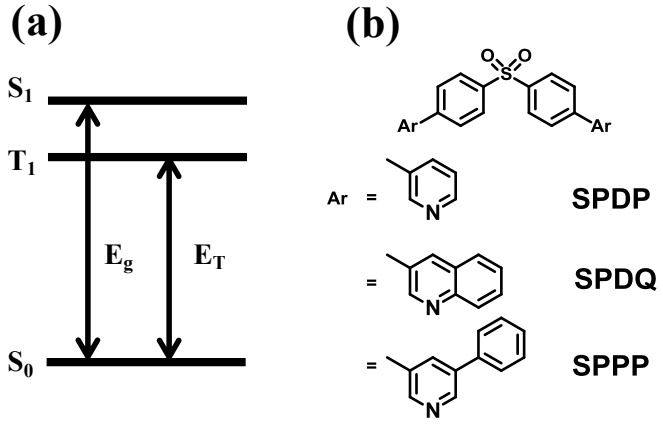

Chart 5.1. Diagram of singlet energy (S_1) and triplet energy (T_1) (a) and diphenylsulfone core structure with different substituents (b).

In this section, we report the synthesis, experimental and theoretical electronic structure, photophysics, and thermal and electron-transport properties of a series of new sulfone-based high triplet energy materials and demonstrate their use as efficient electron transport materials in high performance blue PhOLEDs. The new electron transport materials (ETMs) include 3,3'-(4,4'-sulfonylbis(4,1-

phenylene))dipyridine (**SPDP**), 5,5'-(4,4'-sulfonylbis(4,1-phenylene))bis(3-phenylpyridine) (**SPPP**), and 3,3'-(4,4'-sulfonylbis(4,1-phenylene))diquinoline (**SPDQ**). The new sulfone-based ETMs, whose molecular structures are shown in Chart 5.1, have a diphenylsulfone core with different electron withdrawing substituents (pyridine, phenylpyridine, and quinoline) aimed at controlling the triplet energy (E_T), band gap (E_g) and electron transport properties. The triplet energy (E_T) of the new electron transport materials was measured from the low temperature (77K) phosphorescence spectra and compared to density functional theory (DFT) based predicted values. The electron mobility of the ETMs was measured in space-charge limited current (SCLC) experiments on evaporated thin films. Finally, a series of blue PhOLEDs was fabricated and evaluated toward investigation of the electron transport and exciton blocking properties of the new sulfone-based ETMs. The results demonstrate that the new sulfone-based molecules are promising electron transport materials with high triplet energy for high-performance PhOLEDs.

5.1.2. Experimental Section

Materials Bis(4-chlorophenyl) sulfone, 3-pyridinylboronic acid, quinoline-3-boronic acid, phenylboronic acid, tetrakis(triphenylphosphine)palladium(0), potassium carbonate, 3,5-dibromopyridine, *n*-butyllithium, 1,4-dioxane, trimethyltin chloride, copper iodide, anhydrous toluene and tetrahydrofuran (Aldrich) were used without further purification.

Synthesis 3-Bromo-5-phenylpyridine (**1**). A mixture of 3,5-dibromopyridine (5.0 g, 21.1 mmol), phenylboronic acid (3.08 g, 25.3 mmol) and tetrakis(triphenylphosphine)palladium(0) (5 mol %) in 80 mL of 1,4-dioxane was refluxed under argon for 12 h. To the reaction mixture was added slowly a solution of potassium carbonate (2 M, 80 mL). After cooling to room temperature,

the reaction mixture was extracted with dichloromethane and water. The organic layer was evaporated with a rotary evaporator. The product was purified by column chromatography using ethyl acetate and hexane mixture (10 : 90) and a white solid product was obtained (3.5 g, 72 % yield). ^{1}H NMR (300 MHz, $CDCl_3$, ppm): δ 8.74-8.64 (d, 2H), 7.99 (s, 1H), 7.54- 7.38 (m, 5H).

4,4'-Sulfonylbis(4,1-phenylene)bis(trimethylstannane) (**2**). To a solution of bis(4-chlorophenyl) sulfone (3.0 g, 10.4 mmol) in 50 mL anhydrous tetrahydrofuran, 2.5 M solution of *n*-BuLi (9.19 mL, 22.9 mmol) was added dropwise at -78 ^{o}C. The solution was stirred at -78 ^{o}C for 2 h and 1.0 M solution of trimethyltin chloride (22.9 mL, 22.9 mmol) in tetrahydrofuran was added. The solution was warmed to room temperature and 50 mL of water and 50 mL of ethyl ether were added. The organic layer was washed twice with 50 mL of water and dried over anhydrous $MgSO_4$. The organic layer was evaporated and dried over vacuum to afford white solid (5.5 g, 97 % yield). ^{1}H NMR ($CDCl_3$, 300 MHz, ppm): δ 7.72-7.66 (m, 4H), 7.34-7.28 (m, 4H), 0.42 (s, 18H).

3,3'-(4,4'-Sulfonylbis(4,1-phenylene))dipyridine (**SPDP**). A mixture of bis(4-chlorophenyl) sulfone (2.0 g, 6.96 mmol), 3-pyridinylboronic acid (1.02 g, 8.35 mmol) and tetrakis(triphenylphosphine)palladium(0) (5 mol %) in 20 mL of anhydrous tetrahydrofuran was refluxed under argon for 12 h. To the reaction mixture was slowly added a solution of potassium carbonate (2 M, 20 mL). After cooling to ambient temperature, the reaction mixture was extracted with dichloromethane and water. The organic layer was evaporated with a rotary evaporator. The product was purified by column chromatography using ethyl acetate and *n*-hexane mixture (10 : 90) and a white solid product was obtained (1.65 g, 63 % yield); T_m 239 ^{o}C. ^{1}H NMR (300 MHz, $CDCl_3$, ppm): δ 8.85 (s, 2H), 8.67 (s, 2H), 8.12- 8.09 (d, 4H), 7.90-7.87 (d, 2H), 7.76-7.74 (d, 4H), 7.45-7.40 (m, 2 H).^{13}C NMR (500 MHZ, $CDCl_3$, ppm) : δ 149.7, 148.3,

142.9, 141.0, 134.6, 128.5, 128.1, 123.7. MALDI-TOF/MS: 373 [$(M + H)^+$]. Anal. Calcd. for $C_{22}H_{16}N_2O_2S$: C, 70.95; H, 4.33; N, 7.52; S, 8.61. Found: C, 70.99; H, 4.19; N, 7.50; S, 8.45.

5,5'-(4,4'-Sulfonylbis(4,1-phenylene))bis(3-phenylpyridine) (**SPPP**). 3-Bromo-5-phenylpyridine (**1**) (3.0 g, 12.8 mmol) and 4,4'-sulfonylbis(4,1-phenylene)bis(trimethylstannane) (**2**) (4.18 g, 7.68 mmol) and catalyst tetrakis(triphenylphosphine)palladium (0) (5 mol %) and copper iodide (1 mol %) in anhydrous toluene (30 mL) were heated at 120 ^oC for 24 h. The solution was warmed to room temperature and extracted with 50 mL of water and 50 mL of dichloromethane. The organic layer was dried over anhydrous $MgSO_4$. The product was purified by column chromatography using ethyl acetate and *n*-hexane mixture (10 : 40) and a white solid product was obtained. Yield 45 %; T_m 180 ^oC. ^1H NMR ($CDCl_3$, 300 MHz, ppm): δ 8.93-8.90 (d, 4H), 8.12 (s, 2H), 7.69-7.47(m, 18H). ^{13}C NMR (500 MHZ, $CDCl_3$, ppm) : δ 148.0, 146.9, 137.3, 137.0, 133.4, 133.0, 129.3, 128.5, 127.3. MALDI-TOF/MS: 525 [$(M + H)^+$]. Anal. Calcd. for $C_{34}H_{24}N_2O_2S$: C, 77.84; H, 4.61; N, 5.34; S, 6.11. Found: C, 77.90; H, 4.58; N, 5.31; S, 5.98.

3,3'-(4,4'-Sulfonylbis(4,1-phenylene))diquinoline (**SPDQ**). A mixture of bis(4-chlorophenyl)sulfone (1.77 g, 6.10 mmol), quinoline-3-boronic acid (2.56 g, 14.7 mmol) and tetrakis(triphenylphosphine)palladium(0) (5 mol %) in 20 mL of anhydrous tetrahydrofuran was refluxed under argon for 12 h. To the reaction mixture was slowly added a solution of potassium carbonate (2 M, 20 mL). After cooling to ambient temperature, the reaction mixture was extracted with dichloromethane and water. The organic layer was evaporated with a rotary evaporator. The product was purified by column chromatography using ethyl acetate and *n*-hexane mixture (10 : 90) and a white solid product was obtained (0.90 g, 32 % yield); T_m 229 ^oC. ^1H NMR (300 MHz, $CDCl_3$, ppm): δ 9.17 (s, 2H), 8.35 (s, 2H), 8.20- 8.10 (m, 4H), 7.98-7.78 (m, 8H), 7.67-7.62 (m, 2H), 7.55-7.53 (m, 2H). ^{13}C NMR (500 MHZ, $CDCl_3$, ppm) : δ 149.2, 147.9,

143.1, 143.0, 140.9, 140.6, 140.1, 140.0, 134.1, 131.8, 130.3, 129.7, 129.3, 129.2, 128.6, 128.5, 128.3, 128.2, 127.7, 127.5. MALDI-TOF/MS: 473 [$(M + H)^+$]. Anal. Calcd. for $C_{30}H_{20}N_2O_2S$: C, 76.25; H, 4.27; N, 5.93; S, 6.79. Found: C, 76.14; H, 4.21; N, 4.89; S, 7.34.

General Analysis ^{1}H NMR spectra were recorded on a Bruker AV300 at 300 MHz, whereas ^{13}C NMR spectra were recorder on a Bruker AV500 at 500 MHz using $CDCl_3$ as the solvent. The MLADI-TOF mass spectra were recorded using a Bruker Autoflex II spectrometer. The Ultraviolet–Visible (UV-Vis) spectra were obtained by means of a Perkin-Elmer model Lambda 900 UV/vis/near-IR spectrophotometer and the photoluminescence (PL) spectra were recorded on a Photon Technology International (PTI) Inc. Model QM 2001-4 spectrofluorimeter. The UV-Vis absorption and solution PL emission spectra of electron transport materials (ETMs) were obtained from dilute toluene solution, while the solid PL spectra were obtained from thin films prepared by vacuum evaporation. Triplet energy values of the ETMs were obtained from the photoluminescence spectra at 77K using liquid nitrogen. The differential scanning calorimeter (DSC) measurements were performed on a TA Instruments Q100 under nitrogen at a heating rate of 10 °C min^{-1} to measure the melting point (T_m) and glass transition temperature (T_g). Thermogravimetric analysis (TGA) was done on a TA Instruments Q50 under flowing nitrogen at a heating rate of 20 ^{o}C min^{-1}. The energy levels were measured by using cyclic voltammetry (CV). Each ETM was dissolved in anhydrous acetonitrile with 0.1 M tetrabutylammonium hexafluorophosphate as the electrolyte to measure the reduction CV from which the LUMO energy level was estimated. We used a platinum wire electrode both working and counter electrode and a saturated Ag/AgCl reference electrode. Ferrocene was used as the standard reference. All solutions were purged with nitrogen for 10 minutes before each experiment.

Device Fabrication and Characterization The phosphorescent emission layer (EML) consisted of a blend of poly(*N*-vinylcarbazole) (PVK) and 1,3-bis(2-(4-tert-butylphenyl)-1,3,4-oxadiazo-5-yl)benzene (OXD-7) (PVK:OXD-7 = 60:40, wt%:wt%) as a host and 10.0 wt % FIrpic as the blue dopant. A solution of Clevios PVP Al 4083 PEDOT:PSS (poly-(ethylenedioxythiophene)-polystyrenesulfonate) as received, was filtered before spin-coating to make a 30 nm hole injection layer onto a precleaned ITO glass. Then the film was annealed at 150 ºC under vacuum to remove residual water. The 70 nm polymer EML was obtained by spin coating of the PVK:OXD-7:FIrpic blend in chlorobenzene onto the PEDOT:PSS layer and vacuum dried at 100 ºC. Sulfone-based ETM was vacuum-deposited onto the EML followed by deposition of 1 nm LiF and 100 nm Al cathode without breaking the vacuum. The device structure with different thickness of **SPDP** ETL: ITO/PEDOT:PSS/Blue EML/**SPDP**/Al with 5, 15, and 30 nm thick **SPDP**. A set of blue PhOLEDs were also fabricated; Device I: ITO/PEDOT:PSS/Blue EML/LiF/Al; Device II: ITO/PEDOT:PSS/Blue EML/**SPDP** (15 nm)LiF/Al; Device III: ITO/PEDOT:PSS/Blue EML/**SPPP** (15 nm)/LiF/Al; and Device IV: ITO/PEDOT:PSS/Blue EML/**SPDQ** (15 nm)/LiF/Al.

Film thickness was measured by using an Alpha-Step 500 profilometer (KLA-Tencor, San Jose, CA). Electroluminescence (EL) spectra were obtained by using the same spectrofluorimeter described above. Device performance of the PhOLEDs was measured by using a HP4155A semiconductor parameter analyzer (Yokogawa Hewlett-Packard, Tokyo). The luminance was simultaneously measured by using a model 370 optometer (UDT Instruments, Baltimore, MD) equipped with a calibrated luminance sensor head (Model 211) and a 5× objective lens. The device external quantum efficiency (EQE) was calculated from the luminance, current density and EL spectrum assuming a Lambertian distribution using procedures reported previously.[27] All

the device fabrication and device characterization steps were carried out under ambient laboratory conditions.

Devices for space-charge-limited current (SCLC) measurement were fabricated with single carrier device structure: ITO/Sulfone-based ETM (100 nm)/Al. The 100 nm sulfone-based ETM was deposited onto the plasma cleaned ITO substrate followed by vacuum-deposition of Al electrode. Current density-voltage (*J-V*) characteristics of SCLC devices were measured using the same semiconductor parameter analyzer as for the characterization of PhOLEDs. The SCLC

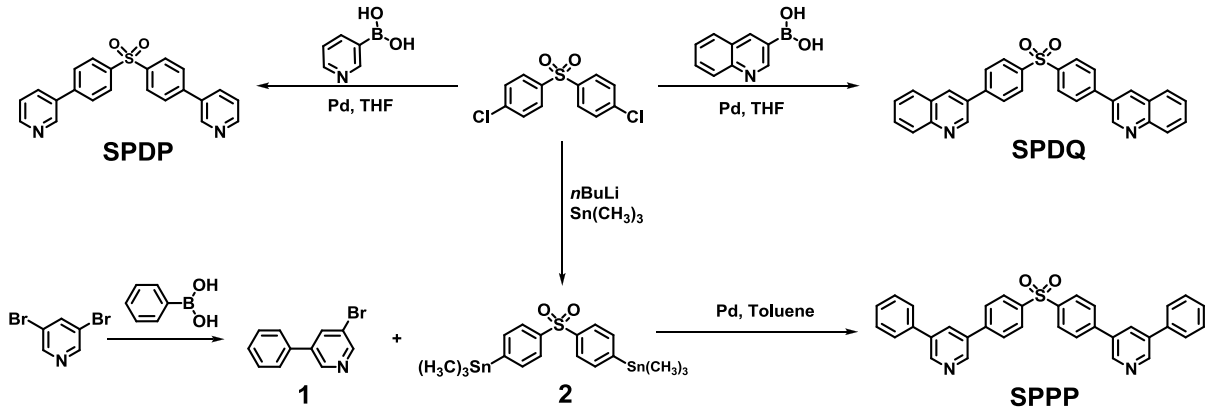

Scheme 5.1. Synthetic route of sulfone-based ETMs SPDP, SPDQ, and SPPP.

measurements were performed under dark and ambient conditions.

5.1.3. Results and Discussion

Synthesis and Characterization. The synthetic route to the new sulfone-based electron transport materials is shown in Scheme 5.1. The compounds, 3,3'-(4,4'-sulfonylbis(4,1-phenylene))dipyridine (**SPDP**) and 3,3'-(4,4'-sulfonylbis(4,1-phenylene))diquinoline (**SPDQ**), were synthesized by Suzuki coupling reaction of bis(4-chlorophenyl) sulfone with 3-pyridylboronic acid and quinoline-3-boronic acid, respectively using tetrakis(triphenylphosphine)palladium(0) in anhydrous tetrahydrofuran. The reaction of 3,5-

dibromopyridine with phenylboronic acid in the presence of palladium catalyst in 1,4-dioxane gave 3-bromo-5-phenylpyridine (**1**) in 72% yield. 4,4'-Sulfonylbis(4,1-phenylene)bis(trimethylstannane) (**2**) was prepared by stannylation of bis(4-chlorophenyl) sulfone with 97 % yield. The compound 5,5'-(4,4'-sulfonylbis(4,1-phenylene))bis(3-

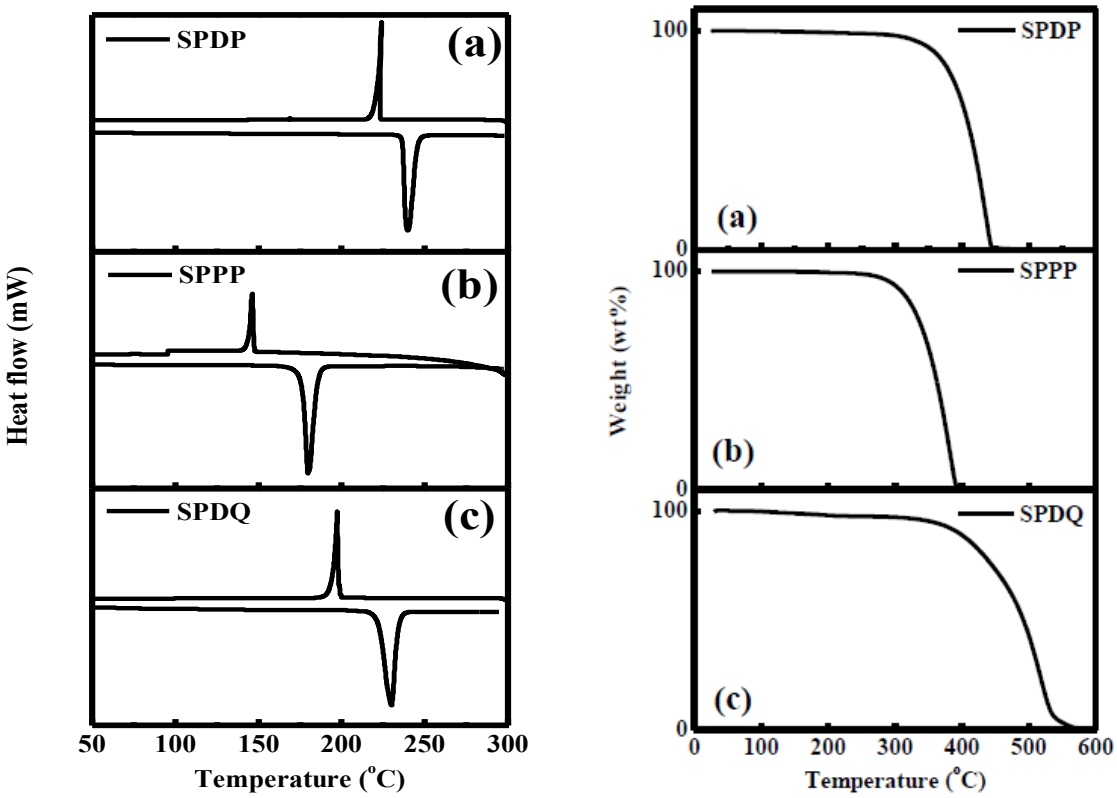

Figure 5.1. DSC and TGA thermograms of sulfone-based ETMs: (a) SPDP; (b) SPPP; and (c) SPDQ.

phenylpyridine) (**SPPP)** was synthesized by Stille coupling reaction between **1** and **2** with tetrakis(triphenylphosphine)palladium(0) and copper iodide in anhydrous toluene. The three final products (**SPDP**, **SPPP**, **SPDQ**) were purified by column chromatography and molecular structures were confirmed by ^{1}H NMR, ^{13}C NMR and elemental analysis.

Thermal properties of the sulfone-based ETMs were characterized by thermogravimetric analysis (TGA) and differential scanning calorimetry (DSC). TGA and DSC curves of the new sulfone-based ETMs are shown in Figure 5.1. Numerical values extracted from the TGA and DSC scans

are given in Table 5.1. Three distinct transitions were seen in the second-heating/cooling DSC

Table 5.1. Thermal and photophysical properties of sulfone-based ETMs.

	T_m (°C)	T_d (°C)	λ_{max}^{abs} (nm)			λ_{max}^{em} (nm)		HOMO/ LUMO (eV)	E_g (eV)	E_T (eV)
			Solution	log ϵ ($M^{-1}cm^{-1}$)	Film	Solution	Film			
SPDP	239	386	285	4.33	296	291	399	-6.17/-2.57	3.6	2.9
SPPP	180	342	281	4.36	289	294	393	-6.16/-2.37	3.79	2.81
SPDQ	229	453	298	3.47	279,306	375	409	-6.32/-2.7	3.64	2.53

scans of **SPDP, SPPP** and **SPDQ**. These materials showed a high melting point (T_m) of 239, 180 and 229 °C, respectively, whereas they did not exhibit a glass transition temperature (T_g) up to the T_m. The sulfone-based materials crystallize upon cooling from the melt. The **SPDP**, **SPPP** and **SPDQ** showed onset crystallization temperature (T_c) at 223, 146 and 197 °C, respectively. The onset decomposition temperature (T_d) of the new sulfone-based materials showed high values in the range of 386 to 453 °C, which demonstrate their thermal robustness. The new ETMs are stable to temperatures above 350 °C. The fact that apparent complete thermal decomposition with zero % weight remaining is observed in the TGA curves suggests that the materials can be readily evaporated to form thin films.

Photophysical Properties Optical absorption and photoluminescence (PL) spectra of the **SPDP**, **SPPP** and **SPDQ** molecules in dilute toluene solution (5×10^{-5} M) and thin films are shown in Figure 5.2. The solid state absorption and PL emission spectra of **SPDP**, **SPPP** and **SPDQ** were obtained from thermally evaporated thin films. The key numerical values of the photophysical properties of the sulfone-based ETMs, including absorption maximum (λ_{max}^{abs}), molar absorption

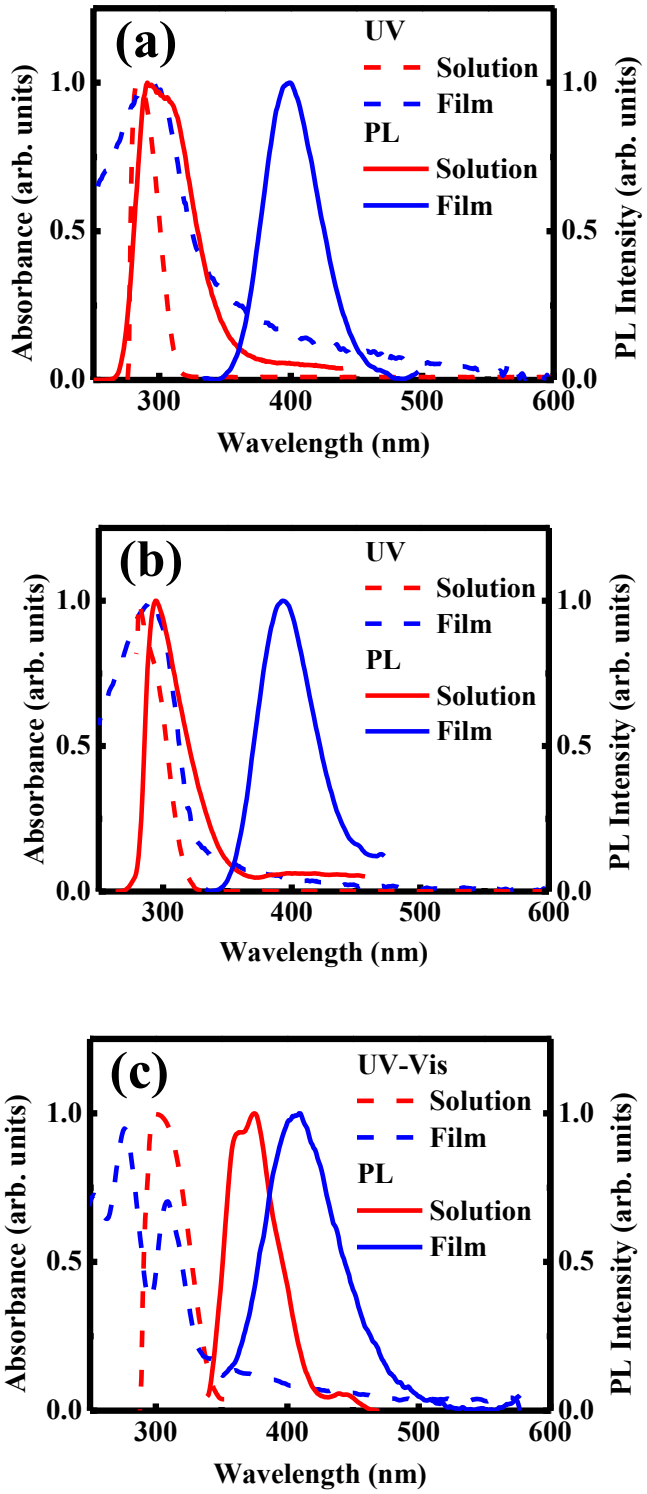

Figure 5.2. Normalized absorption and PL emission spectra of sulfone-based ETMs in dilute toluene solution (5×10^{-5} M) and thin solid films: (a) SPDP; (b) SPPP; and (c) SPDQ.

coefficient (log ϵ), PL emission maximum (λ_{max}^{em}) and optical band gap (E_g) are summarized in Table 5.1. A strong solution absorption peak was observed between 281nm and 298 nm which is assigned to the absorption of the diphenylsulfone unit in the molecules. Similar absorption spectra were observed in the three ETMs due to the common diphenylsulfone core in the molecules. In the case of **SPDP**, it showed an absorption maximum (λ_{max}^{abs}) at 285 nm (log ϵ = 4.33). The thin film absorption spectrum has a similar line shape except that λ_{max}^{abs} is at 296 nm. **SPPP** has an absorption with a maximum centered at 281 nm (log ϵ = 4.36) in solution

but red shifts to 289 nm in thin film. The absorption spectrum of the quinoline functionlized ETM, **SPDQ**, has a λ_{max}^{abs} at 298 nm (log ϵ = 3.47) in solution. However, the absorption spectrum of **SPDQ** thin films showed two absorption peaks at 279 nm and 306 nm; the latter λ_{max}^{abs} value originates from quinoline ring.[15] The red-shift of the π-π^* band between solution and thin film was 11 nm for **SPDP**, indicating an increase in electron delocalization in the bulk solid state. In addition, the π-π^* band in **SPPP** and **SPDQ** in both dilute solution and thin film is red-shifted by 8 nm compared to that of **SPDP**. This means that the extent of electron delocalization is greater with phenylpyridine and quinoline than with the pyridine. The PL emission maximum (λ_{max}^{em}) of **SPDP**, **SPPP** and **SPDQ** was observed at 291, 294 and 375 nm, respectively. The emission maximum is red-shifted with increasing π-conjugation. Optical band gaps of **SPDP**, **SPPP** and **SPDQ** were estimated from the absorption edge of the UV-Vis spectra, revealing E_g of 3.6, 3.79 and 3.64 eV, respectively.

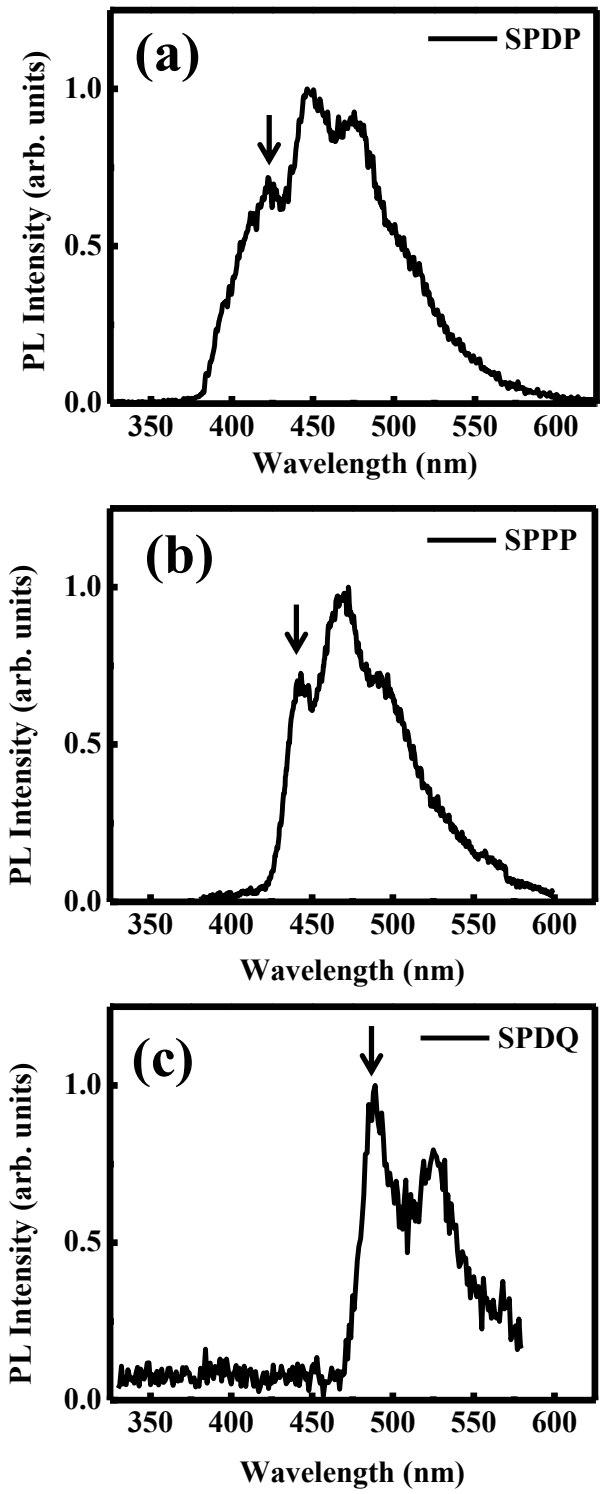

Figure 5.3. Normalized phosphorescence spectra of sulfone-based ETMs at 77 K: (a) SPDP; (b) SPPP; and (c) SPDQ.

The triplet energy (E_T) of the new ETMs was estimated from the shortest wavelength emission peak of the phosphorescence spectrum obtained at low temperature (77K) in dilute 2-methyl tetrahydrofuran solution. The phosphorescent spectra of the sulfone-based ETMs are shown in Figure 5.3. The measured triplet energies of the three ETMs are given in Table 5.1. In the case of **SPDP** and **SPPP**, their E_T values of 2.9 eV and 2.8 eV, respectively, are high enough to confine the triplet excitons of blue emitting FIrpic which has a triplet energy of 2.7 eV.[14,15] These triplet energy values are much higher than those of commercial ETMs, such as 2,9-dimethyl-4,7-diphenyl-1,10-phenanthroline (BCP) (E_T = 2.5 eV).[28] The E_T value of **SPDQ** (2.53 eV), which is comparable to that of

BCP, is too low to confine the triplet excitons of blue emitters but could be more useful for green and red triplet emitters.

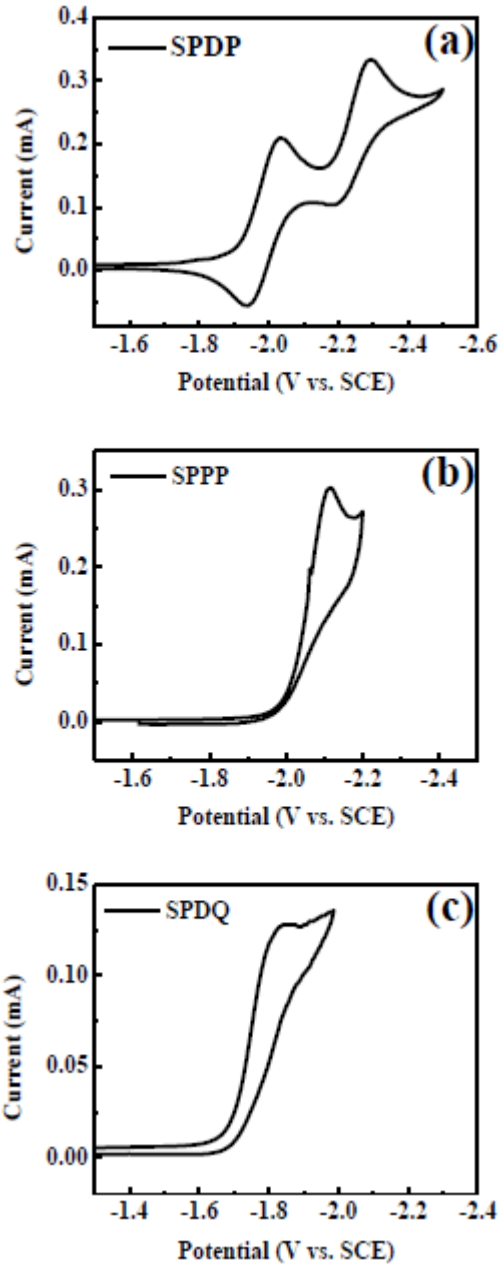

Figure 5.4. Cyclic Voltammogramms of sulfone-based ETMs in solution: (a) SPDP; (b) SPPP; and (c) SPDQ.

Cyclic Voltammetry and Electronic Structure Electronic structure (LUMO/HOMO energy levels) of the sulfone-based ETMs was studied by cyclic voltammetry (CV). The cyclic voltammograms of the ETMs in solution are shown in Figure 5.4. **SPDP** show two reversible reduction waves whereas the reduction CVs of **SPPP** and **SPDQ** were not reversible. The onset reduction potentials (E_{red}^{onset}) of the sulfone-based ETMs **SPDP**, **SPPP** and **SPDQ** are -1.83, -2.03 and -1.7 V (vs SCE), respectively. The LUMO energy levels of the ETMs were obtained according to the equation $E_{LUMO} = eE_{red}^{onset} + 4.4$ eV,[8,29] using ferrocene as the internal standard. The LUMO levels of **SPDP**, **SPPP** and **SPDQ** were found to be -2.57, -2.37 and -2.7 eV, respectively. Oxidation CV was not observed for any of the sulfone-based materials. The HOMO levels of **SPDP**,

SPPP and **SPDQ** were found to be -6.17, -6.16 and -6.32 eV, respectively, as estimated from the difference between the LUMO level and the optical band gap (E_g). The HOMO levels of **SPDP** and **SPPP** are similar to those of other ETMs with deep HOMO level such as BCP (-6.1 eV) or 4,7-diphenyl-1,10-phenanthroline (BPhen) (-6.2 eV).[30] Similar with BCP and Bphen, we believe that the low-lying HOMO energy levels of the new materials suggest good exciton and hole blocking properties. The LUMO/HOMO energy levels of the sulfone-based ETMs are shown together in Figure 5.5.

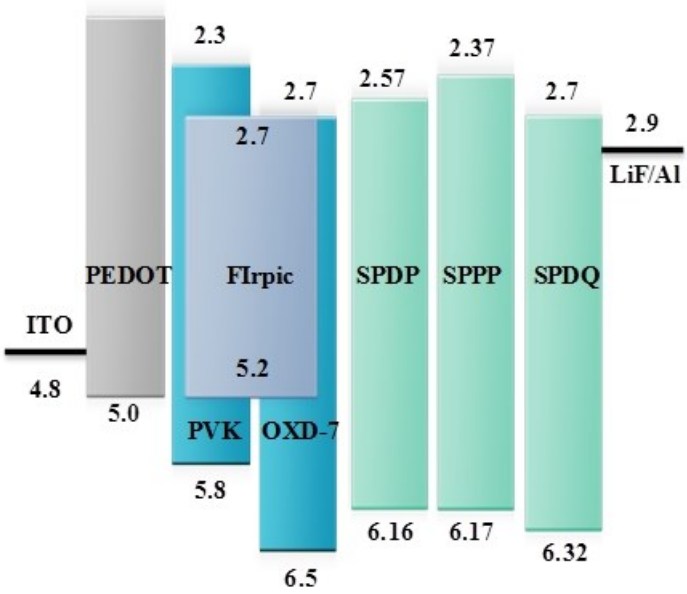

Figure 5.5. Energy level diagram of the blue PhOLEDs with sulfone-based ETMs.

Space-Charge-Limited Current (SCLC) Carrier Mobility We investigated the electron transport properties of the sulfone-based materials by space-charge-limited current (SCLC) measurement of the electron mobility. The current density-voltage (*J-V*) characteristics of the SCLC devices with the structure of ITO/Sulfone-based ETM (100 nm)/Al are shown in **Figure 5.6**. The sulfone-based ETMs were thermally vacuum-evaporated to form 100 nm thick layers followed by Al deposition. The electron mobility was extracted by fitting the current density-voltage (*J-V*) curves in the near quadratic region according to the modified Mott-Gurney equation,[33,34]

$$J = \frac{9}{8}\,\varepsilon\varepsilon_0\mu\frac{V^2}{L^3}exp\left(0.89\beta\frac{\sqrt{V}}{\sqrt{L}}\right)$$

where J is the current density, ε_0 is the permittivity of free space, ε is the relative permittivity, μ is the zero-field mobility, V is the applied voltage, L is the thickness of active layer, and β is the field-activation factor. We fixed the maximum electric field at 3.0×10^5 V cm^{-1}. The zero-field electron mobility of **SPDP** was found to be 5.9×10^{-6} cm^2 V^{-1} s^{-1} ($\beta = 3.9 \times 10^{-5}$ $cm^{1/2}$ $V^{-1/2}$) whereas the value for **SPDQ** was 1.6×10^{-6} cm^2 V^{-1} s^{-1} ($\beta = 4.7 \times 10^{-5}$ $cm^{1/2}$ $V^{-1/2}$). The electron mobility of **SPDP** is higher than that of **SPDQ** although they are of the same order of magnitude. However, **SPPP** showed a relatively low electron mobility of 7.3×10^{-8} cm^2 V^{-1} s^{-1} ($\beta = 1.3 \times 10^{-5}$ $cm^{1/2}V^{-1/2}$), which is two orders of magnitude lower than the electron mobility of **SPDP** and **SPDQ.** The low carrier mobility in **SPPP** could be due to the poor intermolecular interactions as a result of the phenyl groups on each side. Attached phenyl ring disturbs planar molecular structure and thus hinders efficient molecular packing.

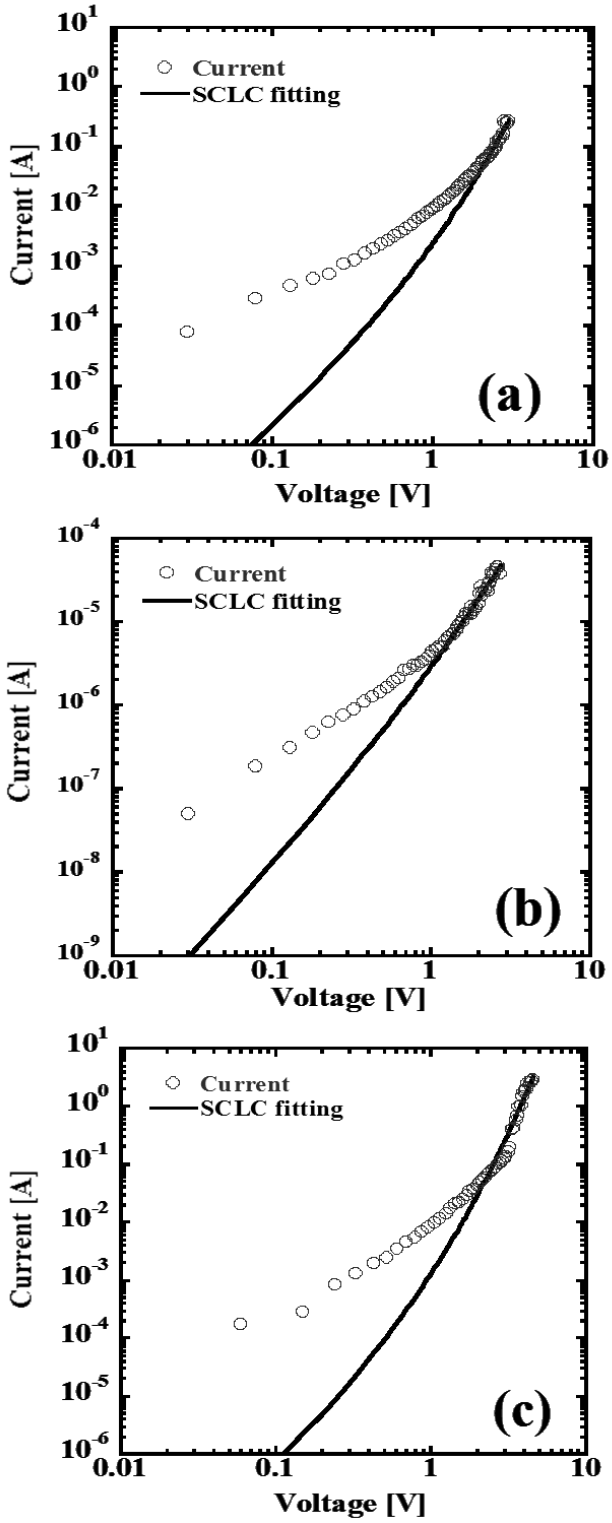

Figure 5.6. Current-voltage characteristics of the SCLC devices with the structure of ITO/sulfone-based ETM(100 nm)/Al; (a) SPDP; (b) SPPP; and (c) SPDQ.

Blue PhOLEDs with Sulfone-based Electron Transport Layer

To evaluate electron-transport and exciton blocking ability of the new sulfone-based ETMs, we initially fabricated PhOLEDs with **SPDP** ETL. In order to optimize device performance, the thickness of **SPDP** ETL was varied as 5, 15, and 30 nm in blue PhOLEDs. Figure 5.7 shows the electrical characteristics and performance of PhOLEDs with different thicknesses of **SPDP**. The PhOLEDs with 5 and 15 nm thick **SPDP** showed similar current densities whereas the device with 30 nm thick **SPDP** showed a lower current density due to its much larger thickness. The maximum

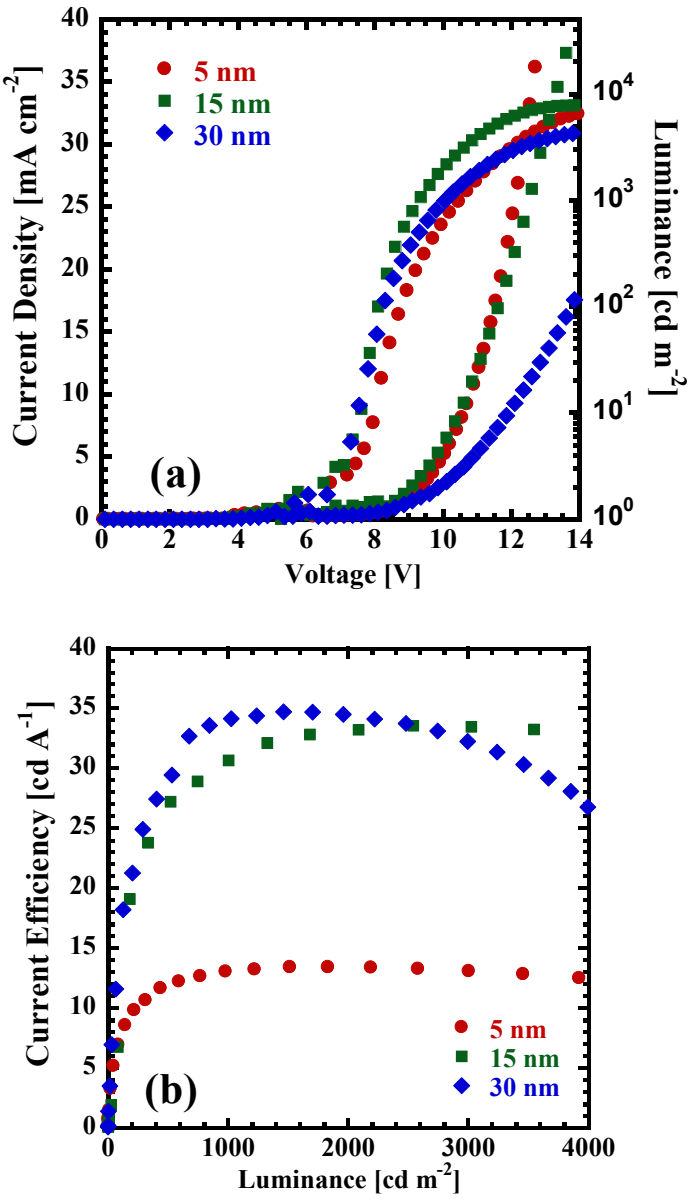

Figure 5.7. (a) Current density-voltage-luminance (J-V-L) characteristics (b) Current efficiency-luminance (CE-L) of blue PhOLEDs with different thicknesses of SPDP ETL.

luminance (brightness) decreased with increasing thickness of the **SPDP** ETL. However, the performance of the PhOLEDs significantly increased with 15 and 30 nm **SPDP** ETL compared to the 5 nm ETL. The PhOLEDs with 5 nm thick **SPDP** showed a high turn-on voltage of 6.6 V and a current efficiency (CE) of 13.4 cd A^{-1} (power efficiency (PE) = 3.9 lm W^{-1}). The performance of the PhOLEDs dramatically changes with thicker **SPDP** ETL (15 and 30 nm). PhOLEDs with 15 nm **SPDP** ETL showed a reduced turn-on voltage (5.2 V) and also a significantly increased efficiency (Figure 5.7b). This represents a 2.5-fold higher efficiency compared to the device with 5 nm ETL thickness. As the thickness of **SPDP** increases to 30 nm, device showed a slightly higher turn-on voltage (5.5 V) compared to the device with 15 nm ETL thickness. The CE and PE of the PhOLEDs with 30 nm thick **SPDP**

ETL was comparable to the device with 15 nm thick **SPDP**. Nevertheless, the current efficiency of the 30 nm **SPDP** device showed the highest value of 33.9 cd A^{-1}. The device with 15 nm **SPDP** ETL had a high current efficiency of 33.6 cd A^{-1}, which is similar to the 30 nm **SPDP** ETL device performance. We could observe severe roll-off in efficiency in the PhOLED with 30 nm thick **SPDP** whereas the device with 15 nm thick **SPDP** showed a reduced roll-off in efficiency at high luminance.

Electroluminescence (EL) spectra of all the blue PhOLEDs with different thicknesses of **SPDP** are shown in Figure 5.8. The EL spectra showed that[14] the blue emission originated from FIrpic triplet emitter with the maximum peak at 472 nm. We can clearly see the EL intensity of shoulder peak around 500 nm increases as the thickness of **SPDP** increases. The increased EL intensity of the shoulder peak is due to a microcavity effect[35], which is also consistent with the increased device performance. Commission Internationale de L'Eclairage (CIE) 1931 coordinates of the devices changed from (0.13, 0.28) to (0.14, 0.34) when the thickness of **SPDP** changed from 5 to 30 nm. This result imply that although increased EL intensity of the shoulder peak around 500 nm is effective for the enhancement of the device performance, there is an undesirable change in the purity of blue color due to the green emission. Therefore, we

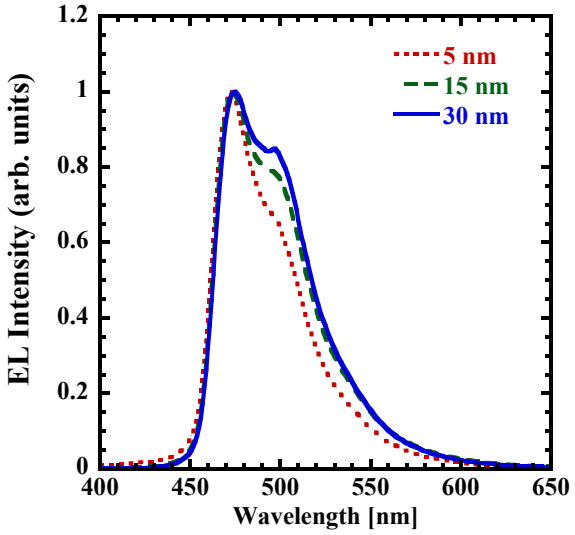

Figure 5.8. Normalized EL spectra of the blue PhOLEDs with different thicknesses of SPDP ETL.

consider the 15 nm thickness as the optimum for high efficiency and low roll-off in efficiency for blue PhOLEDs using sulfone-based ETMs.

We fabricated blue PhOLEDs with all the sulfone-based ETMs (**SPDP**, **SPPP**, and **SPDQ**) with the ETL thickness fixed at 15 nm. Standard device configuration for the blue PhOLEDs were ITO/PEDOT:PSS/PVK:OXD-7:FIrpic/ETM/LiF/Al. Four different series of PhOLEDs were fabricated to investigate the effect of high triplet energy, electron mobility and energy levels on device performance. Device I had no ETL and devices II, III, and IV had **SPDP**, **SPPP**, and **SPDQ** ETL, respectively.

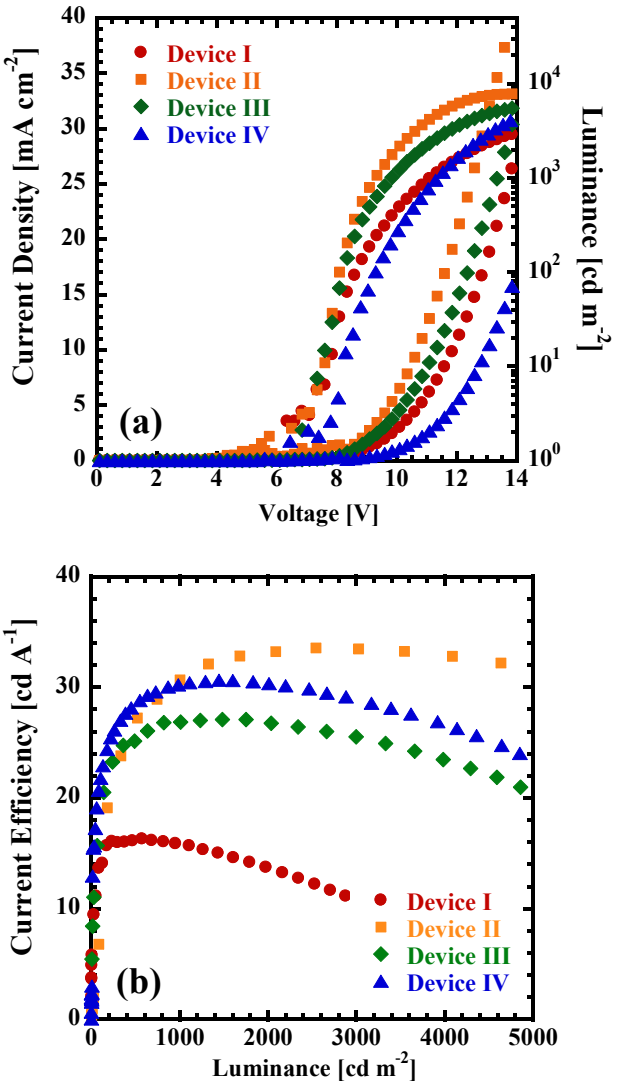

Figure 5.9. (a) Current density-voltage-luminance (J-V-L) of blue PhOLEDs with sulfone-based ETLs. (b) Current efficiency-luminance (CE-L) of blue PhOLEDs with sulfone-based ETMs.

The current density – voltage – luminance (*J-V-L*), and current efficiency – luminance (*CE-L*) characteristics of PhOLEDs with sulfone-based ETMs as the electron transport layer are shown in Figure 5.9. PhOLEDs with sulfone-based ETLs all showed enhanced device

performance (devices II, III, and IV) compared to the device without ETL (device I) as shown in Figure 5.9 and Table 5.2. Device II showed a significantly reduced turn-on voltage (5.2 V) and had an increased current efficiency (CE) of 33.6 cd A^{-1} with an external quantum efficiency (EQE) of 19.6 %, while device I showed a high turn-on voltage (6.3 V) and a CE of 16.2 cd A^{-1} with an EQE of 10.2%. Devices III and IV also had enhanced device performance, showing CE of 27.1 and 30.6 cd A^{-1} (EQE = 13.9 and 15.7%), respectively. However, the maximum luminance of device IV was much lower than that of device II and device III, which is presumably due to the low current density. Comparing the current densities, device II showed the highest current density and the device IV showed the lowest current density, which can be correlated with the energy levels of the sulfone-based ETMs. **SPDP** has an energy barrier of only 0.27 eV with PVK-based polymeric host material (**Figure 5.4**), whereas **SPDQ** has a large energy barrier of 0.4 eV with the host material. Although the energy barrier between **SPPP** and PVK host material is very small (0.07 eV), the electron mobility of **SPPP** is very low (~ 10^{-8} cm^2 $V^{-1}s^{-1}$) compared to the **SPDP** and **SPDQ** (~ 10^{-6} cm^2 $V^{-1}s^{-1}$), which is consistent with the performance of the blue PhOLEDs.

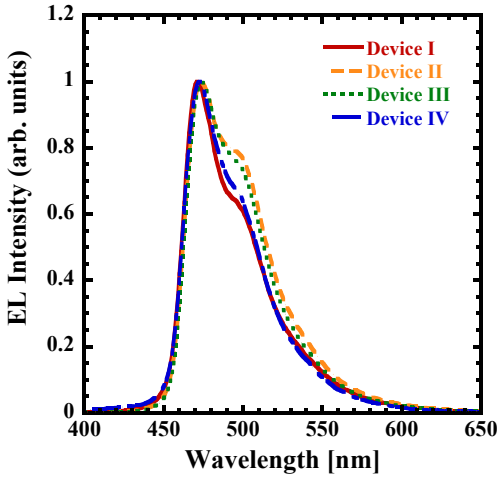

Figure 5.10. Normalized EL spectra of the blue PhOLEDs with sulfone-based ETMs.

Device IV with **SPDQ** also showed significantly enhanced device performance despite the relatively low triplet energy value of **SPDQ** (E_T = 2.53 eV) compared to the other high triplet energy sulfone-based ETMs (**SPDP**, E_T = 2.9 eV and

SPPP, E_T = 2.8 eV). We note that in order to confine triplet excitons effectively inside the EML, the triplet energy of ETL should be higher than that of the FIrpic emitter (2.7 eV).[9,36] Nevertheless, **SPDQ** ETL with a low triplet energy significantly improved the PhOLED efficiency, which implies that facilitating efficient injection and electron transport by an ETM with high electron mobility is also an important factor to obtain high performance PhOLEDs even without a high triplet energy. Furthermore, EL spectrum of device IV with **SPDQ** ETL showed blue emission with very weak shoulder peak around 500 nm with CIE coordinates of (0.13, 0.28) while the EL spectrum of device III with **SPPP** ETL had a more prominent shoulder peak with CIE coordinates (0.14, 0.32) with unwanted greenish emission (Figure 5.10). These results suggest that an appropriate LUMO level of the ETM is essential while high electron mobility is also important to facilitate electron-transport to achieve high-performance PhOLEDs.

Table 5.2. Device chracteristics of blue PhOLEDs based on sulfone-based ETMs. [a]

Device	ETL	V_{on} [b] [V]	Drive Voltage [V]	Current Density [mA cm^{-2}]	Luminance [cd m^{-2}]	Current Efficiency [cd A^{-1}]	Power Efficiency [lm W^{-1}]	External Quantum Efficiency [%]
Device I	None	6.3	15.4 *9.8*	53.4 *2.2*	3490 *360*	6.5 *16.2*	1.3 *4.1*	4.1 *10.2*
Device II	**SPDP**	5.2	13.8 *10.4*	39.6 *33.4*	7810 *2730*	19.2 *33.6*	4.3 *10.6*	11.2 *19.6*
Device III	**SPPP**	6.7	15.4 *10.0*	49.7 *4.1*	6010 *1100*	12.1 *27.1*	2.1 *8.9*	6.2 *13.9*
Device IV	**SPDQ**	6.3	14.8 *10.2*	37.2 *4.5*	5990 *1390*	16.1 *30.6*	3.2 *8.2*	7.3 *15.7*

[a]Values in italic correspond to those at maximum device efficiencies. [b]Turn-on voltage (at luminance of ~1 cd m-^{2}).

5.1.4. Conclusions

A series of new sulfone-based electron transport materials with high triplet energies and wide band gaps are synthesized, characterized and demonstrated to lead to highly efficient blue PhOLEDs. The combination of a diphenylsulfone core with electron withdrawing end groups such as pyridine, phenylpyridine, and quinoline is found to be effective in achieving a high triplet energy (2.8 – 2.9 eV) and a wide energy gap (3.6 – 3.8 eV), resulting in efficient exciton/hole blocking with good electron-transport characteristics. SCLC derived electron mobility was $(2 – 6) \times 10^{-6}$ $cm^2 V^{-1}s^{-1}$ for **SPDP** and **SPDQ** thin films but was significantly lower in the case of **SPPP** (7×10^{-8} cm^2 $V^{-1}s^{-1}$). Density functional theory (DFT) calculated triplet energy values of the sulfone-based materials were found to be in good agreement (within 5 – 10%) of experimental values measured from low temperature phosphorescence spectra. Blue PhOLEDs incorporating the new sulfone-based materials as an electron transport layer had a significantly enhance performance with a current efficiency of up to 33.6 cd A^{-1} and external quantum efficiency of 19.6%. The results suggest that sulfone-based electron transport materials are promising for achieving high-performance phosphorescent optoelectronic devices.

5.2. Blue Phosphorescent OLEDs with Dibenzosuberane-based High Triplet Energy Electron-Transport Materials

5.2.1. Introduction

Spirobifluorene-based materials are promising class of electron-transport materials (ETMs) due to their high luminescence efficiency, high charge carrier mobility and excellent thermal stability. We theoretically investigated spiro-based materials which can have high mobility and good electron transport property. We have also designed spiro-based materials containing dibenzosuberane unit with the aim to increase the triplet energy. Furthermore, there is no patent related to the spiro structure containing dibenzosuberane core as electron transport materials in PhOLEDs. The molecular structures of the spiro-based materials are shown in Chart 5.2. The dibenzosuberane unit is formed by two aromatic phenyl rings fused with a seven-atom ring with a non-conjugated structure. Advantage of the dibenzosuberane unit designed here is that it can have a high triplet energy ($E_T > 3.0$ eV) with potentially good electron transport properties.

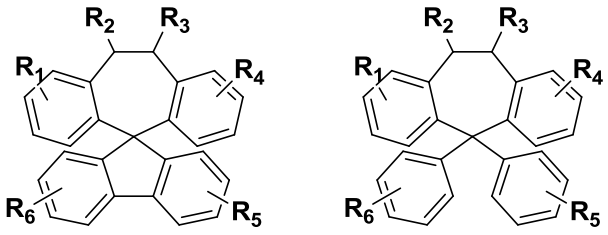

Chart 5.2. Molecular structure of possible dibenzosuberane-based ETMs.

Initial molecular simulation results of the new dibenzosuberane-based ETMs are shown in Figure 5.11. The *ab initio* calculations were performed using a suite of Gaussian 03 programs

and the molecular structures of the newly designed dibenzosuberane-based materials were fully optimized by density functional theory (DFT) using Beck'e three parameterized Lee-Yang-Parr exchange functional (B3LYP) with 6-31G* basis sets. The HOMO orbitals are distributed over the whole structure of the dibenzosuberane-based materials. This indicates that HOMO levels of these new dibenzosuberane-based ETMs is determine largely by the fluorene structure. The LUMO orbitals of the pyridine substituents are dispersed in the fluorene and suberane moieties. However, the molecular structure of quinoline substituted compounds, and the LUMO orbital was distributed into the quinoline groups. By this mean, the LUMO mostly depends on the substituents with strong electron transport properties, leading to the LUMO level for electron injection. It is expected that the dibenzosuberane-based ETMs with quinoline substitution will show better electron transport properties than dibenzosuberane-based ETM with pyridine substituents.

The calculated data of triplet energy and HOMO/LUMO energy levels are shown in Table 5.3. The calculated results indicate that the triplet energy of **3,7-DPSDF**, **10,11-DPSDF**, **3,7-DQSDF** and **10,11-DQSDF** are 3.01, 3.01, 2.70 and 2.66 eV, respectively.

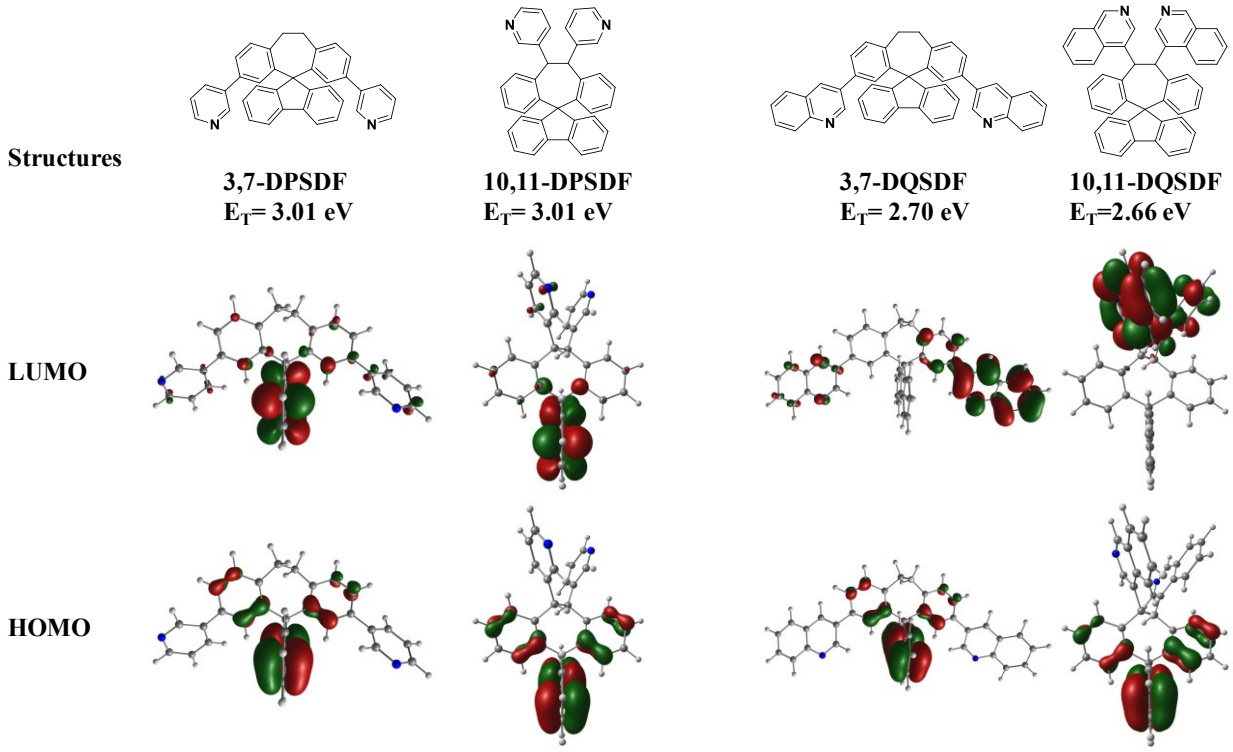

Figure 5.11. Molecular structures and calculated HOMO/LUMO orbitals of dibenzosuberane-based materials.

Table 5.3. Calculated energy levels and E_T of dibenzosuberane-based ETMs.

	HOMO (eV)	LUMO (eV)	E_g (eV)	E_T (eV)
3,7-DPSDF	-5.82	-0.99	4.83	**3.01**
10,11-DPSDF	-5.79	-0.97	4.81	**3.01**
3,7-DQSDF	-5.77	-1.41	4.35	2.70
10,11-DQSDF	-5.76	-1.48	4.27	2.66

5.2.2. Experimental Section

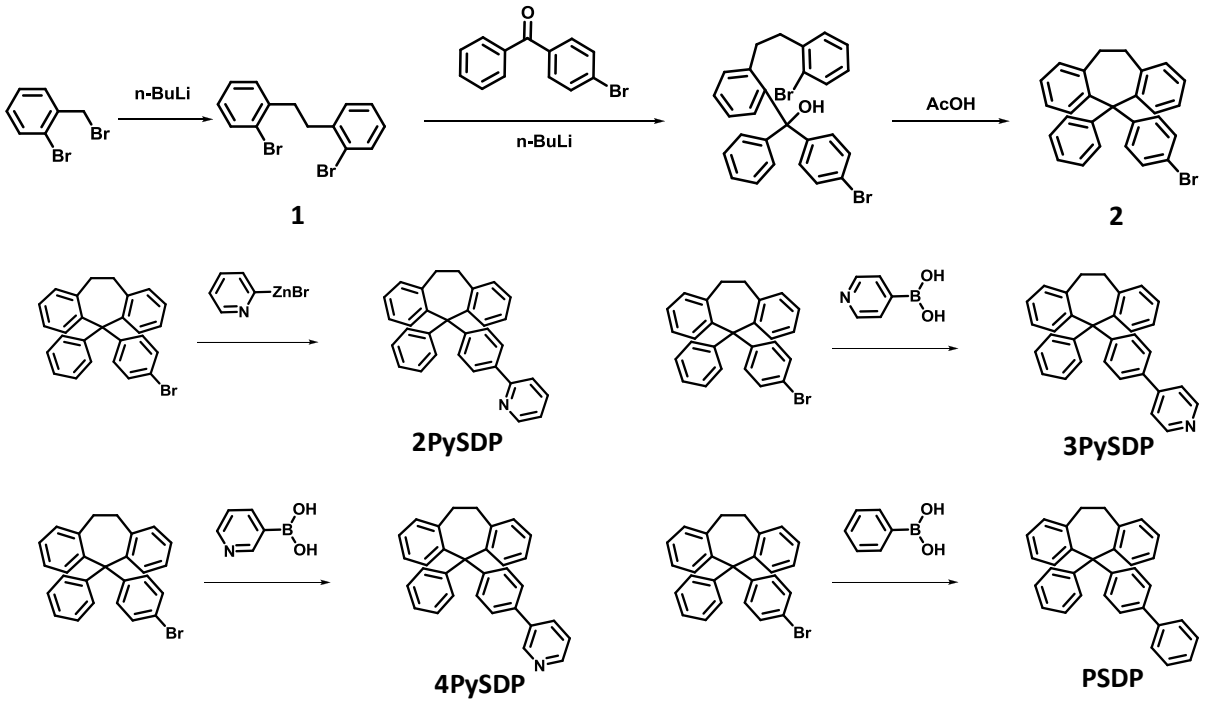

Scheme 5.4. Synthesis of the 2PySDP, 3PySDP, 4PySDP and PSDP.

Synthesis of Monosubstituted Dibenzosuberane-based ETMs. Synthetic routes of monosubstituted dibenzosuberane-based electron transport materials are shown in Scheme 5.4. We have synthesized four spiro-compounds with a new backbone structure, 5,5-(4-bromophenyl)(phenyl)-9H-dibenzosuberane (**2**) using 4-bromobenzophenone. A coupling reaction of 2-bromobenzyl bromide with n-BuLi in tetrahydrofuran gave 1,2-bis(2-bromophenyl)ethane (**1**) in 91% yield, and **2** was prepared by lithiation of **1** with over 60 % yield and followed by cyclization using acid-catalysts. A palladium-catalyzed Negishi cross coupling reaction between 2-pyridylzinc bromide and **2** was conducted to get **2PySDP**. The other final compounds **3PySDP**, **4PySDP** and **PSDP** were synthesized by a Suzuki coupling reaction with pyridinylboronic acid and phenylboronic acid using tetrakis(triphenylphosphine)palladium(0)

catalyst in anhydrous tetrahydrofuran. The four final products (**2PySDP**, **3PySDP**, **4PySDP** and **PSDP**) were purified by column chromatography.

Synthesis of Disubstituted Dibenzosuberane-based ETMs. The synthetic routes of the disubstituted dibenzosuberane-based electron transport materials are shown in Scheme 5.5. We have synthesized three spiro-compounds with a new backbone structure, 5,5-bis(4-bromophenyl)-9H-dibenzosuberane (**2**) using 4,4'-dibromobenzophenone. The coupling reaction of 2-bromobenzyl bromide with n-BuLi in tetrahydrofuran gave 1,2-bis(2-bromophenyl)ethane (**1**) in 91% yield, and **2** was prepared by lithiation of **1** with over 67 % yield and followed by cyclization using acid-catalysts. The three final compounds **3DPySDP**, **4DPySDP** and **DPSDP** were synthesized by a Suzuki coupling reaction with pyridinylboronic acid or phenylboronic acid using tetrakis(triphenylphosphine)palladium(0) catalyst in anhydrous tetrahydrofuran. The three products (**3DPySDP**, **4DPySDP** and **DPSDP**) were purified by column chromatography.

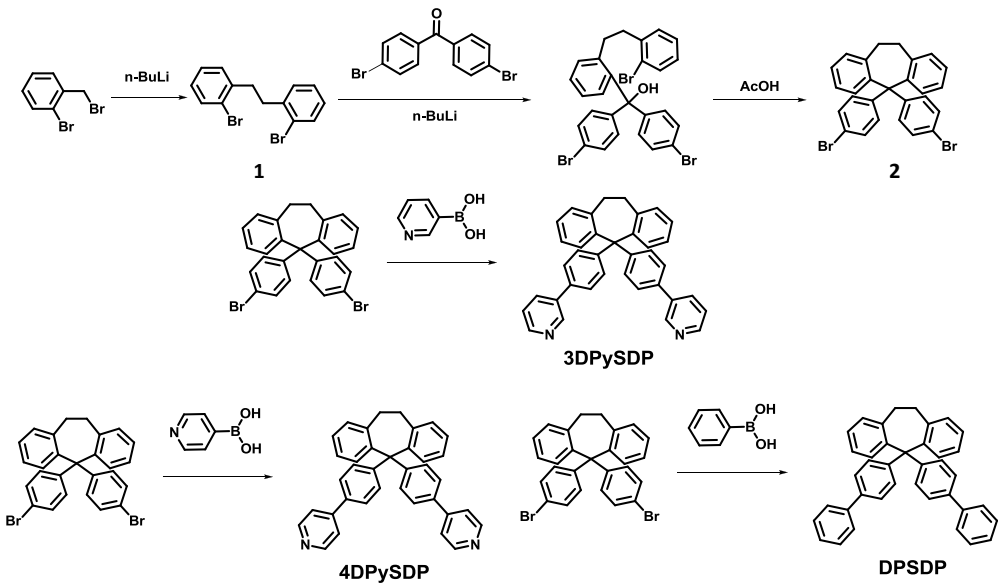

Scheme 5.5. Synthesis of 3DPySDP, 4DPySDP, and DPSDP.

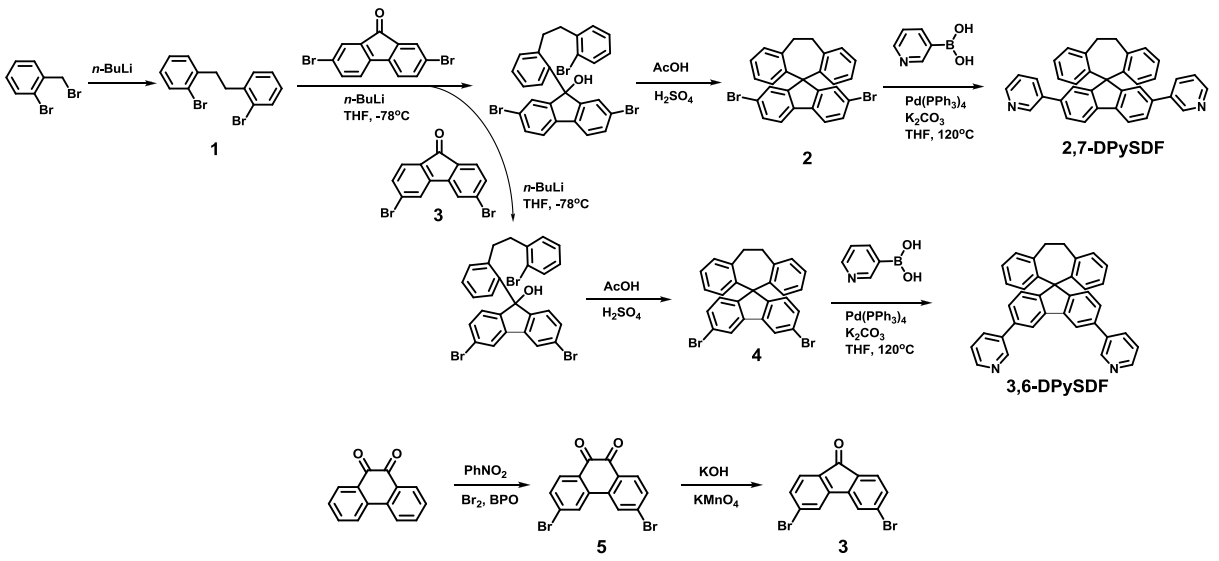

Scheme 5.6. Synthesis of 2,7-DpySDF and 3,6-DPySDF.

Synthesis of 2,7- and 3,6-Substituted Spiro[fluorene-9,5'-dibenzosuberane] ETMs. The synthetic routes of disubstituted dibenzosuberane-based electron transport materials are shown in Scheme 5.6. We have synthesized four spiro-compounds with a new backbone structure, 2,7-dibromo-spiro[fluorene-9,5'-dibenzosuberane] (**2**) and 3,6-dibromo-spiro[fluorene-9,5'-dibenzosuberane] (**4**) using 2,7-dibromofluorenone and 3,6-dibromofluorenoen, respectively. A coupling reaction of 2-bromobenzyl bromide with n-BuLi in tetrahydrofuran gave 1,2-bis(2-bromophenyl)ethane (**1**) in 91% yield, and **2** was prepared by lithiation of **1** with over 60 % yield and followed by cyclization using acid-catalysts. The final compounds: **2,7-DPySDPF** and **3,6-DPySDF** were synthesized by a Suzuki coupling reaction with pyridinylboronic acid using tetrakis(triphenylphosphine)palladium(0) catalyst in anhydrous tetrahydrofuran. The two final products (**2,7-DPySDPF** and **3,6-DPySDF**) were purified by column chromatography.

5.2.3. Results and Discussion

Photophysical, Electrochemical, and Thermal Properties of Monosubstituted dibenzosuberane-containing ETMs. UV-vis optical absorption and photoluminescence (PL) spectra of monosubstituted dibenzosuberane-based ETMs in dilute THF solution (10^{-5} M) and thin films are shown in Figure 5.12. Photophysical properties of the four ETMs are summarized in Table 5.4. The absorption peak of **2PySDP** was 275 nm in dilute THF solution and 259 nm with a shoulder peak at 280 nm in thermally evaporated thin films. In the case of **3PySDP** and **PSDP**, the absorption maximum (λ_{max}^{abs}) values were 258 nm and 257 nm, respectively, in solution as well as thin films. The absorption peak of **4PySDP** was found at 264 nm in solution and at 268 nm in thin film. The similarity of the λ_{max}^{abs} values of these four ETMs is originated from the same core molecular structure: 5,5'-bis(phenyl)-9H-dibenzosuberane. The optical band gaps (E_g^{opt}) of the four ETMs determined from the absorption edge of the thin film spectra was found to be 3.88 - 4.00 eV (**Table 8**). The PL emission peak of **3PySDP** and **4PySDP** in solution were observed at 298 nm whereas **2PySDP** and **PSDP** showed at 310 nm and 307 nm, respectively. Thin film PL emission peak were found in the 414 to 425 nm range. The solid-state emission spectra were dramatically red shifted from the solution spectra, which implied high intermolecular interactions.

Thermal properties of the four different compounds (**2PySDP**, **3PySDP**, **4PySDP** and **PSDP**) were characterized by differential scanning calorimetry (DSC) and thermogravimetric analysis (TGA) (Figure 5.13). We could not observe glass transition temperatures (T_g) or a melting temperatures (T_m) from DSC scans in the 30 – 300 ^oC range. The onset decomposition temperatures (T_d) of the dibenzosuberane-based materials were high (> 329 ^oC), which

demonstrates their thermal robustness. This means that the dibenzosuberane-based materials have amorphous structure and indeed thermally stable.

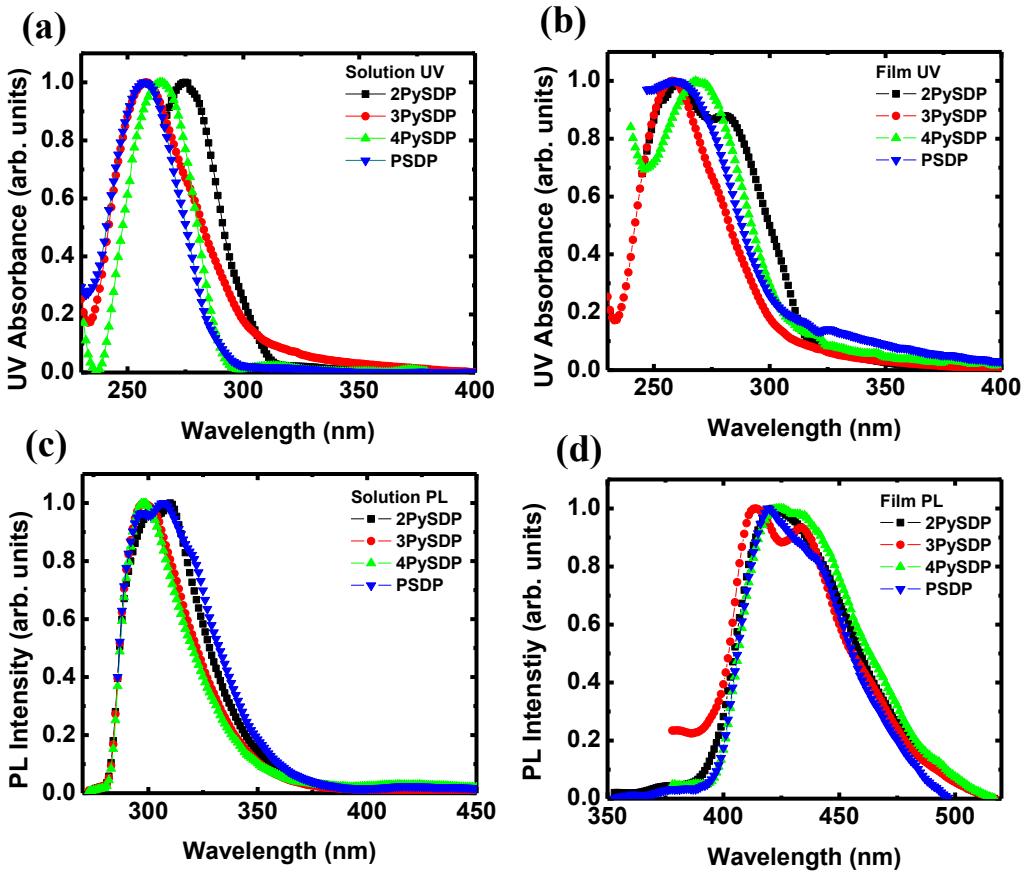

Figure 5.12. Normalized absorption and PL emission spectra of (a) 2PySDP (black square); (b) 3PySDP (red circle); (c) 4PySDP (green triangle); and (d) PSDP (blue inverse triangle).

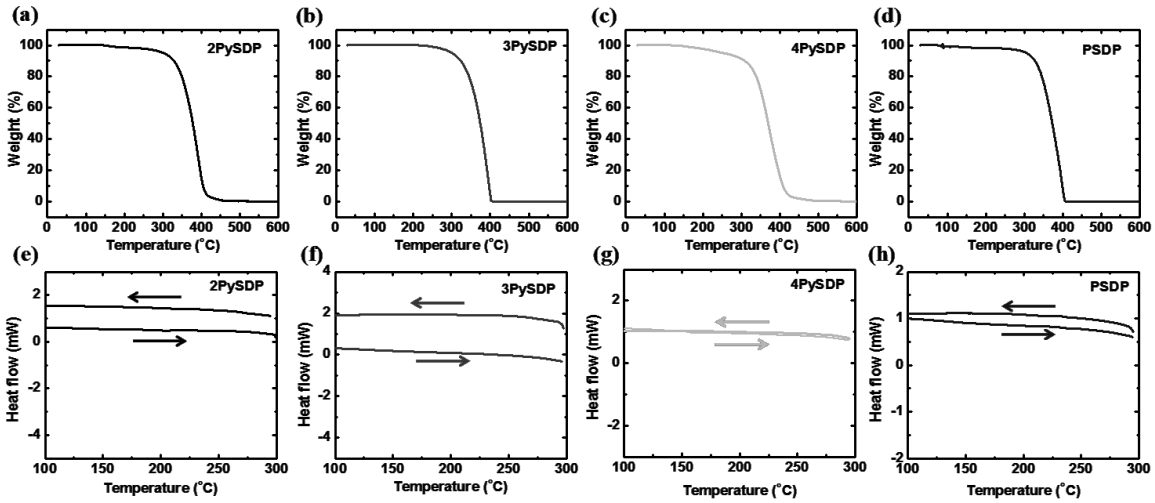

Figure 5.13. TGA and DSC thermograms of four monosubstituted dibenzosuberane-based ETMs (a),(e) 2PySDP; (b),(f) 3PySDP; (c),(g) 4PySDP; and (d),(h) PSDP.

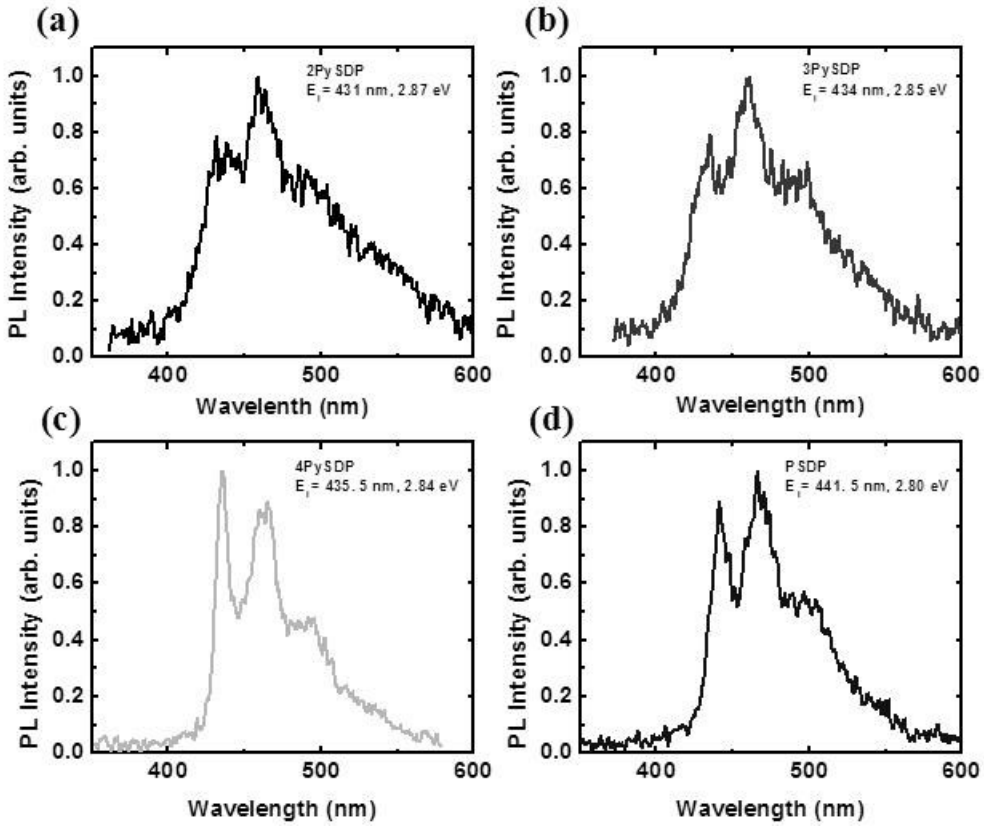

Figure 5.14. Normalized phosphorescence spectra of dibenzosuberane-based ETMs at 77 K: (a) 2PySDP; (b) 3PySDP; (c) 4PySDP; and (d) PSDP.

The HOMO/LUMO energy levels of **2PySDP**, **3PySDP**, **4PySDP** and **PSDP** were estimated from cyclic voltammetry (CV) and in some cases in combination with the absorption edge optical band gap. The HOMO/LUMO energy levels of dibenzosuberane-based materials are summarized in Table 5.4. The LUMO levels of **2PySDP**, **3PySDP**, **4PySDP** and **PSDP** were obtained from the onset reduction potential of the CV, giving LUMO levels of -2.43, -2.33, -2.4 and -2.32 eV, respectively, which are much higher than that of well-known ETM tris(8-hydroxyquinoline)aluminum (Alq_3) (-3.0 eV) and similar to well-known hole-blocking material 2,9-dimethyl-4,7-diphenyl-phenathroline (BCP) (-2.4 eV). The HOMO levels of the four compounds were found to be -6.3, -6.33, -6.33 and -6.29 eV, respectively, which were estimated from the difference between LUMO level and the optical band gap. It may also be possible to use these ETMs as host materials because the HOMO/LUMO energy levels of the four molecules are very similar with those of *N,N*-dicarbazolyl-3,5-benzene (mCP) (-6.1 eV/-2.4 eV), which is a very well-known host material in highly efficient PhOLEDs.

Phosphorescence spectra were obtained at 77 K to measure the triplet energies of the ETMs as shown in Figure 5.14. The triplet energies of the four mono-substituted dibenzosuberane-based ETMs (**2PySDP**, **3PySDP**, **4PySDP**, **PDSP**) were determined from the highest energy peak of the low temperature phosphorescent PL spectra and found to be 2.80-2.87 eV (Table 5.4). The triplet energies of the four ETMs are high enough to confine the triplet excitons of blue FIrpic (E_T = 2.7 eV). The results demonstrate that these four materials with high triplet energy are very promising for blue PhOLEDs.

Table 5.4. Photophysical, electrochemical, and thermal properties of 2PySDP, 3PySDP, 4PySDP and PSDP.

		2PySDP	3PySDP	4PySDP	PSDP
λ_{max}^{abs} (nm)	Solution[a] (log ϵ)[b]	275 (4.64)	258 (4.97)	264 (4.87)	257 (5.04)
	Thin film[c]	259, 280	258	268	258
λ_{max}^{em} (nm)	Solution[a]	310	298	298	307
	Thin film[c]	421	414	425	419
E_g^{opt}(eV)[d]		3.88	4.00	3.93	3.97
E_T (eV)		2.87	2.85	2.84	2.80
LUMO (eV)		-2.43	-2.33	-2.4	-2.32
HOMO (eV)		-6.3	-6.33	-6.33	-6.29
T_m (^oC)		170	154	155	200
T_d (^oC)		347	349	329	342

[a]The absorption and emission spectra in dilute THF solution (10^{-5}M). [b]log ϵ calculated at λ_{max}^{abs}. [c]The thin films were thermally evaporated. [d]Calculated from the absorption band edge of the thin film.

Photophysical, Electrochemical, and Thermal Properties of Disubstituted Dibenzosuberane-based ETMs. Optical absorption and photoluminescence (PL) spectra of the **3DPySDP**, **4DPySDP** and **DPSDP** in dilute THF solution (10^{-5} M) and in thin films are shown (Figure 5.15). The solid state absorption and PL emission spectra of **3DPySDP**, **4DPySDP** and **DPSDP** were obtained from thermally evaporated thin films. The key numerical values of the photophysical properties of the disubstituted dibenzosuberane-based ETMs, including absorption maximum (λ_{max}^{abs}), molar absorption coefficient (log ϵ), PL emission maximum (λ_{max}^{em}) and optical band gap (E_g^{opt}) are summarized in **Table 9**. A strong solution absorption peak was observed between 254 nm and 263 nm which is assigned to the absorption of the spirodibenzosuberane unit in the molecules. Similar absorption spectra were observed in the three ETMs due to the common spirodibenzosuberane core in the molecules. The absorption peak of **3DPySDP**, **4DPySDP** and **DPSDP** were observed 266, 271 and 262 nm, respectively, as thin films. The PL emission maximum (λ_{max}^{em}) of **3DPySDP**, **4DPySDP** and **DPSDP** was

observed at 375, 381 and 374 nm, respectively in THF solution. The emission maxima in the films are red shifted around 20 nm from the solution spectra. Optical band gaps of **3DPySDP**, **4DPySDP** and **DPSDP** were estimated from the absorption edge of the UV-Vis spectra, revealing E_g^{opt} of 3.4, 3.44 and 3.46 eV, respectively.

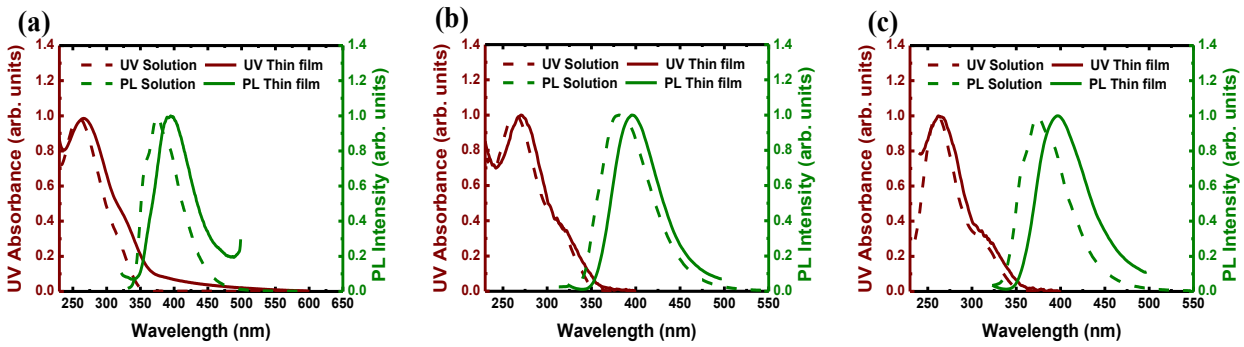

Figure 5.15. Normalized absorption and PL emission spectra of dibenzosuberane-based ETMs: (a) 3DPySDP; (b) 4DPySDP; and (c) DPSDP.

The triplet energy (E_T) of the new ETMs was estimated from the shortest wavelength emission peak of the phosphorescence spectrum obtained at low temperature (77K) in dilute 2-methyl tetrahydrofuran solution. The phosphorescent spectra of the disubstituted dibenzosuberane-based ETMs are shown in Figure 5.16. The measured triplet energies of the three ETMs are given in **Table 5.5**. **3DPySDP**, **4DPySDP** and **DPSDP** with E_T values over 3.0 eV are high enough to confine the triplet excitons of FIrpic triplet emitter with E_T of 2.7 eV. The measured triplet energy values of disubstituted dibenzosuberane-based ETMs are much higher than those of commercial ETMs, such as 2,9-dimethyl-4,7-diphenyl-1,10-phenanthroline (BCP) (E_T = 2.5 eV) and 1,3,5-tri(*m*-pyrid-3-yl-phenyl) (TmPyPB) (E_T= 2.78 eV).

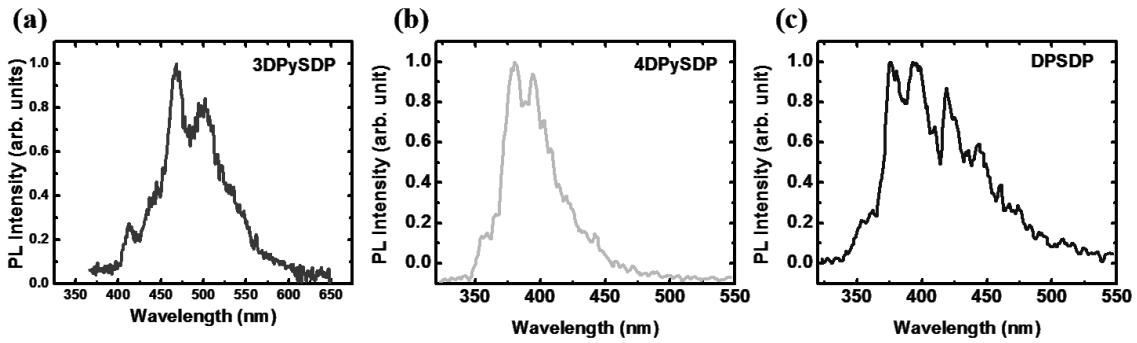

Figure 5.16. Normalized phosphorescence spectra of dibenzosuberane-based ETMs at 77 K: (a) 3DPySDP; (b) 4DPySDP; and (c) DPSDP.

Electronic structure (LUMO/HOMO energy levels) of the disubstituted dibenzosuberane-based ETMs was studied by cyclicvoltammetry (CV). The cyclic voltammograms of the ETMs in solution are shown in Figure 5.17. The reduction CVs of three materials were not reversible. The LUMO levels of **3DPySDP**, **4DPySDP** and **DPSDP** were found to be -2.7, -2.51 and -2.48 eV, respectively. Oxidation was not observed for any of the disubstituted dibenzosuberane-based materials. The HOMO levels of **3DPySDP**, **4DPySDP** and **DPSDP** were found to be -6.1, -5.95 and -5.94 eV, respectively, estimated from the optical band gap (E_g^{opt}). We believe that the new disubstituted dibenzosuberane-based ETMs have good exciton as well as hole blocking properties for blue PhOLEDs.

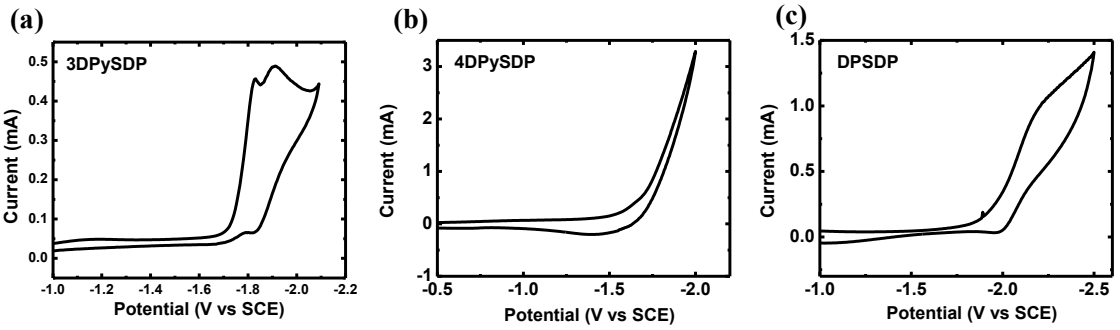

Figure 5.17. Cyclic voltammograms of dibenzosuberane-based ETMs (a) 3PySDP; (b) 4PySDP; and (c) DPSDP.

Thermal properties of the disubstituted dibenzosuberane-based ETMs were characterized by thermogravimetric analysis (TGA) and differential scanning calorimetry (DSC). TGA and DSC curves of dibenzosuberane-based ETMs are shown in Figure 5.18 and Figure 5.19, respectively. Numerical values extracted from the TGA and DSC scans are given in Table 5.5. Three distinct transitions were observed in the second-heating/cooling DSC scans of **3DPySDP**, **4DPySDP** and **DPSDP**. Both **3DPySDP** and **DPSDP** did not show glass transition temperature (T_g) whereas **4DPySDP** showed at 112 ^oC. Disubstituted dibenzosuberane-based materials showed onset decomposition temperature (T_d) in the range of 382 to 418 ^oC demonstrating their thermal robustness. A complete thermal decomposition with remained weight ratio of zero% suggests that the materials can be readily evaporated to form thin films.

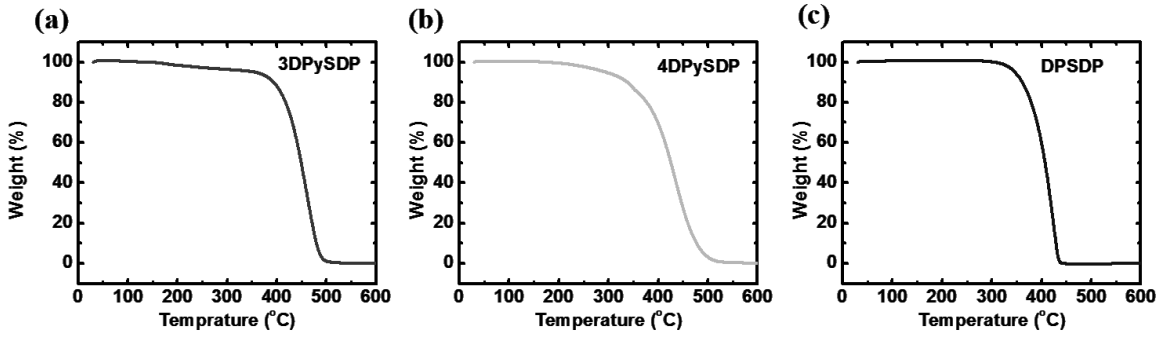

Figure 5.18. TGA thermograms of (a) 3DPySDP; (b) 4DPySDP; and (c) DPSDP.

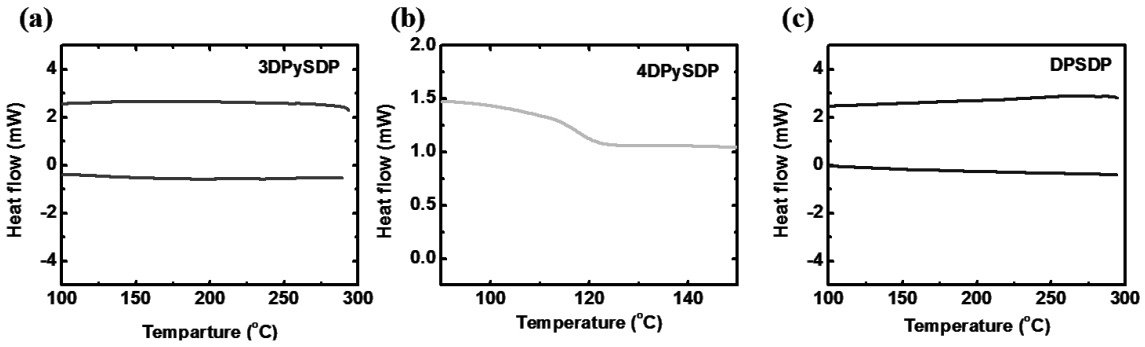

Figure 5.19. DSC thermograms of (a) 3DPySDP; (b) 4DPySDP; and (c) DPSDP.

Table 5.5. Photophysical, electrochemical, and thermal properties of 3DPySDP, 4DPySDP and DPSDP.

		3DPySDP	4DPySDP	DPSDP
λ_{max}^{abs} (nm)	Solution[a] (log ϵ)[b]	258 (4.45)	263 (4.80)	260 (4.56)
	Thin film[c]	266	271	262
λ_{max}^{em} (nm)	Solution[a]	375	381	374
	Thin film[c]	395	396	397
E_g^{opt}(eV)[d]		3.4	3.44	3.46
E_T (eV)		3.0	3.26	3.29
LUMO (eV)		-2.7	-2.51	-2.48
HOMO (eV)		-6.1	-5.95	-5.94
T_g (°C)		None	112	None
T_m (°C)		157	None	None
T_d (°C)		418	382	404

[a]The absorption and emission spectra in dilute THF solution (10^{-5} M). [b]log ϵ calculated at λ_{max}^{abs}. [c]Thin films were thermally evaporated. [d]Calculated from the thin film absorption band edge.

Photophysical, Electrochemical, and Thermal Properties of 2,7- and 3,6-Substituted Spiro[fluorene-9,5'-dibenzosuberane] ETMs. Optical absorption and photoluminescence (PL) spectra of the **2,7-DPySDF** and **3,6-DPySDF** in dilute toluene solution (10^{-6} M) and thin films are shown in **Figure 19**. Photophysical properties of the new ETMs were summarized in Table

5.6. The absorption peaks of **2,7-DPySDF** and **3,6-DPySDF** are observed at 311 nm and 254 nm in THF solution. The PL emission spectra of **2,7-DPySDF** and **3,6-DPySDF** showed maximum peak around 355 nm with a shoulder peak around 370 nm in solution and the PL emission maximum peak at 395 nm in thin films. The optical band gaps of the two compounds were 3.4 and 3.53 eV, respectively, determined from the absorption edges of the thin films.

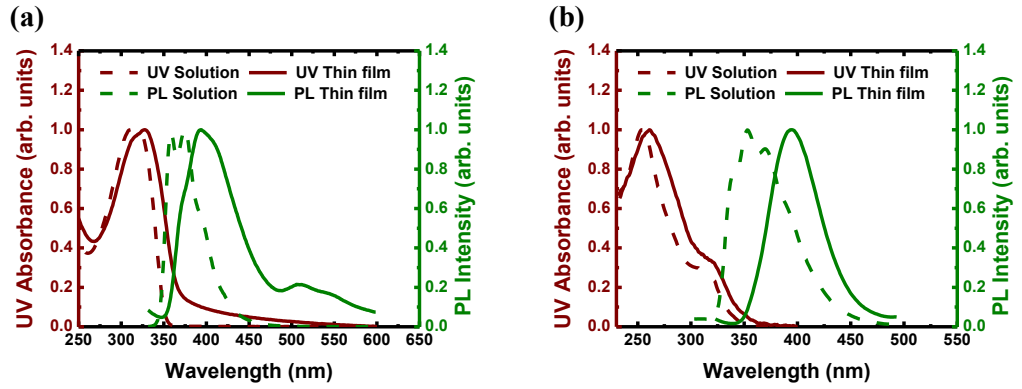

Figure 5.20. Normalized absorption and PL emission spectra of dibenzosuberane-based ETMs in dilute THF solution (10^{-5}M)and thin films: (a) 2,7-DPySDF and (b) 3,6-DPySDF.

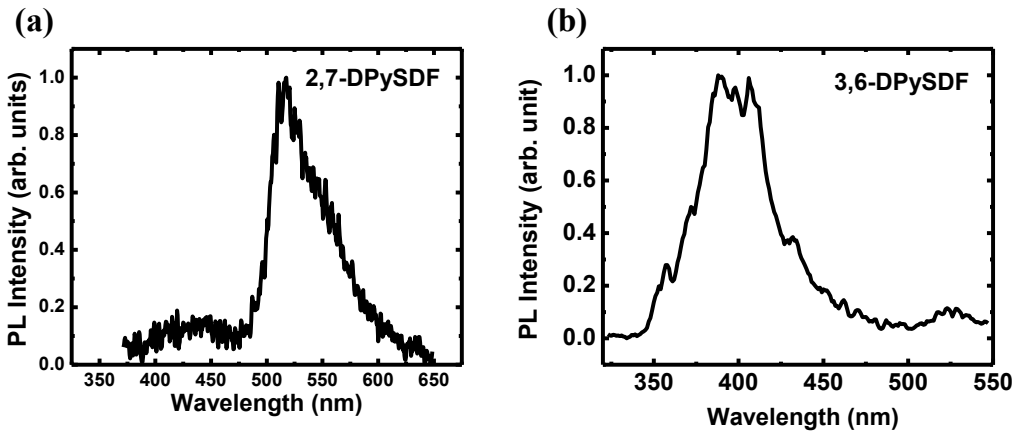

Figure 5.21. Normalized phosphorescence spectra of dibenzosuberane-based ETMs at 77 K: (a) 2,7-DPySDF and (b) 3,6-DPySDF.

The phosphorescence spectra were also obtained at 77 K to measure the triplet energy of ETMs as shown in Figure 5.21. The triplet energy of **2,7-DPySDF** and **3,6-DPySDF** was also determined from the highest energy peak of the low temperature PL spectrum and found to be 2.45 eV and 3.17 eV, respectively. In the case of **3,6-DPySDF**, the triplet energy is high enough to confine the triplet excitons of FIrpic (E_T = 2.7 eV). The HOMO/LUMO and triplet energy levels of dibenzosuberane-based materials are summarized in Table 5.6.

The HOMO/LUMO energy levels of **2,7-DPySDF** and **3,6-DPySDF** were estimated by cyclic voltammetry (CV) and absorption edge of the UV-Vis spectrum. The cyclic voltamogramms are shown in Figure 5.22. The LUMO levels of **2,7-DPySDF** and **3,6-DPySDF** were estimated from the onset reduction potential of CV, giving LUMO levels of -2.61 eV and -2.71 eV, respectively. The HOMO levels of the **2,7-DPySDF** and **3,6-DPySDF** were -6.01 eV and -6.24 eV, estimated from the optical band gap. We believe that the HOMO and LUMO levels of both materials are suitable for facile electron-injection. **3,6-DPySDF** showed large optical band gaps (3.53 eV), high lying LUMO energy levels with high triplet energy (3.17 eV). The results demonstrate that the dibenzosuberane-based materials are promising for high-performance blue PhOLEDs.

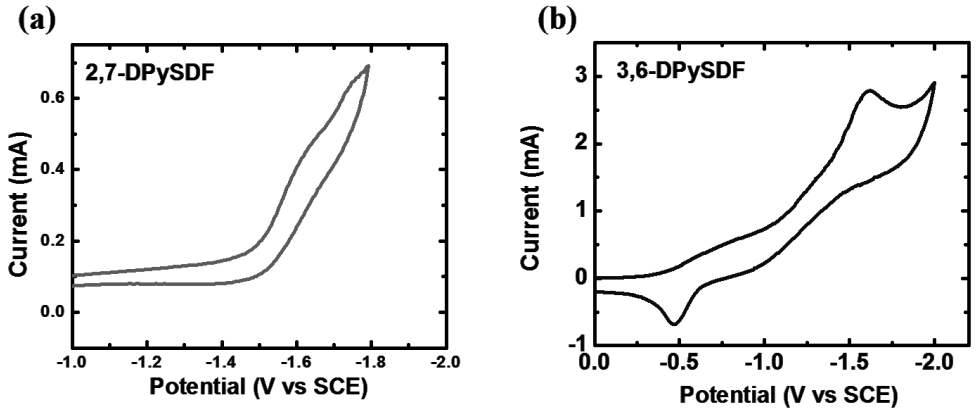

Figure 5.22. Cyclic voltammograms of dibenzosuberane-based ETMs (a) 2,7-DPySDF and (b) 3,6-DPySDF.

TGA and DSC curves of the **2,7-DPySDF** and **3,6-DPySDF** ETMs are shown in **Figure 22** and **Figure 23**, respectively. Thermal properties of the **2,7-DPySDF** and **3,6-DpySDF** were characterized by differential scanning calorimetry (DSC) and thermogravimetric analysis (TGA) and are summarized in **Table 10**. We could not observe a melting temperature (T_m) from the DSC scans in the range of 30 – 300 ^oC whereas glass transition temeperatures (T_g) were observed at 100 and 130 ^oC. The onset decomposition temperatures (T_d) of the dibenzosuberane-based materials were high more than 415 ^oC, which shows their thermal robustness. These results suggest that changing the attached position of the pyridine to the spiro-structure can lead to a significant increase of the thermal stability.

Table 5.6. Photophysical, electrochemical, and thermal properties of 2,7-DPySDF and 3,6-DPySDF.

		2,7-DPySDF	**3,6-DPySDF**
λ_{max}^{abs} (nm)	Solution[a] (log ϵ)[b]	311 (4.55)	254 (4.89)
	Thin film[c]	327	261
λ_{max}^{em} (nm)	Solution[a]	358, 375	353, 370
	Thin film[c]	393.5	395
E_g^{opt}(eV)[d]		3.4	3.53
E_T (eV)		2.45	3.17
LUMO (eV)		-2.61	-2.71
HOMO (eV)		-6.01	-6.24
T_g (^oC)		100	130
T_m (^oC)		163	None
T_d (^oC)		415	439

[a]The solution absorption and emission spectra in dilute THF solution (5×10^{-5}M). [b]log ϵ calculated at λ_{max}^{abs}. [c]The thin films were thermally evaporated. [d]Calculated from the thin film absorption band edge.

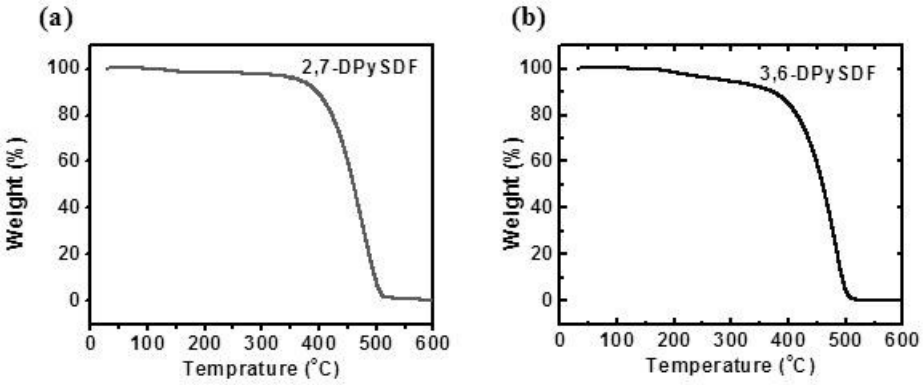

Figure 5.23. TGA thermograms of (a) 2,7-DPySDF, and (b) 3,6-DpySDF.

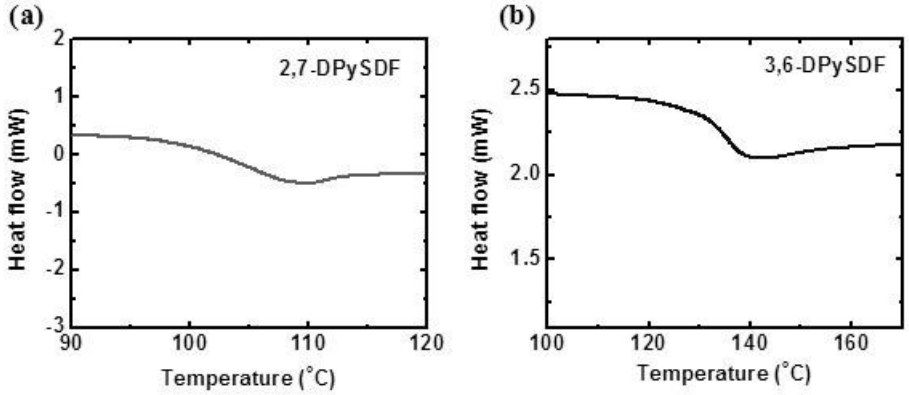

Figure 5.24. DSC thermograms of (a) 2,7-DPySDF, ad (b) 3,6-DpySDF.

Device Performance. We evaluated the use of new dibenzosuberane-based materials as electron-transport layers (ETLs) in blue phosphorescent organic light-emitting diodes (PhOLEDs). Blue PhOLEDs with dibenzosuberane-based ETL showed enhanced device performance compared to the device without an ETL. Molecular structures of the new dibenzosuberane materials are shown in Chart 5.3. To verify the effectiveness of dibenzosuberane-based small molecules as ETLs, a set of blue PhOLEDs were fabricated using PVK-based emission layer (EML) doped with triplet emitter. Device I without ETL: ITO/PEDOT:PSS/Blue EML/LiF/Al; Device II with **3DPySDP** ETL: ITO/PEDOT:PSS/Blue

EML/**3DPySDP** (10 nm)LiF/Al; Device III with **4DPySDP** ETL: ITO/PEDOT:PSS/Blue EML/**4DPySDP** (10 nm)/LiF/Al; Device IV with **2,7-DPySDF** ETL: ITO/PEDOT:PSS/Blue EML/**2,7-DPySDF** (10 nm)/LiF/Al; Device V with **3,6-DPySDF** ETL: ITO/PEDOT:PSS/Blue EML/**3,6-DPySDF** (10 nm)/LiF/Al; Device VI with **2PySDP** ETL: ITO/PEDOT:PSS/Blue EML/**2PySDP** (10 nm)/LiF/Al; Device VII with **3PySDP** ETL: ITO/PEDOT:PSS/Blue EML/**3PySDP** (10 nm)/LiF/Al; Device VIII with **4PySDP** ETL: ITO/PEDOT:PSS/Blue EML/**4PySDP** (10 nm)/LiF/Al; Device IX with **PSDP** ETL: ITO/PEDOT:PSS/Blue EML/**PSDP** (10 nm)/LiF/Al; and Device X with **DPSDP** ETL: ITO/PEDOT:PSS/Blue EML/**DPSDP** (10 nm)/LiF/Al. Blue EML was consisted of PVK:OXD-7=6:4 (wt/wt) host doped with 10 wt% of FIrpic blue triplet emitter solution-deposited by spin-coating and all ETLs were vacuum-evaporated onto EML followed by evaporation of 1 nm LiF and 100 nm Al without breaking the vacuum.

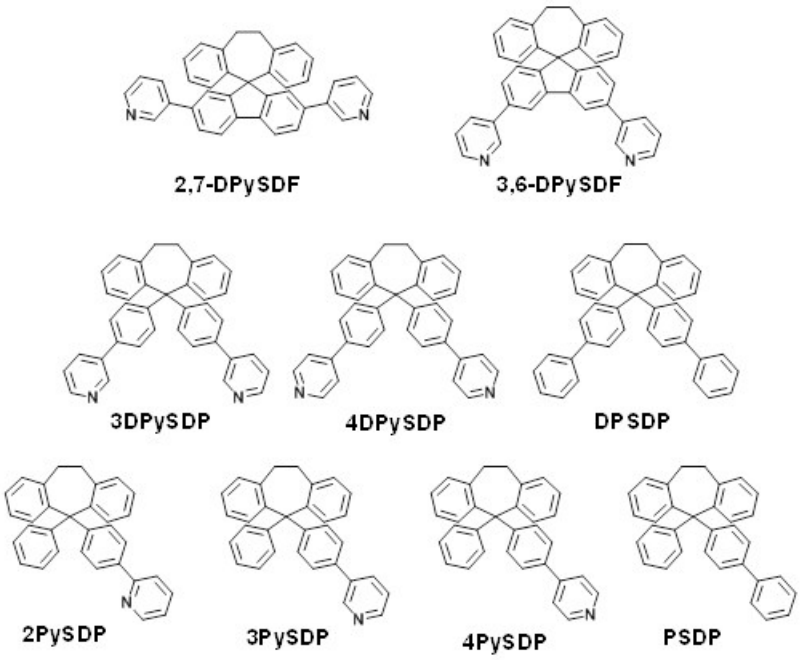

Chart 5.3. Molecular structures of new dibenzosuberane-based electron-transport materials: materials showed here are specified as blue.

The current density-voltage (*J-V*) characteristics are shown in log and linear scales (Figure 5.25). The current densities of the blue PhOLEDs with new dibenzosuberane ETLs increased compared to the device without ETL, except the devices with **2PySDP** (device VI) and **DPSDP** (device X). The luminance-voltage (*L-V*) characteristics of the PhOLEDs are shown in Figure 5.26. The turn-on voltage of the PhOLEDs with dibenzosuberane ETLs were all reduced (5.4 – 5.8 V) compared to the device without ETL (6.3 V). Blue PhOLEDs with **3DPySDP** and **4DPySDP** ETLs showed significantly increased brightness of 11920 and 11350 cd/m^2, respectively. The brightness of the blue PhOLED with dibenzosuberane-based ETL all showed increased brightness compared to the device without ETL (~ 3500 cd/m^2). However, PhOLEDs with **2PySDP** (device VI) and **DPSDP** (device X) showed rather poor brightness compared to other devices with dibenzosuberane-based ETLs.

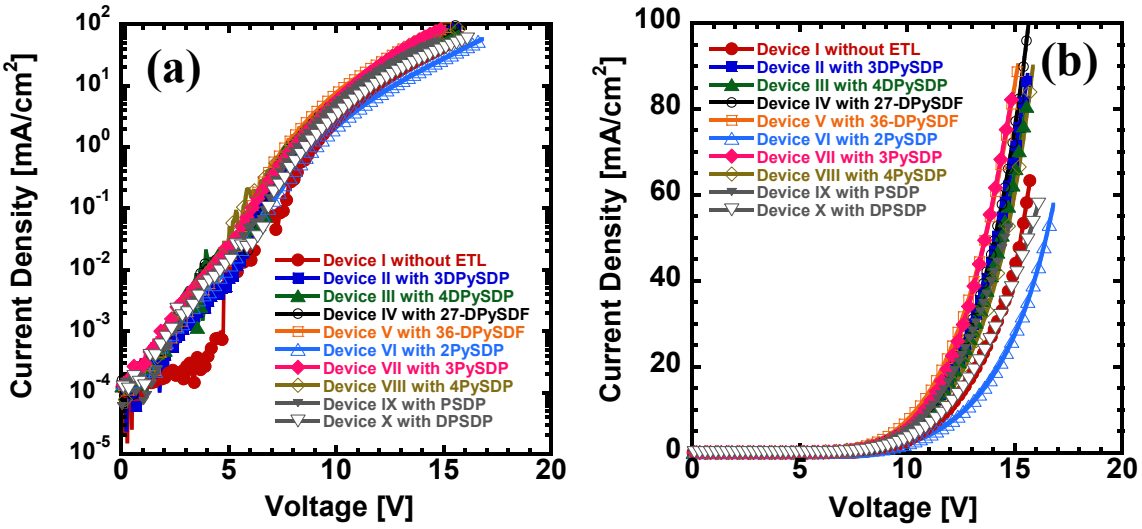

Figure 5.25. Current density-voltage (*J-V*) characteristics of the blue PhOLEDs with dibenzosuberane-based ETMs in (a) log-scale and (b) linear scale. Device I without ETL: ITO/PEDOT:PSS/Blue EML/LiF/Al; Device II with 3DPySDP ETL: ITO/PEDOT:PSS/Blue EML/3DPySDP (10 nm)LiF/Al; Device III with 4DPySDP ETL: ITO/PEDOT:PSS/Blue EML/4DPySDP (10 nm)/LiF/Al; Device IV with 2,7-DPySDF ETL: ITO/PEDOT:PSS/Blue EML/2,7-DPySDF (10 nm)/LiF/Al; Device V with 3,6-DPySDF ETL: ITO/PEDOT:PSS/Blue EML/3,6-DPySDF (10 nm)/LiF/Al; Device VI with 2PySDP ETL: ITO/PEDOT:PSS/Blue EML/2PySDP (10 nm)/LiF/Al; Device VII with 3PySDP ETL: ITO/PEDOT:PSS/Blue EML/3PySDP (10 nm)/LiF/Al; Device VIII with 4PySDP ETL: ITO/PEDOT:PSS/Blue EML/4PySDP (10 nm)/LiF/Al; Device IX with PSDP ETL: ITO/PEDOT:PSS/Blue EML/PSDP (10 nm)/LiF/Al; and Device X with DPSDP ETL: ITO/PEDOT:PSS/Blue EML/DPSDP (10 nm)/LiF/Al. Blue EML was consisted of PVK:OXD-7=6:4 (wt/wt) host doped with 10 wt% of FIrpic blue triplet emitter solution-deposited by spin-coating and all ETLs were vacuum-evaporated onto EML followed by evaporation of 1 nm LiF and 100 nm Al without breaking the vacuum.

The blue PhOLEDs with dibenzosuberane-based ETLs showed significantly increased efficiency compare to the device without ETL (**Figure 5.26**). The luminous efficiency (LE) value of the PhOLED with **4DPySDP** ETL (device III) showed the highest LE value of 38.1 cd/A at 2030 cd/m^2 and power efficiency (PE) = 13.9 lm/W with an EQE of 20.0 %, significantly higher compared to the device without ETL (16.3 cd/A at 600 cd/m^2 and 5.4 lm/W). PhOLED with PSDP also showed high LE (37.8 cd/A) and PE (14.0 lm/W) values with an EQE of 19.8 % (device IX), however, the device showed severe roll-off of efficiencies with increased luminance. All device performance of blue PhOLEDs with new dibenzosuberane-based materials are summarized in Table 5.7. The blue PhOLEDs with dibenzosuberane-based ETM showed improved device performances. These results demonstrate that these new dibenzosuberane-based ETMs can be promising ETMs with good exciton blocking ability in PhOLEDs.

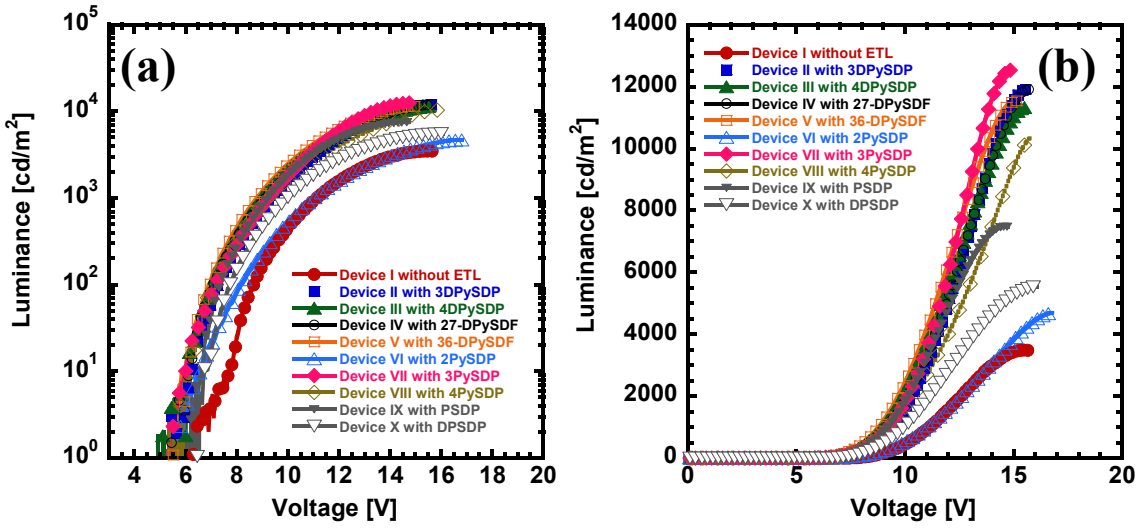

Figure 5.26. Luminance-voltage (*L-V*) characteristics of the blue PhOLEDs with dibenzosuberane-based ETMs in (a) log-scale and (b) linear scale.

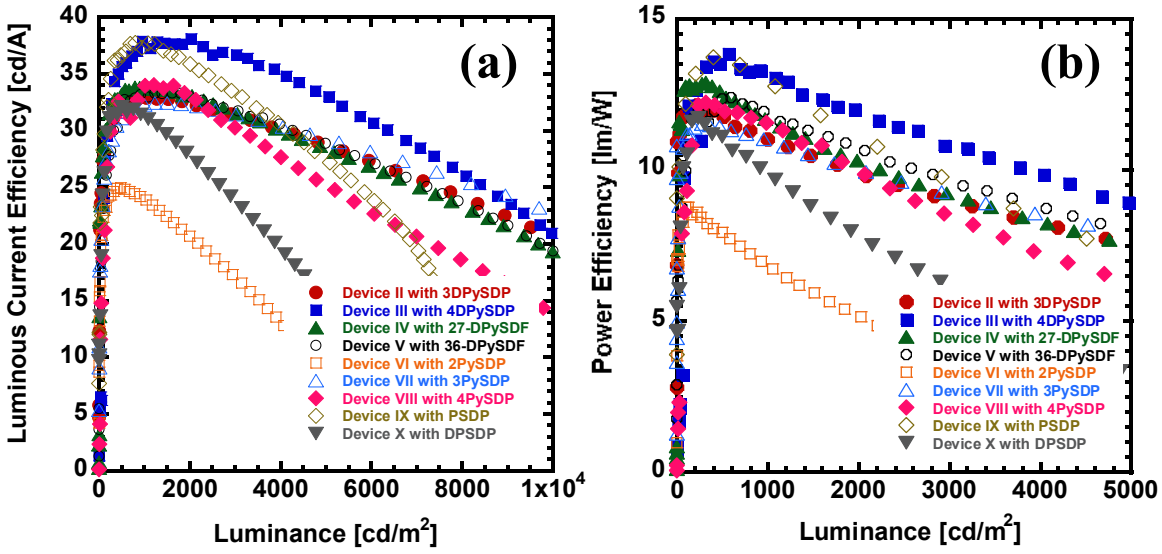

Figure 5.27. (a) Luminous efficiency-luminance (*LE-L*) and (b) power efficiency-luminance (*PE-L*) characteristics of the blue PhOLEDs with new dibenzosuberane-based ETMs.

Although blue PhOLEDs with dibenzosuberane ETLs with high triplet energy showed similar device performance, we expect that these materials will function as an excellent host material in order to confine high energy triplet excitons within the EML, for example deep blue triplet emitter. These results suggest that dibenzosuberane-based materials have large potential as ETMs as well as host materials for high-performance PhOLEDs.

Table 5.7. Device chracteristics of PhOLEDs with dibenzosuberane-based materials. [a]

Device	ETL	V_{on}[b] [V]	Drive voltage [V]	Current density [mA/cm^2]	Luminance [cd/m^2]	Device efficiency [cd/A, lm/W, (%EQE)]
Device I	None	6.3	16.4 *9.9*	63.3 *2.5*	3480 *600*	5.5, 1.1, (2.8) *16.3, 5.4, (8.5)*
Device II	3DPySDP	5.4	15.6 *9.5*	88.0 *3.3*	11920 *1090*	13.5, 2.7, (7.1) *32.9, 12.2, (17.2)*
Device III	4DPySDP	5.4	15.6 *9.9*	80.6 *5.3*	11350 *2030*	14.1, 2.8, (7.4) *38.1, 13.9, (20.0)*
Device IV	2,7-DPySDF	5.5	15.7 *8.8*	102.3 *2.4*	11920 *760*	11.6, 2.3, (6.1) *33.9, 13.0, (17.7)*
Device V	3,6-DPySDF	5.5	15.2 *8.2*	90.3 *1.7*	11500 *570*	12.8, 2.6, (6.7) *33.1, 12.5, (17.4)*
Device VI	2PySDP	5.8	16.8 *9.8*	57.8 *1.8*	4700 *460*	8.1, 1.5, (4.2) *25.0, 8.7, (13.1)*
Device VII	3PySDP	5.4	13.6 *9.8*	187.8 *4.8*	12500 *1560*	15.0, 3.2, (7.9) *32.5, 11.5, (17.0)*
Device VIII	4PySDP	5.4	15.9 *9.1*	90.0 *2.2*	10370 *880*	11.5, 2.3, (6.0) *34.3, 11.7, (18.0)*
Device IX	PSDP	6.0	14.8 *9.2*	53.3 *2.6*	7480 *1000*	14.0, 3.0, (7.3) *37.8, 14.0, (19.8)*
Device X	DPSDP	6.1	16.1 *9.2*	57.9 *1.6*	5540 *530*	9.6, 1.9, (5.0) *32.3, 11.7, (16.9)*

[a] Values in *italic* correspond to those at maximum device efficiencies. [b] Turn-on voltage (at brightness of 1 cd/m^2).

5.2.4. Conclusion

We have developed new classes of electron-transport materials (ETMs) based on dibenzosuberane for highly efficient phosphorescent organic light-emitting diodes (PhOLEDs). New high triplet energy ETMs based on dibenzosuberane core unit showed substantially high triplet energy (E_T > 3.0 eV) with good thermal and electrochemical properties. Blue PhOLEDs

with dibenzosuberane-based ETMs showed significantly improved device performances (CE = 38.1 cd/A and EQE = 20.0 %), demonstrating that these high triplet energy ETMs are a promising class of ETMs with excellent singlet/triplet exciton blocking ability.

5.3. References

(1) Reineke, S.; Lindner, F.; Schwartz, G.; Seidler, N.; Walzer, K.; Lüssem, B.; Leo, K. *Nature* **2009**, 459, 234-238.

(2) Baldo, M. A.; Obrien, D. F.; You, Y.; Shoustikov, A.; Sibley, S.; Thompson, M. E.; Forrest, S. R. *Nature* **1998**, 395, 151-154.

(3) Xiao, L.; Su, S.-J.; Agata, Y.; Lan, H.; Kido J. *Adv. Mater.* **2009**, 21, 1271-1274.

(4) Adachi, C.; Baldo, M. A.; Thompson, M. E.; Forrest, S. R. *J. Appl. Phys.* **2001**, 90, 5048-5051.

(5) Su, S.-J.; Tanaka, D.; Li, Y.-J.; Sasabe, H.; Takeda, T.; Kido, J. *Org. Lett.* **2008**, 10, 941-944.

(6) Chopra, N.; Lee, J.; Zheng, Y.; Eom, S.-H.; Xue, J.; So, F. *Appl. Phys. Lett.* **2008**, 93, 143307.

(7) Jeon, S. O.; Lee, J. Y. *J. Mater. Chem.* **2012**, 22, 4233-4243.

(8) Kulkarni, A. P.; Tonzola, C. J.; Babel, A.; Jenekhe, S. A. *Chem. Mater.* **2004**, 16, 4556-4573.

(9) Su, S.-J.; Chiba, T.; Takeda, T.; Kido, J. *Adv. Mater.* **2008**, 20, 2125-2130.

(10) Sasabe, H.; Gonmori, E.; Chiba, T.; Li, Y.-J.; Tanaka, D.; Su, S.-J. Takeda, T.; Pu, Y.-J.;. Nakayama, K.-I; Kido, J. *Chem. Mater.* **2008**, 20, 5951-5953.

(11) Sasabe, H.; Chiba, T.; Su, S.-J.; Pu, Y.-J.; Nakayama, K.-I.; Kido, J. *Chem. Comm.* **2008**, 5821-5823.

(12) Su, S.-J.; Sasabe, H.; Pu, Y.-J.; Nakayama, K.-I.; Kido, J. *Adv. Mater.* **2010**, 22, 3311-3316.

(13) Inomata, H.; Goushi, K.; Masuko, T.; Konno, T.; Imai, T.; Sasabe, H.; Brown, J. J.; Adachi, C. *Chem. Mater.* **2004**, 16, 1285-1291.

(14) Earmme, T.; Ahmed, E.; Jenekhe, S. A. *Adv. Mater.* **2010**, 22, 4744-4748.

(15) Ahmed, E.; Earmme, T.; Jenekhe, S. A. *Adv. Funct. Mater.* **2011**, 21, 3889-3899.

(16) Burrows, P. E.; Padmaperuma, A. B.; Sapochak, L. S.; Djurovich, P.; Thompson, M. E. *Appl. Phys. Lett.*, **2006**, 88, 183503.

(17) Jeon, S. O.; Yook, K. S.; Joo, C. W.; Lee, J. Y. *J. Phys. D: Appl. Phys.* **2009**, 42, 225103.

(18) Jeon, S. O.; Yook, K. S.; Joo, C. W.; Lee, J. Y. *J. Mater. Chem.* **2009**, 19, 5940-5944.

(19) Yook, K. S.; Lee, J. Y. *Org. Electron.*, **2011**, 12, 1293-1297.

(20) Lu, B.; Li, Y.; Xu, J. *J. Electroanal. Chem.* **2010**, 643, 67-76.

(21) Tonzola, C. J.; Alam, M. M.; Jenekhe, S. A. *Adv. Mater*. **2002**, 14, 1086-1090.

(22) Tonzola, C.J.; Kulkarni, A. P.; Gifford, A. P.; Kaminsky, W.; Jenekhe, S.A. Adv. Funct. Mater. **2007**, 17, 863-874.

(23) Kulkarni, A. P.; Gifford, A. P.; Tonzola, C. J.; Jenekhe, S. A. *Appl. Phys. Lett.* **2005**, 86, 061106.

(24) Hsu, F.-M.; Chien, C.-H.; Hsieh, Y.-J.; Wu, C.-H.; Shu, C.-F.; Liub, S.-W.; Chen, C.-T. *J. Mater. Chem.* **2009**, 19, 8002-8008.

(25) Sasabe, H.; Seino, Y.; Kimura, M.; Kido, J. *Chem. Mater.* **2012**, 24, 1404-1406.

(26) Kim, S.-J.; Leroy, J.; Zuniga, C.; Zhang, Y.; Zhu, L.; Sears, J. S.; Barlow, S.; Brédas, J.-L.; Marder, S. R.; Kippelen, B. *Org. Electron.* **2011**, 12, 1314-1318.

(27) Kulkarni, A. P.; Jenekhe, S. A. *Macromolecules*, **2003**, 36, 5285-5296.

(28) Baldo, M. A.; Forrest, S. R. *Phys. Rev. B*, **2000**, 62, 10958-10966.

(29) Agrawal, A. K.; Jenekhe, S. A. *Chem. Mater.* **1996**, 8, 579-589.

(30) Jeon, S. O.; Yook, K. S.; Joo, C. W.; Lee, J. Y. *Adv. Funct. Mater.* **2009**, 19, 3644-3649.

(31) Young, D. Computational Chemistry: A Practical Guide for Applying Techniques to Real World Problems; John Wiley & Sons, Inc: New York, USA, **2001**.

(32) Hehre, W.J.; Ditchfie, R.; Pople, J.A. J. Chem. Phys. **1972**, 56, 2257–2261.

(33) Murgatroyd, P. N. *J. Physics D: Appl. Phys.* **1970**, 3, 1488-1490.

(34) Mott, N. F.; Gurney, D. *Electronic Processes in Ionic Crystals*, Academic Press, New York, USA, **1970**.

(35). So, F.; Krummacher, B.; Mathai, M. K.; Poplavskyy, D.; Choulis, S. A.; Choong, V.-E. *J. Appl. Phys.* **2007**, 102, 091101.

(36) Su, S.-J.; Takahashi, Y.; Chiba, T.; Takeda, T.; Kido, J. *Adv. Funct. Mater.* **2009**, 19, 1260.

Chapter 6. Highly Efficient All-Polymer Solar Cells Enabled by New n-Type Acceptor Polymers

The chapter investigates polymer/polymer solar cells, *i.e.* all-polymer solar cells based on new acceptor polymers and new processing method. The results in this chapter are reprinted in part with permission from Earmme, et al. (Copyright 2013 American Chemical Society) and will be submitted to Wiley-VCH.

6.1. All-Polymer Solar Cells Based on Naphthalene Diimide-Selenophene Copolymer Acceptor

6.1.1. Introduction

Solution-processed organic photovoltaic devices are promising low cost solar energy technologies.[1] Much progress has been made in developing polymer/fullerene solar cells in the last decade, with efficiencies now approaching 10 %.[2] In contrast, the performance of all-polymer solar cells, composed of both *donor* and *acceptor* polymers and free of fullerenes, has remained relatively low with no significant advance in the same period.[3] All-polymer active layers of solar cells have potential advantages over polymer/fullerene systems, including enhanced absorption coefficients, increased photovoltage, superior photochemical, thermal, and mechanical robustness, and facile control of solution viscosity and industrial coating process. Perylene diimide (PDI) and naphthalene diimide (NDI) have been the most widely explored building blocks[3,4] in the design and investigation of acceptor (n-type) polymers for all-polymer solar cells.[3,4] A PDI-based acceptor polymer in combination with polythiophene derivatives has produced bulk heterojunction (BHJ) solar cells with a power conversion efficiency (PCE) of

2.23 %.[3h] An NDI-bithiophene copolymer (PNDI2OD-T2) with very high field-effect electron mobilities (0.1 - 0.85 cm^2/Vs) and moderate bulk electron mobility (~ 10^{-3} cm^2/Vs) has so far shown only low efficiencies of 0.2 - 1.4 % PCE in BHJ solar cells using P3HT donor polymer.[3e,3l] Among acceptor polymers in BHJ solar cells, a benzothiadiazole-fluorene copolymer has the highest PCE (2.7 %) reported to date.[3k] The short circuit current density (J_{sc} < 6.3 mA/cm^2) and external quantum efficiency (EQE < 43 %) obtained to date in all-polymer solar cells[3] have also been far lower than in polymer/fullerene devices.[1,2]

In this section, we report all-polymer solar cells with 3.3% PCE enabled by a novel polymer/polymer blend system composed of a new NDI-selenophene copolymer acceptor and a thiazolothiazole-dithienylsilole copolymer donor. Three n-type polymer semiconductors, including an NDI-thiophene copolymer (PNDIT) and two new NDI-selenophene copolymers (PNDIS, PNDIS-HD) whose molecular structures are shown in Figure 6.1a, are investigated as electron acceptors in BHJ solar cells for the first time. We show that these NDI-based copolymers exhibit *unipolar* electron transport with high field-effect and bulk mobilities. The donor polymer, poly[(4,4′-bis(3-(2-ethyl-hexyl)dithieno[3,2-*b*:″,3′-*d*]silole)-2,6-diyl-*alt*-(2,5-bis-(3-(2- ethylhexyl)thiophen-2-yl)thiazolo[5,4-*d*]thiazole)] (PSEHTT, Figure 6.1a) has previously been shown to be a promising electron donor and hole-conducting material in polymer/fullerene BHJ solar cells.[5] The morphology of the polymer/polymer blends was imaged by atomic force microscopy (AFM). Charge transport in the active layer blends was investigated by organic field-effect transistors (OFETs) and space-charge-limited current (SCLC) measurements. Finally, we show that the all-polymer solar cells can be as efficient as the similarly evaluated $PC_{60}BM$/PSEHTT BHJ devices.

6.1.2. Experimental Section

PNDIT and PNDIS were synthesized by Stille coupling copolymerization of 4,9-dibromo-2,7-bis(2-decyltetradecyl)benzo[*lmn*][3,8]-phenanthroline-1,3,6,8-tetraone with 2,5-bis(trimethylstannyl)thiophene and 2,5-bis(trimethylstannyl)selenophene, respectively, in the presence of $Pd_2(dba)_3$ and P(*o*-tolyl)$_3$ in chlorobenzene solvent.

Poly{[N,N'-bis(2-decyltetradecyl)-naphthalene-1,4,5,8-bis(dicarboximide)-2,6-diyl]-*alt*-5,5'-selenophene)} (PNDIS). 4,9-Dibromo-2,7-bis(2-decyltetradecyl)benzo[lmn][3,8]phenanthroline-1,3,6,8-tetraone (480.6 mg, 0.44 mmol), 2,5-bis(trimethylstannyl)selenophene (200 mg, 0.44 mmol), $Pd_2(dba)_3$ (8 mg, 0.0088 mmol) and P(o-tolyl)$_3$ (10.7 mg, 0.035 mmol) were added into a 100 mL three-neck round-bottom flask. The flask equipped with a condenser was then degassed and filled with argon three times. Afterwards, 22 mL of chlorobenzene was added and degassed and filled with argon three times. The reaction mixture was refluxed for 72 h under argon. After cooling down to room temperature, the polymerization mixture was poured and stirred into 200 mL methanol and 5 mL hydrochloric acid solution for 3 h. The polymer precipitated out as a dark reddish purple solid and was filtered using a filter paper. The polymer was purified by Soxhlet extraction with methanol, hexane, and acetone. **PNDIS** (365 mg; yield = 81.9 %), ^{1}H NMR ($CDCl_3$, 300 MHz): d (ppm) 9.1 (2H), 7.7 (2H), 4.2 (4H), 2.1 (2H), 0.9–1.5 (92H). GPC: Mw = 31.5 kDa, Mn = 26.1 kDa, PDI = 1.2. TGA: T_d = 415 °C.

Poly{[N,N'-bis(2-hexyldexyl)-naphthalene-1,4,5,8-bis(dicarboximide)-2,6-diyl]-*alt*-5,5'-selenophene)} (PNDIS-HD). 4,9-Dibromo-2,7-bis(2-hexyldecyl)benzo[lmn][3,8]phenanthroline-1,3,6,8-tetraone (200 mg, 0.23 mmol), 2,5-bis(trimethylstannyl)selenophene (104.6 mg, 0.23 mmol), $Pd_2(dba)_3$ (4.2 mg, 0.0046 mmol) and

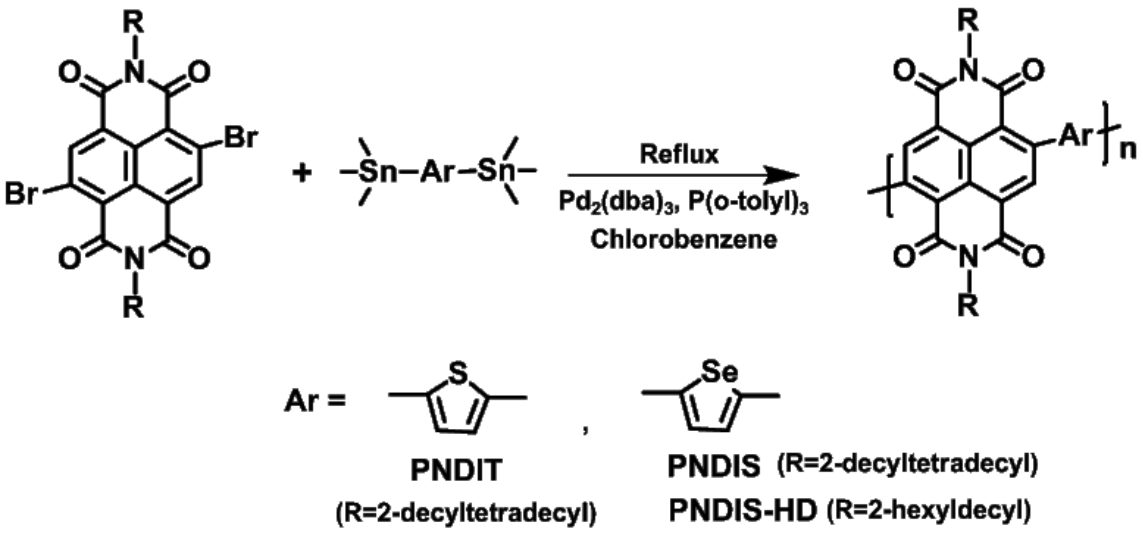

Scheme 6.1. Synthetic route of NDI-copolymers: PNDIT, PNDIS, and PNDIS-HD.

$P(o\text{-tolyl})_3$ (5.6 mg, 0.0184 mmol) were added into a 100 mL three-neck round-bottom flask. The flask equipped with a condenser was then degassed and filled with argon three times. Afterwards, 10 mL of chlorobenzene was added and degassed and filled with argon three times. The reaction mixture was refluxed for 72 h under argon. After cooling down to room temperature, the polymerization mixture was poured and stirred into 200 mL methanol and 5 mL hydrochloric acid solution for 3 h. The polymer precipitated out as a dark reddish purple solid and was filtered using a filter paper. The polymer was purified by Soxhlet extraction with methanol, hexane, and acetone. **PNDIS-HD** (165 mg; yield = 82.3 %), ^1H NMR ($CDCl_3$, 300 MHz): d (ppm) 9.15 (2H),

7.8 (2H), 4.2 (4H), 2.05 (2H), 0.8-1.5 (60H). GPC: Mw = 177.9 kDa, Mn = 79 kDa, PDI = 2.3. TGA: T_d = 400 °C.

Poly{[N,N'-bis(2-decyltetradecyl)-naphthalene-1,4,5,8-bis(dicarboximide)-2,6-diyl]-*alt*-5,5'-thiophene)} (PNDIT). 4,9-Dibromo-2,7-bis(2-decyltetradecyl)benzo[lmn][3,8]phenanthroline-1,3,6,8-tetraone (350 mg, 0.32 mmol), 2,5-bis(trimethylstannyl)thiophene (130.7 mg, 0.32 mmol), $Pd_2(dba)_3$ (5.84 mg, 0.0064 mmol) and P(*o*-tolyl)$_3$ (7.77 mg, 0.026 mmol) were added into a 100 mL three-neck round-bottom flask. The flask equipped with a condenser was then degassed and filled with argon three times. Afterwards, 15 mL of chlorobenzene was added and degassed and filled with argon three times. The reaction mixture was refluxed for 72 h under argon. After cooling down to room temperature, the polymerization mixture was poured and stirred into 200 mL methanol and 5 mL hydrochloric acid solution for 3 h. The polymer precipitated out as a dark reddish purple solid and was filtered using a filter paper. The polymer was purified by Soxhlet extraction with methanol, hexane, and acetone. **PNDIT** (310 mg; yield = 92.3 %), ^{1}H NMR ($CDCl_3$, 300 MHz): d (ppm) 9.0 (2H), 7.5 (2H), 4.2 (4H), 2.1 (2H), 0.8-1.45 (92H). GPC: Mw = 31.6 kDa, Mn = 23.9 kDa, PDI = 1.3. TGA: T_d = 430 °C.

Characterization. The molecular structure and physical properties of PNDIBS and PNDIBT were investigated by ^{1}H NMR, gel permeation chromatography (GPC) analysis, thermogravimetric analysis (TGA), and X-ray diffraction (XRD). ^{1}H NMR spectra at 300 MHz were recorded on a Bruker-AF300 spectrometer. GPC analysis of the copolymers was performed on GPC Model 120 (DRI, PLBV400HT viscometer) against polystyrene standards in chlorobenzene at 60 °C. TGA thermograms were obtained on a TA Instruments Q50 TGA at a heating rate of 20 °C/min under nitrogen gas flow. XRD data were obtained from Bruker D8 Discover with a Cu Kα beam using GADD XRD system, and the samples were prepared by

drop-casting of polymer solutions in chloroform onto glass substrates followed by annealing at 200 °C for 10 min. Optical and electrochemical properties were investigated by UV-vis absorption spectroscopy and cyclic voltammetry. Absorption spectra were measured on a PerkinElmer model Lambda 900 UV/vis/near-IR spectrophotometer. Solution and solid state absorption spectra were obtained from polymer solutions in chloroform and as thin films on glass substrates, respectively. Cyclic voltammetry (CV) experiments were done on an EG&G Princeton Applied Research potentiostat/galvanostat (model 273A) in an electrolyte solution of 0.1 M tetrabutylammonium hexafluorophosphate (Bu_4NPF_6) in acetonitrile at a scan rate of 100 mV/s. A three-electrode cell was used in this analysis. Platinum wires were used as counter and working electrodes, and Ag/Ag^+ (Ag in 0.1 M $AgNO_3$ solution, Bioanalytical System, Inc.) was used as a reference electrode. Ferrocene/ferrocenium was used as an internal standard by running CV at the end, and this data was used to convert the potential to saturated calomel electrode (SCE) scale. The films of the copolymer were coated onto the Pt wires by dipping the wires into 1 wt % polymer solutions in chloroform.

Fabrication and Characterization of Inverted All-Polymer Solar Cells. Solar cells with the inverted device structure of ITO/ZnO/active layer/MoO_3/Ag were fabricated. ITO substrates were cleaned as the same procedure mentioned above, followed by oxygen plasma treatment. Zinc oxide (ZnO) precursor was prepared by dissolving 1 g of zinc acetate dehydrate (99.999 % trace metals basis, Aldrich) in 10 mL of 2-methoxyethanol (99.8 %, anhydrous, Aldrich) with adding 0.28 g of ethanolamine (≥99.5 %, Aldrich) under stirring for overnight in ambient conditions., spin-coated on top of the ITO and annealed at 250 °C for 1 hr in air. The ZnO film thickness was approximately 30 nm which is confirmed by the profilometer (Alpha Step 500). The active layer was then spin-coated from the PSEHTT:PNDIT or PNDIS mixture solution to

make a thin film of 80 nm thickness and thermally annealed at 150 °C for 10 min in a glovebox. The substrates were then loaded in a thermal evaporator (BOC Edwards, 306) to deposit an anode composed of thin layer of 7.5 nm MoO_3 and 100 nm Ag under high vacuum (8×10^{-7} Torr). Five solar cells, each with an active area of 4 mm^2, were fabricated per ITO substrate. The current density–voltage (*J–V*) curves of solar cells were measured using a HP4155A semiconductor parameter analyzer under laboratory ambient air conditions. An AM1.5 illumination at 100 mW/cm^2 was provided by a filtered Xe lamp and calibrated by using an NREL-calibrated Si diode. The external quantum efficiency (EQE) was measured using a QEX10 solar cell quantum efficiency measurement system (PV Measurements, Inc.) and was calibrated with a NREL-certified Si diode before measurement. Film thickness was measured by an Alpha-Step 500 profilometer (KLA-Tencor, San Jose, CA). AFM characterization of surface morphology was done on a Veeco Dimension 3100 Scanning Probe Microscope (SPM) system. The AFM images were directly measured on the same devices used for *J-V* characterization.

6.1.3. Results and Discussion

The number average molecular weight (M_n) of PNDIT and PNDIS was 23.9 and 26.1 kDa with polydispersity index (PDI) of 1.3 and 1.2, respectively. PNDIS-HD had a much higher M_n of 79.0 kDa with a PDI of 2.3. These polymers had onset decomposition temperature (T_d) of 400 - 430 ˚C. X-ray diffraction (XRD) analysis of solution-cast films of PNDIT, PNDIS, and PNDIS-HD revealed lamellar crystallinity with intense (100) peak. A lamellar *d*-spacing (d_{100}) of 24.86 Å, 22.92 Å and 21.53 Å, respectively, was observed for PNDIT, PNDIS, and PNDIS-HD. The shorter d_{100} spacing compared to the alkyl chain length (2 × 14 C) of 43.12 Å indicates interdigitation of the alkyl chains. As expected, PNDIS-HD has a smaller d_{100} value compared to

the other two polymers with 2-decyltetradecyl side chains. The shorter d_{100} spacing of PNDIS compared to PNDIT is due to a larger torsion angle between NDI and selenophene moieties, which is a consequence of the larger Se orbitals compared to S. The observed π- π stacking distance (d_{010}) of 4.16 Å in PNDIS and PNDIS-HD and 4.2 Å in PNDIT are comparable with values seen in other NDI-based copolymers (~ 4.0 Å).[6]

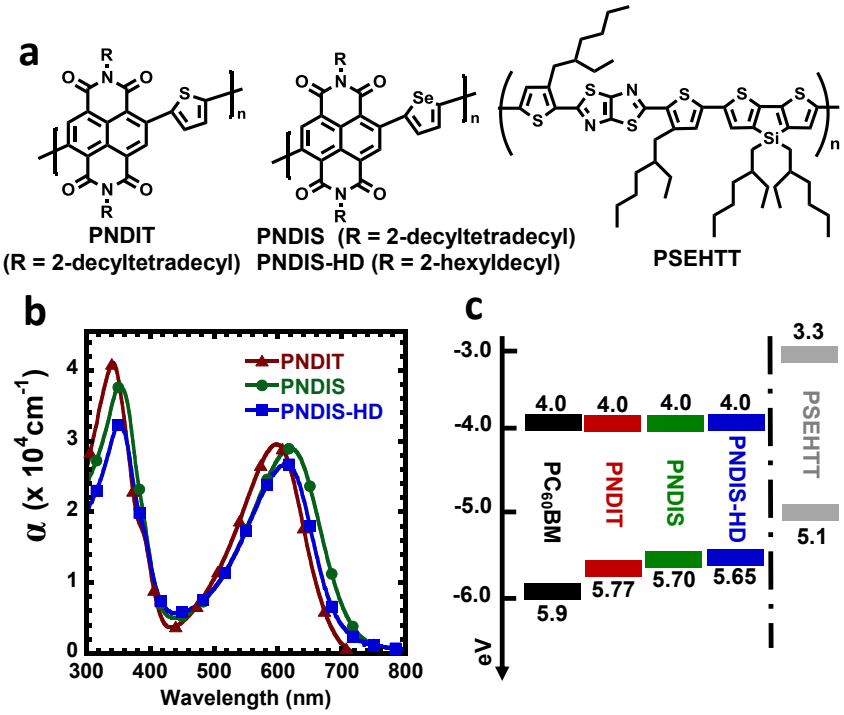

Figure 6.1. (a) Molecular structures of acceptor (PNDIT, PNDIS, and PNDIS-HD) and donor (PSEHTT) polymers. (b) UV-vis absorption spectra of PNDIT, PNDIS, and PNDIS-HD. (c) LUMO/HOMO energy levels of PNDIT, PNDIS, PNDIS-HD, $PC_{60}BM$, and PSEHTT.

Optical absorption spectra of PNDIT, PNDIS, and PNDIS-HD thin films (Figure 6.1b) and dilute (~ 10^{-6} M) $CHCl_3$ solutions show two distinctive absorption peaks, one due to π- π* transition at 340 - 360 nm and the other centered at 598 - 621 nm, which is a result of intramolecular charge transfer (ICT) (Table 6.1). It is interesting that the selenophene-linked polymers, PNDIS and PNDIS-HD, have slightly smaller band gaps and broader full-width-at-half-maximum (fwhm) in the ICT bands, which imply potentially better near-infrared light harvesting compared to the thiophene-linked PNDIT. At their visible absorption maxima of 598 - 621 nm, all three NDI copolymers have an absorption

coefficient (α) of (2.7 - 2.9) × 10^4 cm^{-1}. In contrast, an absorption coefficient of 1.1 × 10^5 cm^{-1} is observed at the absorption maximum (584 nm) of the donor polymer (PSEHTT). The lowest unoccupied and highest occupied molecular orbitals (LUMO/HOMO) energy levels of the NDI copolymers along with those of $PC_{60}BM$[7] and PSEHTT[5] are shown in Figure 6.1c. The LUMO energy levels of the NDI copolymers were estimated from cyclic voltammetry while the corresponding HOMO energy levels were obtained from the LUMO levels and the optical band gaps.

Table 6.1. Molecular Weight, Thermal Stability, Photophysical, and XRD Properties of NDI-Copolymers.

Polymer	M_w (kDa)	M_n (kDa)	PDI	T_d (°C)	λ_{max}^{sol}	λ_{max}^{film}	E_g (eV)	d_{100} (Å)	d_{010} (Å)
PNDIT	31.5	23.9	1.3	430	326, 542	341, 598	1.77	24.86	4.20
PNDIS	31.6	26.1	1.2	415	341, 556	353, 621	1.70	22.92	4.16
PNDIS-HD	177.9	79.0	2.3	400	341, 556	351, 614	1.65	21.53	4.16

Electron transport properties of PNDIT, PNDIS, and PNDIS-HD thin films were characterized by using organic field-effect transistors (OFETs) with bottom gate / top contact geometry. The OFETs showed only n-channel transistor behavior with unipolar electron transport. The average saturated region field-effect electron mobilities of PNDIT, PNDIS, and PNDIS-HD were 2 × 10^{-4}, 2 × 10^{-3}, and 7 × 10^{-3} cm^2/Vs, respectively. The order of magnitude higher electron mobility of PNDIS and PNDIS-HD compared to PNDIT can be understood from the larger π-orbitals of selenium compared to sulfur, which improves overlap of the orbitals. In addition, interaction between Se-Se atoms could enhance the crystallinity of the copolymers and interchain charge transport.[8] The higher electron mobility of PNDIS and PNDIS-HD can also be explained by their favorable solid state morphology and molecular packing with shorter d_{100} and

d_{010} spacings compared to PNDIT (Table 6.1). The higher electron mobility of PNDIS-HD with shorter hexyldecyl side chains compared to PNDIS with decyltetradecyl side chains can be largely understood in terms of the higher molecular weight of PNDIS-HD.

We fabricated and evaluated polymer/polymer blend solar cells with inverted device structure of ITO/ZnO/blend/MoO_3/Ag. The active layer blend was PNDIT:PSEHTT, PNDIS:PSEHTT, or PNDIS-HD:PSEHTT, each spin-coated from chlorobenzene with an optimum composition of 1:1 *wt/wt*. The optimal composition (1:1 *wt/wt*) to focus our detailed investigation was determined by the initial performance of solar cells fabricated from different blend compositions (1:0.75, 1:1, and 1:2 *wt/wt*). The photodiodes were fabricated in a glove box and tested under AM 1.5 solar illumination at 100 mW/cm^2 in ambient conditions. Representative current density-voltage (*J-V*) curves of PNDIT:PSEHTT, PNDIS:PSEHTT, and PNDIS-HD:PSEHTT solar cells are shown in Figure 6.2a. The photovoltaic parameters including the short-circuit current density (J_{sc}), the open-circuit voltage (V_{oc}), and fill factor (*FF*) are summarized in Table 6.2.

Table 6.2. Photovoltaic Properties of All-polymer Solar Cells.

Active layer (1:1 *wt/wt*)	J_{sc} (mA/cm^2)	V_{oc} (V)	FF	PCE^{avg} (%)	PCE^{max} (%)
PNDIT:PSEHTT	3.80	0.61	0.56	1.20 ± 0.09	1.30
PNDIS:PSEHTT	6.53	0.75	0.60	2.84 ± 0.15	2.96
PNDIS-HD:PSEHTT	7.78	0.76	0.55	3.16 ± 0.10	3.26

BHJ devices based on the thiophene-linked PNDIT acceptor showed the lowest performance among the three NDI copolymer acceptors, including a maximum 1.30 % PCE and a rather low photocurrent (Table 6.2). The performance of the BHJ solar cells increased significantly by using

the selenophene-linked PNDIS acceptor; the observed maximum PCE of 2.96 % means a 2.4-fold increase compared with the PNDIT devices. This improvement arises from the higher J_{sc} of 6.53 mA/cm^2 as well as the increased V_{oc} of 0.75 V. The best performance, with a maximum PCE of 3.26 %, J_{sc} = 7.78 mA/cm^2, and V_{oc} = 0.76 V, was observed in PNDIS-HD:PSEHTT blend solar cells, where the acceptor polymer has smaller hexyldecyl (HD) side chains. We note that both the PCE and photocurrent observed in PNDIS-HD devices are the highest for all-polymer solar cells reported to date.

The EQE spectra of the photovoltaic devices showed that the photocurrent generation starts at 720 nm (Figure 6.2b) and are consistent with the absorption spectra of the blends. The PNDIS-HD:PSEHTT device shows the highest photoconversion efficiency with a maximum EQE of 47% with more than 45% over the 500 - 650 nm wavelength range. The J_{sc} calculated by integrating the EQE spectrum of the PNDIS-HD:PSEHTT solar cell with an AM 1.5 reference spectrum is 7.76 mA/cm^2, which is in excellent agreement with the 7.78 mA/cm^2 measured directly from the *J-V* curve. We note that J_{sc} values calculated from the EQE spectra for the PNDIS and PNDIT devices were also within 3 % of the J_{sc} values from *J-V* measurements. The maximum EQE seen in PNDIS-HD devices is the highest so far in all-polymer solar cells.

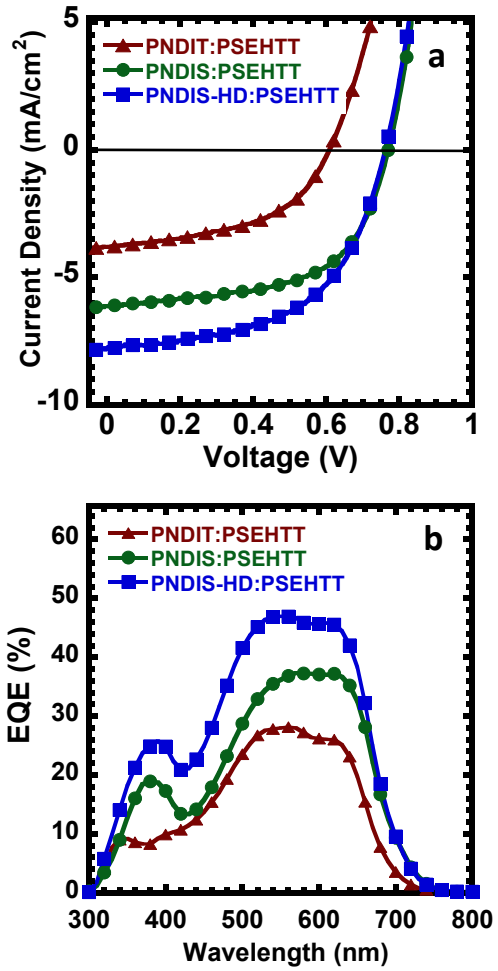

Figure 6.2. (a) Current density (*J*) – voltage (*V*) characteristics and (b) external quantum efficiency (EQE) spectra of all-polymer BHJ solar cells from 1:1 wt/wt blend each of PSEHTT:PNDIT, PSEHTT:PNDIS, and PSEHTT:PNDIS-HD.

We also fabricated polymer/fullerene solar cells with PSEHTT:$PC_{60}BM$ (1:2 *wt/wt*) active layer and the same inverted device structure as a reference for comparison with the polymer/polymer blend solar cells. In this case, we used the previously reported optimized composition and processing conditions to deposit the PSEHTT:$PC_{60}BM$ active layer, including 3.0 vol% DIO additive in *o*-dichlorobenzene.[5b] From the *J-V* characteristics we obtained J_{sc} = 8.46 mA/cm^2, V_{oc} = 0.64 V, FF = 0.62, and a maximum PCE of 3.3% (average PCE 3.23 ± 0.11). This performance is in good agreement with the previous report.[5b] The EQE spectrum of the optimum PSEHTT:$PC_{60}BM$ cell shows the same onset of photocurrent as the above all-polymer devices; however, the 54% maximum EQE is higher than the 47% observed for the all-polymer BHJ solar cells. Although the EQE and the photocurrent of $PC_{60}BM$ devices are higher than those of the polymer acceptor PNDIS-HD, the power conversion efficiencies of BHJ solar cells using the two types of acceptors are identical largely because of the superior photovoltage of the all-polymer devices.

The charge transport properties of the polymer/polymer blends (PSEHTT:PNDIT, PSEHTT:PNDIS, and PSEHTT:PNDIS-HD) in the all-polymer solar cells were investigated by both OFET devices and space-charge-limited current (SCLC) measurements are summarized in Figure 6.3. and Table 6.3. Field-effect electron mobility in PNDIS-HD blends (1.3×10^{-4} cm^2 /Vs) was slightly better than in PNDIS blends but an order of magnitude higher than in PNDIT blends. In contrast, the field-effect hole mobility was about the same in all three series of blends (3.5 - 6.4) $\times 10^{-4}$ cm^2 /Vs. Hole-only devices, composed of ITO/PEDOT:PSS/blend/Au, and electron-only devices, consisting of ITO/ZnO/blend/LiF/Al, enabled estimate of the bulk charge transport properties of the BHJ blend films. Electron mobility in the bulk blend film is also highest in the PNDIS-HD blends (1.0×10^{-4} cm^2 /Vs), slightly lower in PNDIS blends (5.8×10^{-5} cm^2 /Vs) and a factor of 6 lower in the PNDIT blends (1.8×10^{-5} cm^2 /Vs). Balasnced and high hole and electron mobilities are thus observed in the PNDIS-HD blends (Table 6.3), which can largely explain the highest performance in terms of J_{sc}, EQE, and PCE values for the BHJ solar cells using this polymer acceptor.

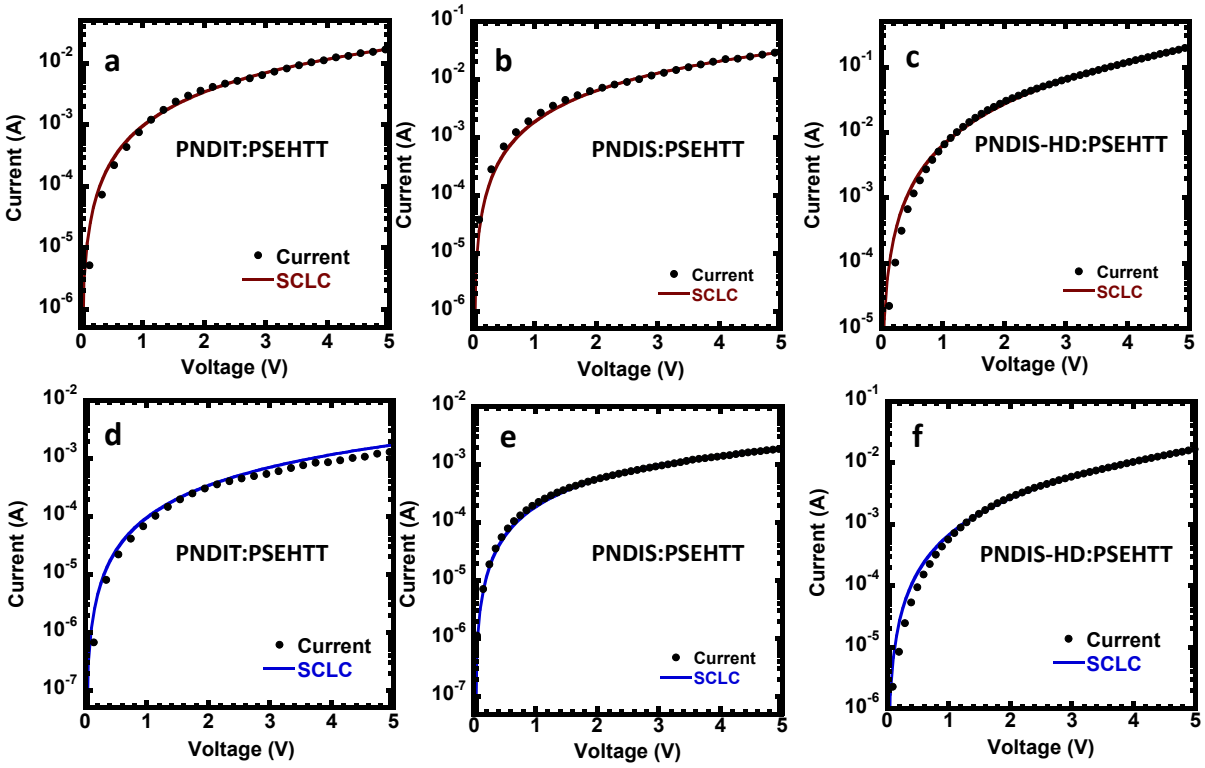

Figure 6.3. Current (*I*) -voltage (*V*) characteristics and space-charge-limited current (SCLC) fittings of devices measured in ambient conditions. Hole-only SCLC devices: ITO/PEDOT:PSS/blend/Au with (a) PNDIT:PSEHTT=1:1, (b) PNDIS:PSEHTT=1:1, and (c) PNDIS-HD:PSEHTT=1:1 blends; Electron-only SCLC devices: ITO/ZnO/blend/LiF/Al with (d) PNDIT:PSEHTT=1:1, (e) PNDIS:PSEHTT=1:1, and (f) PNDIS-HD:PSEHTT=1:1 blends.

Table 6.3. Charge Transport Properties of Polymer/Polymer Blends used in All-polymer Solar Cells.

Blend (1:1 *wt/wt*)	μ_h[a] (cm^2/Vs) (OFET)	μ_e[b] (cm^2/Vs) (OFET)	μ_h[c] (cm^2/Vs) (SCLC)	μ_e[d] (cm^2/Vs) (SCLC)
PNDIT:PSEHTT	4.0×10^{-4}	1.0×10^{-5}	4.5×10^{-5}	1.8×10^{-5}
PNDIS:PSEHTT	3.5×10^{-4}	7.5×10^{-5}	9.6×10^{-5}	5.8×10^{-5}
PNDIS-HD:PSEHTT	6.4×10^{-4}	1.3×10^{-4}	2.0×10^{-4}	1.0×10^{-4}

Average charge carrier mobility of blend from p-channel[a] and n-channel[b] organic field-effect transistors (OFETs). [c]Hole and [d]electron mobility of blend extracted from space-charge-limited current (SCLC) measurement using single charge carrier devices.

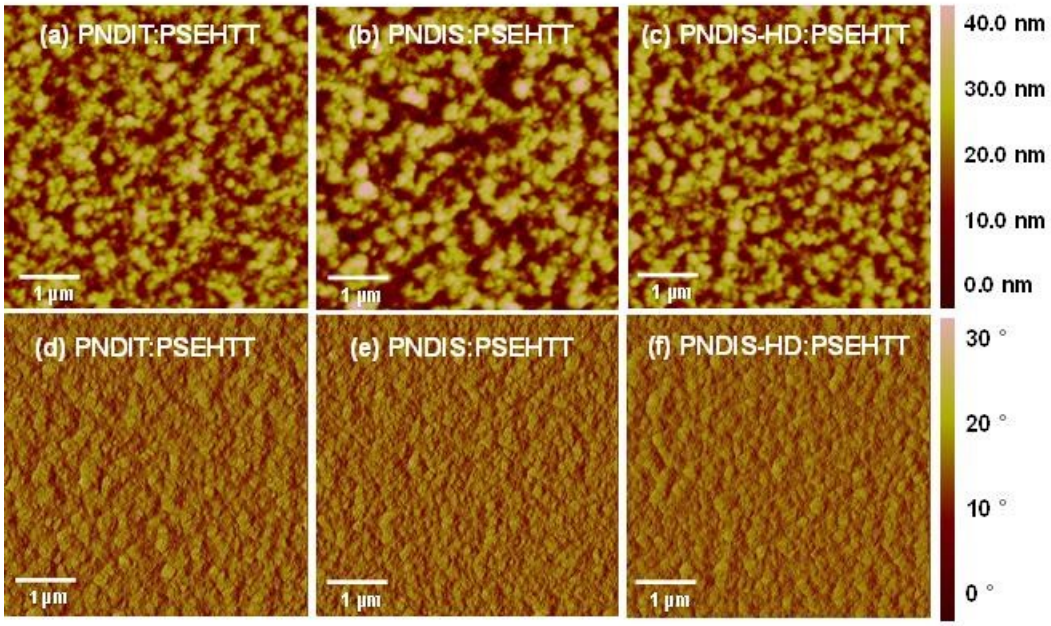

Figure 6.4. AFM topographical images (5 × 5 µm) of the surfaces of all-polymer solar cells: (a) PNDIT:PSEHTT, (b) PNDIS:PSEHTT, and (c) PNDIS-HD:PSEHTT; and the corresponding phase images of (d) PNDIT:PSEHTT, (e) PNDIS:PSEHTT, and (f) PNDIS-HD:PSEHTT.

AFM imaging was used to investigate the surface morphology of the all-polymer solar cells. AFM topographic and the corresponding phase images taken directly from the surfaces of devices are shown in Figure 6.4. The observed phase separated morphology with domain sizes of 200 - 500 nm is identical in all three blend systems (PNDIT, PNDIS, and PNDIS-HD). The similarity of the morphology of all the three different polymer/polymer BHJ devices implies that the observed large variation in the photocurrent and PCE does not originate in the blend morphologies. On the other hand, the large scale of the observed phase separation in the blends suggests that there is still room for further improvement of the photovoltaic properties of PNDIS:PSEHTT and PNDIS-HD:PSEHTT blends by reducing the domain sizes of the phase separated blend morphology through strategies such as co-solvents[3e,3h] and processing additives.[9]

6.1.4. Conclusions

In conclusion, two new semicrystalline NDI copolymers (PNDIS, PNDIS-HD) and a known one (PNDIT) have been synthesized, characterized and, for the first time, evaluated as acceptors in BHJ organic solar cells. We found that all-polymer solar cells composed of PNDIS-HD acceptor and PSEHTT donor have a record performance (PCE = 3.3 %, J_{sc} = 7.78 mA/cm^2, and EQE = 47 %), which is comparable to similarly evaluated $PC_{60}BM$:PSEHTT BHJ solar cells. Balanced electron and hole transport was observed in the PNDIS-HD:PSEHTT blend active layers. The superior photovoltaic properties of PNDIS-HD compared to PNDIS and prior NDI copolymers[3e,3n] suggest that unipolar electron transport with high bulk mobility, good crystallinity, size of alkyl side chains, and molecular weight are all important factors in the design of suitable acceptor polymers for BHJ solar cells.

6.1.5. References

(1) (a) Günes, S.; Neugebauer, H.; Sariciftci, N. S. *Chem. Rev.* **2007**, *107*, 1324. (b) Thompson, B. C.; Fréchet, J. M. J. *Angew. Chem. Int. Ed.* **2008**, *47*, 58. (c) Li, G.; Zhu, R.; Yang, Y. *Nat. Photon.* **2012**, *6*, 153.

(2) (a) You, J.; Dou, L.; Yoshimura, K.; Kato, T.; Ohya, K.; Moriarty, T.; Emery, K.; Chen, C.-C.; Gao, J.; Li, G.; Yang, Y. *Nat. Commun.* **2013**, *4*, 1446. (b) He, Z.; Zhong, C.; Su, S.; Xu, M.; Wu, H.; Cao, Y. *Nat. Photon.* **2012**, *6*, 591. (c) Small, C. E.; Chen, S.; Subbiah, J.; Amb, C. M.; Tsang, S.-W.; Lai, T.-H.; Reynolds, J. R.; So, F. *Nat. Photon.* **2012**, *6*, 115.

(3) (a) McNeill, C. R. *Energy Environ. Sci.* **2012**, *5*, 5653. (b) Facchetti, A. *Mater. Today* **2013**, *16*, 123. (c) Halls, J. J. M.; Walsh, C. A.; Greenham, N. C.; Marseglia, E. A.; Friend, R. H.; Moratti, S. C.; Holmes, A. B. *Nature* **1995**, *376*, 498. (d) Alam, M. M.; Jenekhe, S. A. *Chem. Mater.* **2004**, *16*, 4647. (e) Schubert, M.; Dolfen, D.; Frisch, J.; Roland, S.; Steyrleuthner, R.; Stiller, B.; Chen, Z.; Scherf, U.; Koch, N.; Facchetti, A.; Neher, D. *Adv. Energy Mater.* **2012**, *2*, 369. (f) Jenekhe, S. A.; Yi, S. *Appl. Phys. Lett.* **2000**, *77*, 2635. (g) Zhou, E.; Tajima, K.; Yang, C.; Hashimoto, K. *J. Mater. Chem.* **2010**, *20*, 2362. (h) Zhou, E.; Cong, J.; Wei, Q.; Tajima, K.; Yang, C.; Hashimoto, K. *Angew. Chem. Int. Ed.* **2011**, *50*, 2799. (i) Kietzke, T.; Hörhold, H.-H.; Neher, D. *Chem. Mater.* **2005**, *17*, 6532. (j) Holcombe, T. W.; Woo, C. H.; Kavulak, D. F. J.; Thompson, B. C.; Fréchet, J. M. J. *J. Am. Chem. Soc.* **2009**, *131*, 14160. (k) Mori, D.; Benten, H.; Ohkita, H.; Ito, S.; Miyake, K. *ACS Appl. Mater. Interfaces* **2012**, *4*, 3325. (l) Zhan, X.; Tan,

Z. a.; Domercq, B.; An, Z.; Zhang, X.; Barlow, S.; Li, Y.; Zhu, D.; Kippelen, B.; Marder, S. R. *J. Am. Chem. Soc.* **2007**, *129*, 7246. (m) Zhou, E.; Cong, J.; Zhao, M.; Zhang, L.; Hashimoto, K.; Tajima, K. *Chem. Comm.* **2012**, *48*, 5283. (n) Hwang, Y.-J.; Ren, G.; Murari, N. M.; Jenekhe, S. A. *Macromolecules* **2012**, *45*, 9056. (o) Cao, Y.; Lei, T.; Yuan, J.; Wang, J.-Y.; Pei, J. *Polym. Chem.* **2013**, *4*, 5228. (p) Moore, J. R.; Albert-Seifried, S.; Rao, A.; Massip, S.; Watts, B.; Morgan, D. J.; Friend, R. H.; McNeill, C. R.; Sirringhaus, H. *Adv. Energy Mater.* **2011**, *1*, 230. (q) Brenner, T. J. K.; Hwang, I.; Greenham, N. C.; McNeill, C. R. *J. Appl. Phys.* **2010**, *107*, 114501. (r) Guo, C.; Lin, Y.-H.; Witman, M. D.; Smith, K. A.; Wang, C.; Hexemer, A.; Strzalka, J.; Gomez, E. D.; Verduzco, R. *Nano. Lett.* **2013**, *13*, 2957.

(4) (a) Anthony, J. E.; Facchetti, A.; Heeney, M.; Marder, S. R.; Zhan, X. *Adv. Mater.* **2010**, *22*, 3876. (b) Mishra, A.; Bäuerle, P. *Angew. Chem. Int. Ed.* **2012**, *51*, 2020.

(5) (a) Subramaniyan, S.; Xin, H.; Kim, F. S.; Shoaee, S.; Durrant, J. R.; Jenekhe, S. A. *Adv. Energy Mater.* **2011**, *1*, 854. (b) Xin, H.; Subramaniyan, S.; Kwon, T.-W.; Shoaee, S.; Durrant, J. R.; Jenekhe, S. A. *Chem. Mater.* **2012**, *24*, 1995.

(6) (a) Hwang, Y.-J.; Murari, N. M.; Jenekhe, S. A. *Polym. Chem.* **2013**, *4*, 3187. (b) Guo, X.; Kim, F. S.; Seger, M. J.; Jenekhe, S. A.; Watson, M. D. *Chem. Mater.* **2012**, *24*, 1434.

(7) Scharber, M. C.; Mühlbacher, D.; Koppe, M.; Denk, P.; Waldauf, C.; Heeger, A. J.; Brabec, C. J. *Adv. Mater.* **2006**, *18*, 789.

(8) (a) Chen, Z.; Lemke, H.; Albert-Seifried, S.; Caironi, M.; Nielsen, M. M.; Heeney, M.; Zhang, W.; McCulloch, I.; Sirringhaus, H. *Adv. Mater.* **2010**, *22*, 2371. (b) Hollinger, J.; Jahnke, A. A.; Coombs, N.; Seferos, D. S. *J. Am. Chem. Soc.* **2010**, *132*, 8546.

(9) Ren, G.; Ahmed, E.; Jenekhe, S. A. *Adv. Energy Mater.* **2011**, *1*, 946.

6.2. Enhanced Performance of All-Polymer Solar Cells Achieved by Control of Blend Morphology

6.2.1. Introduction

Much progress has been made in the field of bulk heterojuction (BHJ) organic photovoltaics based on polymer donor and fullerene derivative acceptor such as phenyl-C_{61}-butyric acid methyl ester (PCBM) in the last decade, already reporting power conversion efficiencies (PCEs) nearly 10 %.[1] In contrast, development of polymer/polymer solar cells with free of fullerenes has been remained very challenging with much lower photovoltaic performances, in spite of their potential robustness such as thermal and morphological stability of polymer blends.[2] Facile molecular design to tune intrinsic properties of both *donor* and *acceptor* conjugated polymers can also be achieved, including optical absorption, electronic structure, crystallinity, solubility, and charge transport. Especially, polymer/polymer blend can absorb light from visible and near infrared region by acceptor polymers for effective light harvesting throughout the solar spectrum, which is often neglected by polymer/fullerene system. This implies that the excitons formed by the light absorption of the acceptor polymer can contribute to overall photocharge generation via efficient photoinduced charge transfer.

However, one of the major reasons for much lower performance of polymer/polymer solar cells compared to polymer/fullerene is that the planar nature of both conjugated polymers in all-polymer BHJ systems could facilitate unwanted formation of intramolecular excimers or intermolecular exciplexes with consequent retardation of charge separation.[3] High π-π conjugation strength of polymers tends to create large phase-separated with disconnected domains which leads to poor charge separation and transport in the photoactive blend. Formation

of interconnected polymer domains in few tens of nanometers length scale with better polymer/polymer interfacial area can be a solution to overcome this issue.[4] Such a nanophase-separated morphology of polymer blend can be achieved by different casting solvents, processing additives or solvent mixtures during solution-deposition of thin films. The use of different solvents provides a way for tuning the degree of phase separation by the use of solvents with different volatilities. Although varying the polymer blend morphology by using different composition of processing solvent has been widely known, there have been only few reports regarding enhancing photovoltaic performance of all-polymer solar cells by this approach.[5]

We have recently reported all-polymer solar cells with 3.3% PCE enabled by new n-type naphthalene diimide (NDI)-selenophene copolymer acceptor (PNDIS-HD) blended with thiazolothiazole-dithienylsilole copolymer donor (PSEHTT).[7] We have showed that the new NDI-based acceptor copolymer with good electron transport is promising for efficient all-polymer BHJ solar cells. Nevertheless, the large phase separated morphology with domain sizes of 200 - 500 nm was observed in PSEHTT:PNDIS-HD blend solar cells that provides an opportunity for the further improvement of device performance by control of blend morphology.

In this section, we report all-polymer BHJ solar cells with a record 4.8 % efficiency achieved by control of donor PSEHTT and acceptor PNDIS-HD blend morphology. The observed high short circuit current density of 10.47 mA cm^{-2} and external quantum efficiency (EQE) of 57.3 % with a fill factor (FF) of 0.60 are also the best photovoltaic parameters seen in all-polymer solar cells. We show that the blend morphology of PSEHTT:PNDIS-HD was successfully modified to obtain optimal nanophase-separated domains with improved interconnection by chlorobenzene (CB):1,2-dichlorobenzene (DCB) solvent mixture processing. Enhanced and balanced charge transport property of PSEHTT:PNDIS-HD blend processed from CB:DCB co-solvent were

investigated by space-charge-limited current characterization. Furthermore, we demonstrate that the photovoltaic performance of PSEHTT:PNDIS-HD blend solar cells exceeds that of reference PSEHTT:PCBM solar cell for the first time. This result suggests that the photocharge generation originated from the light absorption of PNDIS-HD plays a significant role in polymer/polymer solar cells and thus efficient photoinduced hole transfer from acceptor polymer is important as much as photoinduced electron transfer from donor polymer.

6.2.2. Experimental Section

PSEHTT (poly[(4,4′-bis(3-(2-ethyl-hexyl)dithieno[3,2-b:″,3′-d]silole)-2,6-diyl-*alt*-(2,5-bis-(3-(2-ethylhexyl)thiophen-2-yl)thiazolo[5,4-d]thiazole)]) and PNDIS-HD (poly{[*N*,*N'*-bis(2-hexyldexyl)-naphthalene-1,4,5,8-bis(dicarboximide)-2,6-diyl]-*alt*-5,5'-selenophene) were synthesized as previously described. The number average molecular weight (M_n) of PSEHTT and PNDIS-HD was 22.6 and 40.8 kDa with polydispersity index (PDI) of 3.1 and 1.3, respectively. Zinc oxide (ZnO) layer was sol-gel derived from spin-coating of ZnO precursor solution. ZnO precursor solution was prepared by dissolving 1 g of zinc acetate dihydrate (99.999 % trace metals basis, Aldrich) in 10 mL of 2-methoxyethanol (99.8 %, anhydrous, Aldrich) with adding 0.28 g of ethanolamine (≥99.5 %, Aldrich) under stirring for overnight in ambient conditions. Phenyl-C_{61}-butyric acid methyl ester (PCBM, ≥99.5 %) was obtained from American Dye Source, Inc. (Quebec, Canada). Chlorobenzene (CB), 1,2-dichlorobenzene (DCB, anhydrous, Sigma-Aldrich) solvents and 1,8-diiodooctane (DIO) (98 %, Aldrich) processing additive were used as received. The molecular structures of PSEHTT, PNDIS-HD and PCBM are shown in Figure 6.5.

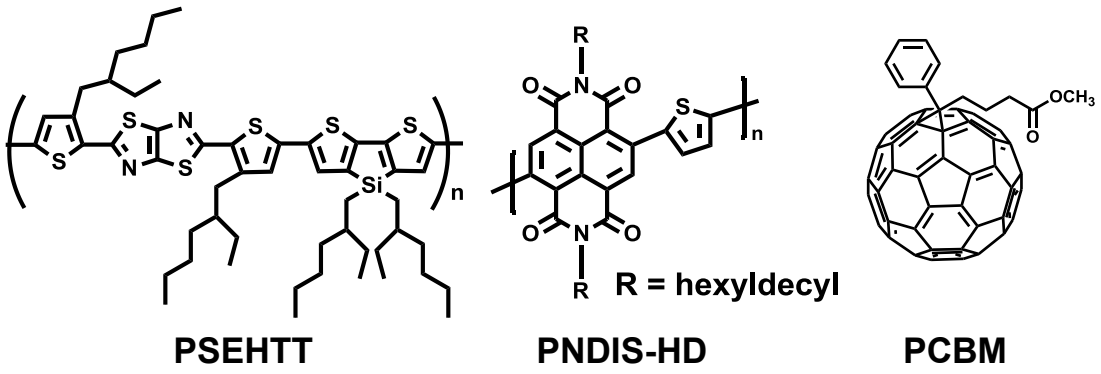

Figure 6.5. Molecular structures of donor (PSEHTT), acceptor (PNDIS-HD) polymers and PCBM.

We fabricated and evaluated polymer/polymer solar cells with inverted structure of ITO/ZnO/PSEHTT:PNDIS-HD/MoO_3/Ag. ITO glass substrate was cleaned sequentially in ultrasonic baths of acetone and isopropanol then dried at 60 °C in a vacuum oven overnight. The substrate was plasma treated right before use. ZnO precursor solution was spin-coated onto the ITO at 5000 rpm for 60 seconds, annealed at 250 °C for 1 hour to make ~30 nm thickness ZnO layer and transferred into glove box. The active layer PSEHTT:PNDIS-HD blend (1:1 *wt/wt*) solution was spin-coated using different solvent composition: CB only or CB:DCB=90:10 (*v/v*) mixed solvent. The optimal composition (1:1 *wt/wt*) was determined previously. After spin-coating, the film was annealed at 175 °C for 10 minutes inside the glove box followed by thermal vacuum deposition of MoO_3 (7.5 nm) and Ag anode (100 nm). The thickness of active layer after annealing was 70-80 nm. The photovoltaic cells were fabricated in inert conditions but tested under AM 1.5 solar illumination at 100 mW cm^{-2} in ambient conditions.

6.2.3. Results and Discussion

Representative current density-voltage (*J-V*) curves of PSEHTT:PNDIS-HD solar cells processed from the two different solvents are shown in Figure 6.6a. The photovoltaic parameters

including the short-circuit current density (J_{sc}), the open-circuit voltage (V_{oc}), fill factor (FF), and maximum EQE are summarized in Table 6.4. PSEHTT:PNDIS-HD blend devices spin-coated from chlorobenzene showed a maximum 3.98 % PCE and high photocurrent of 9.80 mA cm^{-2} with a FF of 0.55. These photovoltaic parameters are higher than the values that we previously reported for the same polymer blend, largely because of the higher molecular weight of PSEHTT and also the surface modification of ZnO by ethanolamine. The performance of the PSEHTT:PNDIS-HD blend solar cells significantly increased by spin-coating from CB:DCB mixture; the best observed PCE of 4.81 % means that a more than 20 % increase is achieved compared to the devices spin-casted from chlorobenzene solvent. This improvement arises from the higher J_{sc} of 10.47 mA cm^{-2} as well as the increased V_{oc} (0.76 V) and FF (0.60). We point out that the observed photovoltaic properties of PSEHTT:PNDIS-HD solar cells spin-coated from CB:DCB co-solvent including the PCE, photocurrent, and EQE are the highest for all-polymer solar cells reported to date.

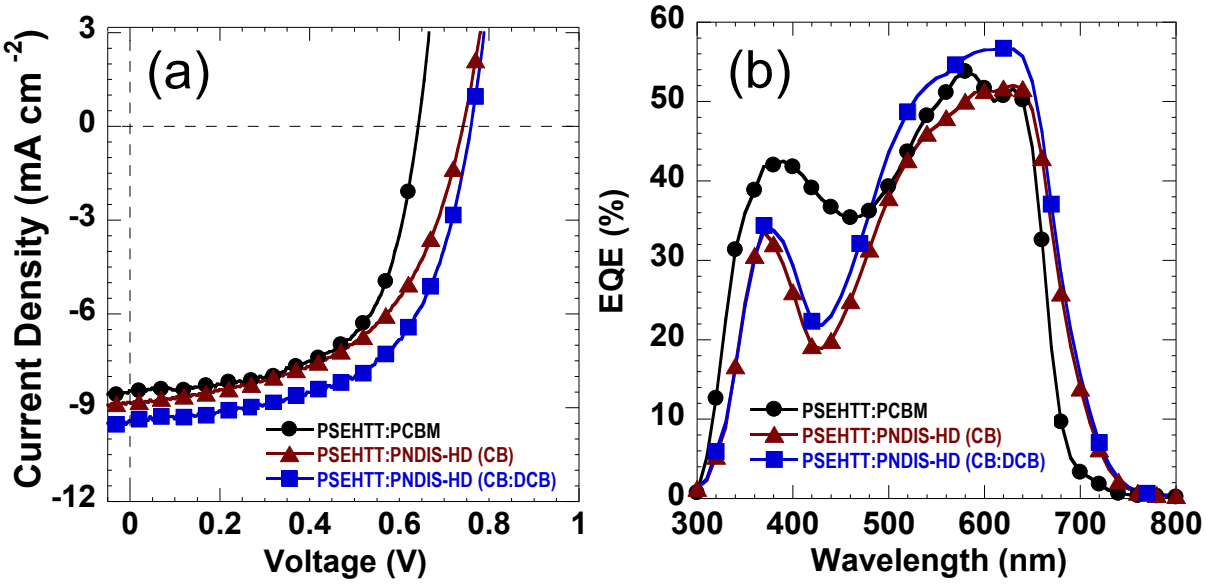

Figure 6.6. (a) Current density (J) – voltage (V) characteristics and (b) external quantum efficiency (EQE) spectra of all-polymer PSEHTT:PNDIS-HD blend solar cells processed from different solvents: Chlorobenzene (CB) and CB:dichlorobenzene (DCB) (90:10 vol/vol %). Results for PSEHTT:PCBM solar cell are shown in (a) and (b) for comparison.

Table 6.4. Photovoltaic Properties of BHJ Solar Cells.

Active layer (Solvent used)	J_{sc} (mA cm^{-2})	V_{oc} (V)	FF	PCE (%)	EQE^{max} (%)	R_{SH} (Ω cm^2)	R_S (Ω cm^2)
PSEHTT:PNDIS-HD (Chlorobenzene)	9.80	0.74	0.55	3.98 (3.80 ± 0.16)	52.3	675	9.6
PSEHTT:PNDIS-HD (CB:DCB=90:10)	10.47	0.76	0.60	4.81 (4.68 ± 0.13)	57.3	500	7.7
PSEHTT:PCBM (DCB:DIO=97:3)	8.46	0.64	0.62	3.34 (3.23 ± 0.11)	53.7	630	7.3

a) Different volume composition of casting solvent was used to solution-deposit the active layer.

We also fabricated and evaluated polymer/fullerene solar cells with PSEHTT:PCBM (1:2 *wt/wt*) active layer and the same inverted device structure for comparison with the all-polymer solar cells. We used the previously reported optimized composition and processing conditions to deposit the polymer:PCBM BHJ active layer, including 3.0 vol % DIO processing additive in DCB.[6] The PSEHTT:PCBM solar cells showed J_{sc} of 8.46 mA cm^{-2}, V_{oc} = 0.64 V, *FF* = 0.62, with a maximum PCE of 3.3% (Table 1), in good agreement with the previous report.[6] The *J-V* characteristics of the PSEHTT:PCBM solar cells are also shown in Figure 2a; clearly the performance of the all-polymer PSEHTT:PNDIS-HD solar cells is far superior to the reference PSEHTT:PCBM solar cells.

EQE spectra of the photovoltaic devices (Figure 6.6b) correspond to the all-polymer BHJ solar cells whose *J-V* curves are shown in Figure 6.6a. The all-polymer solar cells spin-coated from CB:DCB co-solvent show the highest photoconversion efficiency with a maximum EQE of 57.3% at 630 nm. The peak EQE at 630 nm is originated from concomitant photoexcitation of both blend components which implies efficient photocharge generation by the simultaneous photoexcitation in donor and acceptor polymers. The photoresponse of the all-polymer

PSEHTT:PNDIS-HD solar cells begins at higher wavelength around 750 nm which covers the entire visible region whereas PSEHTT:PCBM solar cells starts around 700 nm. The wider coverage of solar spectrum by PSEHTT:PNDIS-HD solar cell is mainly due to the light absorption of PNDIS-HD, since PSEHTT nor PCBM do not absorb light from wavelength higher than 700 nm.[6] The higher and broader EQE spectra of PSEHTT:PNDIS-HD solar cells compared to the PSEHTT:PCBM demonstrate that the acceptor PNDIS-HD significantly contribute to the photocurrent generation as much as the donor PSEHTT in the photovoltaic devices, and thus photoinduced hole transfer from the acceptor polymer becomes an important pathway for the charge generation while efficient photoinduced electron transfer is still active.[9] The photocurrent values calculated from the EQE spectra were found to be consistent with the J_{sc} values from *J–V* curves for all the devices, showing a small mismatch between the two values within 3-7 %. This discrepancy could be due to spectral mismatch between the simulated light source and the AM1.5 solar spectrum.

The surface morphology of the PSEHTT:PNDIS-HD blend solar cells was investigated by AFM imaging. AFM height and phase images ($1 \times 1\ \mu m^2$) taken directly from the surfaces of the devices are shown in Figure 6.7. PSEHTT:PNDIS-HD solar cells spin-coated from chlorobenzene show a phase separated morphology with large domain sizes of 100 - 200 nm (Figure 6.7a,c) which is not ideal for efficient exciton dissociation. In contrast, the PSEHTT:PNDIS-HD devices spin-coated from CB:DCB co-solvent show a phase-separated morphology with domain sizes of 10–20 nm (Figure 6.7b,d), which is a characteristic spacing close to the typical exciton diffusion length and thus more favourable for efficient charge separation. The observed surface morphology of the devices spin-coated from the CB:DCB co-solvent show much fine domain sizes and more interconnected structure (Figure 6.7d,h) than the

coarser and less connected structure of devices from cholorobenzene (Figure 6.7e,g). These results demonstrate that the morphology of the polymer/polymer blend solar cells was successfully varied by using a solvent mixture (CB:DCB). Such a large difference in morphology can be expected to translate to differences in not only charge separation at the donor/acceptor interfaces but also charge transport in the blends.

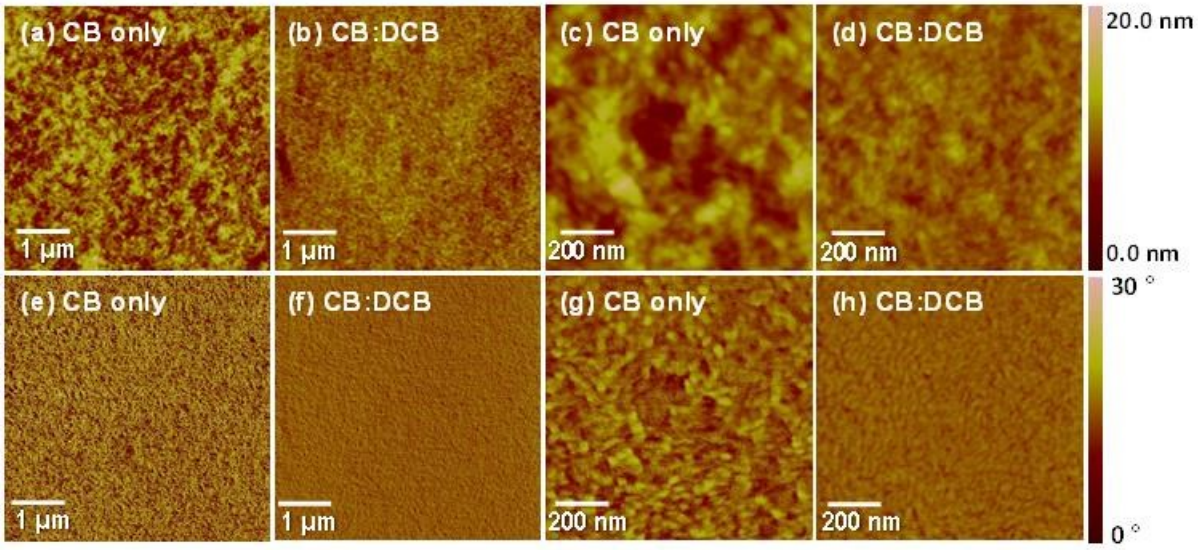

Figure 6.7. AFM topographical images (5 × 5 µm) of the surfaces of PSEHTT:PNDIS-HD solar cells: (a) deposited from CB only solvent, and (b) deposited from CB:DCB co-solvent; AFM topographical images in smaller scale (1 × 1 µm): (c) deposited from CB only solvent, and (d) deposited from CB:DCB co-solvent. The corresponding phase images of PSEHTT:PNDIS-HD solar cells: (e), (g) deposited from CB only solvent, and (f), (h) deposited from CB:DCB co-solvent.

We measured charge transport properties of the PSEHTT:PNDIS-HD blend films spin-coated from different solvents (chlorobenzene or CB:DCB) by the space-charge-limited current (SCLC) technique. Hole-only devices were composed of ITO/PEDOT:PSS/ blend/MoO_3/Au whereas electron-only devices consisted of ITO/ZnO/blend/LiF/Al. The bulk mobility was extracted by fitting the *I-V* curves in the near quadratic region according to the modified Mott-Gurney equation. Electron and hole mobilities of PSEHTT:PNDIS-HD blend films deposited from chlorobenzene were found to be 1.0×10^{-4} and 2.6×10^{-4} $cm^2V^{-1}s^{-1}$, respectively, and are similar to the previously reported values.[7] In contrast, PSEHTT:PNDIS-HD blend films deposited from

CB:DCB co-solvent had electron (2.6×10^{-4} $cm^2V^{-1}s^{-1}$) and hole (5.4×10^{-4} $cm^2V^{-1}s^{-1}$) mobilities that are 2-fold higher. The observed balanced and increased hole and electron mobilities in the PSEHTT:PNDIS-HD blend films deposited from CB:DCB co-solvent can largely explain the enhanced photovoltaic performance in terms of J_{sc}, EQE, *FF* and thus the high PCE values of these all-polymer solar cells.

The light intensity dependence of all-polymer solar cells was measured to further investigate the suppressed bimolecular charge recombination through improved nanophase-separated blend morphology. The dependence of current density and normalized open circuit voltage on the illuminated light intensity of all-polymer solar cells with different casting solvents are plotted in Figure 6.8. The light intensity of AM 1.5 sunlight from a filtered Xenon lamp was adjusted by using a set of neutral density filters.

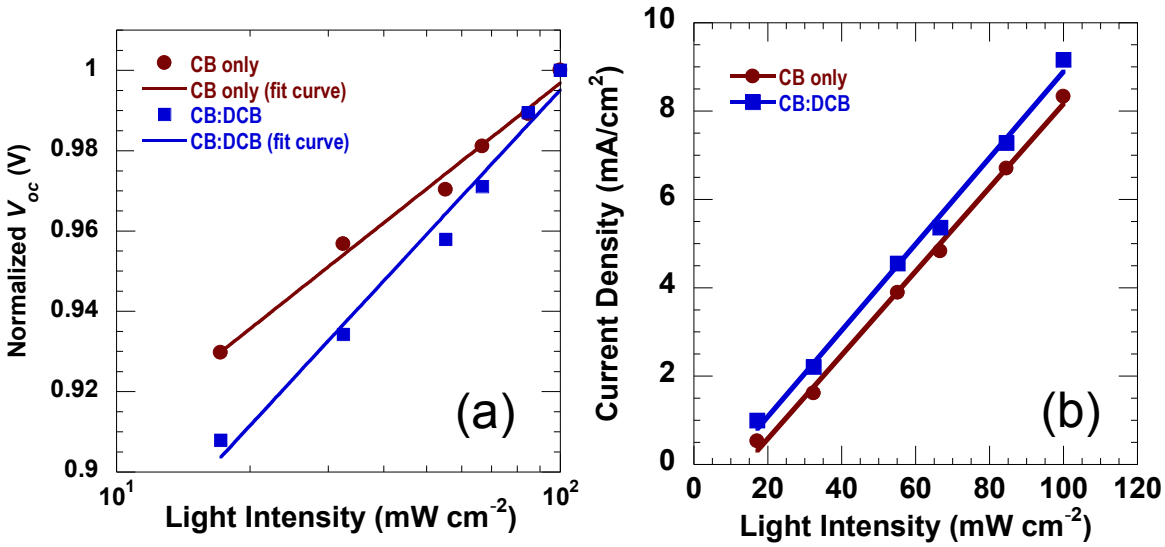

Figure 6.8. Light intensity dependence of (a) V_{oc} and (b) J_{sc} of PSEHTT:PNDIS-HD solar cells with different casting solvents.

The light intensity dependencies of the open circuit voltage and photocurrent of PSEHTT:PNDIS-HD blend solar cells were measured to further investigate charge recombination in the devices and effects of improved nanophase-separated blend morphology

achieved by processing from different solvents. The dependence of normalized V_{oc} on the illuminated light intensity of the blend devices spin-coated from different solvents is shown in Figure 6.8a. The fitted line from data for devices spin-coated from chlorobenzene show a slope of 1.09 kT/q (k = Boltzmann constant, T = temperature, and q = elementary charge), which suggests that the bimolecular Langevin recombination is dominant over the germinate recombination.[10] In contrast, a similar fitting of the data for the PSEHTT:PNDIS-HD blend photovoltaic device processed from CB:DCB co-solvent revealed a steeper slope of 1.53 kT/q, which typically represents the dominate geminate recombination caused by large trap density.[10b,c]

However, observed similar linear current density dependence on light intensity (Figure 6.8b) and the space-charge-limited characteristics in single carrier devices with balanced hole and electron mobilities for both devices indicates that there is no reason for the presence of a large trap density that could cause substantial increase of geminate recombination in the device processed from CB:DCB co-solvent. This discrepancy has been explained by considering the fact that trap-assisted germinate and bimolecular recombination are both competing processes.[11] The steeper slope of V_{oc} dependence on the light intensity of the device processed from CB:DCB co-solvent is presumably the evidence of largely suppressed bimolecular recombination rate compared to germinate recombination by improved blend morphology.[11a] We conclude from these results that the charge in polymer/polymer blend achieved by spin-coating from a co-solvent system is effective in reducing bimolecular recombination and thus enhancing charge separation in the present all-polymer solar cells.

6.2.4. Conclusions

In summary, all-polymer (PSEHTT:PNDIS-HD) blend solar cells with record 4.8 % PCE and 10.5 $mAcm^{-2}$ short-current density have been achieved by film processing from a chlorobenzene:dichlorobenzene co-solvent system. AFM imaging of the PSEHTT:PNDIS-HD blend active layer processed from chlorobenzene:dichlorobenzene (90:10 *vol/vol*) co-solvent showed that much smaller (20 – 40 nm) phase-separated domains were obtained compared to those deposited from chlorobenzene solvent (> 100 nm domains). Carrier mobilities were enhanced and more balanced in the polymer/polymer blend active layers solution-deposited from the co-solvent system in agreement with the enhanced photovoltaic properties. As a result of the siginificant light harvesting by the acceptor polymer (PNDIS-HD), both photoinduced hole transfer and photoinduced electron transfer contributed about equally to charge photogeneration in these all-polymer solar cells.

The observed far superior performance of all-polymer PSEHTT:PNDIS-HD solar cells compared to the corresponding PSEHTT:PNDIS-HD solar cells compared to the corresponding PSEHTT:PCBM devices suggest that even higher efficiencies are achievable with suitable choice of donor and acceptor polymers.

6.2.5. References

[1] a) J. You, L. Dou, K. Yoshimura, T. Kato, K. Ohya, T. Moriarty, K. Emery, C. –C. Chen, J. Gao, G. Li, Y. Yang, *Nat. Commun.* **2013**, *4*, 1446. b) C. E. Small, S. Chen, J. Subbiah, C. M. Amb, S.-W. Tsang, T.-H. Lai, J. R. Reynolds, F. So, *Nat. Photon.* **2012**, *6*, 115. c) G. Li, R. Zhu, Y. Yang, *Nat. Photon.* **2012**, *6*, 153. d) B. C. Thompson, J. M. J. Fréchet, *Angew. Chem. Int. Ed.* **2008**, *47*, 58. e) S. Günes, H. Neugebauer, N. S. Sariciftci, *Chem. Rev.* **2007**, *107*, 1324.

[2] (a) Y.-J. Hwang, N. M. Murari, S. A. Jenekhe, *Polym. Chem.* **2013**, *4*, 3187. b) A. Facchetti, *Mater. Today* **2013**, *16*, 123. c) J. R. Moore, S. Albert-Seifried, A. Rao, S. Massip, B. Watts, D. J. Morgan, R. H. Friend, C. R. McNeill, H. Sirringhaus, *Adv. Energy Mater.* **2011**, *1*, 230. d) S. Fabiano, Z. Chen, S. Vahedi, A. Facchetti, B. Pignataro, M. A. Loi, *J. Mater. Chem.* **2011**, *21*, 5891. e) Z. Tan, E. Zhou, X. Zhan, X. Wang, Y. Li, S. Barlow, S. R. Marder, *Appl. Phys. Lett.* **2008**, *93*, 073309. f) C. R. McNeill, A. Abrusci, J. Zaumseil, R. Wilson, M. J. McKiernan, J. H. Burroughes, J. J. M. Halls, N. C. Greenham, R. H. Friend, *Appl. Phys. Lett.* **2007**, *90*, 193506. g) M. M. Mandoc, W. Veurman, L. J. A. Koster, M. M. Koetse, J. Sweelssen, B. de Boer, P. W. M. Blom, *J. Appl. Phys.* **2007**, *101*, 104512. h) T. Kietzke, H.-H. Hörhold, D. Neher, *Chem. Mater.* **2005**, *17*, 6532. i) M. M. Alam, C. J. Tonzola, S. A. Jenekhe, *Macromolecules* **2003**, *36*, 6577. j) Y.-J. Hwang, G. Ren, N. M. Murari, S. A. Jenekhe, *Macromolecules* **2012**, *45*, 9056. k) D. Mori, H. Benten, I. Okada, H. Ohkita, S. Ito, *Adv. Energy Mater.* **2014**, *4*, 1301006. l) Y. Zhou, Q. Yan, Y. –Q. Zheng, J. -Y. Wang, D. Zhao, J. Pei, *J. Mater. Chem.* A **2013**, *1*, 6609.

[3] S. A. Jenekhe, J. A. Osaheni, *Science* **1994**, *265*, 765.

[4] C. R. McNeill, *Energy Environ. Sci.* **2012**, *5*, 5653.

[5] a) N. Zhou, H. Lin, S. J. Lou, X. Yu, P. Guo, E. F. Manley, S. Loser, P. Hartnett, H. Huang, M. R. Wasielewski, L. X. Chen, R. P. H. Chang, A. Facchetti, T. J. Marks, *Adv. Energy Mater.* **2014**, *4*, 1300785. b) E. Zhou, J. Cong, K. Hashimoto, K. Tajima, *Adv. Mater.* **2013**, *25*, 6991. c) E. Zhou, J. Cong, Q. Wei, K. Tajima, C. Yang and K. Hashimoto, *Angew. Chem. Int. Ed.* **2011**, *50*, 2799.

[6] a) S. Subramaniyan, H. Xin, F. S. Kim, S. Shoaee, J. R. Durrant, S. A. Jenekhe, *Adv. Energy Mater.* **2011**, *1*, 854. b) H. Xin, S. Subramaniyan, T.-W. Kwon, S. Shoaee, J. R. Durrant, S. A. Jenekhe, *Chem. Mater.* **2012**, *24*, 1995.

[7] T. Earmme, Y.-J. Hwang, N. M. Murari, S. Subramaniyan, S. A. Jenekhe, *J. Am. Chem. Soc.* **2013**, *135*, 14960.

[8] S. A. Jenekhe, L. D. Lu, M. M. Alam, *Macromolecules* **2001**, *34*, 7315.

[9] G. Ren, C. W. Schlenker, E. Ahmed, S. Subramaniyan, S. Olthof, A. Kahn, D. S. Ginger, S. A. Jenekhe, *Adv. Funct. Mater.* **2013**, *23*, 1238.

[10] a) S. R. Cowan, A. Roy, A. J. Heeger, *Phys. Rev. B* **2010**, *82*, 245207. b) M. M. Mandoc, W. Veurman, L. J. A. Koster, B. de Boer, P. W. M. Blom, *Adv. Funct. Mater.* **2007**, *17*, 2167. c)

L. J. A. Koster, V. D. Mihailetchi, R. Ramaker, P. W. M. Blom, *Appl. Phys. Lett.* **2005**, *86*, 123509. d) M. M. Mandoc, F. B. Kooistra, J. C. Hummelen, B. de Boer, P. W. M. Blom, *Appl. Phys. Lett.* **2007**, *91*, 263505. e) D. Credgington, F. C. Jamieson, B. Walker, T.-Q. Nguyen, J. R. Durrant, *Adv. Mater.* **2012**, *24*, 2135.

[11] a) G.-J. A. H. Wetzelaer, M. Kuik, P. W. M. Blom, *Adv. Energy Mater.* **2012**, *2*, 1232. b) C. M. Proctora,M. Kuika, T. –Q. Nguyen*, Prog. Polym. Sci.* **2013**, *38*, 1941.

[12] B. R. Lee, E. D. Jung, Y. S. Nam, M. Jung, J. S. Park, S. Lee, H. Choi, S. -J. Ko, N. R. Shin, Y. -K. Kim, S. O. Kim, J. Y. Kim, H. -J. Shin, S. Cho, M. H. Song, *Adv. Mater.* **2014**, *26*, 494.

Chapter 7. Conclusions and Outlook

7.1. Conclusions

Throughout this work, I have investigated novel organic semiconductors and processing methods to obtain high-performance optoelectronic devices: organic light-emitting diodes (OLEDs) and organic solar cells (OSCs). To address many challenges in the research field of organic electronics, especially feasible low-cost and large area device fabrication, I have focused on the study on solution-based optoelectronic devices regarding development of new electron-transport materials, orthogonal solution-processing, novel solution-doping method for solution-processed multilayered phosphorescent OLEDs (PhOLEDs), and also new conjugated polymers and processing strategy for polymer/polymer solar cells with enhanced photovoltaic performance.

I have investigated bisindenoanthrazolines as a new class of n-type organic semiconductors for the application in organic light-emitting diodes. The high electron affinity (3.7 eV) and high electron mobility (10^{-7} to 10^{-4} cm^2/Vs) of the bisindenoanthrazolines makes them attractive candidates for electron transport in organic electronics. The bisindenoanthrazolines emitted unique electroluminescence with a high brightness and high efficiency depending on their chemical structures. Some of the bisindenoanthrazolines indeed functioned as excellent electron-transport materials in realizing high performance polymeric PhOLEDs.

Studies of multilayered PhOLEDs fabricated by novel orthogonal sequential solution-processing methods enabled by new organic semiconductor materials were conducted. Dendritic oligoquinolines were synthesized and demonstrated to be effective vacuum- as well as solution-processable electron-transport layers (ETLs) in PhOLEDs. The new oligoquinolines have robust thermal stability with high decomposition temperatures and high melting temperatures. The new electron transport materials were deposited onto polymer emission layer by orthogonal solution-

processing to achieve multilayered blue polymer-based PhOLEDs with the highest efficiency reported to date. Furthermore, I have expanded the orthogonal solution-processing method to deposit various commercial electron-transport materials. The PhOLEDs with solution-processed ETLs showed superior device performance compared to the devices with vacuum-deposited ETLs. I have found solution-based processing provides a great opportunity to achieve efficient charge-transport properties by tuning the interfacial surface morphology, which cannot be obtained by typical thermal vacuum-processing. I have shown that the nanostructured surface morphology and charge carrier mobility of the electron-transport layers can be tuned and controlled by the solution-processing.

I also have showed for the first time that alkali metal salt doped ETLs can be solution-deposited to fabricate high performance, multi-layered, phosphorescent OLEDs. The solution-processing approach is applicable to diverse electron-transport materials and any desirable metal salt. Blue PhOLEDs with solution-deposited Cs_2CO_3-doped ETLs have a luminous efficiency of 37.7 cd/A with an EQE of 19.0 % at a high brightness 1300 cd/m^2, which is the best performance reported for all-solution-processed blue PhOLEDs. Studies of the surface morphology and electron transport properties of the alkali metal salt doped electron transport layers showed that doping dramatically enhances the electron mobility and modifies the ETL/cathode interface morphology, enabling efficient electron-injection and transport. The results demonstrated that the properties and nanomorphology of the solution-processed ETLs can be fine-tuned by the concentration of the metal salt (M_2CO_3) and type of metal (M = Cs, K, Na, or Li). These findings highlight the effectiveness of orthogonal solution-processing of metal salt-doped ETLs for the fabrication of high-performance multi-layered organic electronic devices.

Additionally, I have investigated new electron transport materials (ETMs) with high triplet energies and wide band gaps. A novel series of sulfone-based ETMs are synthesized, characterized and demonstrated to obtain highly efficient blue PhOLEDs. The combination of a diphenylsulfone core with electron withdrawing end groups such as pyridine, phenylpyridine, and quinoline is found to be effective in achieving a high triplet energy (2.8 – 2.9 eV) and a wide energy gap (3.6 – 3.8 eV), resulting in efficient exciton/hole blocking with good electron-transport characteristics. A new class of dibenzosuberane-based ETMs was also investigated for highly efficient PhOLEDs. New high triplet energy ETMs based on dibenzosuberane which showed substantially high triplet energy (E_T > 3.0 eV) with good thermal and electrochemical properties. Blue PhOLEDs with dibenzosuberane-based ETMs showed significantly improved device performances (CE = 38.1 cd/A and EQE = 20.0 %), demonstrating that these high triplet energy ETMs are a promising class of ETMs with excellent singlet/triplet exciton blocking ability.

Finally, a study of polymer/polymer solar cells was conducted based on two new semicrystalline NDI copolymers (PNDIS, PNDIS-HD) as new polymer acceptors. We found that all-polymer solar cells composed of PNDIS-HD acceptor and PSEHTT donor have a record performance at the time (PCE = 3.3 %, J_{sc} = 7.78 mA/cm^2, and EQE = 47 %), which is comparable to similarly evaluated PSEHTT:$PC_{60}BM$ BHJ solar cells. Balanced electron and hole transport was observed in the PSEHTT:PNDIS-HD blend active layers. The superior photovoltaic properties of PNDIS-HD compared to PNDIS and prior NDI copolymers suggest that unipolar electron transport with high bulk mobility, good crystallinity, size of alkyl side chain, and molecular weight are all important factors in the design of suitable acceptor polymers for BHJ solar cells. Furthermore, a control of polymer blend morphology was demonstrated to

achieve improved photovoltaic properties. The blend morphology was successfully tuned by using co-solvent to obtain nanophase-separated polymer domains. PSEHTT:PNDIS-HD solar cells showed a record efficiency of 4.2 % with J_{sc} = 9.40 mA cm^{-2} and EQE = 56.7 %, which are the highest photovoltaic parameters in all-polymer solar cells reported to date. Enhanced charge separation and transport properties were observed by tuning the polymer blend morphology.

Overall, this work has significantly impacted the development of solution-processing technology, and also added new knowledge to the recent progress made in the area of organic optoelectronics by the scientific and industrical communities. Knowledge and skills obtained from this study provide huge opportunities to achieve enhanced performance and better production of optoelectronic devices for the next generation electronics. Further investigation should be continued to widen our knowledge and achieve deeper understanding to advance the technology in this field.

7.2. Outlook

The field of organic electronics is growing and widely studied as the needs from the society become much more growing than before. For example, organic light-emitting diodes (OLEDs) have been already successfully launched into the market and currently being sold as televisions and moniters (flat panel display), mobile devices (smart phones, touch pads, GPS, biomedical devices, wearable electronics), solid-state lighting and in other various applications such as automobiles, aviation systems, and home appliances, etc. However, major challenges in the field still remain: how to design suitable organic materials and control the related solid-state morphology, how to achieve durability for the improved cycle life, and the most importantly, how to manufacture in a large scale with assured productivity. To address these challenges, a study of solution-based processing and related material designs is essential. Detailed

investigation of structure-processing-property-performance relationship induced by solution-processing will provide better understanding that would lead us to significant advances in this technology.

One example of studies to be done in the very near future would be an application of orthogonal solution-processing to other device architectures. I have only showed orthogonal solution-processing in phosphorescent OLEDs with conventional device structure, but it can be applied to inverted structures as well as other multilayered devices with various materials. Although I have successfully showed in Chapter 4 that electron-transport layers can be easily n-doped by orthogonal solution-processing of alkali metal salts as n-dopants, only a few examples of metal salts have been demonstrated. There are a number of other possible candidates that would work as efficient n-dopants via orthogonal solution-processing. Furthermore, the solution-doping mechanism has not been fully understood yet which I assume it would be pretty much different from what has been established for n-doped system by thermal vacuum evaporation.

Development of new polymer/polymer solar cell systems would be interesting for further studies in organic electronics. Compared to polymer/fullerene solar cells, polymer/polymer solar cells have been reported much less efficient and challenging to fabricate high-performance devices. Nevertheless, regarding the durability and robustness that the system potentially possesses, polymer/polymer blend solar cells are a strong candidate to become the next generation organic solar cells. Toward achievement of highly efficient polymer/polymer solar cells, there are many challenges and questions to be addressed. Electronic/chemical structures, molecular weight, charge transport property, and complimentary absorption spectra of donor/acceptor polymers are the crucial keys to achieve high performance solar cells. I think the processing technique of viscous polymer solution to control the blend morphology plays an

important role to obtain high photovoltaic performance. Not only limited to binary blend of polymers, multi-phase polymer blends can be promising research area to investigate for future photovoltaic devices. Additionally, incorporating various multilayered device architectures as well as organic-inorganic hybrid system would open a new possibility of polymer solar cells for the development of low-cost, scalable future renewable energy sources.

VITA

Taeshik Earmme was born in Pawtucket, Rhode Island, on April 27, 1976. He moved to Seoul, South Korea with his parents at age two and grew up there. He attended Seoul Science High School, a prestigious high school in Korea for gifted students in science. After graduation from high school, he attended Seoul National University and earned a Bachelor of Science and a Master of Science in Chemical Engineering in 1999 and 2001, respectively. He worked at Samsung SDI in the Li-ion Polymer Battery Division, as a technical research personnel for his obligatory Korean military service alternative. After fulfilling his 5-year responsibility, he moved to Seattle, WA and pursued his Ph. D. degree in Chemical Engineering at the University of Washington and performed research on organic optoelectronic devices under the guidance of Professor Samson A. Jenekhe. During his graduate studies, he earned his Master of Science in Chemical Engineering in 2009 and received the Faculty Lecture Award in 2013 from the Department of Chemical Engineering. He is a member of the Materials Research Society, the American Chemical Society, the American Institute of Chemical Engineers, the Electrochemical Society, and the Korean-American Scientists and Engineers Association. He is the co-author of the following publications.

1. **Earmme, T.**; Hwang, Y.-J.; Murari, N. M.; Subramaniyan, S.; Jenekhe, S. A. "All-Polymer Solar Cells with 3.3% Efficiency Based on Naphthalene Diimide-Selenophene Copolymer Acceptor," *J. Am. Chem. Soc.,* **2013***, 135,* 14960-14963.

2. **Earmme, T.**; Jenekhe S. A. "Improved Electron Injection and Transport by Use of Baking Soda as a Low-cost, Air-stable, n-Dopant for Solution-processed Phosphorescent Organic Light-Emitting Diodes," *Appl. Phys. Lett.* **2013**, *102*, 233305. * *Selected for APL: Org. Electron. Photonics, 2013, 6 (6).*

3. **Earmme, T.**; Jenekhe S. A. "Solution-Processed, Alkali Metal-Salt-Doped, Electron-Transport Layers for High-Performance Phosphorescent Organic Light-Emitting Diodes," *Adv. Funct. Mater.* **2012**, *22*, 5126-5136.

4. **Earmme, T.**; Jenekhe, S. A. "High-Performance Multilayered Phosphorescent OLEDs by Solution-Processed Commercial Electron-Transport Materials," *J. Mater. Chem.* **2012***, 22*, 4660-4668. ***** *Selected as* ***HOT PAPER*** *by the Editor.*

5. Ahmed, E.; **Earmme, T.**; Jenekhe, S. A. "New Solution-Processable Electron Transport Materials for Highly Efficient Blue Phosphorescent OLEDs," *Adv. Funct. Mater.* **2011**, *21*, 3889-3899.

6. **Earmme, T.**; Ahmed, E.; Jenekhe, S. A. "Solution-Processed Highly Efficient Blue Phosphorescent Polymer Light-Emitting Diodes Enabled by a New Electron Transport Material," *Adv. Mater.* **2010**, *22*, 4744-4748.

7. Ahmed, E.; **Earmme, T.**; Ren, G.; Jenekhe, S. A. "Novel n-Type Conjugated Ladder Heteroarenes: Synthesis, Self-assembly of Nanowires, Electron Transport, and Electroluminescence of Bisindenoanthrazolines," *Chem. Mater.* **2010**, *22*, 5786-5796.

8. **Earmme, T.**; Ahmed, E.; Jenekhe, S. A. "Highly Efficient Phosphorescent Light-Emitting Diodes by Using an Electron-Transport Materials with High Electron Affinity," *J. Phys. Chem. C.* **2009**, *113*, 18448-18450.

9. Jang, J.; **Earmme, T.** "Interfacial study of polyimide/copper system using silane-modified polyvinylimidazoles as adhesion promoters," *Polymer* **2001**, *42*, 2871-2876.

10. Li, H.; **Earmme T.**; Ren, G.; Saeki, A.; Toshikawa, S.; Murari, N. M.; Subramaniyan, S.; Crane, M. J.; Seki, S.; Jenekhe, S. A. "Beyond Fullerene: Oligobenzodifluoranthene Diimide Acceptors for Efficient Non-Fullerene Organic Photovoltaics," **2014***, submitted.*

11. Hwang, Y. –J.; **Earmme, T.**; Subramaniyan, S.; Jenekhe, S. A.; "Side Chain Engineering of n-Type conjugated Polymer Enhances Photocurrent and Efficiency of All-Polymer Solar Cells," **2014**, *submitted.*

12. **Earmme, T**; Jeon, S. O.; Jenekhe, S. A. "New Sulfone-Based Electron-Transport Materials with High Triplet Energy for Highly Efficient Blue Phosphorescent Organic Light-Emitting Diodes," **2014***, to be submitted.*

13. **Earmme, T**; Jeon, S. O.; Jenekhe, S. A. "Electron-Transport and Ambipolar Host Materials for Fluorescent and Phosphorescent Organic Light-Emitting Diodes, [Review]," **2014**, *in preparation.*

14. **Earmme, T.**; Hwang, Y.-J.; Subramaniyan, S.; Jenekhe, S. A. "Enhanced Performance of All-Polymer Solar Cells with 4.8 % Efficiency Achieved by Control of Blend Morphology," **2014***, in preparation.*

15. Hwang, Y. –J.; **Earmme, T.**; Murari, N. M.; Jenekhe, S. A. "Miscibility, Phase Separation, and Photovoltaic Properties of Naphthalene Diimide Copolymer/Poly(3-hexylthiophene) Blends," *in preparation.*

16. Subramaniyan, S.; **Earmme, T.**; Murari, N. M.; Hwang, Y. –J.; Jenekhe, S. A. "New Naphthobisthiazole diimide-based n-Channel Polymer Semiconductors,", *in preparation.*

17. Li, H.; **Earmme, T.**; Ren, G.; Murari, N. M.; Kim, F. S.; Subramaniyan, S.; O'Brian, C.; Jenekhe, S. A. Tetraazabenzodifluoranthene Diimide Copolymers as an Efficient Acceptor for All-Polymer Solar Cells," *in preparation*.

18. Murari, N. M.; **Earmme, T.**; Hwang, Y. –J.; Jenekhe, S. A. "Evidence of Thermally Induced Vertical Phase Segregation in Polymer/Polymer Bulk Heterojunction Photovoltaic Cells," *in preparation.*

19. Ahmed, E.; Briseno, A. L.; Kim, F. S.; **Earmme, T.**; Qi, Y.; Kim, E.-G.; Brédas, J. L.; Kahn, A.; Jenekhe, S. A. "New Class of Organic Semiconductors Based on Indoloquinolines: Synthesis, Self-assembly, Electronic Structure, Charge Transport and Light-Emitting Diodes," *in preparation*.